

***Catalysts Based on 2D Layered Supports: Influence of  
a Sandwich Confinement on Catalysis and Stability of  
Nanoparticles***

**Doctoral Thesis**

submitted to obtain the academic degree of Doctor of Natural Sciences

(Dr. rer. nat.)

of the Bayreuth Graduate School of Mathematical and Natural Sciences

(BayNAT)

of the University of Bayreuth

***Kevin Ament***

from *Lichtenfels*

Bayreuth, 2021



This doctoral thesis was prepared at the Department of Inorganic Chemistry I (ACI) at the University of Bayreuth from 11/2016 until 03/2021 and was supervised by Prof. Dr. Josef Breu.

This is a full reprint of the thesis submitted to obtain the academic degree of Doctor of Natural Science (Dr. rer. nat.) and approved by the Bayreuth Graduate School of Mathematical and Natural Sciences (BayNAT) of the University of Bayreuth.

Date of submission: 12.03.2021

Date of defence: 03.03.2022

Acting director: Prof. Dr. Hans Keppler

Doctoral committee:

Prof. Dr. Josef Breu (reviewer)

Prof. Dr. Rhett Kempe (reviewer)

Prof. Dr. Andreas Greiner (chairman)

Prof. Dr. Markus Retsch



Our greatest weakness lies in giving up.

The most certain way to succeed is always to try just one more time.

**Thomas Alva Edison**



Meiner Oma Helga



# Content

1	Summary.....	1
2	Zusammenfassung.....	3
3	Introduction .....	5
3.1	Fundamentals about layered materials.....	5
3.1.1	Synthetic sodium hectorite .....	6
3.1.2	Delamination of NaHec .....	7
3.1.3	Synthetic layered lepidocrocite-type titanate .....	8
3.1.4	Delamination of H <sup>+</sup> -L-titanate .....	9
3.2	Fundamentals about nanoparticles.....	11
3.2.1	Dispersion and quantum effects .....	11
3.2.2	Synthesis strategies for nanoparticles .....	12
3.3	Layered materials as supports for nanoparticles .....	14
3.3.1	Layered silicates as supports .....	14
3.3.2	Layered titanates as supports .....	17
3.4	Fundamentals of catalysis .....	19
3.4.1	Interaction of nanoparticles and supports .....	19
3.4.2	Learning from layered model systems .....	21
3.4.3	Oxidation catalysis .....	23
3.5	Hydrogen storage.....	25
3.6	Scope of this thesis .....	26
4	Synopsis .....	27
4.1	High Temperature Stable Maghemite Nanoparticles Sandwiched between Hectorite Nanosheets .....	29
4.2	Nanoparticles Supported on Sub-Nanometer Oxide Films: Scaling Model Systems to Bulk Materials .....	33
4.3	Enhancing Hydrogen Storage Capacity of Pd Nanoparticles by Sandwiching between Inorganic Nanosheets .....	37

## Content

---

4.4 Enhancing the Catalytic Activity of Palladium Nanoparticles via Sandwich-Like Confinement by Thin Titanate Nanosheets .....	40
5 Literature .....	44
6 Results .....	53
6.1 High Temperature Stable Maghemite Nanoparticles Sandwiched between Hectorite Nanosheets .....	53
6.1.1 Supporting Information .....	60
6.2 Nanoparticles Supported on Sub-Nanometer Oxide Films: Scaling Model Systems to Bulk Materials .....	65
6.2.1 Nanoparticles Supported on Sub-Nanometer Oxide Films: Scaling Model Systems to Bulk Materials (International Edition) .....	67
6.2.2 Nanopartikel auf subnanometer dünnen oxidischen Filmen: Skalierung von Modellsystemen (German Edition) .....	75
6.2.3 Supporting Information .....	83
6.3 Enhancing Hydrogen Storage Capacity of Pd Nanoparticles by Sandwiching between Inorganic Nanosheets .....	99
6.3.1 Supporting Information .....	106
6.4 Enhancing the Catalytic Activity of Palladium Nanoparticles via Sandwich-Like Confinement by Thin Titanate Nanosheets .....	114
6.4.1 Supporting Information .....	124
7 List of publications .....	142
7.1 First author publications .....	142
7.2 Additional publications .....	142
7.3 Conference contributions .....	143
8 Acknowledgements .....	144
9 Erklärung des Verfassers .....	146

## List of Abbreviations

---

### List of Abbreviations

2D	2 dimensional
AFM	Atomic force microscopy
at%	Atomic percent
BE	Binding energy
cec	Cation exchange capacity
CHN	Elemental analysis of the elements C, H, and N
<i>d</i> spacing	Distance from the beginning of one layer to the next layer
DEG	Diethylene glycol
DFT	Density functional theory
DMAP	4-Dimethylaminopyridine
DSC	Differential scanning calorimetry
DOS	Density of states
E <sub>A</sub>	Apparent activation energy
EELS	Electron energy loss spectroscopy
EMSI	Electronic metal-support interaction
fcc	Face-centred cubic
hcp	Hexagonal close-packed
H <sup>+</sup> -L-titanate	Protonated layered titanate ( $\text{H}_{1.07}\text{TiO}_{1.73}\text{O}_4\cdot\text{H}_2\text{O}$ )
HOMO	Highest occupied molecular orbital
IRAS	Infrared reflection absorption spectroscopy
LUMO	Lowest unoccupied molecular orbital
N	Amount of atoms per nanoparticle
NaHec	Sodium hectorite $\text{Na}_{0.5}[\text{Mg}_{2.5}\text{Li}_{0.5}]<\text{Si}_4>\text{O}_{10}\text{F}_2$
p.f.u.	per formula unit
PVP	Polyvinylpyrrolidone
PXRD	Powder X-ray diffraction
r.h.	Relative humidity
SEM	Scanning electron microscopy
SEM-EDX	SEM coupled with energy-dispersive X-ray spectroscopy
SMSI	Strong metal-support interaction
STM	Scanning tunneling microscopy
T <sub>x</sub>	Temperature of x % conversion
TBAOH	Tetrabutylammonium hydroxide
TEM	Transmission electron microscopy
TMAOH	Tetramethylammonium hydroxide
wt%	Weight percent
XPS	X-ray photoelectron spectroscopy

## 1 Summary

Within the scope of this thesis, a modular strategy for intercalating nanoparticles between 2D layered materials was successfully developed. In particular, the synthetic layered silicate hectorite ( $\text{Na}_{0.5}\text{Mg}_{2.5}\text{Li}_{0.5}\text{Si}_4\text{O}_{10}\text{F}_2$ , NaHec) and a layered titanate ( $\text{H}_{1.07}\text{TiO}_{1.73}\text{O}_4 \cdot \text{H}_2\text{O}$ , L-titanate) were investigated for their potential use as catalyst supports. Both are layered materials with a permanent negative layer charge, neutralized by interlayer cations. Furthermore, when immersed in water, these materials form nematic liquid crystalline phases of sub-nanometer thick single nanosheets. Even at low solid contents and distances of more than 50 nm, the nanosheets retain a co-facial orientation to each other due to their large lateral platelet size. Pre-synthesized nanoparticles carrying a positive surface charge can be added to such a nematic phase, and the large gallery height of adjacent nanosheets allows nanoparticles to diffuse between the nanosheets, whereupon the nanosheets collapse and capture the nanoparticles. This process could be seen as a "quasi-ion exchange," and a special catalyst architecture can be obtained: nanoparticles sandwiched between two sub-nanometer thick oxide sheets.

2D layered materials such as layered silicates have already been applied as catalyst supports before, but the use of natural materials that are very heterogeneous and defective or insufficient synthesis methods hampered access to well-structured catalysts. For this reason, the influence of the confinement on the (catalytic) properties of the sandwiched nanoparticles has not been investigated deeply. In contrast, the "quasi-ion exchange" method described above using a nematic phase of the nanosheets and pre-synthesized nanoparticles leads to well-defined architectures.

This thesis demonstrates that the very special sandwich architecture offers great potential regarding increased temperature stability and influencing the electronic structure of nanoparticles, leading to enhanced catalytic activity for CO oxidation and increased H<sub>2</sub> sorption capacity.

In the first part of the presented work,  $\gamma\text{-Fe}_2\text{O}_3$  nanoparticles were synthesized that were colloidally stable in aqueous dispersion and carried a positive surface charge. These nanoparticles were sandwiched between the nanosheets of a nematic NaHec dispersion. Even though the loading of iron oxide was 64 wt%, a lamellar and mesoporous structure was obtained. The sandwich-like confinement stabilized the nanoparticles and hampered Ostwald ripening up to 700 °C, whereas rapid growth of unsupported nanoparticles was observed already at 400 °C. Additionally, the confinement suppressed the phase transition from  $\gamma\text{-Fe}_2\text{O}_3$  to  $\alpha\text{-Fe}_2\text{O}_3$ , normally occurring at 300 °C. Changed thermodynamic phase stabilities of nano-sized iron oxide were responsible for this effect.

## Summary

---

In the second part, the portfolio of nanoparticles that can be intercalated between the nanosheets of a nematic NaHec phase was extended to Pd nanoparticles. The surface potential of these nanoparticles was adjusted by pH that allowed the control of the intercalated loading of nanoparticles. The obtained structure was a potential “bulk version” of literature known model catalysts of flat metal surfaces that were (partially) covered with an ultrathin ( $< 1 \text{ nm}$ ) oxide layer. As a test reaction, CO was oxidized to  $\text{CO}_2$ . The sandwiched Pd nanoparticles proved to be more active than the same nanoparticles deposited on the conventional support  $\gamma\text{-Al}_2\text{O}_3$  (temperature of 50 % conversion  $T_{50}$  of 145 °C and 191 °C, respectively). Electronic interactions between nanoparticles and nanosheets rendered the nanoparticle surface slightly positively charged, which was identified as the reason for the enhanced catalytic activity.

The electron-deficient Pd nanoparticles were investigated for other possible applications in the third part of the thesis. It is known from the literature that the  $\text{H}_2$  sorption capacity of Pd nanoparticles is related to the number of holes in the band structure near the Fermi level.  $\text{H}_2$  pressure-dependent uptake curves and *in situ* X-ray diffraction demonstrated that sandwiching Pd nanoparticles between nanosheets significantly influenced the sorption behaviour. The maximum storage capacity of  $\text{H}_2$  was increased by 86 % compared to identic Pd nanoparticles covered with polyvinylpyrrolidone.

In the last part, the intercalation strategy using a nematic phase of a 2D layered material was extended to L-titanate. As observed for NaHec, electronic interactions between support and Pd rendered the surface of Pd positively charged. However, the catalytic activity for the oxidation of CO proceeded already below 100 °C ( $T_{50}$  of 86 °C). That implied that L-titanate provided an additional enhancing effect for oxidation catalysis besides electronic influence. Kinetic experiments revealed that L-titanate could donate activated oxygen from its lattice at the support/metal interface (Mars-van Krevelen type mechanism). This bypassed CO poisoning of the noble metal surface at low temperatures. The special sandwich architecture was also of great importance for the enhanced catalytic activity. As the nanoparticles were in touch with the support from two directions, a particularly high interface was generated, making oxygen donation very efficient.

The thesis is presented as a cumulative work. The results are discussed in detail in the attached manuscripts.

## 2 Zusammenfassung

Im Rahmen dieser Arbeit wurde eine modulare Strategie für die Interkalation von Nanopartikeln zwischen 2D-Schichtmaterialien entwickelt. Als Schichtmaterialien wurden das synthetische Schichtsilikat Hectorit ( $\text{Na}_{0.5}\text{Mg}_{2.5}\text{Li}_{0.5}\text{Si}_4\text{O}_{10}\text{F}_2$ , NaHec) und ein schichtförmiges Titanat ( $\text{H}_{1.07}\text{TiO}_{1.73}\text{O}_4 \cdot \text{H}_2\text{O}$ , L-titanate) verwendet und deren Potential als katalytisches Trägermaterial untersucht. Beide Materialien bestehen aus Schichten mit einer permanenten negativen Schichtladung und Kationen zur Ladungsneutralität zwischen den Schichten. Sie bilden in Wasser nematische flüssigkristalline Phasen aus (sub)nanometerdicken einzelnen Nanoschichten aus. Selbst bei niedrigen Feststoffgehalten und Distanzen von über 50 nm behalten die Nanoschichten aufgrund ihrer hohen lateralen Ausdehnung eine co-faciale Orientierung zueinander. Bei Zugabe von Nanopartikeln mit positivem Oberflächenpotential zu einer solchen nematischen Dispersion können Nanopartikel zwischen die Schichten diffundieren, die von den daraufhin kollabierenden Nanoschichten stabilisiert werden. Dies entspricht einem "Quasi-Ionenaustausch". Durch diese Syntheseroute wird ein Zugang zu einer speziellen Katalysatorarchitektur ermöglicht: Nanopartikel, die zwischen zwei (sub)nanometer dicken Oxidschichten eingeklemmt sind.

Schichtsilikate wurden bereits vielfältig als Nanopartikelträger eingesetzt, jedoch verhinderten die Verwendung von natürlichem Material oder unzureichende Synthesemethoden den Zugang zu gut strukturierten Katalysatoren. Aus diesem Grund konnte der Einfluss des *confinements* auf die (katalytischen) Eigenschaften der Nanopartikel nicht detailliert untersucht werden. Die oben beschriebene Methode des „Quasi-Ionenaustausches“, die eine nematische Phase der 2D-Schichtmaterialien ausnutzt, führt hingegen zu gut definierten Architekturen der sandwichartig assemblierten Nanopartikel.

Diese Arbeit zeigt, dass die besondere Sandwich-Architektur ein großes Potential bietet, da sie nicht nur die Temperaturstabilität der Nanopartikel erhöhte, sondern auch Einfluss auf deren elektronische Struktur nahm, was zu einer erhöhten katalytischen Aktivität sowie zu einer erhöhten  $\text{H}_2$ -Sorptionskapazität führte.

Im ersten Teil der Arbeit wurden  $\gamma\text{-Fe}_2\text{O}_3$ -Nanopartikel synthetisiert, die in Wasser kolloidal stabil waren und eine positive Oberflächenladung trugen. Diese Nanopartikel wurden zwischen die Nanoschichten einer nematischen NaHec-Dispersion interkaliert. Obwohl die Beladung mit Eisenoxid 64 wt% betrug, wurde eine lamellare und mesoporöse Struktur erhalten. Die sandwichartige Architektur stabilisierte die Nanopartikel und unterdrückte die Ostwald-Reifung bis 700 °C. Bei unstabilisierten Nanopartikeln wurde ein rasches Wachstum bereits bei 400 °C beobachtet. Zusätzlich wurde auch der Phasenübergang von  $\gamma\text{-Fe}_2\text{O}_3$  zu  $\alpha\text{-Fe}_2\text{O}_3$ , der

## Zusammenfassung

---

normalerweise bei Temperaturen um 300 °C beginnt, unterdrückt. Dieser Effekt wurde mit veränderten thermodynamischen Phasenstabilitäten von Eisenoxid auf der Nanoebene erklärt.

Das Portfolio an interkalierbaren Nanopartikeln wurde im zweiten Teil um Pd-Nanopartikel erweitert. Das Oberflächenpotential dieser Nanopartikel konnte durch den pH-Wert eingestellt werden, was wiederum die Kontrolle über die Beladung an interkalierten Nanopartikeln ermöglichte. Die erhaltene Struktur konnte als eine "Bulk-Version" von literaturbekannten Modellkatalysatoren gesehen werden, die aus Metalloberflächen bestehen, die (partiell) mit einer ultradünnen (< 1 nm) Oxidschicht bedeckt sind. Um den Einfluss der Sandwich-Architektur zu studieren, wurde als Testreaktion CO zu CO<sub>2</sub> katalytisch oxidiert. Die sandwichartig stabilisierten Pd-Nanopartikel erwiesen sich als deutlich aktiver als identische Nanopartikel, die auf dem konventionellen Träger γ-Al<sub>2</sub>O<sub>3</sub> abgeschieden wurden (Temperatur bei 50 % Umsatz T<sub>50</sub> von 145 °C zu 191 °C). Die elektronischen Wechselwirkungen zwischen Nanopartikeln und Nanoschichten führten zu einer leicht positiven Ladung der Nanopartikeloberfläche, die als Ursache für die hohe katalytische Aktivität identifiziert wurde.

Die elektronendefizitären Pd-Nanopartikel wurden im dritten Teil der Arbeit für andere mögliche Anwendungen wie der Wasserstoffspeicherung untersucht. Es ist bekannt, dass die H<sub>2</sub>-Sorptionskapazität von Pd-Nanopartikeln mit der Anzahl an Löchern in der Bandstruktur nahe dem Fermi-Niveau korreliert. Druckabhängige H<sub>2</sub> Aufnahmekurven und *in situ* Röntgenbeugung zeigten, dass die Einlagerung von Pd-Nanopartikeln einen signifikanten Einfluss auf das Sorptionsverhalten hatte. Die Speicherkapazität von H<sub>2</sub> wurde im Vergleich zu analogen Pd-Nanopartikeln, die mit einem Polymer bedeckt waren, um 86 % erhöht.

Im letzten Teil wurde die Interkalationsstrategie unter Verwendung einer nematischen Phase eines 2D-Schichtmaterials auf L-titanate angewendet. Wie bei NaHec beobachtet wurde, führten Wechselwirkungen zwischen Träger und Pd zu einer positiv geladenen Pd Oberfläche. Die katalytische Oxidation von CO verlief hier jedoch bereits unterhalb von 100 °C (T<sub>50</sub> von 86 °C), was implizierte, dass L-titanate neben dem elektronischen Einfluss einen zusätzlichen Effekt auf die Oxidationskatalyse hatte. Kinetische Experimente zeigten, dass L-titanate in der Lage war, aktivierten Sauerstoff aus seinem Gitter an der Träger/Metall-Grenzfläche zu übertragen (Mars-van Krevelen-Mechanismus). Dadurch konnte die CO-Vergiftung der Edelmetalloberfläche bei niedrigen Temperaturen umgangen werden. Die spezielle Sandwich-Architektur war ebenfalls von großer Bedeutung für die hohe katalytische Aktivität. Da die Nanopartikel in Kontakt mit zwei Trägeroberflächen standen, wurde eine besonders hohe Grenzfläche erzeugt, die die Sauerstoffübertragung sehr effizient machte.

Diese Arbeit wird als kumulative Arbeit präsentiert. Die Ergebnisse werden in den beigefügten Manuskripten ausführlich diskutiert.

### 3 Introduction

#### 3.1 Fundamentals about layered materials

Layers can often describe the structure of crystalline solids, but truly layered materials are only these materials that have anisotropic bonding properties. A well-known example is graphite that consists of stacked layers of carbon atoms. The carbon atoms are covalently bound within each layer and are arranged in a hexagonal pattern with a C-C distance of 1.42 Å. The layers are stacked in an AB manner, and weak van der Waals forces bind adjacent carbon layers. The C-C distance between layers is 3.35 Å. The differences in the binding situations result in different physical properties parallel and perpendicular to the layers.<sup>[1]</sup> Due to the weak bonds between adjacent layers of graphite, it can be stripped into single layers (graphene) by applying the scotch tape method.<sup>[2]</sup>

Layered materials can be classified by different aspects, such as structure or composition. Furthermore, they can be divided by the charge of their layers. For instance, hexagonal boron nitride (*h*-BN)<sup>[3]</sup> or graphite carry no charge, while layered double hydroxides<sup>[4]</sup> or layered silicates can carry a permanent positive or negative layer charge, respectively.<sup>[5]</sup> For charged layers, ions of opposite charge are necessary between the layers to serve for charge balance. These so-called interlayer ions can be (reversibly) exchanged for other ions (atomic ions, charged organic molecules, or charged clusters) and provide a useful toolbox to synthesize heterogeneous materials with reactive interlayer spaces.

Since an individual layer of a material can behave significantly different from a tactoid of stacked layers, another essential classification parameter of layered materials is their ability to be separated into stacks of only a few layers (exfoliation) or single layers (delamination).<sup>[6]</sup> Individual layers are often called nanosheets, as named for the first time by T. Sasaki in 1996.<sup>[7]</sup> The process to overcome the forces between adjacent layers is very important but can vary for various layered materials. As already mentioned, graphite layers can be separated mechanically by the scotch tape method.<sup>[2]</sup> Other materials such as layered silicates show the ability to swell osmotically in water.<sup>[8]</sup> The solid content in dispersion and the ionic background are two criteria to control the distance between adjacent individual layers and can exceed several tens of nanometers. The ability of a 2D layered material to delaminate is also of utmost importance for the main topic of this thesis as intercalation of nanoparticles without significant kinetic hindrance is only possible at reasonable high distances of adjacent nanosheets.

The phenomenon of osmotic swelling, together with a structural introduction of the materials, will be discussed in the following chapters on the examples of NaHec (**Chapter 3.1.1** and **3.1.2**) and L-titanate (**Chapter 3.1.3** and **3.1.4**).

### 3.1.1 Synthetic sodium hectorite

Synthetic sodium hectorite (NaHec) with the nominal composition of  $\text{Na}_{0.5}^{\text{interlayer}}(\text{Mg}_{2.5}\text{Li}_{0.5})^{\text{oct}}\text{Si}_4^{\text{tet}}\text{O}_{10}\text{F}_2$  belongs to the class of 2:1 layered silicates. A layer consists of two sheets of corner-sharing  $\text{SiO}_4$  tetrahedrons with a layer of edge-sharing  $\text{MgX}_6$  ( $\text{X} = \text{O}^{2-}$ ,  $\text{F}^-$ ) octahedrons in between. The tetrahedral sheets are condensed to the octahedral sheet via their apical oxygen ions. Isomorphous substitution of  $\text{Mg}^{2+}$  for  $\text{Li}^+$  generates a permanent negative layer charge.  $\text{Na}^+$  cations balance this layer charge in the interlayer space, but it can be synthesized with other cations such as  $\text{Li}^+$ ,  $\text{K}^+$ , and  $\text{Cs}^+$ , as well.<sup>[9]</sup> Having a layer charge of 0.5 per formula unit (p.f.u.), NaHec belongs to the class of smectites (range of 0.2 to 0.6 charge p.f.u.). The tetrahedrons form a kagome type lattice with hexagonal cavities where the interlayer  $\text{Na}^+$  cations fit in. The amount of apical oxygen ions is not sufficient to saturate the octahedral layers.  $\text{F}^-$  occupies the missing positions to complete the anion lattice. The total thickness of one lamella of NaHec is 9.6 Å (**Figure 1**). Charge homogeneity within the layer is of great importance concerning osmotic swelling and intracrystalline reactivity. Therefore, the isomorphous substitution of  $\text{Mg}^{2+}$  for  $\text{Li}^+$  must happen statistically. Above a synthesis temperature of 1000 K, the octahedral cations arrange completely statistically to a solid solution.<sup>[10]</sup> Hence, the used NaHec in this work was synthesized via melt synthesis at 1750 °C and annealed at 1045 °C for six weeks.<sup>[11, 12]</sup> The obtained NaHec demonstrates a very homogeneous intracrystalline reactivity and is superior over natural layered silicates such as montmorillonite (another prominent representative of smectites) that is very heterogeneous, defective, and has lateral extensions of only 200 nm (~ 20000 nm for NaHec).<sup>[13]</sup>

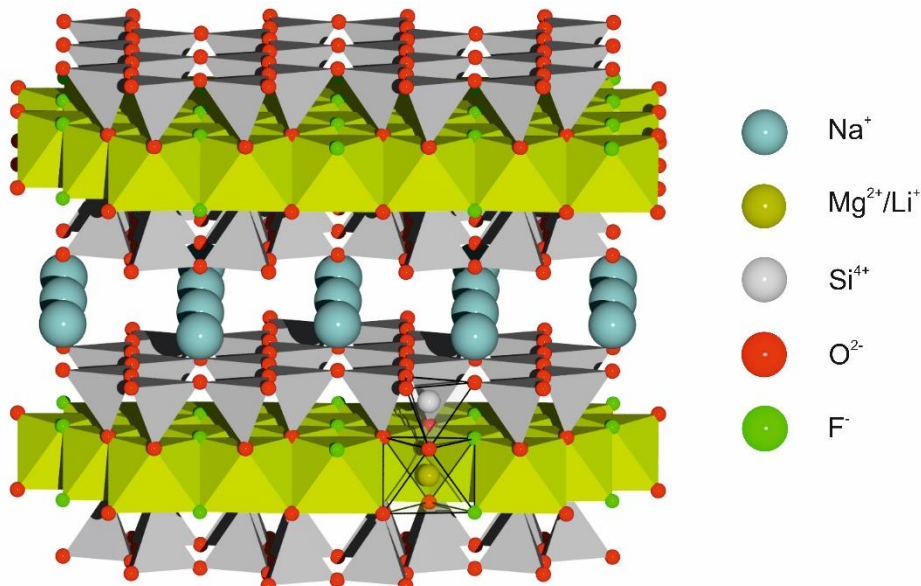


**Figure 1:** Sketch of the structure of NaHec:  $\text{Mg}^{2+}$  and  $\text{Li}^+$  (yellow) are randomly distributed in the centre of the octahedrons.  $\text{Si}^{4+}$  (grey) is in the centre of the tetrahedrons.  $\text{O}^{2-}$  (red) and  $\text{F}^-$  (green) build the anion lattice.  $\text{Na}^+$  (pale blue) is between the layers.

The homogeneous intracrystalline reactivity features several advantages that cannot or only partially be observed for natural layered silicates: NaHec swells spontaneously in water and delaminates easily into single nanosheets. The high temperature synthesis yields very large platelets with lateral dimensions of about 20 µm. Delamination to single nanosheets of subnanometer size leads to an aspect ratio of about 20.000. The large aspect ratio makes NaHec very promising as an additive for polymer films in gas barrier applications.<sup>[14-17]</sup> The interlayer cations can be exchanged for organic molecules to obtain a material class called “microporous organically pillared layered silicates” (MOPS).<sup>[18-22]</sup> As the layer charge is very homogenous, an ordered interlayer structure with well-defined pores can be obtained that is very promising for gas separation applications.<sup>[18-22]</sup> Furthermore, NaHec offers the unique possibility to synthesize ordered heterostructures with two alternating interlayer species.<sup>[23-25]</sup>

### 3.1.2 Delamination of NaHec

As mentioned before, interlayer cations of NaHec can be exchanged for other (small) organic or inorganic cations even in the crystalline and stacked state. In contrast, intercalation of larger molecules such as polymer chains requires an increased distance of the nanosheets to avoid kinetic hindrance.<sup>[27]</sup> This also applies to the intercalation of nanoparticles that is the objective of this thesis. Therefore, osmotic swelling in water can increase the distance of adjacent nanosheets to tens of nanometers. Delamination to individual nanosheets appears when the attractive interaction between negatively charged layers and positively charged interlayer cations can be overcome. The swelling behaviour of NaHec is well understood and is divided into three stages/regimes (**Figure 2**).<sup>[26]</sup>

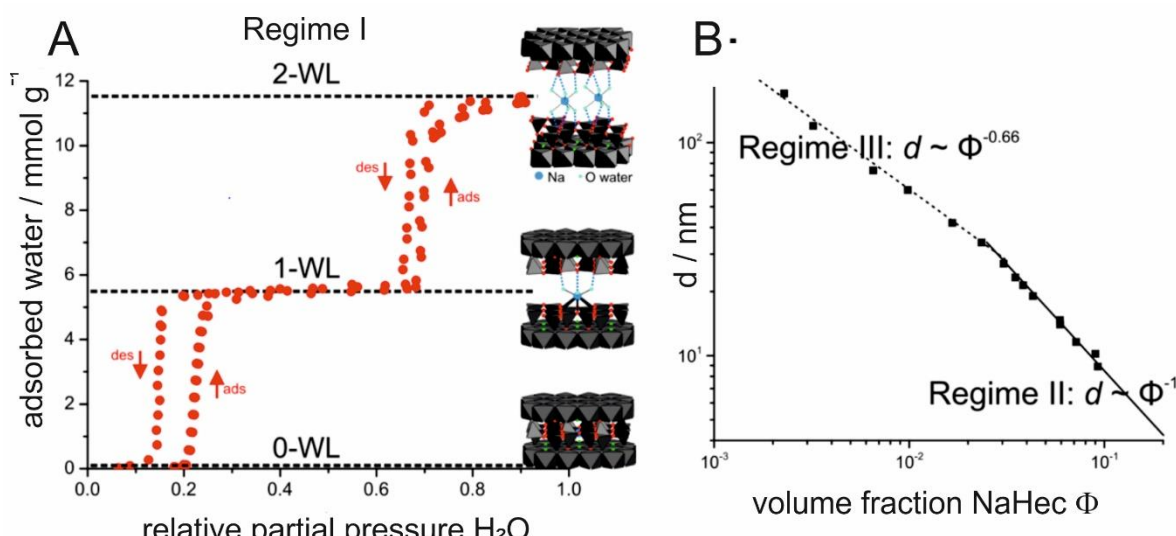


**Figure 2:** Illustration of the three regimes of swelling of synthetic NaHec. A) Water sorption isotherm depending on the relative partial pressure of H<sub>2</sub>O in air (Regime I/crystalline swelling). b)  $d$ -values (layer distances) as a function of the volume fraction of NaHec in liquid H<sub>2</sub>O. The transition from Regime II to Regime III occurs at the kink of the continuous and dashed lines. [Adapted with permission from reference<sup>[26]</sup>. Copyright (2016) American Chemical Society]

The first regime (**Figure 2A**) is called crystalline swelling and depends on the water activity in the air (relative humidity, r.h.).  $\text{Na}^+$  possesses a high hydration enthalpy making NaHec highly hygroscopic.<sup>[28]</sup> Air of about 22 % r.h. is already sufficient to form one water layer in the interlayer space. Three water molecules and three basal oxide ions coordinate  $\text{Na}^+$ .<sup>[29]</sup> At a r.h. of about 70 %, a second water layer forms, and six water molecules coordinate  $\text{Na}^+$ .<sup>[29]</sup> From dry NaHec powder to the one-layer hydrate and the two-layer hydrate, the distance between the layers increases from 0 Å to 2.7 Å to 4.5 Å, respectively.

Further increase of the layer distance can be achieved by swelling in liquid water (**Figure 2B**). Here, the volume fraction  $\Phi$  of NaHec in water determines the distance of the nanosheets. Osmotic swelling can be further divided into two regimes and appears only at a layer charge of 0.55 p.f.u and below. Up to a  $\Phi$  of 2.5 vol% (corresponding to about 7 wt% or a nanosheet distance  $d$  of about 30 nm), the distance of the nanosheets scales linearly with  $d \sim \Phi^{-1}$ .<sup>[26]</sup> This is called the Gouy-Chapman regime, and the NaHec dispersion forms a so-called Wigner crystal.<sup>[26]</sup> This Wigner crystal is characteristic of a highly ordered orientation of parallel aligned nanosheets. Due to the strong repulsive forces, the nanosheets maximize their distance. Even though a layer distance of 30 nm might be sufficiently high to allow nanoparticles below 5 nm core diameter to diffuse between the nanosheets, the large platelets form a very viscous gel, which hampers a fast diffusion. At higher dilutions (< 2.5 vol%), repulsive forces are more and more screened, and the nanosheets start to tilt and form the last regime with a dependence of  $d \sim \Phi^{-0.66}$ .<sup>[26]</sup> However, the high aspect ratio prohibits free rotation and no isotropic phase forms. Instead, even at dilutions as low as 0.5 vol% (1.5 wt%) corresponding to a layer distance of about 60 nm, the nanosheets are still held in a co-facial arrangement forming a nematic liquid crystalline phase. At this stage, the viscosity is sufficiently low for a fast nanoparticle diffusion between the wide-opened galleries of adjacent nanosheets.

### 3.1.3 Synthetic layered lepidocrocite-type titanate

Other layered materials with a permanent negative layer charge are layered transition metal oxides such as layered titanates. These were already investigated as battery material<sup>[30]</sup>, photo<sup>[31]</sup>, and electro<sup>[32]</sup> catalysts. Layered titanates are related to the lepidocrocite family ( $\gamma\text{-FeOOH}$ ) with a general formula of  $\text{A}_x\text{Ti}_{2-y}\text{O}_4\text{M}_y$  ( $\text{A} = \text{K}^+, \text{Cs}^+, \text{Rb}^+, \text{H}^+$ ;  $\text{M} = \text{Li}^+$  or vacancy  $\square$ ;  $x = 0.7\text{--}0.8$ ). The used layered titanate for this work had the formula  $\text{H}_{1.07}\text{Ti}_{1.73}\square_{0.27}\text{O}_4\cdot\text{H}_2\text{O}$  (further abbreviated as  $\text{H}^+\text{-L-titanate}$ ).<sup>[33, 34]</sup> The individual layer consists of a double layer of edge-sharing  $\text{TiO}_6$  tetrahedrons with  $\text{Ti}^{4+}$  vacancies creating a negative layer charge, balanced by interlayer cations (**Figure 3**).

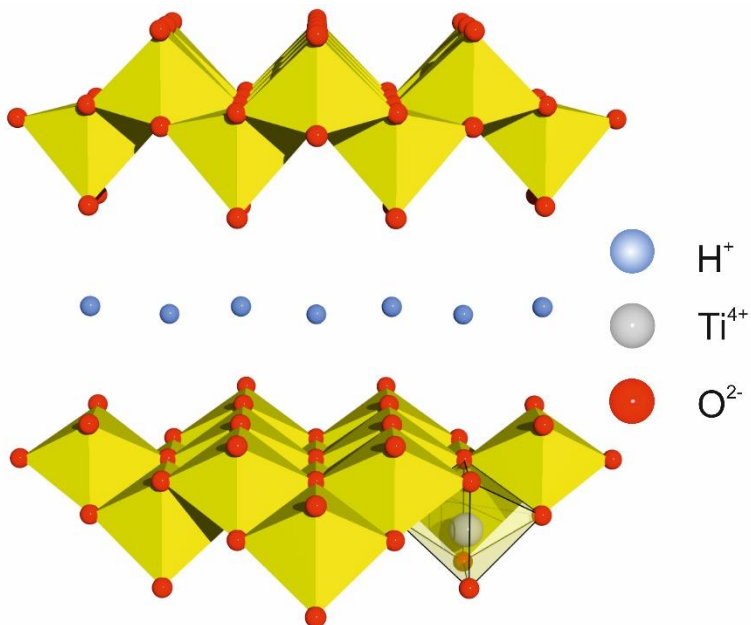


**Figure 3:** Sketch of the structure of lepidocrocite-type layered titanate.  $\text{Ti}^{4+}$  (grey) is coordinated by six oxygen ions. The octahedrons share edges.  $\text{H}^+$  balances the layer charge. It should be noted that actually  $\text{H}_3\text{O}^+$  molecules balance the layer charge.

The synthesis of  $\text{H}^+$ -L-titanate proceeds in two steps. The first one is a solid-state synthesis of  $\text{TiO}_2$ ,  $\text{K}_2\text{CO}_3$ , and  $\text{Li}_2\text{CO}_3$  at 1073 K to obtain  $\text{K}_{0.8}\text{Ti}_{1.73}\text{Li}_{0.27}\text{O}_4$ .<sup>[35]</sup> At this stage of the synthesis,  $\text{Li}^+$  occupies some octahedral positions, and  $\text{K}^+$  is the interlayer cation.  $\text{Li}^+$  is leached out by treatment with 0.5 M HCl and leaves  $\square$  vacancies in the octahedral lattice.  $\text{H}_3\text{O}^+$  between the layers serves for charge balance.<sup>[36]</sup>  $\text{H}_3\text{O}^+$  can be exchanged for other inorganic or organic cations, essential for the delamination process (**Chapter 3.1.4**).

### 3.1.4 Delamination of $\text{H}^+$ -L-titanate

Osmotic swelling is not restricted to NaHec but is known for other 2D layered materials<sup>[8, 37-39]</sup>, and L-titanate is chosen as a second example to explain this phenomenon. NaHec delaminates spontaneously in water, which can be ascribed to the high hydration enthalpy of  $\text{Na}^+$  and a sufficient layer charge of 2.1 charges per  $1 \text{ nm}^2$ . A hectorite with a nominal formula of  $\text{Na}_{0.6}^{\text{interlayer}}(\text{Mg}_{2.4}\text{Li}_{0.6})^{\text{oct}}\text{Si}_4^{\text{tet}}\text{O}_{10}\text{F}_2$  having a higher density of charges cannot delaminate in water anymore due to too strong attractive forces between layer and interlayer cations.  $\text{H}^+$ -L-titanate has a layer charge of 7.1 charges per  $1 \text{ nm}^2$ , making spontaneous delamination in water impossible. However, delamination can be achieved for higher charged layered materials when the layer distance exceeds a critical value (Gouy-Chapman length).<sup>[26]</sup> After exceeding this length, the hydration enthalpy of the interlayer cation overcomes the Coulomb attraction, and the interaction between adjacent nanosheets becomes repulsive.<sup>[40, 41]</sup> Bulky organic molecules with a sufficient high hydration enthalpy are required to increase the distance between two layers over this Gouy-Chapman length. Tetrabutylammonium TBA $^+$  or tetramethylammonium TMA $^+$  are suitable for the delamination of L-titanates.<sup>[35, 42]</sup>  $\text{H}^+$ -L-titanate immersed in a TBA $^+\text{OH}^-$  solution starts to swell and ultimately delaminates to individual

nanosheets after mechanical shaking.<sup>[43]</sup> The nanosheet distance can be controlled by changing the ionic background (ratio of H<sup>+</sup> to TBA<sup>+</sup> added).<sup>[43]</sup> At low ionic backgrounds and high nanosheet separations, a nematic liquid crystalline phase forms, showing structural colours.<sup>[44]</sup> Furthermore, TMA<sup>+</sup> leads to nanosheets of lateral expansions of up to 10 µm, while delamination via TBA<sup>+</sup> leads to 500 nm-sized platelets.<sup>[45]</sup> In the presented work, TBA<sup>+</sup> was used to delaminate H<sup>+</sup>-L-titanate to a nematic phase for Pd nanoparticle intercalation in **Chapter 6.4.**

## 3.2 Fundamentals about nanoparticles

### 3.2.1 Dispersion and quantum effects

Apart from the support that can significantly affect catalytic properties (see **Chapter 3.4**), the catalytically active nanoparticles are of great importance for the overall catalysts. The reasons for the high catalytic activity of nanoparticles are discussed in this chapter.

Nanoparticles offer new perspectives for material and catalytic science and gained much scientific interest in the past decades. The chemical and physical properties of a nanoparticle can be remarkably altered compared to the bulk.<sup>[46]</sup> According to the IUPAC definition, a nanoparticle is “a particle of any shape with dimensions in the  $1 \times 10^{-9}$  and  $1 \times 10^{-7}$  m range.”<sup>[47]</sup> A prominent example of the “nano-size” effect is gold. As a bulk material, Au is yellow and chemically very inert. When the size of an Au particle decreases, it changes its colour from violet over blue to red due to the coherent oscillation of the conduction electrons on the surface called a localized surface plasmon.<sup>[48]</sup> Furthermore, small Au clusters are very active catalysts compared to the inert bulk material.<sup>[49]</sup>

Most of the altered properties can be explained by two phenomena: a higher fraction of surface atoms or quantum size effects.<sup>[46]</sup>

Surface atoms are in an under-coordinated state and thus very reactive. The dispersion of a nanoparticle is a measure of the fraction of surface atoms per nanoparticle. The dispersion scales with  $N^{1/3}$  with  $N$  as the number of atoms per nanoparticle. The dependency implies that the amount of surface atoms increases sharply for very small nanoparticles.<sup>[46]</sup> The increased amount of surface atoms influences the catalytic activity and affects the melting point of a metal being significantly reduced compared to the bulk.<sup>[51]</sup>

The second phenomenon bases on quantum effects. In solids, atomic orbitals of the single atoms overlap to continuous bands. When the number of atoms per nanoparticle decreases, the amount of contributing orbitals also decreases. This influences the *density of states* (DOS)

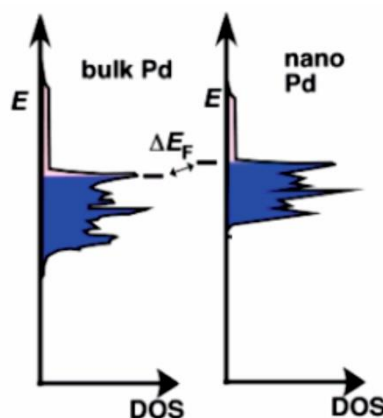


**Figure 4:** Illustration of the DOS near the Fermi level of bulk Pd and Pd nanoparticles of 2.6 nm size. The blue colour represents the occupied states. A difference in the position of Fermi level can be observed. [Reprinted with permission from reference<sup>[50]</sup>. Copyright (2008) American Chemical Society.]

and the Fermi level position and affects the electronic behaviour of a nanoparticle. (**Figure 4**).<sup>[50]</sup> Furthermore, the chemical behaviour of surface atoms alters as the DOS at the Fermi level of small nanoparticles changes. The ability of a nanoparticle surface to donate or accept charge from adsorbate molecules is a crucial property that can significantly influence the course of a catalytic reaction.<sup>[52]</sup> Both the under-coordinated surface atoms and the change in the electronic structure must be considered for the high catalytic activity of small nanoparticles.

Furthermore, nanoparticles show other phenomena that cannot be observed in bulk: Elements that are immiscible in the bulk phase and would always phase segregate or form core-shell structures can be alloyed at the nanoscale.<sup>[53]</sup> Immiscible Pd and Pt form solid solutions of about 6 nm nanoparticles.<sup>[54, 55]</sup> An alloy of immiscible Ru and Cu catalysed the CO oxidation with higher performance than single Ru or Cu nanoparticles.<sup>[56]</sup> Crystal structures that have never been observed for bulk materials were accessible on the nanoscale: Ru crystallises in the *hcp* structure, but the *fcc* structure was observed at the nanoscale.<sup>[57]</sup> Those Ru nanoparticles with *fcc* structure were more active for the oxidation of CO than comparable Ru nanoparticles of *hcp* structure.

### 3.2.2 Synthesis strategies for nanoparticles

There are many methods to produce small nanoparticles roughly classified by top-down and bottom-up approaches. Top-down means to break down larger objects into smaller ones, and a classic example of this approach is ball milling. A powerful bottom-up process is chemical vapour deposition.<sup>[58]</sup> Gas-phase molecules react with a surface, whereupon nanoparticles form on this surface. The conditions can be controlled precisely, and thus this technique is beneficial to synthesize well-defined model systems.<sup>[59]</sup> An often applied synthesis route of a bottom-up process for larger scales is wet chemical synthesis. This strategy includes methods such as reduction of precursors (e.g. H<sub>2</sub>, NaBH<sub>4</sub>, or ethanol), precipitation (e.g. iron oxide in basic medium) or hydrothermal treatment.<sup>[60]</sup>

Nanoparticles synthesized without a stabilisation agent would not stay small for a long time as nanoparticles try to minimize the energetically unfavourable high surface by Ostwald ripening or agglomeration. Therefore, ligands can be added to the synthesis to suppress the growth of the nanoparticles. When bulky polymers are used as ligands, this is called steric stabilisation, but in this case, the surface of the nanoparticles might be totally covered. Another approach is the electrostatic stabilisation. This can be achieved either by (de)protonation of surface atoms or by the adsorption of charged molecules to the surface. The charged surfaces of the nanoparticles repel each other and thus, prohibit agglomeration. The  $\zeta$  potential is the potential at the shear plane and is a measure for the stability of a colloidal dispersion. The  $\zeta$  potential is a function of the pH and can be determined by electrophoresis coupled with dynamic light scattering.<sup>[61]</sup> A  $\zeta$  potential of about 30 mV is typically regarded as sufficient for colloidal stability

for a longer time. However, nanoparticles with lower potentials might be stable for a short period of time. Furthermore, the functionalisation of the surface of a nanoparticle by organic molecules can alter its dispersibility. Small charged molecules promote the dispersion in polar media such as water, while molecules with a long organic chain promote nonpolar media dispersion.<sup>[62, 63]</sup> In the presented work, phosphocholine was used as a ligand in **Chapter 6.1** to obtain “cationic” iron oxide, and 4-dimethylaminopyridine (DMAP) was used to obtain “cationic” Pd in **Chapter 6.2, 6.3, and 6.4**.

Synthesis strategies are not restricted to spherical nanoparticles of one composition. Indeed, there is a wide variety to synthesize differently shaped nanoparticles such as cubes<sup>[64]</sup>, 1D objects (rods)<sup>[65, 66]</sup>, or 2D objects such as platelets.<sup>[67]</sup> These can be synthesized using particular capping ligands that preferentially adsorb to specific facets of a nanoparticle and restrict nanoparticle growth in this direction. Furthermore, the seeded growth approach allows for the synthesis of core-shell nanoparticles.<sup>[68, 69]</sup>

Even though nanoscience demonstrates a huge variety of accessible nanoparticles, this work applies spherical nanoparticles of Pd and  $\gamma\text{-Fe}_2\text{O}_3$  to focus on the influence of the 2D layered supports. Nevertheless, by the utilization of more sophisticated nanoparticles concerning shape or composition (core-shell or alloy), the catalytic behaviour could be further fine-tuned.

The application of small nanoparticles for heterogeneous catalysis requires the deposition onto a supporting material to provide good dispersion and suppression of ripening processes. The following **Chapter 3.3** covers the utility of layered silicates and layered titanates as supports for catalytically active nanoparticles.

### 3.3 Layered materials as supports for nanoparticles

#### 3.3.1 Layered silicates as supports

Pillared layered silicates were applied for catalytic reactions such as hydrocracking or organic reactions utilizing their lewis and brønsted acid character.<sup>[71-73]</sup> Furthermore, as natural layered silicates are very abundant and cheap, they were recognized as potential supporting materials for catalytically active nanoparticles.<sup>[74]</sup> The confined space between the two layers was supposed to stabilize and disperse nanoparticles effectively.

There are two commonly used synthesis strategies for the deposition of nanoparticles on/in layered silicates: *In situ* generation by chemical treatment of precursors in the presence of the layered silicate or intercalation of preformed nanoparticles. Moreover, the nanoparticle location can be distinguished between the layers or only on the external surface.

For instance,  $\gamma\text{-Fe}_2\text{O}_3$  nanoparticles of 10 – 30 nm size were precipitated on the outer surface of stacked natural montmorillonite by adding  $\text{NH}_4\text{OH}$  to a mixture of  $\text{Fe}^{2+}/\text{Fe}^{3+}$  salts. The broad size distribution of the nanoparticles was already the first hint that the external surface was insufficient to stabilize the nanoparticles effectively. Moreover, rapid nanoparticle growth was observed at temperatures as low as 400 °C.<sup>[75]</sup>

Nanoparticles can be generated between the layers by applying an *in situ* route. Interlayer cations such as  $\text{Li}^+$  or  $\text{Na}^+$  are exchanged for a precursor species followed by chemical treatment (e. g. reduction by  $\text{NaBH}_4$ , hydrolysis, or hydrothermal ageing). This synthesis strategy was expected to obtain very small nanoparticles as the confined space between the layers would hamper the growth. Dekany and Király exchanged interlayer  $\text{Na}^+$  of natural montmorillonite for  $\text{Pd}^{2+}$  followed by reduction.<sup>[70, 76, 77]</sup> The expected size control was not achieved as rather large nanoparticles of over 10 nm size with a broad size distribution were

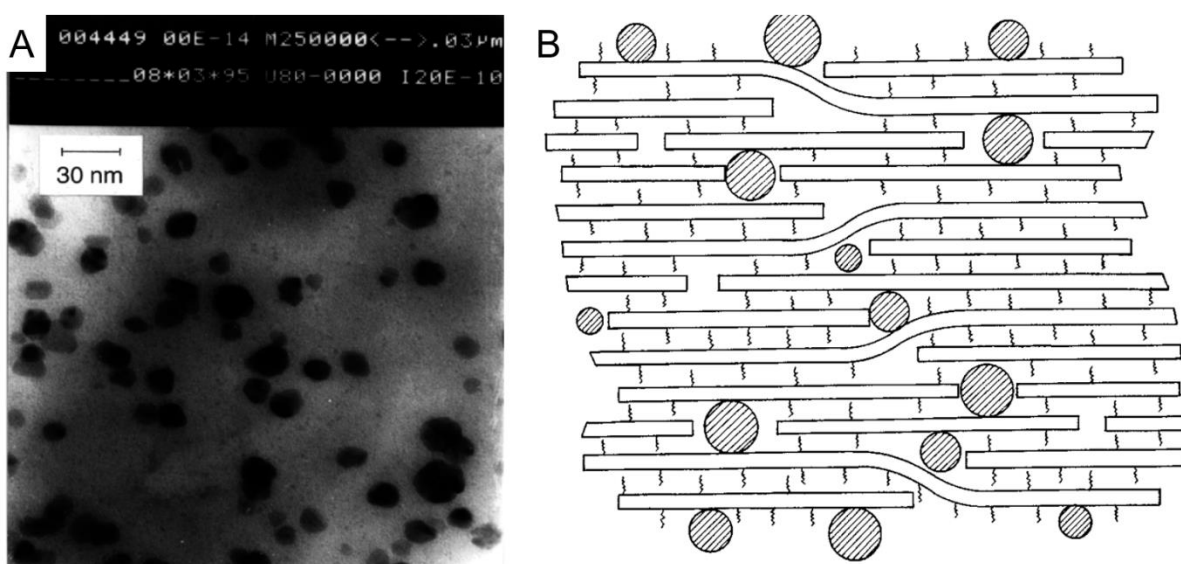


**Figure 5:** A) TEM image of montmorillonite exchanged with  $\text{Pd}^{2+}$  and reduced by ethanol. B) Schematic illustration of the location of Pd nanoparticles in the layered silicate. [Reprinted from reference<sup>[70]</sup>, Copyright (1996), with permission from Elsevier]

obtained. Furthermore, the basal reflection ( $001$  reflection observed from powder X-ray diffraction/PXRD) corresponding to the  $d$  spacing of two adjacent layers was not shifted to higher values. Actually, that would be expected if nanometer-sized particles were located between the layers. This observation was explained by the structure of the natural layered silicate. Natural montmorillonite is very defective with many cavities and small platelets with a maximum extension of about 200 nm. The nanoparticles grew either in the cavities or on the external surface, where size control was lacking (**Figure 5**).

Pre-intercalated polymers such as polyvinylpyrrolidone (PVP) improved control over the nanoparticle size. The polymer chains opened up the galleries and allowed the precursors to penetrate the interlayer space more efficiently.<sup>[78, 79]</sup> Indeed, the Pd nanoparticle size was lowered below 5 nm, and the size distribution was narrower. A drawback of this approach was the occupancy of the interlayer space by the polymer chains that restrained the diffusion of reactant molecules and also blocked the active metal surface.<sup>[79]</sup>

A variety of nanoparticle@layered silicate composites were synthesized and applied for various catalytic reactions. Mühlhaupt *et al.*<sup>[80]</sup> intercalated  $Pd^{2+}$  in montmorillonite and reduced it with hydrazine to Pd nanoparticles. Furthermore, they adsorbed a hydrophobic organic molecule to the surface. This allowed a better dispersibility of the catalyst in organic solvents. The catalyst was active in hydrogenation and Suzuki-Miyaura coupling. As no reference catalyst was applied, the performance can be hardly assessed.

Other noble metals were also deposited by the chemical reduction method: Ag@layered silicate<sup>[81]</sup> proved to have antimicrobial behaviour, Rh<sup>[82]</sup> or Ru<sup>[83]</sup> on montmorillonite were applied for selective hydrogenation of alkenes. Nevertheless, the relatively large size of about 20 nm of Ru nanoparticles suggested a lack of size control by the layered silicate.<sup>[84]</sup> Smaller nanoparticles are usually more active, and therefore, would be appreciated. Furthermore, deposition of nanoparticles is not restricted to noble metals, but semiconductors such as ZnO<sup>[85]</sup>, CdS<sup>[86]</sup> or TiO<sub>2</sub><sup>[87-89]</sup> were deposited on/in layered silicates as well.

Most of these studies have in common that the control of size and size distribution of the formed nanoparticles was hardly feasible as defective natural layered silicates were applied. It is often unclear whether the nanoparticles were located between the layers to take a possible advantage of the confined space. For sure, this prohibits a detailed investigation of the interactions between nanoparticles and layers.

The group of Breu used the synthetic NaHec that is superior over natural material for *in situ* generation of nanoparticles between the layers.  $Na^+$  was exchanged for  $Pd^{2+}$ , and nanoparticles were obtained by microwave irradiation (**Figure 6**).<sup>[90]</sup>

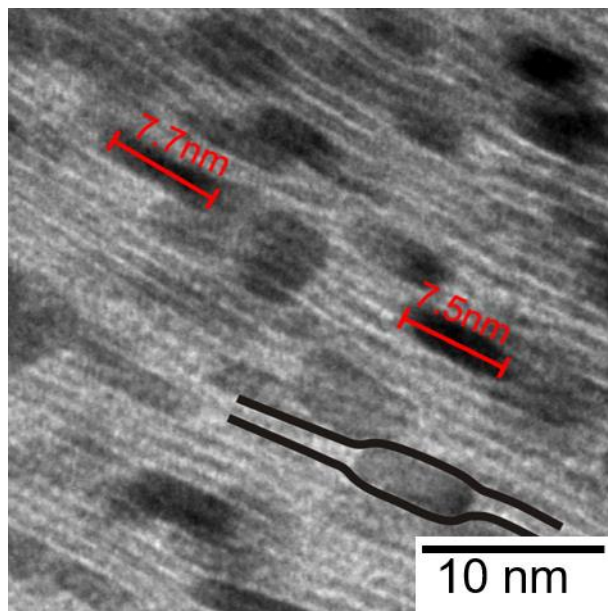


**Figure 6:** TEM image of a cross-section of  $\text{Pd}^{2+}$  exchanged NaHec followed by microwave treatment. The Hec nanosheets encapsulated the Pd nanoparticles.<sup>[90]</sup>

Transmission electron microscopy (TEM) images revealed that elongated nanoparticles were obtained as the confinement hampered the nanoparticle growth perpendicular to the nanosheets to 2 - 3 nm, but the nanoparticles grew along with the layers to 7 - 8 nm. The more serious problem over the size control was the flexibility<sup>[91]</sup> of the nanosheets that encapsulated the nanoparticles. When the distance of adjacent nanoparticles was too high, the nanosheets collapsed. These nanoparticles were not accessible anymore and thus not utilizable for catalysis. This problem originated from the low density of nanoparticles that was restricted by the inherent cation exchange capacity (cec) of NaHec. The cec of NaHec is relatively low with 121 mmol exchangeable monovalent ions per 100 g of NaHec.<sup>[11]</sup> This amount is halved for divalent cations such as  $\text{Pd}^{2+}$ , limiting the possible loading of Pd to about 6 wt%. Assuming a Pd nanoparticle of 3.5 nm, there would be one nanoparticle per  $1500 \text{ nm}^2$  of interlayer space. This low density of nanoparticles is not sufficient to generate a porous structure. A higher nanoparticle density is required to avoid collapsing of the nanosheets, but this is only possible by intercalating pre-synthesized nanoparticles. However, the intercalation of nanoparticles into a stacked tactoid is unfavourable due to the kinetic hindrance of the nano-objects. Therefore, the nanosheets have to be separated to several nanometers by delamination to facilitate the diffusion of pre-synthesized nanoparticles between the nanosheets. The intended strategy is displayed in **Figure 7** on the basis of Pd nanoparticles. Only a few reports about intercalation of pre-synthesised nanoparticles exploit a nematic phase of a layered silicate.<sup>[92]</sup> A possible explanation that this approach has been somewhat overlooked so far is using natural layered silicates. Due to impurities and inhomogeneities, natural montmorillonite does not spontaneously delaminate into single nanosheets. It requires several demanding purification steps to achieve delamination.

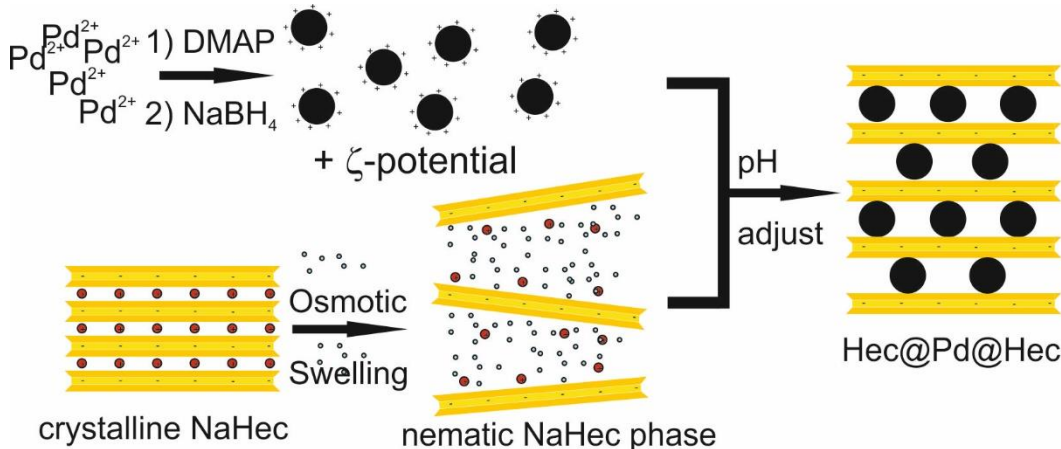


**Figure 7:** Sketch of the intended intercalation strategy. Nanoparticles with a positive  $\zeta$  potential are synthesized first. NaHec is delaminated to a nematic phase with a nanosheet separation  $> 50$  nm. The nanoparticles are added to the nematic phase, whereupon the nanoparticles are captured between the nanosheets. Due to the high density of nanoparticles, collapsing of the nanosheets is avoided. [Reprinted under the terms of CC BY 4.0 license from reference<sup>[93]</sup>]

Belova *et al.*<sup>[94-96]</sup> developed a very interesting approach to intercalate pre-synthesized nanoparticles worth mentioning. They synthesized small Au nanoparticles of 3.5 nm size and intercalated those into a stacked tactoid by ultrasound treatment. The cavities formed by the ultrasound jets damaged the montmorillonite and ripped holes into the surface, and the nanoparticles could penetrate the interlayer space through these holes. However, it was observable from TEM that the nanoparticles were located only on the external surface or in close vicinity to the holes.

### 3.3.2 Layered titanates as supports

Layered titanates are semiconductors and offer great potential for photocatalysis. However, the bandgap of 3.8 eV is even higher than 3.2 eV of anatase.<sup>[97]</sup> This allows exploiting only a very small portion of the sunlight spectrum. The performance was enhanced by the deposition of semiconductor nanoparticles with a narrower bandgap that increased charge separation or served for sensitisation.  $\text{K}_{0.66}\text{Ti}_{1.73}\text{Li}_{0.27}\text{O}_{3.93}$  was first modified with 3-(mercaptopropyl)trimethoxysilane to increase the distance between adjacent layers. It was mixed with  $\text{HAuCl}_4$  and reduced by  $\text{NaBH}_4$ . The as-received nanoparticles had a size of 3.5 nm. Due to the surface plasmon resonance of Au, the photocatalytic oxidation of benzene to phenol was performed with high yield and selectivity.<sup>[98]</sup> A mesoporous composite was obtained by intercalating a positively charged iron oxide colloid into an exfoliated layered titanate. The composite photocatalyst was active for the degradation of pollutants, while the single titanate or iron oxide were not active when illuminated with visible light ( $\lambda > 420$  nm).<sup>[99]</sup> Pre-synthesized anatase nanoparticles were tried to be intercalated between delaminated L-titanate nanosheets, but TEM images revealed a somewhat disordered structure with a high share of collapsed nanosheets. However, the disordered composite was efficient as a photoanode in a solar cell.<sup>[100]</sup> Sasaki *et al.*<sup>[101]</sup> embedded citrate stabilized Au nanoparticles

between L-titanate nanosheets by a layer-by-layer assembly. The coverage of Au by L-titanate enhanced the plasmon resonance. As relatively low amounts of Au nanoparticles were applied, the flexible nanosheets encapsulated the Au nanoparticles similar to what was observed for Pd nanoparticles between NaHec. Thus, a high density of nanoparticles between the nanosheets of L-titanate is mandatory for a porous network.

For layered titanates, most catalytic reactions aimed for photo- or electrocatalysis. However, this class of layered materials may also be promising for (high temperature) oxidation catalysis as  $\text{TiO}_2$  is a proven support for this type of reaction. Factors influencing the activity of nanoparticles are discussed in the next **Chapter 3.4**.

### 3.4 Fundamentals of catalysis

#### 3.4.1 Interaction of nanoparticles and supports

As already mentioned, small nanoparticles have a high surface to volume ratio, and surface species are unsaturated. Thus, they are in an energetically unfavourable state and tend to minimize their surface via different mechanisms (e. g. agglomeration or Ostwald ripening).<sup>[102]</sup> Even though this leads to an energetically more favourable state, it normally causes catalyst deactivation. For this reason, nanoparticles are deposited in low loadings on supporting materials with a high surface to ensure a maximum distance of nanoparticles to each other. Indeed, maintaining the high dispersion of nanoparticles is one essential function of supports that becomes even more challenging at realistic reaction conditions, often including elevated temperatures.<sup>[103]</sup> Deposition on a porous support surface is often not sufficient to prevent catalyst deactivation, which led to more sophisticated support structures. Incorporating nanoparticles in a support matrix<sup>[66, 68, 69]</sup> or coating nanoparticles with a porous shell<sup>[104-107]</sup> are examples of already applied strategies. For this reason, sandwiching nanoparticles between charged layers is a promising strategy to reduce nanoparticle mobility and growth. This is studied in **Chapter 6.1** based on iron oxide nanoparticles.

Apart from the function of stabilisation, the scientific effort has demonstrated that supports have a significant impact on catalyst reactivity.<sup>[108]</sup> There is a huge variety of possible interactions between nanoparticles and supports. Some important ones are electronic metal-support interactions (EMSI), strong metal-support interactions (SMSI), spillover phenomena, and influence on the morphology of the deposited nanoparticle.

Transfer of charge between nanoparticle and support is called electronic metal-support interaction (EMSI). In close contact, nanoparticle and support try to equilibrate differences in their Fermi levels and chemical potentials and the direction of the charge flow and extend depends on the involved species.<sup>[108]</sup> Model systems of small Pt<sup>[109, 110]</sup> or Ir<sup>[111]</sup> clusters and Pd cubes<sup>[112]</sup> deposited on CeO<sub>2</sub> proved that electrons were transferred from the noble metal to the support. An increased amount of the reduced Ce<sup>3+</sup> species determined by X-ray photoelectron spectroscopy (XPS) convincingly evidenced that the clusters/nanoparticles were in a partially oxidized state M<sup>δ+</sup>. Au nanoparticles deposited on MoO<sub>x</sub> demonstrated a charge transfer from support to noble metal.<sup>[113]</sup> In this combination, the electron flow directed towards Au that charged the Au surface negatively.

The impact of this charge on the catalytic performance was evaluated for several systems: Positively charged Pd<sup>[114]</sup> or Au<sup>[115]</sup> species showed a higher catalytic activity for the oxidation of CO to CO<sub>2</sub>. The lack of electrons in the noble metal was discussed to lower the adsorption energy of CO, which led to a reduced CO poisoning<sup>[116]</sup> and reduced reaction barriers.<sup>[117]</sup> These model studies demonstrated that tuning the surface charge of a noble metal is crucial

for optimising the catalyst performance. A partially positively charged surface of Pd was also exploited in **Chapter 6.2** for an improved activity for CO oxidation at lower temperatures.

Strong metal-support interactions (SMSI) in its classical sense cause the migration of suboxides onto the metal nanoparticle and lead to a (partial) coverage.<sup>[108, 118]</sup> This phenomenon was observed for the industrial used Cu/ZnO/Al<sub>2</sub>O<sub>3</sub> catalyst applied for methanol synthesis<sup>[118]</sup> or Au nanoparticles on TiO<sub>2</sub>.<sup>[119]</sup> It can have both advantages and disadvantages: When the metal is entirely overgrown by the oxide, this might lead to complete catalyst deactivation. As long as this overlayer is porous, the catalytic performance and selectivity might be significantly enhanced as reactive interface sites might be more active than individual metal or support.<sup>[120]</sup>

The interface between noble metal and oxide support is of great importance as support and metal might activate different reactants or catalyse different reactions. Furthermore, an adsorbed species might be activated on one surface and then migrate to another surface called spillover.<sup>[121]</sup> The right choice of support can even change the reaction mechanism, which will be explained on the basis of CO oxidation over noble metals. The bonding situation of CO to the surface of a noble metal such as Pd can be explained by the Bhyholder model.<sup>[122]</sup> A  $\sigma$ -bond is formed by overlapping of  $5\sigma$  orbital of the carbon atom and an empty d orbital of the metal. Furthermore,  $\pi$  back donation occurs from an occupied d metal orbital to the anti-bonding  $2\pi^*$  orbital of CO. This creates a very strong bond between CO and noble metals at low temperatures. CO blocks the surface and desorbs only at higher temperatures (typically  $> 130$  °C) which also explains why CO is regarded as a poison for noble metals in low temperature catalysis. CO oxidation over non-reducible support such as Al<sub>2</sub>O<sub>3</sub> proceeds typically via the competitive Langmuir-Hinshelwood mechanism (**Figure 8A**).<sup>[123]</sup> The oxidation occurs on the metal surface and requires both CO and O<sub>2</sub> to adsorb on the metal. As already mentioned, at low temperatures, the metal surface is covered by CO, and it requires sufficient

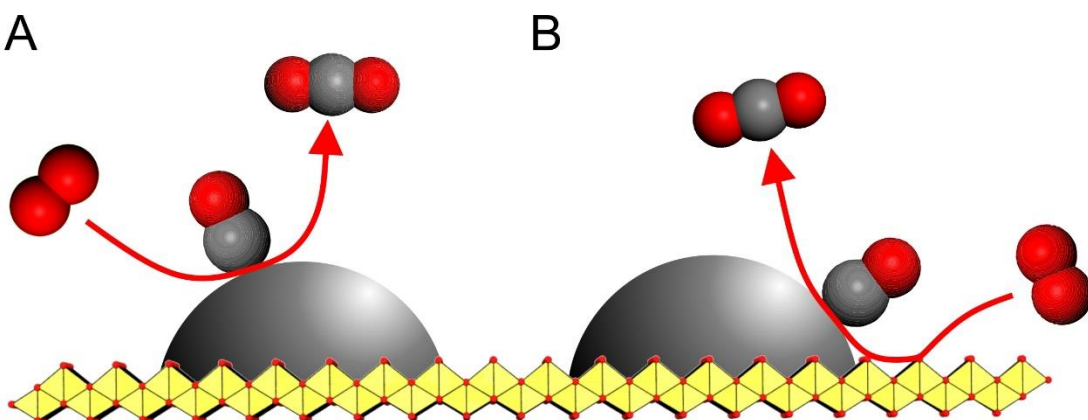


**Figure 8:** Two possible mechanisms for the total oxidation of CO. A) Langmuir-Hinshelwood mechanism: Both O<sub>2</sub> and CO adsorb on the noble metal surface. B) Mars-van Krevelen mechanism: oxygen is activated and donated via the oxygen lattice of the support.

high temperatures so that O<sub>2</sub> can co-adsorb to initiate the reaction.<sup>[114]</sup> It explains why noble metals suffer from low activity for CO oxidation at temperatures below 100 °C. This is a severe problem for exhaust gas purification right after the engine start. The cold catalyst cannot oxidize CO, and thus, toxic CO is emitted into the environment.

Reducible oxides such as TiO<sub>2</sub> or CeO<sub>2</sub> are supports that can overcome this problem.<sup>[124-131]</sup> These materials can switch easily between oxidation states (Ti<sup>4+</sup> ↔ Ti<sup>3+</sup> or Ce<sup>4+</sup> ↔ Ce<sup>3+</sup>). The reduction of the metal is accompanied by the release of lattice oxygen to maintain charge balance. In turn, this lattice oxygen can be donated to the oxide/metal, called oxygen storage capacity. The vacancy in the oxide lattice is refilled by O<sub>2</sub> from the gas phase in a later step of the catalytic reaction. This avoids the necessity of O<sub>2</sub> to adsorb directly to the noble metal surface and allows the reaction to proceed already at lower temperatures. This reaction type is called the Mars-van Krevelen mechanism (**Figure 8B**). For this type of mechanism, model catalysts with different Pd/CeO<sub>2</sub> interface extensions demonstrated that a high interface is crucial for high catalytic performance.<sup>[132]</sup> The higher the interface was, the higher was the catalytic activity for the oxidation of CO. A high interface between a reducible oxide and metal was established in **Chapter 6.4** by sandwiching Pd nanoparticles between two layers of L-titanate.

The last influencing factor to be mentioned is the influence on the morphology of a nanoparticle. The adhesion energy between support and metal affects the mobility of the nanoparticles and influences their shape.<sup>[133]</sup> This leads to the exposure of different facets that can have different catalytic activities.<sup>[134]</sup>

### 3.4.2 Learning from layered model systems

Knowledge about catalysis is often drawn from model systems having very defined structures and tuneable complexity. Understanding the fundamental processes that appear at the surface of the catalyst is of great importance for catalyst tuning.<sup>[135]</sup> In recent years, ultrathin layers of an oxide such as MgO, Al<sub>2</sub>O<sub>3</sub>, or SiO<sub>x</sub> deposited on a flat metal surface gained much scientific interest. The thickness of such a layer ranges from a monolayer to a few layers (**Figure 9A**). As sophisticated methods such as vapour phase deposition are applied, very defined structures can be obtained. Those, in turn, can be studied deeply by techniques such as XPS, scanning tunneling microscopy (STM), infrared reflection absorption spectroscopy (IRAS) or atomic force microscopy (AFM), and computational methods can support findings.<sup>[135]</sup> These model systems demonstrated that electrons could tunnel through a thin but insulating oxide layer: For instance, electrons tunneled from an underlying Ag(001) surface through a

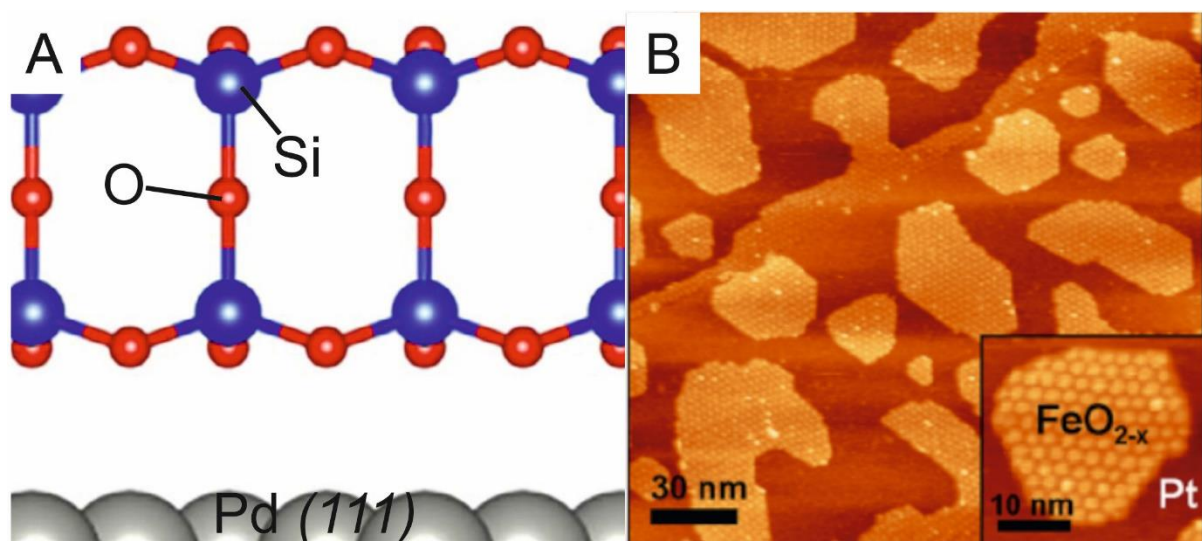


**Figure 9:** Illustration of model systems of oxide layers deposited on flat metal surfaces. A) Sketch of a closed silica bilayer on a Pd (111) surface. [Adapted from reference<sup>[137]</sup>, Copyright (2018), with permission from Elsevier] B) STM image of FeO<sub>2-x</sub> islands on a Pt (111) surface. [Adapted with permission from reference<sup>[138]</sup>. © 2018 Wiley-VCH Verlag GmbH & Co. KGaA, Weinheim]

sufficiently thin layer of MgO.<sup>[136]</sup> When an organic molecule adsorbs to the oxide surface, the tunnelling electron can polarize or even charge this molecule. This cannot only change the strength of bonding but even the bonding mode. The extent and direction of the charge flow depend on the HOMO and LUMO levels of the adsorbate molecule and the Fermi level of the underlying metal. The tunnelling of electrons through the insulating oxide layer is not restricted to molecules but can also affect metal clusters. Au deposited on MgO/Mo(111) led to tunnelling of electrons from Mo to the more electronegative Au and, finally, negatively charged Au clusters.<sup>[136, 139]</sup> These charged species can take a significant influence on the catalytic reaction, as mentioned in the previous **Chapter 3.4.1**.

However, there is also evidence that a thin layer of oxide deposited on metal influences the electronic structure of the underlying metal. At the interface between metal and oxide, a charge displacement can appear, which creates a dipole. The charge displacement arises either from a charge transfer of electrons between oxide and metal or from compressive electrostatic effects.<sup>[140]</sup> This charge displacement alters the metal work function significantly.<sup>[141]</sup> Density functional theory (DFT) calculations demonstrated that SiO<sub>2</sub> and TiO<sub>2</sub> layers on Mo(100) or Mo(112) increased the metal work function by 0.5 – 1 eV due to charge transfer from Mo to the oxide interface, which is in agreement with experimental results.<sup>[142]</sup> Furthermore, charge transfer was computationally studied for a monolayer of lepidocrocite-type titanate deposited either on Pt(111) or Ag(100).<sup>[143]</sup> The charge transfer from the noble metal to the oxide layer was pronounced for Ag compared to Pt. The accumulation of charge on the oxide reduced the H<sub>2</sub> adsorption capacity and disfavoured homolytic splitting for the Ag supported film.

Moreover, only submonolayers of an oxide can be deposited onto a metal surface, leading to the formation of oxide islands (**Figure 9B**).<sup>[138]</sup> The reactive interface at the perimeter leads to a further pushing of the catalytic performance. Pt(111) was partially covered with FeO<sub>x</sub>, and the structure was studied by STM and tested for the oxidation of CO. The film underwent a restructuring process depending on the partial pressures of CO and O<sub>2</sub>, and the already mentioned Mars-van Krevelen mechanism was evidenced for this system.<sup>[144, 145]</sup>

Based on the above explanation, there is clear evidence from model systems that ultrathin oxide layers influence the electronic structure and catalytic activity of noble metals.<sup>[52]</sup> Even though these model catalysts can be produced with excellent precision, transferring this knowledge to improve real catalysts is still challenging.<sup>[137, 146-148]</sup>

In this context, layered oxides such as NaHec or L-titanate are of great potential as they are a source of well-defined subnanometer thin oxide nanosheets. By intercalating nanoparticles between the nanosheets, the model catalysts can be effectively mimicked at a larger scale to be more suitable for real applications. The idea of mimicking the well-studied model catalysts are picked up in **Chapter 6.2** and **Chapter 6.4**.

### 3.4.3 Oxidation catalysis

In this work, the total oxidation of CO to CO<sub>2</sub> is applied as a model catalytic reaction to investigate the catalytic performance of the sandwiched catalysts. Its simple character makes it one of the most studied heterogeneous catalytic reactions. However, this reaction is also vital for exhaust gas purification due to the highly toxic CO.<sup>[149]</sup> Furthermore, CO responds very sensitively to changes in the catalytic system. For instance, the reaction is strongly dependent on the applied support that can even change the reaction mechanism (**Chapter 3.4.1**). Furthermore, a charged surface of the noble metal can influence the adsorption behaviour of CO due to an altered back donation capacity of electron density to CO.

A common way of measuring the catalytic performance of a total oxidation reaction is recording light-off curves. The solid catalyst is placed in a fixed bed reactor, and the reactant gas mixture flows through the catalyst bed. The catalyst bed temperature is stepwise increased, and the course of the conversion or reaction rate as a function of the temperature is recorded. A typical light-off curve is sketched in **Figure 10**. At low temperatures (section 1), the reaction rate slowly increases with increasing temperature as the reaction is under kinetic control.<sup>[150]</sup> The increase is proportional to the activation energy of the catalyst. At low conversions (typically below 10 %), the apparent activation energy E<sub>A</sub> can be determined by the Arrhenius plot (logarithmic plot of the reaction rate against the inverse temperature). Ideally, the relationship is linear, and E<sub>A</sub> can be calculated by:

$$E_A = -a \cdot R \quad (1)$$

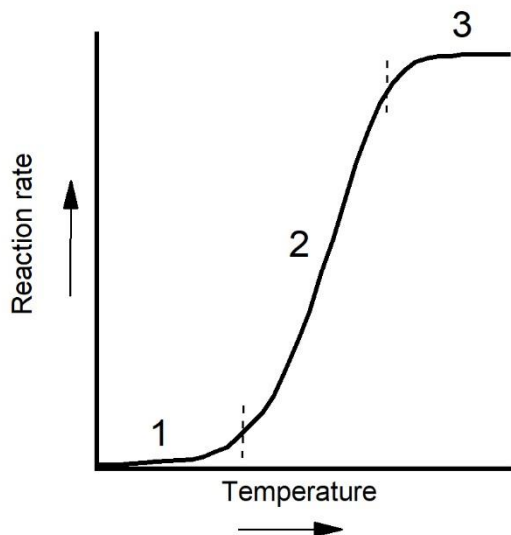


**Figure 10:** Typical light-off curve for a total oxidation reaction over a noble metal catalyst.

$a$  is the slope of the fitted line, and  $R$  is the universal gas constant.

As combustion reactions are typically exothermic, the catalyst warms up with increasing reaction rate, and the reaction rate rises steeply (section 2, **Figure 10**). It is said that the catalyst “lights-off”.<sup>[150]</sup> At higher temperature, the light-off curve flattens (section 3, **Figure 10**). In this region, heat and mass limitations become rate-determining, depending on factors such as the porosity of the catalyst or the reactor design. It should be mentioned that at even higher temperatures, the homogenous gas phase reaction can also occur.<sup>[150]</sup> A measure for performance is the temperature of 50 % conversion ( $T_{50}$ ) or 100 % conversion ( $T_{100}$ ) and the activation energy. One scientific endeavour is the increase of catalytic performance at lower temperatures. When the reaction requires lower temperatures, the threat of catalyst deactivation via nanoparticle ripening is often diminished. In addition, in the case of exhaust gas purification, this reduces the required time for warming the catalyst after the engine start to its working temperature. This leads to lower pollution of toxic volatiles to the environment.

### 3.5 Hydrogen storage

This thesis mainly focuses on the advantages of the unique sandwich architecture concerning catalytic or stability properties. However, Pd intercalated NaHec was also applied for H<sub>2</sub> sorption in **Chapter 6.3**. Pd is a transition metal with a high DOS near the Fermi level, allowing Pd to absorb high volumes of H<sub>2</sub> at ambient pressure and temperature.<sup>[151]</sup> Materials with a high surface area such as activated carbon<sup>[152]</sup> or metal-organic frameworks<sup>[153]</sup> can adsorb H<sub>2</sub> physically, but this requires very low temperatures or high pressures. Metal hydrides such as NaBH<sub>4</sub>, which form chemical bonds, require high temperatures to release H<sub>2</sub>.<sup>[154]</sup> In contrast, Pd can release H<sub>2</sub> at ambient temperatures.

Pd demonstrates a clear nano-size effect concerning its H<sub>2</sub> storage capacity.<sup>[50]</sup> In general, the amount of H<sub>2</sub> that Pd can absorb depends on the DOS at the Fermi level that is altered for nanoparticles (**Figure 4**). As the DOS at the Fermi level decreases with the size of the nanoparticles, the storage capacity for H<sub>2</sub> decreases. For instance, at 303 K, bulk Pd can absorb 0.65 H/Pd at a pressure of 101 kPa while nano-sized Pd of 2.6 nm size absorbs only 0.38 H/Pd.<sup>[50]</sup> However, nanoparticles have the advantage of a faster sorption kinetic due to shortened diffusion paths in the material. Research efforts tried to tune the electronic states of nanoparticulate Pd to increase the maximum sorption capacity as the amount of H<sub>2</sub> that can be absorbed is proportional to the holes in the 4d band of Pd.<sup>[155]</sup> When Pd was alloyed with Ir (replacement of 20 at% of Pd by Ir), the H<sub>2</sub> storage capacity doubled.<sup>[156]</sup> This was attributed to a charge transfer from Pd to Ir that increased the number of holes in the Pd 4d band. Furthermore, when Pd nanoparticles were covered with the metal-organic framework HKUST-1, a charge transfer from Pd to Cu-O groups of the linker was observed that also enhanced H<sub>2</sub> sorption.<sup>[157]</sup> The charge transfer was identified by a shift of the XPS Pd 3d signal to higher binding energy (BE) values. This was interpreted in terms of an electron deficient Pd species. Furthermore, the shift of the Cu 2p signal to lower BE compared to pristine HKUST-1 implied the electron transfer from Pd to the MOF linker groups. These findings demonstrated that partially positively charged Pd species are superior for the H<sub>2</sub> storage capacity over neutral ones. The influence of the confinement of Pd nanoparticles by the Hec nanosheets was investigated in **Chapter 6.3** for its impact on the storage capacity of H<sub>2</sub>.

### 3.6 Scope of this thesis

Noble metal nanoparticles are highly reactive catalysts for many (industrial) reactions. For instance, Pd is very active in oxidation reactions which are crucial for exhaust gas purification. However, the low abundance and high costs of precious metals make it mandatory to push their activity and/or selectivity further and minimize their deactivation with time on stream. Size, shape and composition are possible optimisation strategies on the nanoparticle side. On the other side, the supporting material can influence the catalytic behaviour of nanoparticles. Model catalysts based on ultrathin oxide layers deposited on flat metal surfaces have demonstrated that the oxide layer alters the electronic structure and modifies the catalytic activity of a noble metal. The preparation methods for the model catalysts are very demanding and allow only fabrication at very small scales. However, a larger scale of oxide layers is essential for an application in industrial processes. Layered materials such as NaHec comprise hundreds of stacked ultrathin oxide layers with cations in between that can be separated into single nanosheets when immersed in water. This offers the possibility to get access to a large scale source of well-defined oxide layers.

The presented work aimed to design and develop a modular concept for intercalating nanoparticles between swellable 2D layered materials. The influence of the confinement by two ultrathin oxidic nanosheets on the nanoparticles was evaluated for temperature stability, catalysis and H<sub>2</sub> sorption. This led to a library of nanoparticles and layered supports that can be combined to obtain tailor-made catalysts for the desired application. This thesis addressed the following research steps:

- Synthesis of nanoparticles with suitable properties for the intercalation process, including colloidal stability in water and positive  $\zeta$  potential.
- Intercalation of nanoparticles between NaHec nanosheets by using a nematic phase.
- Structural characterisation of the intended sandwich-like architecture concerning the necessary loading to obtain a porous structure.
- Investigation of the influence of the sandwich-like confinement on the thermal stability employing  $\gamma\text{-Fe}_2\text{O}_3$  at a very high density of nanoparticles.
- Investigation of the influence of the charged nanosheets on the electronic (surface) structure of Pd and its influence on the catalytic activity for CO oxidation.
- Probing the impact of the sandwich-like confinement for other applications such as H<sub>2</sub> storage.
- Transferring the intercalation strategy to a nematic L-titanate phase and evaluating its impact on the catalytic performance of Pd nanoparticles.

## 4 Synopsis

The presented cumulative thesis includes four manuscripts and the german translation of one article. The manuscripts present a modular strategy to intercalate various kinds of nanoparticles into swellable 2D layered materials. The synthesis strategy is based on delamination of the layered materials to a nematic liquid crystalline phase to capture pre-synthesized nanoparticles between the nanosheets. Four manuscripts focus on NaHec as the supporting material and different types of nanoparticles ( $\gamma\text{-Fe}_2\text{O}_3$ , Pd), while the last one applies L-titanate as a second 2D layered support. In addition to demonstrating the modular concept, each manuscript deals with beneficial aspects of the special sandwich architecture, such as improved stability, enhanced catalytic activity or H<sub>2</sub> storage capacity. (graphical synopsis: **Figure 11**).

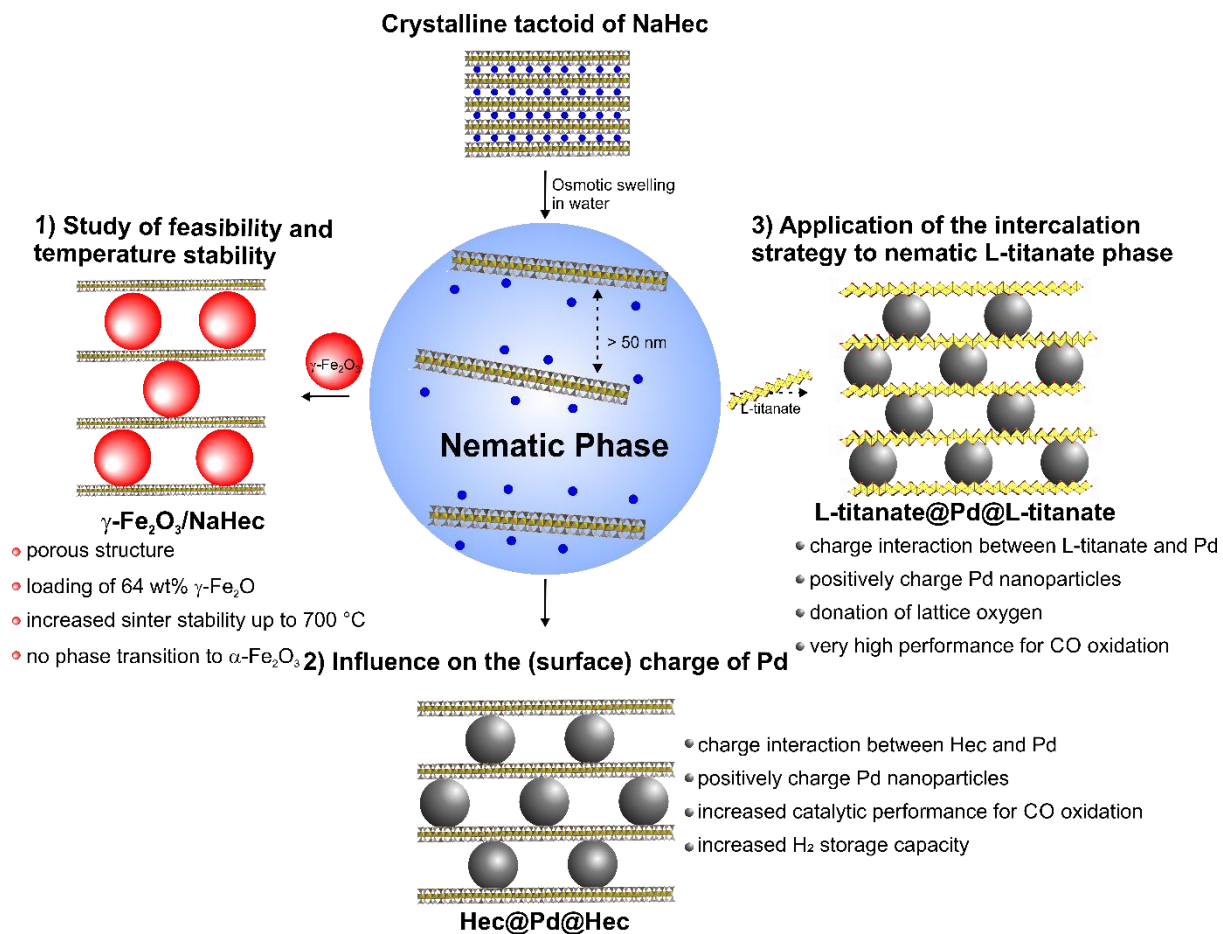


**Figure 11:** Graphical synopsis of this thesis demonstrating the modular intercalation concept. In step 1),  $\gamma\text{-Fe}_2\text{O}_3$  are intercalated between the nanosheets of NaHec and tested for their stability at high temperatures. In step 2), Pd nanoparticles are intercalated between NaHec nanosheets and the influence on the nanoparticle surface charge and influence on catalytic activity and H<sub>2</sub> uptake are investigated. In step 3), the intercalation concept is extended to a nematic phase of L-titanate and the catalyst is probed for its oxidation performance.

**Chapter 4.1** and the publication “High Temperature Stable Maghemite Nanoparticles Sandwiched between Hectorite Nanosheets” (**Chapter 6.1**) serve as a feasibility study as the intercalation of preformed nanoparticles exploiting a liquid crystalline nematic phase of a layered silicate is rather unexplored. Therefore,  $\gamma\text{-Fe}_2\text{O}_3$  nanoparticles with suitable properties are applied as a first nanoparticle species. The obtained sandwich-like structure is characterized to identify advantages over *in situ* generation of nanoparticles between the nanosheets. In addition, the influence of the sandwich confinement on the thermal stability of  $\gamma\text{-Fe}_2\text{O}_3$  is investigated.

In **Chapter 4.2** and the publication “Nanoparticles Supported on Sub-Nanometer Oxide Films: Scaling Model Systems to Bulk Materials” (**Chapter 6.2**), the intercalation concept is extended to the intercalation of small Pd nanoparticles. It is known for layered model systems that electronic interactions between metal and support exist (**Chapter 3.4.2**). Thus, this study focuses on possible electronic interactions between Hec and Pd. The structure of sandwiched nanoparticles is further applied in catalysis to identify the influence of the very special catalyst architecture. The publication claims that exploiting a nematic phase of a swellable 2D layered material such as NaHec is a scalable approach to mimic the model systems obtained by sophisticated but poorly scalable methods such as vapour phase deposition.

**Chapter 4.3** and the publication “Enhancing Hydrogen Storage Capacity of Pd Nanoparticles by Sandwiching between Inorganic Nanosheets” (**Chapter 6.3**) identify another possible application for Pd nanoparticles sandwiched between Hec nanosheets. The  $\text{H}_2$  storage capacity of Pd nanoparticles depends on the electronic states near the Fermi level. The study elaborates an increased  $\text{H}_2$  storage capacity due to electron-deficient Pd nanoparticles as a result of the influence of the Hec nanosheets.

So far, two different types of nanoparticles were applied, but the layered material was always NaHec. To confirm the modular concept claimed above, **Chapter 4.4** and the publication “Enhancing the Catalytic Activity of Palladium Nanoparticles via Sandwich-Like Confinement by Thin Titanate Nanosheets” (**Chapter 6.4**) apply the developed intercalation strategy to the 2D layered material L-titanate. This publication identifies electronic interactions between nanoparticles and support, but in relation to **Chapter 6.2**, the catalytic activity for the oxidation of CO increases significantly. Furthermore, the study applies kinetic experiments to identify the possible reaction mechanism to explain this enhanced catalytic activity.

#### 4.1 High Temperature Stable Maghemite Nanoparticles Sandwiched between Hectorite Nanosheets

In **Chapter 3.3.1**, it was already explained that the exchange of interlayer cations followed by chemical treatment is insufficient to obtain catalysts with a high accessible surface as the flexible nanosheets would encapsulate the nanoparticles. A higher nanoparticle density is mandatory to generate a porous structure, but the intrinsic cec of NaHec is the limit.

Furthermore, some nanoparticles such as iron oxide are even unsuitable for *in situ* generation in the interlayer space.  $\text{Fe}^{3+}$  salts dissolved in water induce an acidic pH between 3 and 4. NaHec already starts dissolving at this low pH, which prohibits the proper exchange of  $\text{Na}^+$  for  $\text{Fe}^{3+}$  without harming the Hec. Adjustment of the pH before intercalation is not possible because an increase of the pH leads to rapid precipitation of iron(oxy)hydroxides. For this reason, iron oxide nanoparticles have to be synthesized first and modified to carry a positive surface charge at a pH  $\geq 5$ . However, intercalation of pre-synthesized nanoparticles between the nanosheets of a stacked tactoid is kinetically unfavourable. Delamination of a 2D layered material to single nanosheets with a sufficient high separation of adjacent layers might solve this problem, but this approach has rather been overlooked so far.

This publication addresses the intercalation of preformed  $\gamma\text{-Fe}_2\text{O}_3$  nanoparticles as a proof of principle that a nematic liquid crystalline phase of NaHec is sufficient to capture high amounts of nanoparticles between the nanosheets. As NaHec delaminates in water and the nanosheets carry a permanent negative charge, two crucial requirements for the nanoparticles are a stable dispersion in water and a positive surface potential. Therefore, iron oxide nanoparticles were synthesized on the application of a modified polyol method.<sup>[158, 159]</sup>  $\text{FeCl}_2 \cdot 4 \text{ H}_2\text{O}$  and  $\text{FeCl}_3 \cdot 6 \text{ H}_2\text{O}$  were dissolved in a molar ratio of 2:1 in diethylene glycol (DEG). DEG acted as both solvent and complexing agent for the iron species. NaOH was added for the hydrolysis at higher temperatures. The formed metal-organic complexes prevented the iron species from precipitation at the initial basic pH. When heated with a controlled ramp of  $2 \text{ K} \cdot \text{min}^{-1}$  to the boiling point of DEG at about 220 °C, nanoparticles formed. According to TEM, the heating ramp allowed the synthesis of nanoparticles with a narrow size distribution of  $(5.5 \pm 1.1) \text{ nm}$ . DEG also served as an initial ligand to stabilize the as-synthesized nanoparticles from agglomeration. Post synthesis, the nanoparticle surface was modified with the organic ligand phosphocholine that enabled stable dispersion of the nanoparticles in water. Furthermore, the quaternary ammonium group led to a positive  $\zeta$  potential of + 42 mV at a pH of 7. According to Mößbauer spectroscopy at 4.2 K, the obtained iron oxide phase was  $\gamma\text{-Fe}_2\text{O}_3$ . Even though  $\text{Fe}^{2+}$  was in the initial precursor solution, the isomeric shift and the hyperfine field splitting indicated  $\text{Fe}^{3+}$  in the inverse spinel structure of  $\gamma\text{-Fe}_2\text{O}_3$ . As the nanoparticles were handled

neither under inert gas atmosphere after synthesis nor was the water degassed,  $\text{Fe}^{2+}$  readily oxidized due to the high surface of the small nanoparticles.

$\text{NaHec}$  was immersed in water (1 wt% solid content) until full delamination to yield a nanosheet separation of about 100 nm. Nanoparticles were added in excess to the  $\text{Hec}$  dispersion under vigorous stirring. After addition, flocculation occurred due to coagulation of the oppositely charged species. The dispersion was still coloured from the remaining nanoparticles that were not intercalated. This implied that only the amount necessary for the charge balance was intercalated. The flocculate was easy to be separated either by centrifugation or by application of a magnet.

The iron oxide content of the obtained composite ( $\gamma\text{-Fe}_2\text{O}_3/\text{NaHec}$ ) was as high as 64 wt%. Furthermore,  $\text{Na}^+$  was not found in the composite, indicating a complete ion exchange. It should be noted that even at this high loading, a mesoporous structure was obtained with a median pore size of 5.5 nm and a BET surface of  $237 \text{ m}^2 \text{ g}^{-1}$ . This high loading was necessary to obtain a porous structure as a composite with only 40 wt% of  $\gamma\text{-Fe}_2\text{O}_3$  was still not porous (unpublished result).

PXRD of a textured sample revealed a  $00l$  series corresponding to the distance of two adjacent nanosheets. The basal  $001$  reflection was found at  $1.3^\circ 2\Theta$  (Cu anode) corresponding to 6.9 nm, which is in good agreement with the expected sum of the nanoparticle size of 5.5 nm and the thickness of one  $\text{Hec}$  nanosheet of  $\sim 1$  nm (**Figure 12A**). Furthermore, TEM images of ultramicrotome slices demonstrated that the nanoparticles were successfully sandwiched

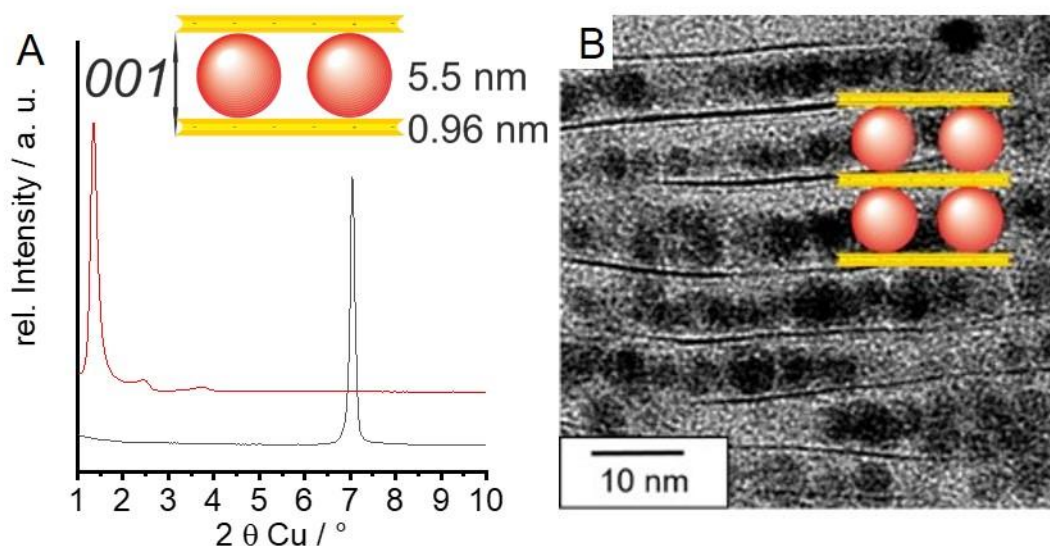


**Figure 12:** Structural characterisation of the lamellar Structure of  $\gamma\text{-Fe}_2\text{O}_3/\text{NaHec}$ . A) PXRD showing a shift of the basal spacing of  $\text{Hec}$  due to the intercalation of nanoparticles (red) in comparison to the basal reflection of  $\text{NaHec}$  (black). B) TEM image of ultramicrotome slice of iron oxide nanoparticles between the nanosheets of  $\text{Hec}$ . [Adapted under the terms of CC BY 4.0 license from reference<sup>[160]</sup>]

between Hec nanosheets (**Figure 12B**). The distance of the adjacent layers (TEM) was in accordance with the PXRD findings.

After successful intercalation and verification of an achieved sandwich-like structure, this special confinement from two directions was tested for its capability of stabilizing the nanoparticles against heat treatment. An efficient catalyst requires to stand high temperatures without rapid deactivation due to nanoparticle ripening processes. Here, NaHec offers another critical advantage over natural layered silicates. The anion lattice of NaHec is completed by  $F^-$ , while  $OH^-$  serves this purpose in natural materials. Dihydroxylation that damages the layers commences at about 500 °C. In contrast,  $F^-$  containing NaHec can stand temperatures up to 800 °C.

$\gamma$ - $Fe_2O_3$ /NaHec was annealed at 700 °C in the air for 20 h to probe the influence of the sandwich-like confinement on the sinter stability. After the treatment, PXRD did not show a narrowing of the broad  $\gamma$ - $Fe_2O_3$  reflections that would suggest an increase in the size of coherent scattering domains (**Figure 13A**). Reflections such as the 2/11 band at 7.1° 2  $\Theta$  (Ag anode) derived from the crystalline nanosheet were still present that implied that the layered structure survived the heat treatment. According to TEM micrographs, the nanoparticles retained their size (**Figure 13B** and **C**). Furthermore, no significant loss of surface appeared. Even at such a high density of nanoparticles, no obvious ripening process occurred.

Mößbauer spectroscopy at room temperature revealed a quadrupole doublet characteristic for fast superparamagnetic relaxation processes of small  $\gamma$ - $Fe_2O_3$  nanoparticles. Measurement at 4.2 K revealed signals still matching  $\gamma$ - $Fe_2O_3$ . No phase transition from the metastable  $\gamma$ - $Fe_2O_3$  to  $\alpha$ - $Fe_2O_3$  appeared even at 700 °C. Differential scanning calorimetry (DSC) further confirmed this finding as an endothermic peak corresponding to the phase transition commencing at about 750 °C was observed. The phase transition of bulk  $\gamma$ - $Fe_2O_3$  appears at about

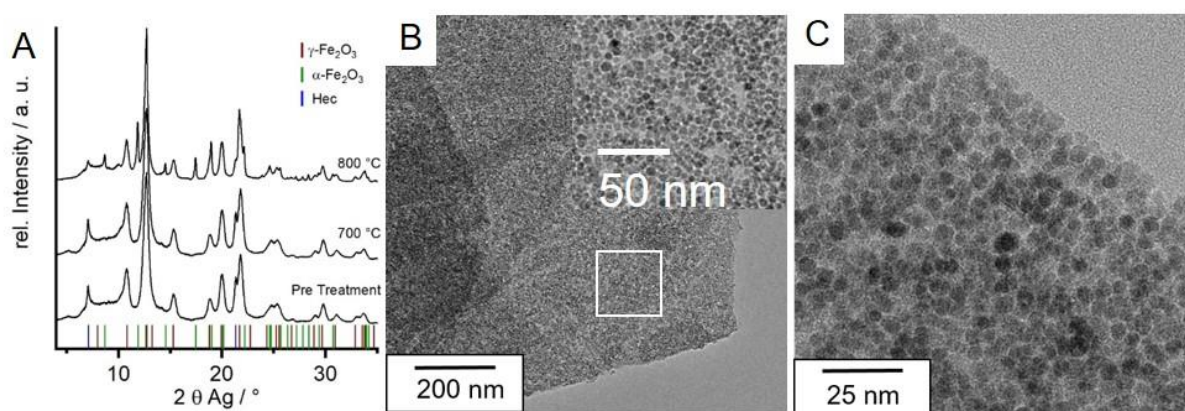


**Figure 13:** A) PXRD of  $\gamma$ - $Fe_2O_3$ /NaHec before and after treatment at 700 °C and 800 °C for 20 h. B) TEM image of  $\gamma$ - $Fe_2O_3$ /NaHec after synthesis showing a homogenous distribution of nanoparticles. The white box is magnified in the inset. C)  $\gamma$ - $Fe_2O_3$ /NaHec after treatment at 700 °C showing no ripened nanoparticles. [Adapted under the terms of CC BY 4.0 license from reference<sup>[160]</sup>]

## Synopsis

---

300 - 350 °C.<sup>[161]</sup> The retarded phase transition was explained by altered thermodynamic stabilities of the iron oxide phases at the nanoscale.<sup>[162, 163]</sup> The phase transition only occurred above a certain threshold size of about 10 nm.<sup>[164-166]</sup> This was an additional proof that nanoparticles must have retained their size upon heat treatment. Only above the thermal stability of Hec at about 800 °C, the stabilisation effect faded and nanoparticle growth was observed accompanied by the phase transition to  $\alpha\text{-Fe}_2\text{O}_3$ . As a control experiment, the nanoparticles were dried without support. Sharp reflections of  $\alpha\text{-Fe}_2\text{O}_3$  indicating a microcrystalline powder were already observed at temperatures above 400 °C as determined by PXRD, which means that the sandwich confinement increased sinter stability at least by 300 K.

This publication provided proof that exploiting a nematic liquid crystalline phase of a 2D layered material is viable for intercalating nanoparticles and obtaining an ordered lamellar structure. Furthermore, it was also shown that this special sandwich architecture retarded nanoparticle mobility and suppressed sintering effects. This demonstrated the possible utility for high temperature applications of such a sandwich-like structure.

## 4.2 Nanoparticles Supported on Sub-Nanometer Oxide Films: Scaling Model Systems to Bulk Materials

As already mentioned in **Chapter 3.4.2**, thin layers of oxides alter the catalytic performance of metal nanoparticles. However, it was only studied for model catalysts requiring demanding synthesis strategies, restricting their potential use to only small scale applications. However, oxidic silicate nanosheets of sub-nanometer size can be obtained on a large scale by delamination of NaHec. The scope was to synthesize a “bulk version” of these model catalysts and investigate the influence of the special sandwich-architecture on the catalytic activity of Pd nanoparticles.

Pd nanoparticles that were dispersible in water were synthesized by a modified literature method.<sup>[167]</sup>  $\text{Na}_2[\text{PdCl}_4]$  and 4-dimethylaminopyridine (DMAP) were dissolved in water to form a complex that was reduced by  $\text{NaBH}_4$ . The core size of the nanoparticles was  $(3.5 \pm 0.5)$  nm, according to TEM. The positive  $\zeta$  potential was adjustable by pH variation between + 14 mV to + 34 mV, whereas the layer charge was independent of pH.

The solid content of the NaHec dispersion was increased to 1.5 wt% (nanosheet separation of about 60 nm according to small-angle X-ray scattering) to make larger scales possible. Scales up to about 1 g of catalysts were synthesized and successfully manageable. NaHec was added to the nanoparticles either at a pH of 9.5 ( $\zeta$  potential: 28 mV) or 10.8 (22 mV). With the variation of the  $\zeta$  potential, the number of intercalated nanoparticles was controllable. At 22 mV, the loading was as high as 72 wt% Pd ( $\text{Hec@Pd72@Hec}$ ) and 65 wt% ( $\text{Hec@Pd65@Hec}$ ) at 28 mV. Elemental analysis (CHN), XPS, and scanning electron microscopy coupled with energy-dispersive X-ray spectroscopy (SEM-EDS) revealed that neither  $\text{Na}^+$  nor organic molecules remained in the structure after washing. This strongly suggested that the nanoparticles were responsible for the charge balance of the negatively charged nanosheets.

After intercalation, an ordered lamellar structure was observed for  $\text{Hec@Pd65@Hec}$  (**Figure 14A**). The architecture mimicked the ideal structure of a metal (partially) covered by a thin oxide layer. On the contrary, for  $\text{Hec@Pd72@Hec}$ , some agglomerated nanoparticles were observed in the interlayer space (**Figure 14B**). The surface potential was too low to achieve charge balance with only one layer of nanoparticles. A rational  $00l$  series with a periodicity of 4.7 nm implied a high degree of crystalline order along the stacking direction of  $\text{Hec@Pd65@Hec}$ . BET and CO chemisorption gave evidence for a mesoporous structure and accessible Pd surface of  $\text{Hec@Pd65@Hec}$ . The metal dispersion was 24 %. The catalytic activity was probed for CO oxidation. For comparison, the same nanoparticles used for  $\text{Hec@Pd@Hec}$  were also deposited on  $\gamma\text{-Al}_2\text{O}_3$  ( $\text{Pd}_{\text{ext}}@\text{Al}_2\text{O}_3$ ) as a standard catalyst support and on the external surface of non-swollen NaHec ( $\text{Pd}_{\text{ext}}@\text{Hec}$ ). The Pd loading of the references was only 1 wt% to avoid agglomeration during the deposition process.

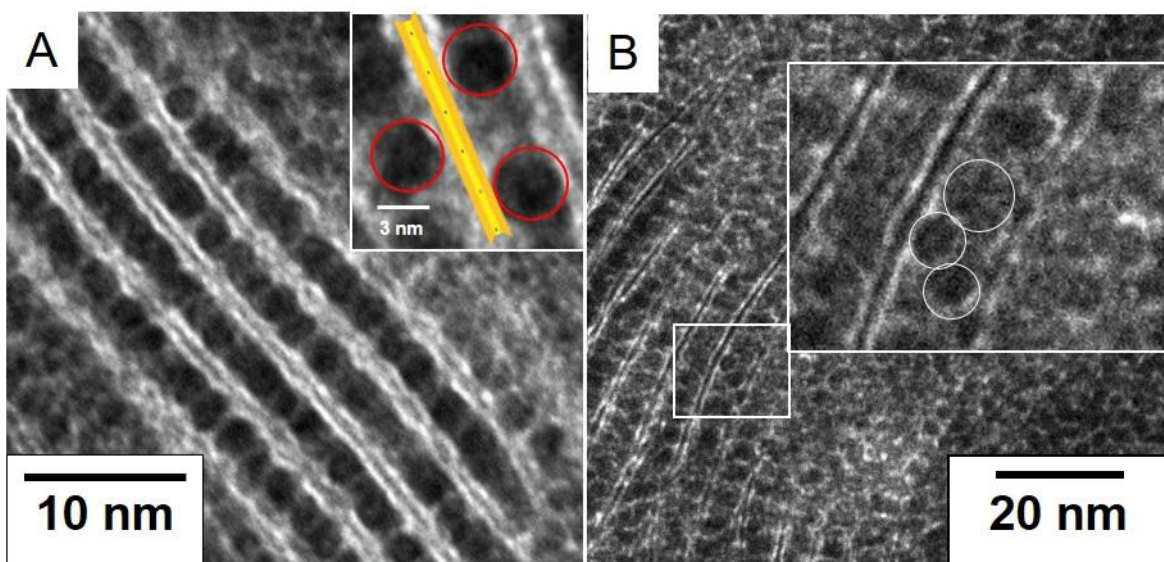


**Figure 14:** TEM micrographs of cross-sections of A) Hec@Pd65@Hec showing a lamellar structure of Pd nanoparticles between hectorite nanosheets. The inset shows that a mesopore was opposite a nanoparticle. B) Hec@Pd72@Hec showing some Pd agglomerates between the nanosheets. [Adapted under the terms of CC BY 4.0 license from reference<sup>[93]</sup>]

The catalytic performance of Hec@Pd65@Hec was the highest with a  $T_{50}$  already at 145 °C. The  $T_{50}$  values of Hec@Pd72@Hec and  $Pd_{ext}@Hec$  were already higher, with 163 °C and 172 °C, respectively. The same nanoparticles on the standard support  $\gamma\text{-Al}_2\text{O}_3$  showed the worst performance with a  $T_{50}$  of 191 °C (**Figure 15A**).

XP spectra of Hec@Pd65@Hec revealed the Pd 3d<sub>5/2</sub> signal at a binding energy (BE) of 335.8 eV (**Figure 15B**). This was considerably shifted from 335.0 eV reported for bulk Pd.<sup>[168]</sup> Such a shift was interpreted in terms of a slightly electron-deficient Pd species, which is reasonable as the Pd nanoparticles have to carry a positive charge to balance the negative layer charge of Hec.<sup>[169]</sup> In contrast, the BE values determined for  $Pd_{ext}@Al_2O_3$ ,  $Pd_{ext}@Hec$ , and Hec@Pd72@Hec were 335.2 eV, 335.3 eV, and 335.5 eV, respectively. The BE of

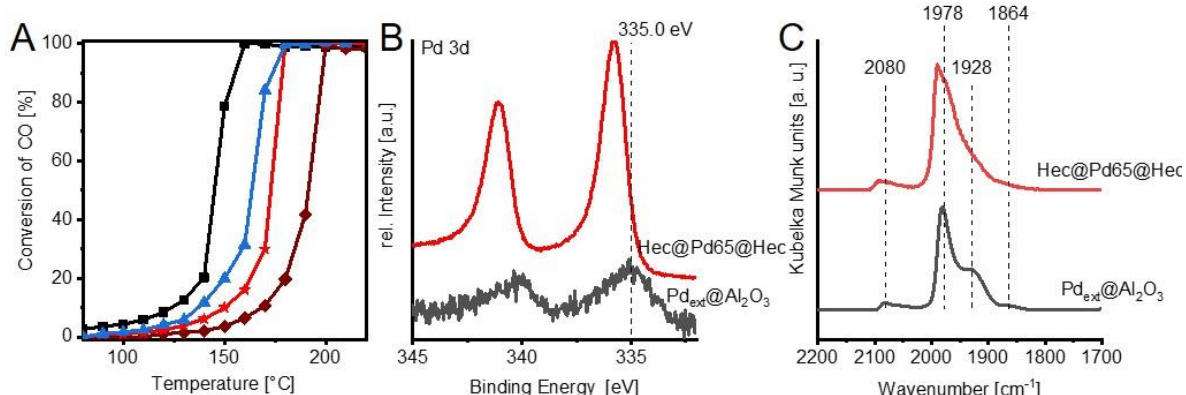


**Figure 15:** A) Light-off curves of Hec@Pd65@Hec (black), Hec@Pd72@Hec (blue),  $Pd_{ext}@Hec$  (red), and  $Pd_{ext}@Al_2O_3$  (brown) for the oxidation of CO. Conditions: 50 mL min<sup>-1</sup> (1 vol% CO, 1 vol% O<sub>2</sub> balanced by N<sub>2</sub>), 1 mg Pd per catalysis. B) XP spectra of Pd 3d region of Hec@Pd65@Hec (red) and  $Pd_{ext}@Al_2O_3$  (black). C) CO-DRIFT spectra of the C-O stretching region at room temperature of Hec@Pd65@Hec (red) and  $Pd_{ext}@Al_2O_3$  (black). [Adapted under the terms of CC BY 4.0 license from reference<sup>[93]</sup>]

Hec@Pd72@Hec was less shifted than Hec@Pd65@Hec that might be attributed to the lower  $\zeta$  potential of the nanoparticles applied in the intercalation process and due to the agglomerates in the interlayer space. As the signal of Pd<sub>ext</sub>@Hec was at 335.3 eV, the sandwich-confinement between two nanosheets seems to be crucial for a maximized shift. Furthermore, a clear trend between the BE shift and the T<sub>50</sub> values was observed. The T<sub>50</sub> decreased with a larger shift of the Pd 3d BE to higher values.

According to diffuse reflectance infrared Fourier transform spectroscopy (CO-DRIFTS) of chemisorbed CO to the Pd surface, a shift of the C-O stretching vibrations of Hec@Pd65@Hec to higher wavenumbers as compared to Pd<sub>ext</sub>@Al<sub>2</sub>O<sub>3</sub> was observed (**Figure 15C**). When less electron density from Pd can be donated to the 2π\* orbital of CO, the internal C-O bond is strengthened, leading to a wavenumber shift to higher values. DFT calculations supported that the adsorption energy of CO to a positive Pd surface was reduced as compared to the neutral surface. On the contrary, the adsorption energy of O<sub>2</sub> was hardly effected by charge. Thus, the higher catalytic activity was explained with two reasons. First, the slightly positive surface of Pd led to weaker binding of CO to the Pd surface. When CO desorbs at lower temperatures to allow O<sub>2</sub> to co-adsorb, the reaction can start already at lower temperatures. Second, DFT calculations proved that charge reduces the activation barriers of the catalytic cycle.<sup>[117]</sup> This was in accordance with the finding that the activity increased with larger BE shifts observed from XPS. The obvious reason for the positively charged surface of Pd was the necessity of balancing the negative charge of the Hec nanosheets. However, as mentioned in **Chapter 3.4.2**, electronic interactions between layered oxides and metals were already observed for model systems. Therefore, electron energy loss spectroscopy (EELS) was performed to

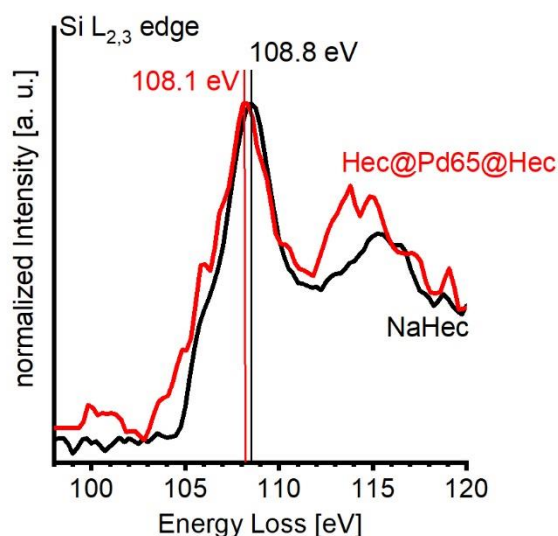


**Figure 16:** EEL spectra at the Si L<sub>2,3</sub> edge of Hec@Pd65@Hec (red) and pristine NaHec (black). [Reprinted under the terms of CC BY 4.0 license from reference<sup>[93]</sup>]

## Synopsis

---

investigate whether such an electronic interaction could also appear in the special architecture of Hec@Pd65@Hec that was supposed to mimic the model systems. A shift of both Si K and L<sub>2,3</sub> edge (**Figure 16**) to lower energy losses compared to pristine NaHec was observed. This implied a slightly reduced Si<sup>4-x</sup> species. These findings suggested that some electron density was transferred from the sandwiched Pd nanoparticles to the oxidic nanosheets implying electronic interactions between nanoparticles and nanosheets.

This publication proved that intercalation of noble metal nanoparticles between oxide nanosheets exploiting a liquid crystalline nematic phase of NaHec is a suitable strategy to synthesize a “bulk version” of previous model systems. The altered electronic surface structure of Pd improved the catalytic activity for the oxidation of CO and demonstrated that tuning the surface charge is a crucial parameter to enhance catalytic performance. The strategy is for sure extendable to other catalytic reactions besides CO oxidation.

### 4.3 Enhancing Hydrogen Storage Capacity of Pd Nanoparticles by Sandwiching between Inorganic Nanosheets

The previous chapter demonstrated that Pd nanoparticles intercalated between Hec nanosheets carry a positive surface charge due to charge balancing and electronic interactions between the oxidic nanosheets and Pd nanoparticles. The enhanced catalytic activity was attributed to the positive Pd surface.

Another application to take advantage of an electron-deficient Pd species is H<sub>2</sub> storage. The maximum amount of H<sub>2</sub> that can be absorbed is related to the number of holes in the 4d band (**Chapter 3.5**), so an electron-deficient Pd species, as suggested for Hec@Pd65@Hec, is interesting for H<sub>2</sub> storage. This study was performed through collaboration with the group of Prof Hiroshi Kitagawa at Kyoto University.

The previous chapter has shown a possible relationship between the applied pH during the intercalation process and the shift of BE observed from the XP spectrum. This encouraged to maximize the  $\zeta$  potential by lowering the pH to 6.0, corresponding to 34 mV. It should be noted that further decreasing the pH caused destabilisation of the nanoparticles and rapid agglomeration. Furthermore, a pH of 9.5 was applied, as used for the synthesis of Hec@Pd65@Hec that granted an ordered structure. The nanoparticle synthesis was the same as applied in **Chapter 4.2**. The obtained metal loading was 39.3 wt% (Hec@Pd39@Hec) and 64.5 wt% (Hec@Pd65@Hec) at pH 6.0 and pH 9.5, respectively. TEM investigation of Hec@Pd65@Hec revealed a well-ordered structure (**Figure 17A, B**). In contrast, the higher positive surface charge in the case of Hec@Pd39@Hec resulted in the intercalation of too low amounts of Pd and led to sections of collapsed nanosheets with no Pd in between (**Figure 17C**). While Ar-physisorption and CO-chemisorption of Hec@Pd65@Hec showed an accessible Pd surface (24 % metal dispersion), the collapsed areas of Hec@Pd39@Hec caused a non-porous structure with a Pd surface below the detection limit due to nanoparticle encapsulation. Even though the loading was largely increased compared to the standard

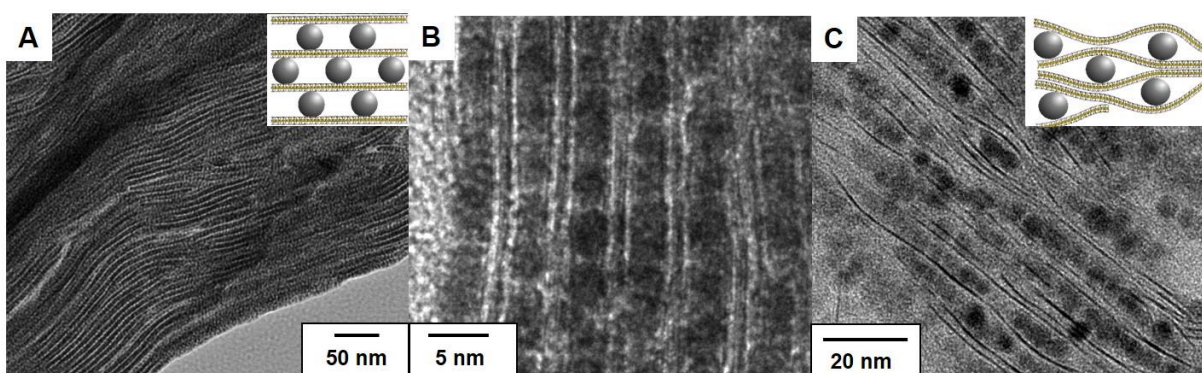


**Figure 17:** TEM cross-section micrographs of A) + B) Hec@Pd65@Hec at different magnifications showing a well-ordered lamellar structure. C) Cross-section of Hec@Pd39@Hec with collapsed nanosheets without nanoparticles in between. [Adapted under the terms of CC BY 4.0 license from reference<sup>[170]</sup>]

“cation exchange and reduction-route” (**Chapter 3.3.1**), that would only grant about 6 wt% Pd, 39.3 wt% were still insufficient for a porous network which emphasized that the proper adjustment of the surface potential was mandatory. The XPS shift of the Pd 3d signal of Hec@Pd39@Hec was larger than Hec@Pd65@Hec (336.0 eV vs 335.8 eV) as expected, but the non-porous network already implied that it might be not useful for H<sub>2</sub> storage. Pressure-composition (PC) isotherms were recorded at 303 K to study the H<sub>2</sub> uptake behaviour of Pd nanoparticles sandwiched between the nanosheets of Hec (**Figure 18A**). Hec@Pd39@Hec absorbed nearly no H<sub>2</sub> as the encapsulated nanoparticles were not accessible even for the small H<sub>2</sub> molecule. Hec@Pd65@Hec absorbed H<sub>2</sub> with increasing H<sub>2</sub> pressure to a maximum of 0.65 H per Pd at 101 kPa. As a reference material, the identical nanoparticles used for the intercalation were covered with PVP. This prevented the nanoparticles from agglomeration during the drying process. However, PVP is regarded to grant H<sub>2</sub> access to the Pd surface and to have little effect on the sorption behaviour of small Pd nanoparticles.<sup>[171, 172]</sup> The maximum sorption capacity of the polymer covered nanoparticles was 0.35 H/Pd, so the intercalation between the inorganic oxide layers increased the storage capacity by 86 %. Furthermore, the plateau-like region was decreased by 35 % compared to Pd black, which means that the miscibility gap between α-phase (a solid solution of Pd+H) and β-phase (formation of a hydride Pd-H) narrowed, typically for nanoparticles.<sup>[173]</sup> The XPS 3d<sub>5/2</sub> signal of the PVP covered Pd nanoparticles was found at 335.1 eV, 0.7 eV less shifted than Hec@Pd65@Hec (**Figure 18B**). The nanoparticles sandwiched between the nanosheets carried an increased number of positive charges, that increased the number of holes in the 4d band. This finally led to the enhanced H<sub>2</sub> storage compared to PVP covered nanoparticles. Similar to the Pd nanocubes covered with HKUST-1, the enhanced storage capacity was attributed to the positively charged Pd nanoparticles.<sup>[157]</sup>

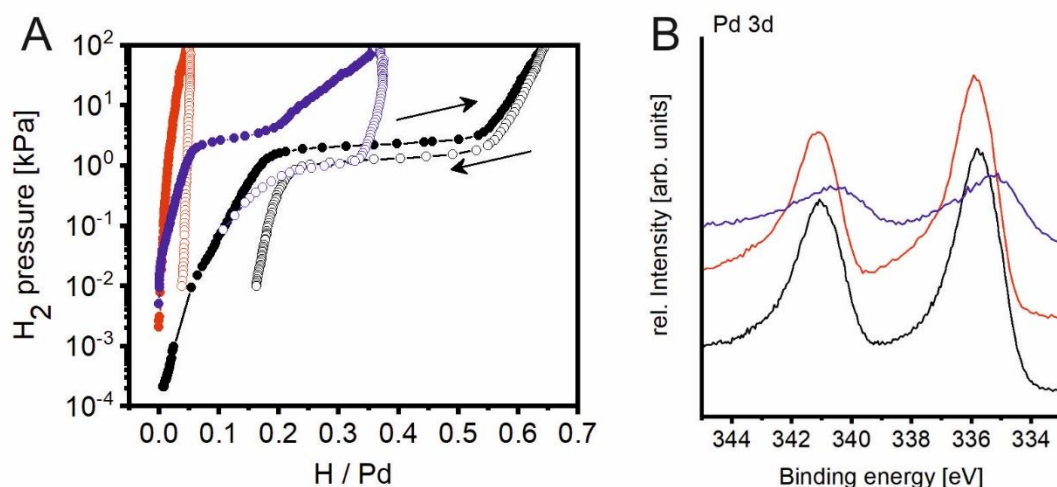


**Figure 18:** A) PC isotherms measured at 303 K and B) XP spectra of Pd 3d region of Hec@Pd39@Hec (red), Hec@Pd65@Hec (black), and PVP covered Pd nanoparticles (blue). [Adapted under the terms of CC BY 4.0 license from reference<sup>[170]</sup>]

However, the enhanced storage capacity of Hec@Pd65@Hec might have another reason besides the increased number of holes in the 4d band. A spillover of H<sub>2</sub> from the nanoparticles to the Hec might occur, which had to be excluded. The formation of the Pd hydride causes a lattice expansion of Pd and, therefore, is a measure for the sorption of H<sub>2</sub> in the nanoparticle.<sup>[157]</sup> *In situ* PXRD patterns were recorded under various H<sub>2</sub> pressures at the synchrotron facility SPring-8 in Japan (**Figure 19**). The reflections corresponding to the fcc lattice (e. g. at about 20° 2 Θ) of Pd shifted to lower angles with increasing H<sub>2</sub> pressure while reflections derived from the Hec bands (e.g. at 10° 2 Θ) kept their position. When decreasing the H<sub>2</sub> pressure again, the reflections returned to their initial position, which is a clear sign of reversibility. The lattice parameter of each diffraction pattern was determined by Le Bail fitting. The lattice expanded with increasing H<sub>2</sub> pressure and shrunk back to its original value when the pressure was reduced. The lattice constant followed the PC isotherm course that strongly suggested that the uptake of H<sub>2</sub> was not due to a spillover phenomenon but through absorption in the Pd lattice. Even though Pd is not the most suitable material for H<sub>2</sub> storage due to its weight and high costs, this publication demonstrated that Hec had a significant influence on the sorption behaviour of Pd nanoparticles when sandwiched between Hec nanosheets. It is another example of the positive influence on nanoparticle properties and states that possible applications are not restricted to catalysis.

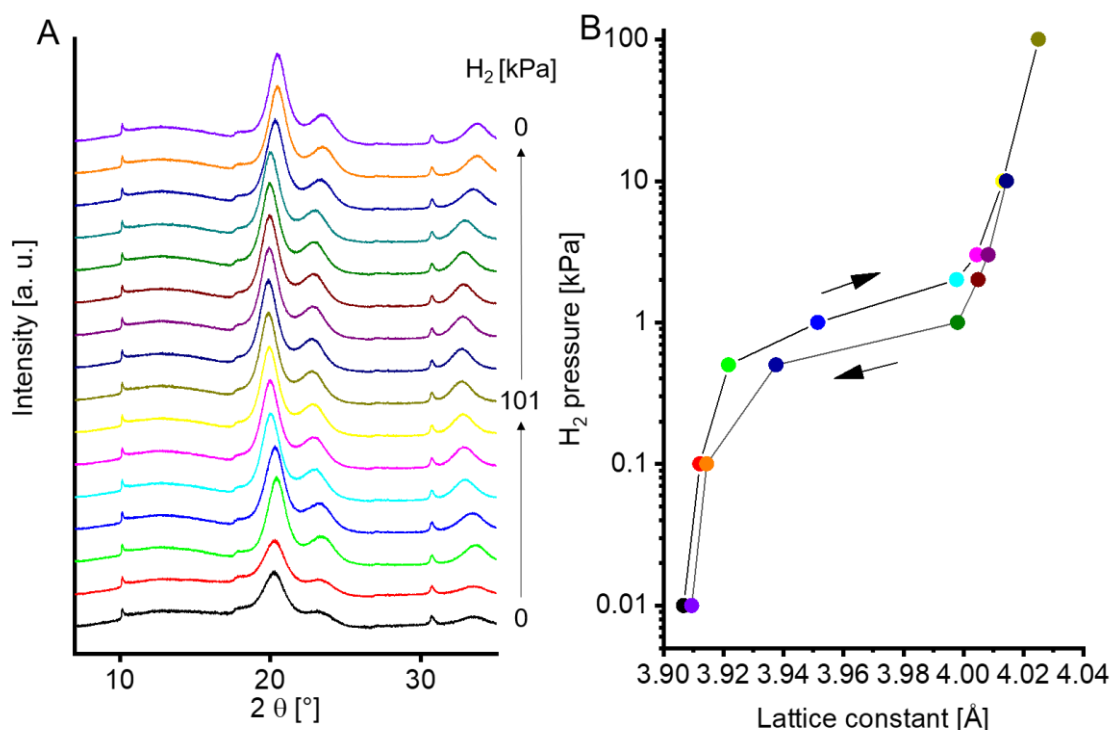


**Figure 19:** A) *In situ* PXRD patterns of Hec@Pd65@Hec at various H<sub>2</sub> pressures. B) Lattice constant derived from Le Bail fitting at various H<sub>2</sub> pressures. The colour of the diffraction pattern in A) corresponds to the same coloured dot in B). [Adapted under the terms of CC BY 4.0 license from reference<sup>[170]</sup>]

#### 4.4 Enhancing the Catalytic Activity of Palladium Nanoparticles via Sandwich-Like Confinement by Thin Titanate Nanosheets

This publication intends to answer whether the intercalation concept can be applied to other 2D layered material such as  $H_{1.07}Ti_{1.73}O_4 \cdot H_2O$  (L-titanate) and identify its influence on the catalytic behaviour. L-titanate that has already been introduced in **Chapter 3.1** was synthesized in cooperation with Prof Takayoshi Sasaki at the National Institute for Materials Research (NIMS) in Japan. Synthesis and delamination conditions can be found in **Chapter 3.1.3** and **Chapter 3.1.4**, respectively.

While a stable dispersion in water and a positive  $\zeta$  potential were the necessary specifications for the nanoparticles in the previous chapters, it turned out that in this case the nanoparticles had to be stable at a  $pH \geq 10$  and still carry a positive surface charge. The high pH was mandatory as the nematic phase of L-titanate was only stable at the basic pH. The Pd nanoparticles used for Hec@Pd@Hec fulfilled this additional criterion, which offered good comparability between Hec and L-titanate as supporting materials. As  $TBA^+$  was necessary for the delamination process (**Chapter 3.1.4**), the question appeared whether the bulky organic molecule would somehow influence the intercalation. The strategy was the same as in the previous chapters, and the obtained catalyst was denoted as L-titanate@Pd@L-titanate. After synthesis, the elemental analysis revealed that some  $TBA^+$  (~ 20 % of the cec) remained in the structure, but this could be removed by calcination in the air at  $500\text{ }^\circ C$ . During calcination, Pd was oxidized to PdO but could be reduced back to Pd metal by  $H_2$  treatment at  $200\text{ }^\circ C$  according to PXRD (**Figure 20A**). The Pd loading after calcination und reduction was as high as 49 wt%. Furthermore, reflections derived from L-titanate ( $hk$  bands, denoted with T in **Figure 20A**) were still present, proving that the layered support survived the procedure. TEM cross-sections revealed a lamellar structure comparable to Hec@Pd@Hec (**Figure 20B**). The

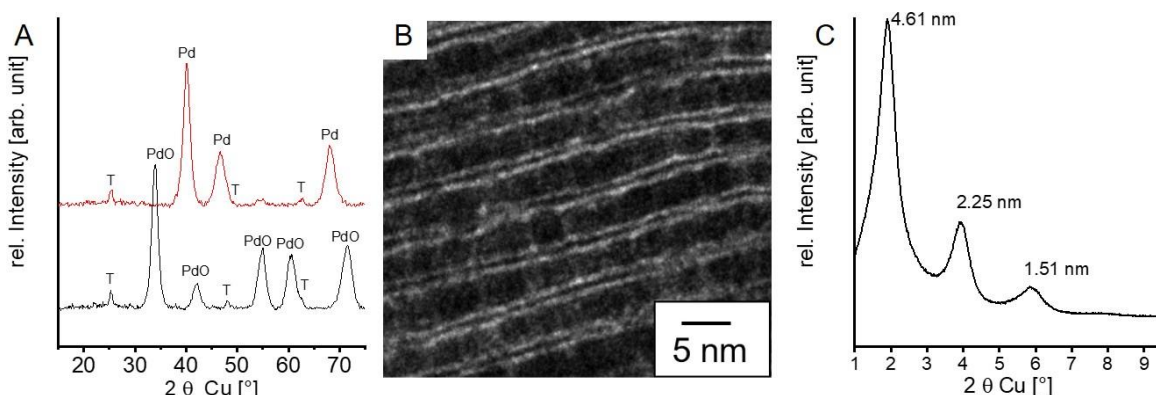


**Figure 20:** Structural characterisation of L-titanate@Pd@L-titanate: A) PXRD after calcination at  $500\text{ }^\circ C$  for 5 h (black) and reduction by  $H_2$  at  $200\text{ }^\circ C$  (red). No evident narrowing of the width of the reflections was observed. T stands for reflections derived from L-titanate. B) TEM cross-section showing the lamellar structure after calcination and reduction process. C) PXRD at low angles displaying a  $00l$  series. [Adapted under the terms of CC BY 4.0 license from reference<sup>[174]</sup>]

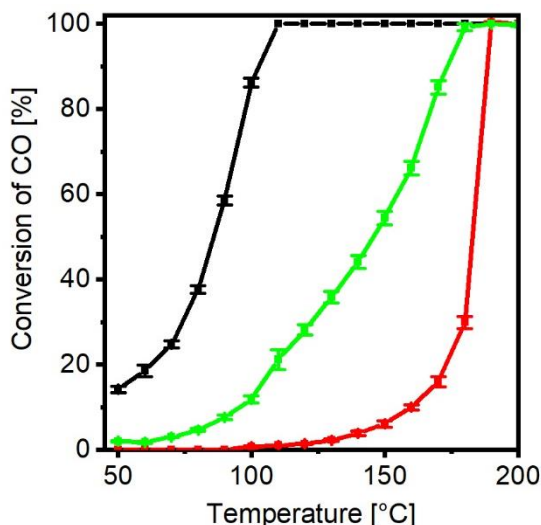


**Figure 21:** Light-off curves of L-titanate@Pd@L-titanate (black), Pd<sub>ext</sub>@P25 (green), and Pd<sub>ext</sub>@Al<sub>2</sub>O<sub>3</sub> (red). Conditions: 1 mg of Pd per catalysis; 50 mL min<sup>-1</sup> (1 vol% CO, 1 vol% O<sub>2</sub>, N<sub>2</sub> balance). [ Adapted under the terms of CC BY 4.0 license from reference<sup>[174]</sup>]

special sandwich-architecture stabilized the nanoparticles during the the pretreatment process against ripening as the size of the nanoparticles was still (3.8 ± 0.6) nm (**Figure 20B**).

PXRD at low angles revealed a periodicity of the *00l* series of 4.6 nm, which is in good agreement with the expected value of the nanosheet thickness of 0.75 nm and the core size of the nanoparticles of 3.8 nm (**Figure 20C**). In contrast, when pristine L-titanate was treated at 500 °C, it readily transformed into the thermodynamically stable anatase phase, a known phenomenon from the literature.<sup>[34]</sup> However, when single nanosheets are sufficiently separated, the phase transition is unfavoured.<sup>[175]</sup> This provided additional proof that the nanoparticles kept the nanosheets apart from each other. Ar physisorption and CO chemisorption revealed a mesoporous network with an accessible Pd surface and a metal dispersion of 19 % after the calcination process.

The catalytic activity of L-titanate@Pd@L-titanate was probed for the oxidation of CO and compared with identical nanoparticles deposited on the surface of Degussa P25 (a mixture of anatase and rutile, Pd<sub>ext</sub>@P25) and γ-Al<sub>2</sub>O<sub>3</sub> (Pd<sub>ext</sub>@Al<sub>2</sub>O<sub>3</sub>). The T<sub>50</sub> value of L-titanate@Pd@L-titanate was already observed at 86 °C, significantly lower than the values of the reference catalysts Pd<sub>ext</sub>@P25 (148 °C) or Pd<sub>ext</sub>@Al<sub>2</sub>O<sub>3</sub> (183 °C) (**Figure 21**). To find a possible explanation for the high catalytic activity, the catalyst was investigated for a possible positive surface charge similar to **Chapter 4.2**. Indeed, both the Pd 3d region derived from XPS (**Figure 22A**) and the C-O stretching vibration derived from CO-DRIFTS implied a partial positive Pd surface similar to Hec@Pd65@Hec. However, the catalytic performance was much higher, especially below 100 °C as compared to Hec@Pd65@Hec. The highly increased activity implied the existence of an additional promoting effect of L-titanate. In **Chapter 3.4.1**, it was explained that CO oxidation could proceed via various mechanisms that might include lattice

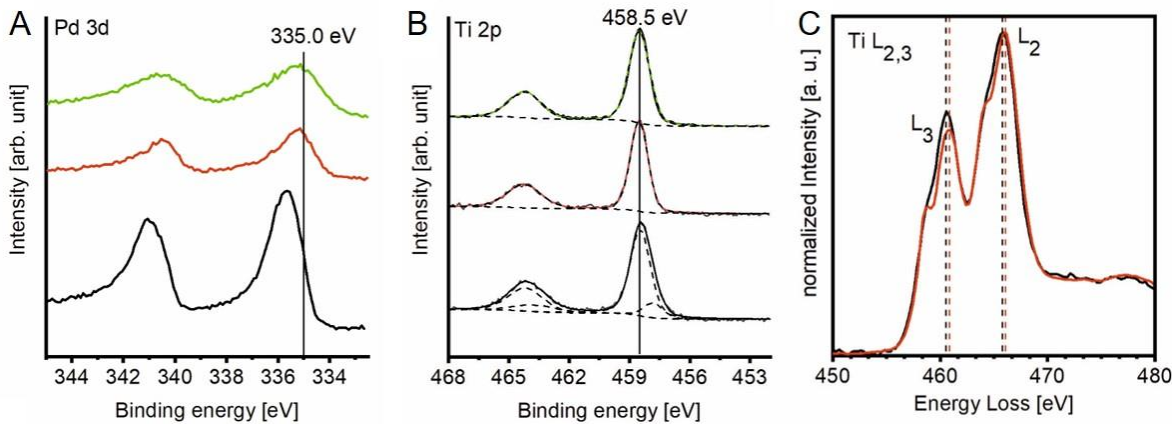


**Figure 22:** Evaluation of charge states of L-titanate@Pd@L-titanate and references. A) XP spectra of Pd 3d region of L-titanate@Pd@L-titanate (black), Pd<sub>ext</sub>@P25 (red), and Pd<sub>ext</sub>@Al<sub>2</sub>O<sub>3</sub> (green). The position of the d<sub>5/2</sub> signal at 335.0 eV of bulk Pd is marked. B) XP spectra of the Ti 2p region of L-titanate@Pd@L-titanate (black), pristine H<sup>+</sup>-L-titanate (red), and Pd<sub>ext</sub>@P25 (green). The position of Ti<sup>4+</sup> at 458.5 eV is marked. The dashed lines represent the deconvoluted spectra, and the coloured lines are the overall fitted spectra. A reduced Ti species is only present in L-titanate@Pd@L-titanate. C) EEL spectra at Ti L<sub>2,3</sub> edge of L-titanate@Pd@L-titanate (black) and pristine H<sup>+</sup>-L-titanate (red). Dashed lines mark the positions of the peaks. [Adapted under the terms of CC BY 4.0 license from reference<sup>[174]</sup>]

oxygen participation from the support. As anatase<sup>[125, 126]</sup> is capable of lattice oxygen donation, the question was whether a single nanosheet of L-titanate would be able to do the same.

Kinetic measurements revealed that the reaction orders of L-titanate@Pd@L-titanate were + 0.13 for CO and + 0.29 for O<sub>2</sub>. The reaction orders of Pd<sub>ext</sub>@Al<sub>2</sub>O<sub>3</sub> were - 0.67 for CO and + 0.91 for O<sub>2</sub>. In the case of Pd<sub>ext</sub>@Al<sub>2</sub>O<sub>3</sub>, the increase of CO partial pressure exacerbates the CO poisoning, while an increase in O<sub>2</sub> partial pressure helps O<sub>2</sub> to displace CO from the Pd surface. A high negative reaction order with respect to the CO partial pressure and a high positive reaction order for O<sub>2</sub> are typical for a Langmuir-Hinshelwood mechanism expected for Pd on γ-Al<sub>2</sub>O<sub>3</sub>.<sup>[114]</sup> This mechanism was also identified for Hec@Pd@Hec (unpublished result). In contrast, the low positive order for O<sub>2</sub> of L-titanate@Pd@L-titanate indicated that the reaction rate was rather independent of the O<sub>2</sub> partial pressure and suggested that the required oxygen was donated from the support lattice. The positive reaction order for CO also suggested that the catalyst did not suffer from CO poisoning at low temperatures. These were all signs for a Mars-van Krevelen type mechanism and explained the catalytic activity below 100 °C. In this case, it is not required that gas-phase O<sub>2</sub> has to displace CO from the surface and proved that single nanosheets of L-titanate were also capable of lattice oxygen donation as it is reported for TiO<sub>2</sub>.

The much higher catalytic activity compared to Pd<sub>ext</sub>@P25 that also followed the Mars-van Krevelen mechanism was attributed to the special sandwich architecture of L-titanate@Pd@L-titanate. XPS (**Figure 22A**) and DRIFTS revealed a more positively charged surface compared to Pd<sub>ext</sub>@P25. Furthermore, model catalysts proved that a large metal/support interface is mandatory for a high catalytic activity for oxygen donating

## Synopsis

---

supports.<sup>[132]</sup> For this reason, it was claimed that contact with the support from two directions due to the sandwich-like confinement played a crucial role in the high catalytic activity of L-titanate@Pd@L-titanate and made oxygen donation especially efficient.

As observed for Hec@Pd65@Hec, electronic interactions between support and Pd appeared as deconvolution of the Ti 2p region (XPS, **Figure 22B**) revealed an additional reduced species at lower BE. The EEL spectrum at the Ti L<sub>2,3</sub> edge (**Figure 22C**) of L-titanate@Pd@L-titanate revealed features (shift, the ratio of L<sub>2</sub> to L<sub>3</sub>, crystal field splitting) that also indicated a reduced Ti species. This was further corroborated as the O K edge showed a reduced crystal field splitting compared to pristine H<sup>+</sup>-L-titanate, which occurs when reduced Ti<sup>x</sup> species ( $x < +4$ ) are involved.

This publication demonstrated that the intercalation strategy of exploiting a nematic phase of a 2D layered material is not restricted to NaHec, but worked for L-titanate. This leads to the assumption that the strategy will work for other delaminated materials, such as layered antimony phosphates.<sup>[38]</sup> The special catalyst architecture offered both electronic interaction between support and metal and improved oxygen donation that made this catalyst highly active at low temperatures.

## 5 Literature

- [1] D. D. L. Chung: Review Graphite, *J. Mater. Sci.* **2002**, 37, 1475-1489.
- [2] K. S. Novoselov, A. K. Geim, S. V. Morozov, D. Jiang, Y. Zhang, S. V. Dubonos, I. V. Grigorieva, A. A. Firsov: Electric Field Effect in Atomically Thin Carbon Films, *Science* **2004**, 306, 666-669.
- [3] K. Zhang, Y. Feng, F. Wang, Z. Yang, J. Wang: Two dimensional hexagonal boron nitride (2D-hBN): synthesis, properties and applications, *J. Mater. Chem. C* **2017**, 5, 11992-12022.
- [4] Y. Wang, D. Yan, S. El Hankari, Y. Zou, S. Wang: Recent Progress on Layered Double Hydroxides and Their Derivatives for Electrocatalytic Water Splitting, *Adv. Sci.* **2018**, 5, 1800064.
- [5] F. Bergaya, B. K. G. Theng, G. Lagaly, *Handbook of Clay Science*, Vol. 1, Elsevier Science, Amsterdam, **2006**.
- [6] J. E. F. C. Gardolinski, G. Lagaly: Grafted organic derivatives of kaolinite: II. Intercalation of primary n-alkylamines and delamination, *Clay Miner.* **2005**, 40, 547-556.
- [7] T. Sasaki, M. Watanabe, H. Hashizume, H. Yamada, H. Nakazawa: Macromolecule-like Aspects for a Colloidal Suspension of an Exfoliated Titanate. Pairwise Association of Nanosheets and Dynamic Reassembling Process Initiated from It, *J. Am. Chem. Soc.* **1996**, 118, 8329-8335.
- [8] A. Lerf: Storylines in intercalation chemistry, *Dalton Trans.* **2014**, 43, 10276-10291.
- [9] J. Breu, W. Seidl, W. Stoll: Disorder in Smectites in Dependence of the Interlayer Cation, *Z. Anorg. All. Chem.* **2003**, 629, 513-515.
- [10] E. J. Palin, M. T. Dove, A. Hernández-Laguna, C. I. Sainz-Díaz: A computational investigation of the Al/Fe/Mg order-disorder behavior in the dioctahedral sheet of phyllosilicates, *Am. Mineral.* **2004**, 89, 164-175.
- [11] M. Stöter, D. A. Kunz, M. Schmidt, D. Hirsemann, H. Kalo, B. Putz, J. Senker, J. Breu: Nanoplatelets of sodium hectorite showing aspect ratios of  $\approx$ 20,000 and superior purity, *Langmuir* **2013**, 29, 1280-1285.
- [12] J. Breu, W. Seidl, A. J. Stoll, K. G. Lange, T. U. Probst: Charge Homogeneity in Synthetic Fluorohectorite, *Chem. Mater.* **2001**, 13, 4213-4220.
- [13] K. Jasmund, G. Lagaly, *Tonminerale und Tone*, Steinkopff, Heidelberg, **1993**.
- [14] T. Schilling, C. Habel, S. Rosenfeldt, M. Röhrl, J. Breu: Impact of Ultraconfinement on Composite Barriers, *ACS Appl. Polym. Mater.* **2020**, 2, 3010-3015.
- [15] C. Habel, E. S. Tsurko, R. L. Timmins, J. Hutschreuther, R. Kunz, D. D. Schuchardt, S. Rosenfeldt, V. Altstädt, J. Breu: Lightweight Ultra-High-Barrier Liners for Helium and Hydrogen, *ACS Nano* **2020**, 14, 7018-7024.
- [16] C. Habel, M. Schöttle, M. Daab, N. J. Eichstaedt, D. Wagner, H. Bakhshi, S. Agarwal, M. A. Horn, J. Breu: High-Barrier, Biodegradable Food Packaging, *Macromol. Mater. Eng.* **2018**, 303, 1800333.
- [17] E. S. Tsurko, P. Feicht, C. Habel, T. Schilling, M. Daab, S. Rosenfeldt, J. Breu: Can high oxygen and water vapor barrier nanocomposite coatings be obtained with a waterborne formulation?, *J. Membr. Sci.* **2017**, 540, 212-218.
- [18] M. Rieß, J. Senker, R. Schobert, J. Breu: Microporous Organically Pillared Layered Silicates (MOPS): A Versatile Class of Functional Porous Materials, *Chem. Eur. J.* **2019**, 25, 2103-2111.
- [19] M. M. Herling, M. Rieß, H. Sato, L. Li, T. Martin, H. Kalo, R. Matsuda, S. Kitagawa, J. Breu: Purely Physisorption-Based CO-Selective Gate-Opening in Microporous Organically Pillared Layered Silicates, *Angew. Chem. Int. Ed.* **2018**, 57, 564-568.
- [20] K. Bärwinkel, M. M. Herling, M. Rieß, H. Sato, L. Li, Y. S. Avadhut, T. W. Kemnitzer, H. Kalo, J. Senker, R. Matsuda, S. Kitagawa, J. Breu: Constant Volume Gate-Opening by Freezing Rotational Dynamics in Microporous Organically Pillared Layered Silicates, *J. Am. Chem. Soc.* **2017**, 139, 904-909.

- [21] M. M. Herling, U. Lacher, M. Rieß, S. Seibt, M. Schwedes, H. Kalo, R. Schobert, J. Breu: Sub-micron pore size tailoring for efficient chiral discrimination, *Chem. Commun.* **2017**, *53*, 1072-1075.
- [22] M. Rieß, R. Siegel, J. Senker, J. Breu: Diammonium-Pillared MOPS with Dynamic CO<sub>2</sub> Selectivity, *Cell Rep. Physical Science* **2020**, *1*, 100210.
- [23] M. Stöter, S. Gödrich, P. Feicht, S. Rosenfeldt, H. Thurn, J. W. Neubauer, M. Seuss, P. Lindner, H. Kalo, M. Möller, A. Fery, S. Förster, G. Papastavrou, J. Breu: Controlled Exfoliation of Layered Silicate Heterostructures into Bilayers and Their Conversion into Giant Janus Platelets, *Angew. Chem. Int. Ed.* **2016**, *55*, 7398-7402.
- [24] M. Stöter, B. Biersack, N. Reimer, M. Herling, N. Stock, R. Schobert, J. Breu: Ordered Heterostructures of Two Strictly Alternating Types of Nanoreactors, *Chem. Mater.* **2014**, *26*, 5412-5419.
- [25] M. W. Möller, D. Hirsemann, F. Haarmann, J. Senker, J. Breu: Facile Scalable Synthesis of Rectorites, *Chem. Mater.* **2010**, *22*, 186-196.
- [26] S. Rosenfeldt, M. Stöter, M. Schlenk, T. Martin, R. Q. Albuquerque, S. Förster, J. Breu: In-Depth Insights into the Key Steps of Delamination of Charged 2D Nanomaterials, *Langmuir* **2016**, *32*, 10582-10588.
- [27] Z. Wang, K. Rolle, T. Schilling, P. Hummel, A. Philipp, B. A. F. Kopera, A. M. Lechner, M. Retsch, J. Breu, G. Fytas: Tunable Thermoelastic Anisotropy in Hybrid Bragg Stacks with Extreme Polymer Confinement, *Angew. Chem. Int. Ed.* **2020**, *59*, 1286-1294.
- [28] D. W. Smith: Ionic hydration enthalpies, *J. Chem. Educ.* **1977**, *54*, 540-542.
- [29] H. Kalo, W. Milius, J. Breu: Single crystal structure refinement of one- and two-layer hydrates of sodium fluorohectorite, *RSC Adv.* **2012**, *2*, 8452-8459.
- [30] P. Xiong, X. Zhang, F. Zhang, D. Yi, J. Zhang, B. Sun, H. Tian, D. Shanmukaraj, T. Rojo, M. Armand, R. Ma, T. Sasaki, G. Wang: Two-Dimensional Unilamellar Cation-Deficient Metal Oxide Nanosheet Superlattices for High-Rate Sodium Ion Energy Storage, *ACS Nano* **2018**, *12*, 12337-12346.
- [31] K. Saito, M. Kozeni, M. Sohmiya, K. Komaguchi, M. Ogawa, Y. Sugahara, Y. Ide: Unprecedentedly enhanced solar photocatalytic activity of a layered titanate simply integrated with TiO<sub>2</sub> nanoparticles, *Phys. Chem. Chem. Phys.* **2016**, *18*, 30920-30925.
- [32] R. Gao, G. Yu, W. Chen, G.-D. Li, S. Gao, Z. Zhang, X. Shen, X. Huang, X. Zou: Host-Guest Interaction Creates Hydrogen-Evolution Electrocatalytic Active Sites in 3d Transition Metal-Intercalated Titanates, *ACS Appl. Mater. Interfaces* **2018**, *10*, 696-703.
- [33] X. Cai, R. Ma, T. C. Ozawa, N. Sakai, A. Funatsu, T. Sasaki: Superlattice assembly of graphene oxide (GO) and titania nanosheets: fabrication, *in situ* photocatalytic reduction of GO and highly improved carrier transport, *Nanoscale* **2014**, *6*, 14419-14427.
- [34] L. Wang, T. Sasaki: Titanium oxide nanosheets: graphene analogues with versatile functionalities, *Chem. Rev.* **2014**, *114*, 9455-9486.
- [35] T. Sasaki, F. Kooli, M. Iida, Y. Michiue, S. Takenouchi, Y. Yajima, F. Izumi, B. C. Chakoumakos, M. Watanabe: A Mixed Alkali Metal Titanate with the Lepidocrocite-like Layered Structure. Preparation, Crystal Structure, Protonic Form, and Acid-Base Intercalation Properties, *Chem. Mater.* **1998**, *10*, 4123-4128.
- [36] T. Tanaka, Y. Ebina, K. Takada, K. Kurashima, T. Sasaki: Oversized Titania Nanosheet Crystallites Derived from Flux-Grown Layered Titanate Single Crystals, *Chem. Mater.* **2003**, *15*, 3564-3568.
- [37] P. Davidson, C. Penisson, D. Constantin, J.-C. P. Gabriel: Isotropic, nematic, and lamellar phases in colloidal suspensions of nanosheets, *Proc. Natl. Acad. Sci. U. S. A.* **2018**, *115*, 6662-6667.
- [38] J.-C. P. Gabriel, F. Camerel, B. J. Lemaire, H. Desvaux, P. Davidson, P. Batail: Swollen liquid-crystalline lamellar phase based on extended solid-like sheets, *Nature* **2001**, *413*, 504-508.
- [39] Y. Liu, Z. Xu, W. Gao, Z. Cheng, C. Gao: Graphene and Other 2D Colloids: Liquid Crystals and Macroscopic Fibers, *Adv. Mater.* **2017**, *29*, 1606794.

- [40] M. Daab, N. J. Eichstaedt, C. Habel, S. Rosenfeldt, H. Kalo, H. Schiessling, S. Förster, J. Breu: Onset of Osmotic Swelling in Highly Charged Clay Minerals, *Langmuir* **2018**, 34, 8215-8222.
- [41] M. Daab, N. J. Eichstaedt, A. Edenhalter, S. Rosenfeldt, J. Breu: Layer charge robust delamination of organo-clays, *RSC Adv.* **2018**, 8, 28797-28803.
- [42] F. Geng, R. Ma, Y. Ebina, Y. Yamauchi, N. Miyamoto, T. Sasaki: Gigantic Swelling of Inorganic Layered Materials: A Bridge to Molecularly Thin Two-Dimensional Nanosheets, *J. Am. Chem. Soc.* **2014**, 136, 5491-5500.
- [43] T. Sasaki, M. Watanabe: Osmotic Swelling to Exfoliation. Exceptionally High Degrees of Hydration of a Layered Titanate, *J. Am. Chem. Soc.* **1998**, 120, 4682-4689.
- [44] K. Sano, Y. S. Kim, Y. Ishida, Y. Ebina, T. Sasaki, T. Hikima, T. Aida: Photonic water dynamically responsive to external stimuli, *Nat. Commun.* **2016**, 7, 12559.
- [45] T. Maluangnont, K. Matsuba, F. Geng, R. Ma, Y. Yamauchi, T. Sasaki: Osmotic Swelling of Layered Compounds as a Route to Producing High-Quality Two-Dimensional Materials. A Comparative Study of Tetramethylammonium versus Tetrabutylammonium Cation in a Lepidocrocite-type Titanate, *Chemistry* **2013**, 25, 3137-3146.
- [46] E. Roduner: Size matters: why nanomaterials are different, *Chem. Soc. Rev.* **2006**, 35, 583-592.
- [47] M. Vert, Y. Doi, K.-H. Hellwich, M. Hess, P. Hodge, P. Kubisa, M. Rinaudo, F. Schué: Terminology for biorelated polymers and applications (IUPAC Recommendations 2012), *Pure Appl. Chem.* **2012**, 84, 377-410.
- [48] K. L. Kelly, E. Coronado, L. L. Zhao, G. C. Schatz: The Optical Properties of Metal Nanoparticles: The Influence of Size, Shape, and Dielectric Environment, *J. Phys. Chem. B* **2003**, 107, 668-677.
- [49] A. S. K. Hashmi, G. J. Hutchings: Gold Catalysis, *Angew. Chem. Int. Ed.* **2006**, 45, 7896-7936.
- [50] M. Yamauchi, R. Ikeda, H. Kitagawa, M. Takata: Nanosize Effects on Hydrogen Storage in Palladium, *J. Phys. Chem. C* **2008**, 112, 3294-3299.
- [51] P. Schlexer, A. B. Andersen, B. Sebok, I. Chorkendorff, J. Schiøtz, T. W. Hansen: Size-Dependence of the Melting Temperature of Individual Au Nanoparticles, *Part. Part. Syst. Charact.* **2019**, 36, 1800480.
- [52] G. Pacchioni, H.-J. Freund: Controlling the charge state of supported nanoparticles in catalysis: lessons from model systems, *Chem. Soc. Rev.* **2018**, 47, 8474-8502.
- [53] K. Kusada, H. Kitagawa: A Route for Phase Control in Metal Nanoparticles: A Potential Strategy to Create Advanced Materials, *Adv. Mater.* **2016**, 28, 1129-1142.
- [54] H. Kobayashi, M. Yamauchi, H. Kitagawa, Y. Kubota, K. Kato, M. Takata: Atomic-Level Pd-Pt Alloying and Largely Enhanced Hydrogen-Storage Capacity in Bimetallic Nanoparticles Reconstructed from Core/Shell Structure by a Process of Hydrogen Absorption/Desorption, *J. Am. Chem. Soc.* **2010**, 132, 5576-5577.
- [55] E. D. Goodman, S. Dai, A.-C. Yang, C. J. Wrasman, A. Gallo, S. R. Bare, A. S. Hoffman, T. F. Jaramillo, G. W. Graham, X. Pan, M. Cargnello: Uniform Pt/Pd Bimetallic Nanocrystals Demonstrate Platinum Effect on Palladium Methane Combustion Activity and Stability, *ACS Catal.* **2017**, 7, 4372-4380.
- [56] B. Huang, H. Kobayashi, T. Yamamoto, S. Matsumura, Y. Nishida, K. Sato, K. Nagaoka, S. Kawaguchi, Y. Kubota, H. Kitagawa: Solid-Solution Alloying of Immiscible Ru and Cu with Enhanced CO Oxidation Activity, *J. Am. Chem. Soc.* **2017**, 139, 4643-4646.
- [57] K. Kusada, H. Kobayashi, T. Yamamoto, S. Matsumura, N. Sumi, K. Sato, K. Nagaoka, Y. Kubota, H. Kitagawa: Discovery of Face-Centered-Cubic Ruthenium Nanoparticles: Facile Size-Controlled Synthesis Using the Chemical Reduction Method, *J. Am. Chem. Soc.* **2013**, 135, 5493-5496.
- [58] P. M. Martin in *Handbook of Deposition Technologies for Films and Coatings (Third Edition)* (Ed.: P. M. Martin), William Andrew Publishing, Boston, **2010**, pp. 1-31.
- [59] M. Bäumer, H.-J. Freund: Metal deposits on well-ordered oxide films, *Prog. Surf. Sci.* **1999**, 61, 127-198.

- [60] J. Hühn, C. Carrillo-Carrion, M. G. Soliman, C. Pfeiffer, D. Valdeperez, A. Masood, I. Chakraborty, L. Zhu, M. Gallego, Z. Yue, M. Carril, N. Feliu, A. Escudero, A. M. Alkilany, B. Pelaz, P. del Pino, W. J. Parak: Selected Standard Protocols for the Synthesis, Phase Transfer, and Characterization of Inorganic Colloidal Nanoparticles, *Chem. Mater.* **2016**, 29, 399-461.
- [61] M. Kosmulski: Isoelectric points and points of zero charge of metal (hydr)oxides: 50 years after Parks' review, *Adv. Colloid Interface Sci.* **2016**, 238, 1-61.
- [62] F. Zhang, E. Lees, F. Amin, P. Rivera-Gil, F. Yang, P. Mulvaney, W. J. Parak: Polymer-Coated Nanoparticles: A Universal Tool for Biolabelling Experiments, *Small* **2011**, 7, 3113-3127.
- [63] D. I. Gittins, F. Caruso: Spontaneous Phase Transfer of Nanoparticulate Metals from Organic to Aqueous Media, *Angew. Chem. Int. Ed.* **2001**, 40, 3001-3004.
- [64] R. Wang, H. He, L.-C. Liu, H.-X. Dai, Z. Zhao: Shape-dependent catalytic activity of palladium nanocrystals for the oxidation of carbon monoxide, *Catal. Sci. Technol.* **2012**, 2, 575-580.
- [65] J. Pérez-Juste, I. Pastoriza-Santos, L. M. Liz-Marzán, P. Mulvaney: Gold nanorods: Synthesis, characterization and applications, *Coord. Chem. Rev.* **2005**, 249, 1870-1901.
- [66] K. Yoon, Y. Yang, P. Lu, D. Wan, H. C. Peng, K. Stamm Masias, P. T. Fanson, C. T. Campbell, Y. Xia: A highly reactive and sinter-resistant catalytic system based on platinum nanoparticles embedded in the inner surfaces of CeO<sub>2</sub> hollow fibers, *Angew. Chem. Int. Ed.* **2012**, 51, 9543-9546.
- [67] X. Sun, S. Dong, E. Wang: Large-Scale Synthesis of Micrometer-Scale Single-Crystalline Au Plates of Nanometer Thickness by a Wet-Chemical Route, *Angew. Chem. Int. Ed.* **2004**, 43, 6360-6363.
- [68] R. Zboril, A. Bakandritsos, M. Mashlan, V. Tzitzios, P. Dallas, C. Trapalis, D. Petridis: One-step solid state synthesis of capped γ-Fe<sub>2</sub>O<sub>3</sub> nanocrystallites, *Nanotechnology* **2008**, 19, 095602.
- [69] E. Taboada, M. Gich, A. Roig: Nanospheres of Silica with an ε-Fe<sub>2</sub>O<sub>3</sub> Single Crystal Nucleus, *ACS Nano* **2009**, 3, 3377-3382.
- [70] Z. Király, I. Dékány, A. Mastalir, M. Bartók: *In Situ* Generation of Palladium Nanoparticles in Smectite Clays, *J. Catal.* **1996**, 161, 401-408.
- [71] A. Cornélis, A. Gerstmans, P. Laszlo, A. Mathy, I. Zieba: Friedel-Crafts acylations with modified clays as catalysts, *Catal. Lett.* **1990**, 6, 103-109.
- [72] R. W. McCabe, J. M. Adams, in *Developments in Clay Science*, Vol. 5 (Eds.: F. Bergaya, G. Lagaly), Elsevier, **2013**, pp. 491-538.
- [73] M. E. Gyftopoulou, M. Millan, A. V. Bridgwater, D. Dugwell, R. Kandiyoti, J. A. Hriljac: Pillared clays as catalysts for hydrocracking of heavy liquid fuels, *Appl. Catal., A* **2005**, 282, 205-214.
- [74] G. B. B. Varadwaj, K. M. Parida: Montmorillonite supported metal nanoparticles: an update on syntheses and applications, *RSC Adv.* **2013**, 3, 13583-13593.
- [75] Z. Orolínová, A. Mockovčiaková, V. Zeleňák, M. Myndyk: Influence of heat treatment on phase transformation of clay–iron oxide composite, *J. Alloys Compd.* **2012**, 511, 63-69.
- [76] I. Dékány, L. Turi, Z. Király: CdS, TiO<sub>2</sub> and Pd<sup>0</sup> nanoparticles growing in the interlamellar space of montmorillonite in binary liquids, *Appl. Clay Sci.* **1999**, 15, 221-239.
- [77] S. Papp, A. Szűcs, I. Dékány: Preparation of Pd<sup>0</sup> nanoparticles stabilized by polymers and layered silicate, *Appl. Clay Sci.* **2001**, 19, 155-172.
- [78] S. Papp, J. Szél, A. Oszkó, I. Dékány: Synthesis of Polymer-Stabilized Nanosized Rhodium Particles in the Interlayer Space of Layered Silicates, *Chem. Mater.* **2004**, 16, 1674-1685.
- [79] S. Papp, R. Patakfalvi, I. Dékány: Metal nanoparticle formation on layer silicate lamellae, *Colloid Polym. Sci.* **2008**, 286, 3-14.

- [80] G. M. Scheuermann, R. Thomann, R. Mülhaupt: Catalysts based upon organoclay with tunable polarity and dispersion behavior: New catalysts for hydrogenation, C-C coupling reactions and fluorous biphasic catalysis, *Catal. Lett.* **2009**, 132, 355-362.
- [81] B. Yahyaei, S. Azizian, A. Mohammadzadeh, M. Pajohi-Alamoti: Preparation of clay/alumina and clay/alumina/Ag nanoparticle composites for chemical and bacterial treatment of waste water, *Chem. Eng. J.* **2014**, 247, 16-24.
- [82] S. Agarwal, J. N. Ganguli: Selective hydrogenation of monoterpenes on Rhodium (0) nanoparticles stabilized in Montmorillonite K-10 clay, *J. Mol. Catal. A: Chem.* **2013**, 372, 44-50.
- [83] L. Zhou, X. Qi, X. Jiang, Y. Zhou, H. Fu, H. Chen: Organophilic worm-like ruthenium nanoparticles catalysts by the modification of CTAB on montmorillonite supports, *J. Colloid Interface Sci.* **2013**, 392, 201-205.
- [84] P. Upadhyay, V. Srivastava: Ruthenium nanoparticle-intercalated montmorillonite clay for solvent-free alkene hydrogenation reaction, *RSC Adv.* **2015**, 5, 740-745.
- [85] J. Németh, G. Rodríguez-Gattorno, D. Díaz, A. R. Vázquez-Olmos, I. Dékány: Synthesis of ZnO Nanoparticles on a Clay Mineral Surface in Dimethyl Sulfoxide Medium, *Langmuir* **2004**, 20, 2855-2860.
- [86] Z. Han, H. Zhu, S. R. Bulcock, S. P. Ringer: One-Step Synthesis and Structural Features of CdS/Montmorillonite Nanocomposites, *J. Phys. Chem. B* **2005**, 109, 2673-2678.
- [87] K. Mogyorósi, I. Dékány, J. H. Fendler: Preparation and Characterization of Clay Mineral Intercalated Titanium Dioxide Nanoparticles, *Langmuir* **2003**, 19, 2938-2946.
- [88] A. Hassani, A. Khataee, S. Karaca: Photocatalytic degradation of ciprofloxacin by synthesized TiO<sub>2</sub> nanoparticles on montmorillonite: Effect of operation parameters and artificial neural network modeling, *J. Mol. Catal. A: Chem.* **2015**, 409, 149-161.
- [89] D. Chen, G. Du, Q. Zhu, F. Zhou: Synthesis and characterization of TiO<sub>2</sub> pillared montmorillonites: Application for methylene blue degradation, *J. Colloid Interface Sci.* **2013**, 409, 151-157.
- [90] H. Kalo, University of Bayreuth, unpublished results.
- [91] D. A. Kunz, J. Erath, D. Kluge, H. Thurn, B. Putz, A. Fery, J. Breu: In-Plane Modulus of Singular 2:1 Clay Lamellae Applying a Simple Wrinkling Technique, *ACS Appl. Mater. Interfaces* **2013**, 5, 5851-5855.
- [92] S.-M. Paek, J.-U. Jang, S.-J. Hwang, J.-H. Choy: Exfoliation–restacking route to Au nanoparticle-clay nanohybrids, *J. Phys. Chem. Solids* **2006**, 67, 1020-1023.
- [93] K. Ament, N. Köwitsch, D. Hou, T. Götsch, J. Kröhnert, C. J. Heard, A. Trunschke, T. Lunkenbein, M. Armbrüster, J. Breu: Nanoparticles Supported on Sub-Nanometer Oxide Films: Scaling Model Systems to Bulk Materials, *Angew. Chem. Int. Ed.* **2021**, 60, 5890-5897.
- [94] V. Belova, H. Möhwald, D. G. Shchukin: Ultrasonic Intercalation of Gold Nanoparticles into a Clay Matrix in the Presence of Surface-Active Materials. Part II: Negative Sodium Dodecylsulfate and Positive Cetyltrimethylammonium Bromide, *J. Phys. Chem. C* **2009**, 113, 6751-6760.
- [95] V. Belova, D. V. Andreeva, H. Möhwald, D. G. Shchukin: Ultrasonic Intercalation of Gold Nanoparticles into Clay Matrix in the Presence of Surface-Active Materials. Part I: Neutral Polyethylene Glycol, *J. Phys. Chem. C* **2009**, 113, 5381-5389.
- [96] V. Belova, H. Möhwald, D. G. Shchukin: Sonochemical intercalation of preformed gold nanoparticles into multilayered clays, *Langmuir* **2008**, 24, 9747-9753.
- [97] N. Sakai, Y. Ebina, K. Takada, T. Sasaki: Electronic Band Structure of Titania Semiconductor Nanosheets Revealed by Electrochemical and Photoelectrochemical Studies, *J. Am. Chem. Soc.* **2004**, 126, 5851-5858.
- [98] Y. Ide, M. Matsuoka, M. Ogawa: Efficient Visible-Light-Induced Photocatalytic Activity on Gold-Nanoparticle-Supported Layered Titanate, *J. Am. Chem. Soc.* **2010**, 132, 16762-16764.
- [99] T. W. Kim, H.-W. Ha, M.-J. Paek, S.-H. Hyun, I.-H. Baek, J.-H. Choy, S.-J. Hwang: Mesoporous Iron Oxide-Layered Titanate Nanohybrids: Soft-Chemical Synthesis,

- Characterization, and Photocatalyst Application, *J. Phys. Chem. C* **2008**, *112*, 14853-14862.
- [100] Y. Bai, Z. Xing, H. Yu, Z. Li, R. Amal, L. Wang: Porous Titania Nanosheet/Nanoparticle Hybrids as Photoanodes for Dye-Sensitized Solar Cells, *ACS Appl. Mater. Interfaces* **2013**, *5*, 12058-12065.
- [101] N. Sakai, T. Sasaki, K. Matsubara, T. Tatsuma: Layer-by-layer assembly of gold nanoparticles with titania nanosheets: control of plasmon resonance and photovoltaic properties, *J. Mater. Chem.* **2010**, *20*, 4371-4378.
- [102] T. W. Hansen, A. T. DeLaRiva, S. R. Challa, A. K. Datye: Sintering of Catalytic Nanoparticles: Particle Migration or Ostwald Ripening?, *Acc. Chem. Res.* **2013**, *46*, 1720-1730.
- [103] E. D. Goodman, J. A. Schwalbe, M. Cargnello: Mechanistic Understanding and the Rational Design of Sinter-Resistant Heterogeneous Catalysts, *ACS Catal.* **2017**, *7*, 7156-7173.
- [104] S. H. Joo, J. Y. Park, C. K. Tsung, Y. Yamada, P. Yang, G. A. Somorjai: Thermally stable Pt/mesoporous silica core-shell nanocatalysts for high-temperature reactions, *Nat. Mater.* **2009**, *8*, 126-131.
- [105] M. Cargnello, J. J. Delgado Jaén, J. C. Hernández Garrido, K. Bakhmutsky, T. Montini, J. J. Calvino Gámez, R. J. Gorte, P. Fornasiero: Exceptional Activity for Methane Combustion over Modular Pd@CeO<sub>2</sub> Subunits on Functionalized Al<sub>2</sub>O<sub>3</sub>, *Science* **2012**, *337*, 713-717.
- [106] L. Adjianto, D. A. Bennett, C. Chen, A. S. Yu, M. Cargnello, P. Fornasiero, R. J. Gorte, J. M. Vohs: Exceptional Thermal Stability of Pd@CeO<sub>2</sub> Core–Shell Catalyst Nanostructures Grafted onto an Oxide Surface, *Nano Lett.* **2013**, *13*, 2252-2257.
- [107] T. M. Onn, S. Zhang, L. Arroyo-Ramirez, Y.-C. Chung, G. W. Graham, X. Pan, R. J. Gorte: Improved Thermal Stability and Methane-Oxidation Activity of Pd/Al<sub>2</sub>O<sub>3</sub> Catalysts by Atomic Layer Deposition of ZrO<sub>2</sub>, *ACS Catal.* **2015**, *5*, 5696-5701.
- [108] T. W. van Deelen, C. Hernández Mejía, K. P. de Jong: Control of metal-support interactions in heterogeneous catalysts to enhance activity and selectivity, *Nat. Catal.* **2019**, *2*, 955-970.
- [109] Y. Lykhach, S. M. Kozlov, T. Skala, A. Tovt, V. Stetsovych, N. Tsud, F. Dvorak, V. Johanek, A. Neitzel, J. Myslivecek, S. Fabris, V. Matolin, K. M. Neyman, J. Libuda: Counting electrons on supported nanoparticles, *Nat. Mater.* **2016**, *15*, 284-288.
- [110] G. N. Vayssilov, Y. Lykhach, A. Migani, T. Staudt, G. P. Petrova, N. Tsud, T. Skala, A. Bruix, F. Illas, K. C. Prince, V. Matolin, K. M. Neyman, J. Libuda: Support nanostructure boosts oxygen transfer to catalytically active platinum nanoparticles, *Nat. Mater.* **2011**, *10*, 310-315.
- [111] Y. Lykhach, J. Kubat, A. Neitzel, N. Tsud, M. Vorokhta, T. Skala, F. Dvorak, Y. Kosto, K. C. Prince, V. Matolin, V. Johanek, J. Myslivecek, J. Libuda: Charge transfer and spillover phenomena in ceria-supported iridium catalysts: A model study, *J. Chem. Phys.* **2019**, *151*, 204703.
- [112] Y. Chen, J. Chen, W. Qu, C. George, M. Aouine, P. Vernoux, X. Tang: Well-defined palladium-ceria interfacial electronic effects trigger CO oxidation, *Chem. Commun.* **2018**, *54*, 10140-10143.
- [113] F. Wang, W. Ueda, J. Xu: Detection and measurement of surface electron transfer on reduced molybdenum oxides (MoO<sub>x</sub>) and catalytic activities of Au/MoO<sub>x</sub>, *Angew. Chem. Int. Ed.* **2012**, *51*, 3883-3887.
- [114] E. J. Peterson, A. T. DeLaRiva, S. Lin, R. S. Johnson, H. Guo, J. T. Miller, J. Hun Kwak, C. H. Peden, B. Kiefer, L. F. Allard, F. H. Ribeiro, A. K. Datye: Low-temperature carbon monoxide oxidation catalysed by regenerable atomically dispersed palladium on alumina, *Nat. Commun.* **2014**, *5*, 4885.
- [115] X. Wang, B. Chen, G. Chen, X. Sun: Oxygen vacancies dependent Au nanoparticle deposition and CO oxidation, *RSC Adv.* **2016**, *6*, 87978-87987.
- [116] Y. Suchorski, S. M. Kozlov, I. Bespalov, M. Datler, D. Vogel, Z. Budinska, K. M. Neyman, G. Rupprechter: The role of metal/oxide interfaces for long-range metal particle activation during CO oxidation, *Nat. Mater.* **2018**, *17*, 519-522.

- [117] P. Begum, R. C. Deka: Effect of Charge on the Catalytic Activity of CO Oxidation by zeolite Supported Single Site Palladium: A Density Functional Study, *ChemistrySelect* **2017**, 2, 8847-8855.
- [118] T. Lunkenbein, J. Schumann, M. Behrens, R. Schlögl, M. G. Willinger: Formation of a ZnO Overlayer in Industrial Cu/ZnO/Al<sub>2</sub>O<sub>3</sub> Catalysts Induced by Strong Metal–Support Interactions, *Angew. Chem. Int. Ed.* **2015**, 54, 4544-4548.
- [119] H. Tang, Y. Su, B. Zhang, A. F. Lee, M. A. Isaacs, K. Wilson, L. Li, Y. Ren, J. Huang, M. Haruta, B. Qiao, X. Liu, C. Jin, D. Su, J. Wang, T. Zhang: Classical strong metal–support interactions between gold nanoparticles and titanium dioxide, *Sci. Adv.* **2017**, 3, e1700231.
- [120] S. Liu, W. Xu, Y. Niu, B. Zhang, L. Zheng, W. Liu, L. Li, J. Wang: Ultrastable Au nanoparticles on titania through an encapsulation strategy under oxidative atmosphere, *Nat. Commun.* **2019**, 10, 5790.
- [121] W. C. Connor, J. L. Falconer: Spillover in Heterogeneous Catalysis, *Chem. Rev.* **1995**, 95, 759-788.
- [122] M. Manzoli: Boosting the Characterization of Heterogeneous Catalysts for H<sub>2</sub>O<sub>2</sub> Direct Synthesis by Infrared Spectroscopy, *Catalysts* **2019**, 9, 30.
- [123] Y. Zhou, Z. Wang, C. Liu: Perspective on CO oxidation over Pd-based catalysts, *Catal. Sci. Technol.* **2015**, 5, 69-81.
- [124] G. Li, L. Li, Y. Yuan, J. Shi, Y. Yuan, Y. Li, W. Zhao, J. Shi: Highly efficient mesoporous Pd/CeO<sub>2</sub> catalyst for low temperature CO oxidation especially under moisture condition, *Appl. Catal., B* **2014**, 158-159, 341-347.
- [125] M. Jin, J.-N. Park, J. K. Shon, J. H. Kim, Z. Li, Y.-K. Park, J. M. Kim: Low temperature CO oxidation over Pd catalysts supported on highly ordered mesoporous metal oxides, *Catal. Today* **2012**, 185, 183-190.
- [126] X. Zhai, C. Liu, Q. Chang, C. Zhao, R. Tan, H. Peng, D. Liu, P. Zhang, J. Gui: TiO<sub>2</sub>-nanosheet-assembled microspheres as Pd-catalyst support for highly-stable low-temperature CO oxidation, *New J. Chem.* **2018**, 42, 18066-18076.
- [127] B. Han, T. Li, J. Zhang, C. Zeng, H. Matsumoto, Y. Su, B. Qiao, T. Zhang: A highly active Rh<sub>1</sub>/CeO<sub>2</sub> single-atom catalyst for low-temperature CO oxidation, *Chem. Commun.* **2020**, 56, 4870-4873.
- [128] H. Guan, J. Lin, B. Qiao, X. Yang, L. Li, S. Miao, J. Liu, A. Wang, X. Wang, T. Zhang: Catalytically Active Rh Sub-Nanoclusters on TiO<sub>2</sub> for CO Oxidation at Cryogenic Temperatures, *Angew. Chem. Int. Ed.* **2016**, 55, 2820-2824.
- [129] S. Song, X. Wang, H. Zhang: CeO<sub>2</sub>-encapsulated noble metal nanocatalysts: enhanced activity and stability for catalytic application, *NPG Asia Mater.* **2015**, 7, e179.
- [130] J. Ye, D.-g. Cheng, F. Chen, X. Zhan: Controlled Synthesis of Sintering-Resistant Pd@CeO<sub>2</sub> Core–Shell Nanotube Catalysts for CO Oxidation, *Ind. Eng. Chem. Res.* **2019**, 58, 21972-21982.
- [131] H. Y. Kim, G. Henkelman: CO Oxidation at the Interface of Au Nanoclusters and the Stepped-CeO<sub>2</sub>(111) Surface by the Mars–van Krevelen Mechanism, *J. Phys. Chem. Lett.* **2013**, 4, 216-221.
- [132] M. Cargnello, V. V. T. Doan-Nguyen, T. R. Grodon, R. E. Diaz, E. A. Stach, R. J. Gorte, P. Fornasiero, C. B. Murray: Control of Metal Nanocrystal Size Reveals Metal-Support Interface Role for Ceria Catalysts, *Science* **2013**, 341, 771-773.
- [133] S. L. Hemmingson, C. T. Campbell: Trends in Adhesion Energies of Metal Nanoparticles on Oxide Surfaces: Understanding Support Effects in Catalysis and Nanotechnology, *ACS Nano* **2017**, 11, 1196-1203.
- [134] S. Kim, D.-W. Lee, K.-Y. Lee: Shape-dependent catalytic activity of palladium nanoparticles for the direct synthesis of hydrogen peroxide from hydrogen and oxygen, *J. Mol. Catal. A: Chem.* **2014**, 391, 48-54.
- [135] H.-J. Freund: The Surface Science of Catalysis and More, Using Ultrathin Oxide Films as Templates: A Perspective, *J. Am. Chem. Soc.* **2016**, 138, 8985-8996.
- [136] G. Pacchioni, H. Freund: Electron transfer at oxide surfaces. The MgO paradigm: from defects to ultrathin films, *Chem. Rev.* **2013**, 113, 4035-4072.

- [137] H. Tissot, X. Weng, P. Schlexer, G. Pacchioni, S. Shaikhutdinov, H.-J. Freund: Ultrathin silica films on Pd(111): Structure and adsorption properties, *Surf Sci.* **2018**, 678, 118-123.
- [138] K. Zhang, L. Li, S. Shaikhutdinov, H.-J. Freund: Carbon Monoxide Oxidation on Metal-Supported Monolayer Oxide Films: Establishing Which Interface is Active, *Angew. Chem. Int. Ed.* **2018**, 57, 1261-1265.
- [139] M. Sterrer, T. Risse, M. Heyde, H.-P. Rust, H.-J. Freund: Crossover from Three-Dimensional to Two-Dimensional Geometries of Au Nanostructures on Thin MgO(001) Films: A Confirmation of Theoretical Predictions, *Phys. Rev. Lett.* **2007**, 98, 206103.
- [140] S. Prada, U. Martinez, G. Pacchioni: Work function changes induced by deposition of ultrathin dielectric films on metals: A theoretical analysis, *Phys. Rev. B* **2008**, 78, 235423.
- [141] L. Giordano, G. Pacchioni: Oxide Films at the Nanoscale: New Structures, New Functions, and New Materials, *Acc. Chem. Res.* **2011**, 44, 1244-1252.
- [142] L. Giordano, F. Cinquini, G. Pacchioni: Tuning the surface metal work function by deposition of ultrathin oxide films: Density functional calculations, *Phys. Rev. B* **2006**, 73, 045414.
- [143] S. Tosoni, G. Pacchioni: Hydrogen Adsorption on Free-Standing and Ag-Pt Supported TiO<sub>2</sub> Thin Films, *J. Phys. Chem. C* **2019**, 123, 7952-7960.
- [144] Y.-N. Sun, L. Giordano, J. Goniakowski, M. Lewandowski, Z.-H. Qin, C. Noguera, S. Shaikhutdinov, G. Pacchioni, H.-J. Freund: The Interplay between Structure and CO Oxidation Catalysis on Metal-Supported Ultrathin Oxide Films, *Angew. Chem. Int. Ed.* **2010**, 49, 4418-4421.
- [145] Y. N. Sun, Z. H. Qin, M. Lewandowski, E. Carrasco, M. Sterrer, S. Shaikhutdinov, H. J. Freund: Monolayer iron oxide film on platinum promotes low temperature CO oxidation, *J. Catal.* **2009**, 266, 359-368.
- [146] W.-D. Schneider, M. Heyde, H.-J. Freund: Charge Control in Model Catalysis: The Decisive Role of the Oxide-Nanoparticle Interface, *Chem. Eur. J.* **2018**, 24, 2317-2327.
- [147] S. Shaikhutdinov, H.-J. Freund: Ultrathin silicate films on metals, *J. Phys.: Condens. Matter* **2015**, 27, 443001.
- [148] H.-J. Freund: Controlling Silica in Its Crystalline and Amorphous States: A Problem in Surface Science, *Acc. Chem. Res.* **2017**, 50, 446-449.
- [149] H.-J. Freund, G. Meijer, M. Scheffler, R. Schlögl, M. Wolf: CO oxidation as a prototypical reaction for heterogeneous processes, *Angew. Chem. Int. Ed.* **2011**, 50, 10064-10094.
- [150] M. F. M. Zwinkels, S. G. Järås, P. G. Menon, T. A. Griffin: Catalytic Materials for High-Temperature Combustion, *Catal. Rev.* **1993**, 35, 319-358.
- [151] F. D. Manchester, A. San-Martin, J. M. Pitre: The H-Pd (hydrogen-palladium) System, *J. Phase Equilib.* **1994**, 15, 62-83.
- [152] W.-C. Xu, K. Takahashi, Y. Matsuo, Y. Hattori, M. Kumagai, S. Ishiyama, K. Kaneko, S. Iijima: Investigation of hydrogen storage capacity of various carbon materials, *Int. J. Hydrg. Energy* **2007**, 32, 2504-2512.
- [153] M. P. Suh, H. J. Park, T. K. Prasad, D.-W. Lim: Hydrogen Storage in Metal–Organic Frameworks, *Chem. Rev.* **2012**, 112, 782-835.
- [154] N. A. A. Rusman, M. Dahari: A review on the current progress of metal hydrides material for solid-state hydrogen storage applications, *Int. J. Hydrg. Energy* **2016**, 41, 12108-12126.
- [155] Y. Chen, O. Sakata, Y. Nanba, L. S. R. Kumara, A. Yang, C. Song, M. Koyama, G. Li, H. Kobayashi, H. Kitagawa: Electronic origin of hydrogen storage in MOF-covered palladium nanocubes investigated by synchrotron X-rays, *Commun. Chem.* **2018**, 1, 61.
- [156] H. Kobayashi, M. Yamauchi, R. Ikeda, T. Yamamoto, S. Matsumura, H. Kitagawa: Double enhancement of hydrogen storage capacity of Pd nanoparticles by 20 at% replacement with Ir; systematic control of hydrogen storage in Pd-M nanoparticles (M = Ir, Pt, Au), *Chem. Sci.* **2018**, 9, 5536-5540.

- [157] G. Li, H. Kobayashi, J. M. Taylor, R. Ikeda, Y. Kubota, K. Kato, M. Takata, T. Yamamoto, S. Toh, S. Matsumura, H. Kitagawa: Hydrogen storage in Pd nanocrystals covered with a metal-organic framework, *Nat. Mater.* **2014**, *13*, 802-806.
- [158] H. Qu, D. Caruntu, H. Liu, C. J. O'Connor: Water-dispersible iron oxide magnetic nanoparticles with versatile surface functionalities, *Langmuir* **2011**, *27*, 2271-2278.
- [159] D. Caruntu, G. Caruntu, Y. Chen, C. J. O'Connor, G. Goloverda, V. L. Kolesnichenko: Synthesis of Variable-Sized Nanocrystals of Fe<sub>3</sub>O<sub>4</sub> with High Surface Reactivity, *Chem. Mater.* **2004**, *16*, 5527-5534.
- [160] K. Ament, D. R. Wagner, F. E. Meij, F. E. Wagner, J. Breu: High Temperature Stable Maghemite Nanoparticles Sandwiched between Hectorite Nanosheets, *Z. Anorg. Allg. Chem.* **2020**, *646*, 1110-1115.
- [161] L. Machala, J. Tuček, R. Zbořil: Polymorphous Transformations of Nanometric Iron(III) Oxide: A Review, *Chem. Mater.* **2011**, *23*, 3255-3272.
- [162] A. Navrotsky, C. Ma, K. Lilova, N. Birkner: Nanophase Transition Metal Oxides Show Large Thermodynamically Driven Shifts in Oxidation-Reduction Equilibria, *Science* **2010**, *330*, 199-201.
- [163] A. Navrotsky, L. Mazeina, J. Majzlan: Size-Driven Structural and Thermodynamic Complexity in Iron Oxides, *Science* **2008**, *319*, 1635-1638.
- [164] F. S. Yen, W. C. Chen, J. M. Yang, C. T. Hong: Crystallite Size Variations of Nanosized Fe<sub>2</sub>O<sub>3</sub> Powders during γ- to α-Phase Transformation, *Nano Lett.* **2002**, *2*, 245-252.
- [165] T. Belin, N. Millot, N. Bovet, M. Gailhanou: In situ and time resolved study of the γ/α-Fe<sub>2</sub>O<sub>3</sub> transition in nanometric particles, *J. Solid State Chem.* **2007**, *180*, 2377-2385.
- [166] S. Lee, H. Xu: Size-Dependent Phase Map and Phase Transformation Kinetics for Nanometric Iron(III) Oxides (γ → ε → α Pathway), *J. Phys. Chem. C* **2016**, *120*, 13316-13322.
- [167] K. A. Flanagan, J. A. Sullivan, H. Müller-Bunz: Preparation and characterization of 4-dimethylaminopyridine-stabilized palladium nanoparticles, *Langmuir* **2007**, *23*, 12508-12520.
- [168] R. Arrigo, M. E. Schuster, S. Abate, S. Wrabetz, K. Amakawa, D. Teschner, M. Freni, G. Centi, S. Perathoner, M. Hävecker, R. Schlögl: Dynamics of palladium on nanocarbon in the direct synthesis of H<sub>2</sub>O<sub>2</sub>, *ChemSusChem* **2014**, *7*, 179-194.
- [169] N. S. Babu, N. L. Lingaiah, R. Gopinath, P. S. S. Reddy, P. S. S. Prasad: Characterization and Reactivity of Alumina-Supported Pd Catalysts for the Room-Temperature Hydrodechlorination of Chlorobenzene, *J. Phys. Chem. C* **2007**, *111*, 6447-6453.
- [170] K. Ament, H. Kobayashi, K. Kusada, J. Breu, H. Kitagawa: Enhancing Hydrogen Storage Capacity of Pd Nanoparticles by Sandwiching between Inorganic Nanosheets, *Z. Anorg. Allg. Chem.* **2022**, e202100370.
- [171] H. Tsunoyama, H. Sakurai, Y. Negishi, T. Tsukuda: Size-Specific Catalytic Activity of Polymer-Stabilized Gold Nanoclusters for Aerobic Alcohol Oxidation in Water, *J. Am. Chem. Soc.* **2005**, *127*, 9374-9375.
- [172] M. Yamauchi, H. Kobayashi, H. Kitagawa: Hydrogen storage mediated by Pd and Pt nanoparticles, *ChemPhysChem* **2009**, *10*, 2566-2576.
- [173] R. Griessen, N. Strohfeldt, H. Giessen: Thermodynamics of the hybrid interaction of hydrogen with palladium nanoparticles, *Nat. Mater.* **2016**, *15*, 311-317.
- [174] K. Ament, D. R. Wagner, T. Götsch, T. Kikuchi, J. Kröhnert, A. Trunschke, T. Lunkenbein, T. Sasaki, J. Breu: Enhancing the Catalytic Activity of Palladium Nanoparticles via Sandwich-Like Confinement by Thin Titanate Nanosheets, *ACS Catal.* **2021**, *11*, 2754-2762.
- [175] K. Fukuda, Y. Ebina, T. Shibata, T. Aizawa, I. Nakai, T. Sasaki: Unusual Crystallization Behaviors of Anatase Nanocrystallites from a Molecularly Thin Titania Nanosheet and Its Stacked Forms: Increase in Nucleation Temperature and Oriented Growth, *J. Am. Chem. Soc.* **2007**, *129*, 202-209.

## 6 Results

### 6.1 High Temperature Stable Maghemite Nanoparticles Sandwiched between Hectorite Nanosheets

#### High Temperature Stable Maghemite Nanoparticles Sandwiched between Hectorite Nanosheets

Kevin Ament<sup>[a,b]</sup>, Daniel R. Wagner<sup>[a,b]</sup>, Frederieke E. Meij<sup>[a,b]</sup>, Friedrich E. Wagner<sup>[c]</sup>, and Josef Breu<sup>\*[a,b]</sup>

*Zeitschrift für Anorganische und Allgemeine Chemie* **2020**, 646, 1110-1115

Impact Factor (2017): 1.179

<https://doi.org/10.1002/zaac.202000077>

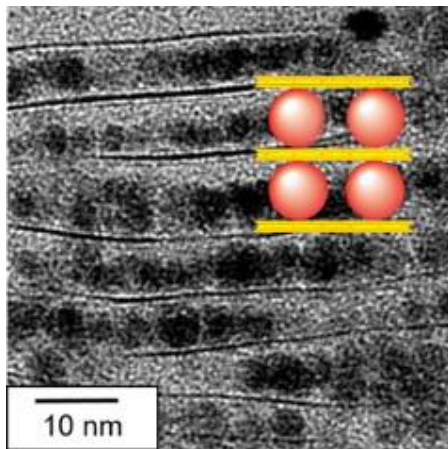
Reprinted under the terms of CC BY 4.0 license (<https://creativecommons.org/licenses/by/4.0/legalcode>)  
© 2020 The Authors. Published by Wiley-VCH Verlag GmbH & Co. KGaA.

[a] Bavarian Polymer Institute, University of Bayreuth, Universitätsstraße 30, 95447 Bayreuth, Germany

[b] Department of Chemistry, University of Bayreuth, Universitätsstraße 30, 95447 Bayreuth, Germany

[c] Physics Department E15, Technical University of Munich, 85747 Garching, Germany

\* E-mail: josef.breu@uni-bayreuth.de



#### Individual Contribution:

Prof J. Breu and I developed the concept of the publication. The manuscript was written by Prof J. Breu and me. The experimental part was done by me and within practical courses of D. Wagner and F. Meij under my supervision. I characterized the sandwich structure and performed the temperature studies. Prof F. Wagner from the Technical University of Munich performed and evaluated the Mößbauer measurements.

My contribution to the publication is approx. 85 %.

## High Temperature Stable Maghemite Nanoparticles Sandwiched between Hectorite Nanosheets

Kevin Ament,<sup>[a,b]</sup> Daniel R. Wagner,<sup>[a,b]</sup> Frederike E. Meij,<sup>[a,b]</sup> Friedrich E. Wagner,<sup>[c]</sup> and Josef Breu<sup>\*[a,b]</sup>

Dedicated to Prof. Dr. Juri Grin on the Occasion of his 65th Birthday

**Abstract.** Maghemite ( $\gamma\text{-Fe}_2\text{O}_3$ ) is a metastable iron oxide phase and usually undergoes fast phase transition to hematite at elevated temperatures ( $>350^\circ\text{C}$ ). Maghemite nanoparticles were synthesized by the polyol method and then intercalated into a highly swollen ( $>100\text{ nm}$  separation) nematic phase of hectorite. A composite of maghemite nanoparticles sandwiched between nanosheets of synthetic hectorite was obtained. The confinement of the nanoparticles hampered Ostwald

ripening up to  $700^\circ\text{C}$  and consequently the phase transition to hematite is suppressed. Only above  $700^\circ\text{C}$   $\gamma\text{-Fe}_2\text{O}_3$  nanoparticles started to grow and undergo phase transition to  $\alpha\text{-Fe}_2\text{O}_3$ . The structure and the phase transition of the composite was evaluated using X-ray diffraction, TEM, SEM, physisorption, TGA/DSC, and Mößbauer spectroscopy.

### Introduction

Due to high abundancy and low toxicity iron oxides are applied as pigments in cosmetics, as advanced (photo-)oxidation catalyst in waste water treatment and for diagnostics, drug delivery, sensoring or magneto optical devices.<sup>[1]</sup> Iron(III) oxide crystallizes in four well known polymorphs ( $\alpha$ ,  $\beta$ ,  $\gamma$ , and  $\epsilon$ -phase). More recently, a new fifth polymorph,  $\zeta$ -phase, was discovered under high pressure conditions.<sup>[2]</sup> All of them exhibit significantly different structural, physical and chemical properties and might be of use for different biomedical, catalytic or magnetic applications.<sup>[3]</sup> Parameters that affect the phase transitions were extensively studied.<sup>[4]</sup> Spinel type  $\gamma\text{-Fe}_2\text{O}_3$  ( $Fd\bar{3}m$ ) is thermodynamically metastable at room temperature and bulk maghemite undergoes a rapid phase transition to corundum type  $\alpha\text{-Fe}_2\text{O}_3$  ( $R\bar{3}\bar{c}$ ) at temperatures around  $350^\circ\text{C}$ .  $\epsilon\text{-Fe}_2\text{O}_3$  ( $Pna2_1$ ) and  $\beta\text{-Fe}_2\text{O}_3$  ( $Ia\bar{3}$ ) are only observed as nanoparticles.<sup>[5]</sup>

Moreover, calorimetric and computational data suggest that the relative thermodynamic stability of the different iron oxide phases may also change on the nanoscale.<sup>[6]</sup> For instance, for nanoparticulate  $\gamma\text{-Fe}_2\text{O}_3$  the phase transition to hematite has been shown to be suppressed until a certain threshold size is reached that is normally above  $10\text{--}20\text{ nm}$ .<sup>[7]</sup> A common way to shift the phase transition to higher temperature is coating or embedding of the particles into a matrix.<sup>[8]</sup> For instance, when nanoparticulate  $\gamma\text{-Fe}_2\text{O}_3$  is coated by an amorphous silica shell, particle growth is prevented and the phase transition is retarded up to  $1000^\circ\text{C}$ .<sup>[9]</sup> A silica xerogel loaded with low amounts of  $\gamma\text{-Fe}_2\text{O}_3$  nanoparticles (molar ratio Fe/Si of 0.013) retards the phase transition up to  $900^\circ\text{C}$ . When the molar ratio is increased to 0.2,  $\alpha\text{-Fe}_2\text{O}_3$  is already observed at  $500^\circ\text{C}$ .<sup>[10]</sup>

Synthetic fluorohectorite ( $\text{NaHec}$ ,  $[\text{Na}_{0.5}]^{\text{inter}}[\text{Mg}_{2.5}\text{Li}_{0.5}]^{\text{oct}}[\text{Si}_4]^{\text{tet}}\text{O}_{10}\text{F}_2$ ) is a 2D layered silicate with permanent negatively charged nanosheets balanced by  $\text{Na}^+$  cations in the interlayer space.  $\text{NaHec}$  can be gently delaminated into individual silicate layers by thermodynamically allowed, repulsive osmotic swelling.<sup>[11]</sup> This most gentle way of delamination preserves the diameter of pristine  $\text{NaHec}$  platelets and yields nanosheets with a thickness of 1 nm and lateral dimensions of  $20\text{ }\mu\text{m}$ .<sup>[12]</sup> Consequently, even in very dilute suspensions (<1 wt%) the separation is insufficient to allow for free rotation of the nanosheets and instead of isotropic suspensions rather a nematic liquid crystalline phase is obtained.<sup>[13]</sup> The strong electrostatic repulsion of the negatively charged nanosheets forces the nanosheets to adopt a cofacial arrangement even with nanosheet separations exceeding 100 nm.<sup>[14]</sup> This nematic phase allows for “intercalation” of nanoparticles carrying a positive surface potential between the nanosheets. By sandwiching nanoparticles in the confined space between two negatively charged nanosheets Ostwald ripening can be retarded and phase transition from  $\gamma\text{-Fe}_2\text{O}_3$  to  $\alpha\text{-Fe}_2\text{O}_3$  can be suppressed up to  $700^\circ\text{C}$ .

\* Prof. Dr. J. Breu  
 E-Mail: josef.breu@uni-bayreuth.de

[a] Bavarian Polymer Institute  
 University of Bayreuth  
 Universitätsstraße 30  
 95447 Bayreuth, Germany

[b] Department of Chemistry  
 University of Bayreuth  
 Universitätsstraße 30  
 95447 Bayreuth, Germany

[c] Physics Department E15  
 Technical University of Munich  
 85747 Garching, Germany

Supporting information for this article is available on the WWW under <http://dx.doi.org/10.1002/zaac.202000077> or from the author.

© 2020 The Authors. Published by Wiley-VCH Verlag GmbH & Co. KGaA. This is an open access article under the terms of the Creative Commons Attribution License, which permits use, distribution and reproduction in any medium, provided the original work is properly cited.

## Results and Discussion

*Composite Synthesis, Characterization, and Location of the Nanoparticles*

For intercalation of nanoparticulate  $\gamma\text{-Fe}_2\text{O}_3$  a positive surface charge is required. We applied a polyol method that allows for modification of the surface with phosphocholine post synthesis yielding a positive surface charge.<sup>[15]</sup> Briefly, a mixture of  $\text{FeCl}_2\cdot 4\text{H}_2\text{O}$  and  $\text{FeCl}_3\cdot 6\text{H}_2\text{O}$  was dissolved in diethylene glycol and ramped by  $2\text{ K}\text{ min}^{-1}$  to  $220\text{ }^\circ\text{C}$ . After refluxing for two hours the dispersion was allowed to cool to  $90\text{ }^\circ\text{C}$  and [calcium (phosphocholine)] chloride tetrahydrate was added (1 mmol in 20 g diethylene glycol). After precipitation with acetone and decantation of diethylene glycol, the nanoparticles were redispersed in water.

According to transmission electron micrographs (TEM), the as prepared nanoparticles exhibited a size of  $5.5 \pm 1.1\text{ nm}$  (100 particles, Figure 1A and B). According to dynamic light scattering (DLS) the hydrodynamic diameter was determined to be  $6.9 \pm 1.3\text{ nm}$  (Figure 1C). This value is higher than the core size determined by TEM as the hydrodynamic diameter probed by DLS also includes the capping ligand and the solvation shell. At a pH of 7 the particles had a positive surface charge with a  $\zeta$ -potential of  $+42\text{ mV}$ . The aqueous dispersion was stable for several weeks when stored at room temperature. The amount of phosphocholine capping ligand was determined to be 5.5 wt% according to thermogravimetric analysis (TGA, Figure 1D).

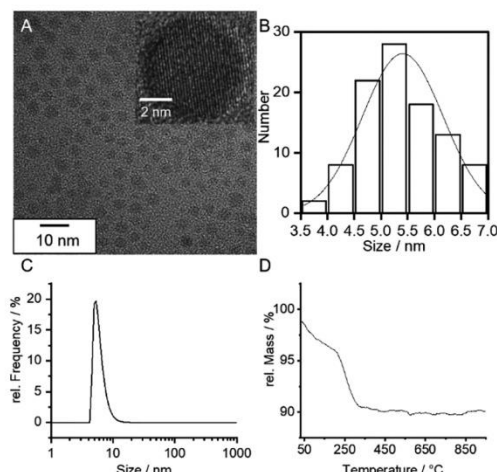


**Figure 1.** Analysis of nanoparticulate  $\gamma\text{-Fe}_2\text{O}_3$  before intercalation. (A) TEM image of  $\gamma\text{-Fe}_2\text{O}_3$  nanoparticles after synthesis. Inset: High magnification image. (B) Histogram of the core sizes of 100 particles. (C) Hydrodynamic diameter according to DLS measurement. (D) TGA measurement under flowing air.

NaHec powder was swollen in water to a nematic phase with a solid content of 1 wt%. This corresponded to a nanosheet separation of about 100 nm – much larger than the nanoparticle

size of 5.5 nm. The aqueous NaHec dispersion was added rapidly to the aqueous nanoparticle dispersion under mechanical stirring with a weight ratio of  $\gamma\text{-Fe}_2\text{O}_3$  and NaHec of 5:1. Upon addition hetero coagulation was triggered and after about one minute, visible flocculation occurred. The brown to orange flocculate was separated by a magnet from the still slightly brownish supernatant.

The loading level of  $\gamma\text{-Fe}_2\text{O}_3$  was determined by inductively coupled plasma atomic absorption spectroscopy (ICP-AAS). The ratio of Fe to Si was determined to be 2.1:1. This corresponded to a nominal formula of  $(\text{Fe}_2\text{O}_3)_{4.2}(\text{Mg}_{2.5}\text{Li}_{0.5}\text{Si}_4\text{O}_{10}\text{F}_2)$  or a weight fraction of 64 wt%  $\gamma\text{-Fe}_2\text{O}_3$  (Table S1, Supporting Information).

The X-ray diffractogram (XRD) comprised two sets of reflections: In the low angle range a  $00l$  ( $l = 1\text{--}3$ ) series was observed corresponding to the one-dimensionally (1D) ordered intercalation compound (Figure 2A). The basal reflection ( $001$ ) at  $1.30^\circ 2\theta$  (6.9 nm) corresponds to the sum of silicate layer thickness (1 nm) and nanoparticle diameter (5.5 nm). The scanning electron microscopy (SEM) of the composite showed that upon flocculation with the nanoparticles the nanosheets restacked (Figure 2B).

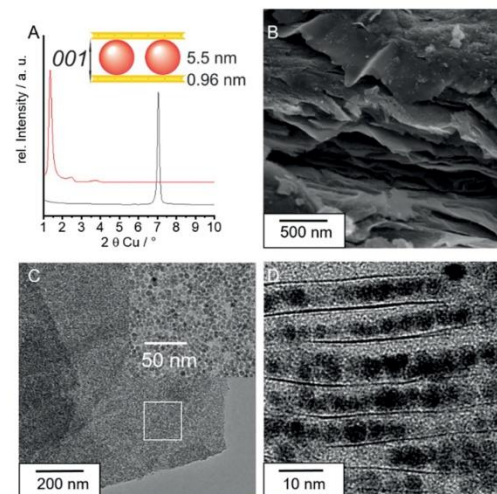


**Figure 2.** Structural analysis of the  $\gamma\text{-Fe}_2\text{O}_3/\text{NaHec}$  composite. (A) Red: XRD of textured sample of  $\gamma\text{-Fe}_2\text{O}_3/\text{NaHec}$ . Black:  $001$  of pristine NaHec for comparison. (B) SEM image of the restacked tactoid. (C) TEM image of top view of the composite. The inset shows the magnification of the white square of highly loaded nanosheets. (D) Cross sectional TEM image with view between the nanosheets.

TEM of the composite drop casted on a copper grid showed highly loaded platelets (Figure 2C). From these images it was not possible to identify the  $z$ -location of the particles nor could be distinguished between surface supported or intercalated. To overcome this problem, the composite was embedded in a resin and sliced applying an ultramicrotome. TEM images of this cross sections granted a look between the nanosheets. Well separated nanosheets with nanoparticles in between were ob-

served (Figure 2D). Due to the particle size distribution of  $\gamma\text{-Fe}_2\text{O}_3$  the nanosheets could not restack perfectly parallel. The average periodicity as measured at 30 different sample spots gave a distance of  $7.1 \pm 1.2$  nm, which is in decent agreement with the basal spacing observed in XRD. The varying distance of the nanosheets also is responsible for the broad reflections and the limited rationality of the  $00l$  series observed from the XRD (Figure 2A).

The second set of peaks in the XRD correspond to the intercalated nanoparticles and could be indexed with a cubic unit cell (space group  $Fd\bar{3}m$ ) of a spinel type iron oxide phase (Figure 3A). No reflections of hematite or another crystalline iron oxide phase were observed. The reflections marked with circles are the  $02/11$  and the  $06$  bands of NaHec derived from the 2D crystal structure of the nanosheets in  $ab$  direction while the relative position along the  $c$  direction is random due to stacking faults.

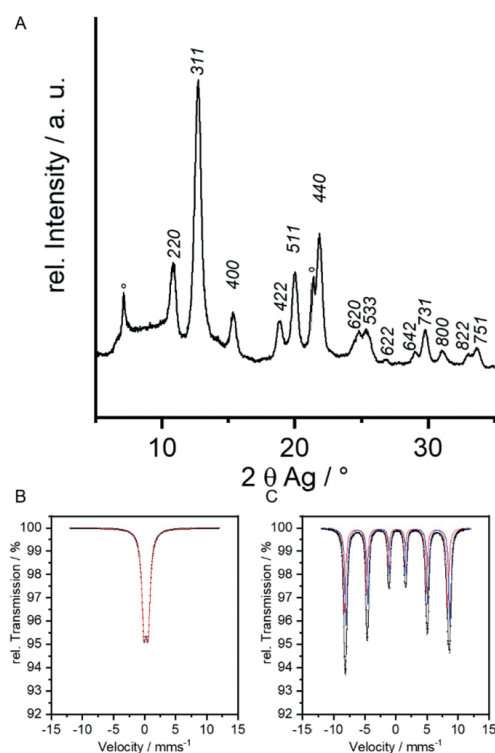


**Figure 3.** Evaluation of the phase of the  $\gamma\text{-Fe}_2\text{O}_3$  nanoparticles in the composite. (A) Wide angle PXRD using  $\text{Ag}-K_{\alpha}$  ( $\lambda = 0.5594075$  Å) radiation. (B) Room temperature Mössbauer spectrum showing only one quadrupole doublet. (C) 4.2 K Mössbauer spectrum with two sextets for  $\text{Fe}^{3+}$  in tetrahedral sites (red) and octahedral sites (blue).

Since for the synthesis in air a mixture of  $\text{Fe}^{2+}$  and  $\text{Fe}^{3+}$  salts was applied to obtain a nanoscopic ferromagnetic phase,

Mössbauer spectroscopy had to be employed to distinguish between the two spinel phases maghemite  $\gamma\text{-Fe}_2\text{O}_3$  and magnetite  $\text{Fe}_3\text{O}_4$ . The RT spectrum showed only one quadrupole doublet due to fast superparamagnetic relaxation processes that is characteristic for small sized iron oxide nanoparticles (Figure 3B). The spectrum recorded at 4.2 K showed two sextets with nearly identical hyperfine fields and nearly no quadrupole interaction (Figure 3C). The isomeric shifts of  $0.05 \text{ mm}\cdot\text{s}^{-1}$  and  $0.33 \text{ mm}\cdot\text{s}^{-1}$  corresponded to the tetrahedral and octahedral sites of  $\text{Fe}^{3+}$ , respectively.  $\text{Fe}^{2+}$  that would indicate a magnetite phase could not be observed. Apparently,  $\text{Fe}^{2+}$  is readily oxidized to  $\text{Fe}^{3+}$  when exposed to air during synthesis. It should be noted that the direct synthesis of  $\gamma\text{-Fe}_2\text{O}_3$  using single valent  $\text{FeCl}_3$  always yielded microcrystalline hematite.

In the TEM micrograph, the  $\gamma\text{-Fe}_2\text{O}_3$  nanoparticles appeared to be densely packed (Figure 2C and D). This, however, is an artefact caused by the superposition/projection of particles in the sample slice that is about 50 nm thick. The Ar-physisorption isotherm showed a type IV(a) behavior that corresponds to a mesoporous network (Figure S2A, Supporting Information). The shape of the hysteresis can be attributed to the H2(b) type. This type of hysteresis in the desorption branch normally is caused by a broad distribution of pore necks.<sup>[16]</sup> This is not surprising given the broad particles size distribution of  $\gamma\text{-Fe}_2\text{O}_3$  acting as pillars. The surface area determined by BET method was  $237 \text{ m}^2\cdot\text{g}^{-1}$  and the average pore size is 5.5 nm (Figure S2B). Clearly, the nanoparticles are not packed densely but rather a mesoporous material with open space between nanoparticles within a given interlayer space was obtained. This renders the composite also interesting for photocatalytic applications as short  $\gamma\text{-Fe}_2\text{O}_3$  nanoparticles are stabilized on a substrate assuring short diffusion lengths of charge carriers.

#### Phase Transition

Deposition of nanoparticles on conventional (porous) supports as  $\text{Al}_2\text{O}_3$  or  $\text{SiO}_2$  normally allows only a very small loading. A higher loading triggers aggregation, blocking of pores of the support or fast Ostwald ripening. With the synthesis protocol presented here, the particle density was very high. One might consequently assume rather fast growth of the nanoparticles. The nanoparticles in the  $\gamma\text{-Fe}_2\text{O}_3/\text{NaHec}$  are, however, not conventionally supported on a single external surface, but were sandwiched between two negatively charged nanosheets.

To study the influence of confinement combined TGA and dynamic scanning calorimetry (DSC) in air was performed (Figure 4). An endothermic weight loss at the beginning can be attributed to desorption of interlayer water (ca. 5 wt%). The second weight loss of about 3.5 wt% can be attributed to the exothermic combustion of the phosphocholine capping ligand. Finally, a very broad exothermic event commenced at  $800$  °C without accompanying weight loss. This peak is related to the phase transition of  $\gamma\text{-Fe}_2\text{O}_3$  to the thermodynamically more stable  $\alpha\text{-Fe}_2\text{O}_3$  phase.<sup>[4]</sup> The very broad peak suggests a rather sluggish transition.

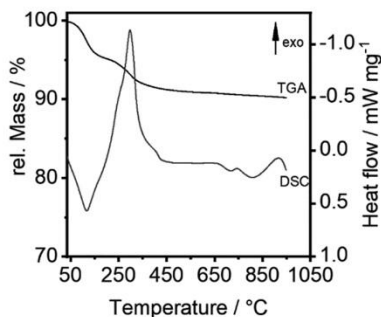


**Figure 4.** Thermal characterization of  $\gamma\text{-Fe}_2\text{O}_3/\text{NaHec}$ . TGA and DSC curves from 30 °C to 950 °C with a heating ramp of 10 K·min<sup>-1</sup> and flowing air as atmosphere.

To rule out kinetic contributions to this high onset temperature of the phase transition, the composite was annealed at 700 °C for 20 h in air. No changes were observed in the PXRD pattern (Figure 5A), nor in the RT and 4.2 K Möbbauer spectra (Figure 5B and C). TEM analysis revealed that the nanoparticles retained their size within experimental error upon annealing ( $5.7 \pm 1.2$  nm, Figure 5F). Furthermore, the nanoparticles were still not faceted but spherical. The Ar-physisorption isotherm showed no significant changes upon annealing at 700 °C for 20 h (Figures S2C and S2D, Supporting Information, BET surface of  $214 \text{ m}^2 \cdot \text{g}^{-1}$  and an average pore size of 5.8 nm). All parameters thus indicated that the confinement between hectorite nanosheets retarded the growth of the particles. Moreover, as long as a certain threshold size is not exceeded, the phase transition to hematite was completely suppressed. It is noteworthy that Ostwald ripening and phase transition was retarded even at such high loadings and only by a sub nanometer thick “coating” layer. In contrast, when  $\gamma\text{-Fe}_2\text{O}_3$  was coated by amorphous  $\text{SiO}_2$  suppression of the phase transition required much thicker coatings.<sup>[9]</sup> Since  $\gamma\text{-Fe}_2\text{O}_3$  that is precipitated on the external surface of the natural layered silicate montmorillonite<sup>[17]</sup> is only thermally stable up to 530 °C, the stabilization by the electrostatic attraction with only one negatively charged surface is insufficient. Apparently, the sandwich-like fixation from two directions is the crucial factor.

Please note that we apply a fluorohectorite that is far more stable than ordinary layered silicates containing hydroxyl groups. XRD, TEM, and TGA/DSC all gave no indication for the formation of a new solid phase.

Pushing it to the limit of thermal stability of NaHec for which decomposition starts at around 800 °C as evidenced by the decrease of intensity of the  $02/11$  band (Figure 5A), the phase transition can finally be triggered: When the composite is heated to 800 °C for 20 h, the PXRD exhibited a mixture of reflections of  $\gamma\text{-Fe}_2\text{O}_3$  and  $\alpha\text{-Fe}_2\text{O}_3$ . It was observed that the reflections of  $\alpha\text{-Fe}_2\text{O}_3$  were much sharper. This suggests that only the bigger particles that reached a certain size underwent phase transition. TEM images suggested (Figure 5G) that at this temperature intercalated  $\gamma\text{-Fe}_2\text{O}_3$  nanoparticles gained

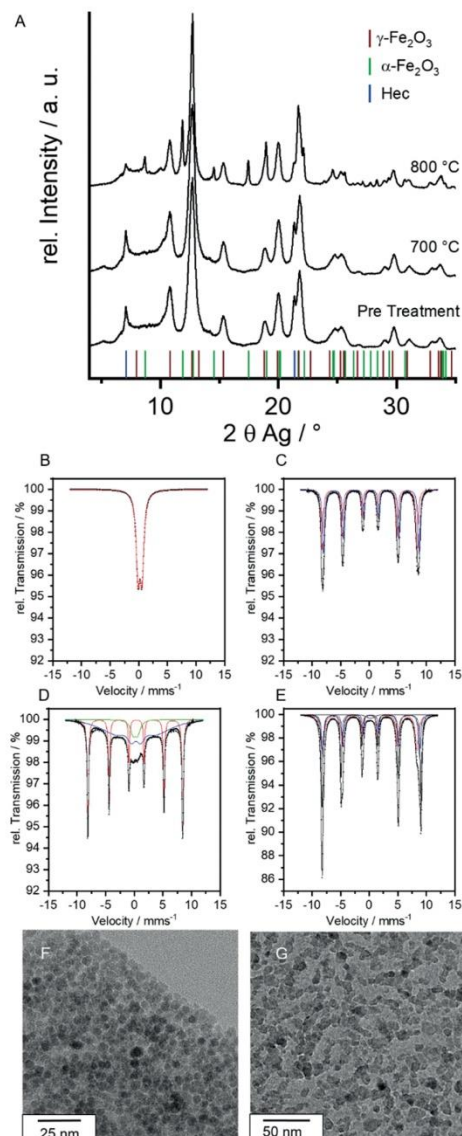


**Figure 5.** Evaluation of the phase and size of the  $\gamma\text{-Fe}_2\text{O}_3$  nanoparticles in the composite after heat treatment. (A) Wide angle XRD using  $\text{Ag}\text{-}K_{\alpha}$  ( $\lambda = 0.5594075 \text{ \AA}$ ) radiation. (B) + (C) Room temperature and 4.2 K Möbbauer spectra after treatment at 700 °C. (D) + (E) Room temperature and 4.2 K Möbbauer spectra after treatment at 800 °C. (F) + (G) TEM images after treatment at 700 and 800 °C.

enough mobility to be able to grow by coalescence to bigger nanoparticles ( $9.2 \pm 2.3$  nm). Furthermore, nanoparticles of irregular shape and dimensions of  $>20$  nm were observed.

The 4.2 K Mößbauer (Figure 5E) spectrum showed not only the two sextets for the tetrahedral and octahedral sites of maghemite (hyperfine fields of 51.3 and 52.5 T, respectively), but an additional sextet (53.7 T) with a shift of 0.32 mm·s<sup>-1</sup> which can be ascribed to well crystalline hematite particles capable of undergoing the Morin transition. According to area under the spectra the composition is 40% hematite and 60% maghemite. The RT spectrum (Figure 5D) exhibited a sextet originating from the hematite particles with an area of 41%. The other very broad sextet belonged to maghemite particles with slower relaxation times as compared to the samples treated at 700 °C, which means that the particles were bigger in size. This is in accord with the bigger nanoparticles observed in the TEM image. The Ar-physisorption isotherm measured for the composite annealed at 800 °C was of type II, which corresponds to a nonporous or macroporous network and the BET surface was drastically reduced to 35 m<sup>2</sup>·g<sup>-1</sup> (Figure S2E, Supporting Information). This also was in line with a collapse of the porous structure upon annealing at 800 °C.

To stress the crucial role of the confinement by the hectorite nanosheets, dried unsupported nanoparticles were annealed as control (Figure S3, Supporting Information). Up to 400 °C the nanoparticles retained their size and phase as no changes in the PXRD were observed. After treatment at 450 °C microcrystalline hematite is the only phase observed. This indicated that also in agreement with results published by Belin et al.<sup>[17b]</sup> unsupported nanoparticles started ripening already above 400 °C accompanied by the phase transition. In contrast, the same nanoparticles confined between the hectorite nanosheets retained their size and phase at least up to 700 °C.

## Conclusions

To hamper phase transition of nanoparticulate  $\gamma\text{-Fe}_2\text{O}_3$  to  $\alpha\text{-Fe}_2\text{O}_3$  at higher temperature the size of the nanoparticles requires to be kept small.<sup>[14]</sup> The essential suppression of Ostwald ripening can be achieved by sandwiching  $\gamma\text{-Fe}_2\text{O}_3$  nanoparticles between hectorite nanosheets. This can simply be achieved by “intercalation” of nanoparticles carrying a positive surface charge into highly swollen (>100 nm gallery height) nematic hectorite suspension. The electrostatic interaction with the negatively charged nanosheets retards Ostwald ripening of the nanoparticles up to 700 °C even at very high loadings (>60 wt%). As the nanoparticles retain their size, they consequently do not undergo phase transition to  $\alpha\text{-Fe}_2\text{O}_3$ .

In general, wrapping with charged nanosheets of hectorite appears to represent an efficient tool to disperse and stabilize small nanoparticles. As the composite structures obtained are mesoporous, they should be interesting heterogeneous catalyst systems not only for  $\text{Fe}_2\text{O}_3$ , but for any kind of nanoparticles.<sup>[18]</sup> Since the accessible surface is preserved even to high temperatures, in particular catalytic reactions at high temperature<sup>[19]</sup> will be tested next.

## Experimental Section

**Materials:**  $\text{FeCl}_2\cdot 4\text{H}_2\text{O}$  (98 %),  $\text{FeCl}_3\cdot 6\text{H}_2\text{O}$  ( $\geq$  99 %), NaOH (pellets,  $\geq$  98 %) and diethylene glycol (99 %) were purchased from Sigma

Aldrich. Phosphocholine chloride calcium salt tetrahydrate (98 %) was purchased from abcr GmbH. The water used was of MilliQ quality (18.2 MΩ). NaHec was synthesized via melt synthesis.<sup>[12]</sup>

**Synthesis of  $\gamma\text{-Fe}_2\text{O}_3$  Nanoparticles:** Nanoparticles were obtained by a slightly modified published procedure.<sup>[15]</sup>  $\text{FeCl}_2\cdot 4\text{H}_2\text{O}$  (398 mg, 1.00 mmol) and  $\text{FeCl}_3\cdot 6\text{H}_2\text{O}$  (1.05 g, 2.00 mmol) were dissolved in 40.0 g diethylene glycol (DEG). NaOH (640 mg, 16.0 mmol) in 80.0 g DEG was added and the solution was degassed under a flow of argon for 3 h. The solution was heated to 220 °C with a ramp of 2 K·min<sup>-1</sup> and kept at this temperature for 2 h. The dispersion was allowed to cool to 90 °C and phosphocholine chloride calcium salt tetrahydrate (330 mg, 1.00 mmol) in 20.0 g DEG was rapidly added under vigorous stirring. The temperature was kept for 1 h and then cooled to room temperature. The particles were precipitated in 600 mL of acetone, washed two times with 400 mL of acetone and then redispersed in water. The dispersion was dialyzed in 4 L of water for 48 h with water being exchanged after 6 and 24 h.

**Synthesis of  $\gamma\text{-Fe}_2\text{O}_3/\text{NaHec}$ :** NaHec was delaminated as 1 wt% dispersion in water. For the intercalation the pH of both NaHec and nanoparticle dispersions was adjusted to pH 7. NaHec was rapidly added to excess of particle dispersion under mechanical stirring. The flocculate was recovered by a magnet, washed 3 times and then dried at 80 °C. To remove organics adsorbed to the surface, the powder was calcined under a flow of clean air at 500 °C for 5 h.

**Characterization:** Hydrodynamic diameter and  $\zeta$ -potential were recorded on a Litesizer 500 (Anton-Paar). Thermogravimetric analysis (TGA) and differential scanning calorimetry (DSC) were acquired with a Netzsch STA 449 F3 Jupiter with a heating ramp of 10 K·min<sup>-1</sup> in flowing air. Textured X-ray diffraction patterns (XRD) at low angles were acquired on a Bragg-Brentano type diffractometer (Empyrean, PANalytical) with nickel filter and  $\text{Cu}\text{-}K_{\alpha}$  radiation ( $\lambda = 1.54187 \text{ \AA}$ ). The higher angle XRD patterns were recorded applying a STOE STADI-P equipped with four MYTHEN2 R 1 K detectors and  $\text{Ag}\text{-}K_{\alpha}$  ( $\lambda = 0.5594075 \text{ \AA}$ ). The samples were filled into 0.5 mm glass capillaries for this purpose. To determine the elemental composition to about 20 mg of the sample was added a mixture of 1.5 mL 30 wt% HCl (Merck), 0.5 mL of 85 wt%  $\text{H}_3\text{PO}_4$  (Merck), 0.5 mL 65 wt%  $\text{HNO}_3$  (Merck) and 1 mL of 48 wt%  $\text{HBF}_4$  (Merck). The sample was digested in a MLS 1200 Mega microwave digestion apparatus for 6.5 min and heated at 600W (MLS GmbH). The sample was allowed to cool to room temperature and the clear solution was diluted to 100 mL and analyzed with a Varian AA100. Scanning electron microscopy (SEM) was performed on a Zeiss Ultra plus with an accelerating voltage of 3 kV. Transmission electron microscopy (TEM) images were acquired using a JEOL JEM-2200FS (200 kV). For cross sectional TEM the powder was embedded and was cut with a Leica Ultramicrotome UC7+FC7. Physisorption isotherms were recorded on a Quantachrome Autosorb-1 with argon as adsorbate at 87 K. The isotherms were evaluated using the Brunauer-Emmet-Teller (BET) method and the pore size distribution was calculated with the NLDFT method. The Mößbauer measurements were performed in transmission geometry with a spectrometer operating with a sinusoidal velocity waveform. The source was about 25 mCi of  $^{57}\text{Co}$  in rhodium. The gamma rays were detected with a proportional counter filled with a krypton/ $\text{CO}_2$  mixture. Measurements at liquid helium temperature were performed in a liquid helium bath cryostat, in which both the source and the absorber were cooled to 4.2 K.

**Supporting Information** (see footnote on the first page of this article): Results of ICP-AAS, Ar-physisorption and control study of unsupported nanoparticles.

## Acknowledgements

This work was supported by the Deutsche Forschungsgemeinschaft (SFB 840). We thank *Marco Schwarzmüller* for preparing TEM samples and *Lena Geiling* for performing SEM. We thank *Stefan Rettinger* for TGA/DSC measurements. We appreciate the support of the Keylab for Optical and Electron Microscopy of the Bavarian Polymer Institute (BPI). KA thanks the Elite Network of Bavaria (ENB) for a research fellowship and the elite study program "Macromolecular Science" for a fellowship. Open access funding enabled and organized by Projekt DEAL.

**Keywords:** Hectorite; Layered compounds; Iron oxide; Phase transitions; Temperature stability

## References

- [1] a) M. Sugimoto, *J. Am. Ceram. Soc.* **1999**, *82*, 269–280; b) Z. Tianshu, L. Hongmei, Z. Huanxing, Z. Ruifang, S. Yusheng, *Sens. Actuators B* **1996**, *32*, 181–184; c) W. Shangguan, A. Yoshida, *J. Phys. Chem. B* **2002**, *106*, 12227–12230; d) L. Han, S. Cai, M. Gao, J. Y. Hasegawa, P. Wang, J. Zhang, L. Shi, D. Zhang, *Chem. Rev.* **2019**, *119*, 10916–10976; e) Y. Shi, H. Li, L. Wang, W. Shen, H. Chen, *ACS Appl. Mater. Interfaces* **2012**, *4*, 4800–4806; f) M. M. Fernandes, H. Mora, E. D. Barriga-Castro, C. Luna, R. Mendoza-Reséndez, C. Ribeiro, S. Lanceros-Mendez, P. Martins, *J. Phys. Chem. C* **2018**, *122*, 19189–19196.
- [2] J. Tuček, L. Machala, S. Ono, A. Namai, M. Yoshiakiyo, K. Imoto, H. Tokoro, S. Ohkoshi, R. Zbořil, *Sci. Rep.* **2015**, *5*, 15091.
- [3] a) A. Kay, I. Cesar, M. Grätzel, *J. Am. Chem. Soc.* **2006**, *128*, 15714–15721; b) G. Carraro, D. Barreca, M. Cruz-Yusta, A. Gasparotto, C. Maccato, J. Morales, C. Sada, L. Sánchez, *ChemPhys-Chem* **2012**, *13*, 3798–3801; c) Y. Zhu, L. P. Stubbs, F. Ho, R. Liu, C. P. Ship, J. A. Maguire, N. S. Hosmane, *ChemCatChem.* **2010**, *2*, 365–374.
- [4] L. Machala, J. Tuček, R. Zbořil, *Chem. Mater.* **2011**, *23*, 3255–3272.
- [5] S. Sakurai, A. Namai, K. Hashimoto, S. Ohkoshi, *J. Am. Chem. Soc.* **2009**, *131*, 18299–18303.
- [6] a) A. Navrotsky, C. Ma, K. Lilova, N. Birkner, *Science* **2010**, *330*, 199; b) A. Navrotsky, L. Mazeina, J. Majzlan, *Science* **2008**, *319*, 1635.
- [7] a) F. S. Yen, W. C. Chen, J. M. Yang, C. T. Hong, *Nano Lett.* **2002**, *2*, 245–252; b) T. Belin, N. Millot, N. Bovet, M. Gailhanou, *J. Solid State Chem.* **2007**, *180*, 2377–2385; c) S. Lee, H. Xu, *J. Phys. Chem. C* **2016**, *120*, 13316–13322.
- [8] R. Zboril, A. Bakandritsos, M. Mashlan, V. Tzitzios, P. Dallas, C. Trapalis, D. Petridis, *Nanotechnology* **2008**, *19*, 095602.
- [9] E. Taboada, M. Gich, A. Roig, *ACS Nano* **2009**, *3*, 3377–3382.
- [10] P. P. C. Sartoratto, K. L. Caiado, R. C. Pedroza, S. W. da Silva, P. C. Morais, *J. Alloys Compd.* **2007**, *434–435*, 650–654.
- [11] a) A. Lerf, *Dalton Trans.* **2014**, *43*, 10276–10291; b) M. Daab, N. J. Eichstaedt, A. Edenthaler, S. Rosenfeldt, J. Breu, *RSC Adv.* **2018**, *8*, 28797–28803; c) M. Daab, N. J. Eichstaedt, C. Habel, S. Rosenfeldt, H. Kalo, H. Schiessling, S. Forster, J. Breu, *Langmuir* **2018**, *34*, 8215–8222.
- [12] M. Stöter, D. A. Kunz, M. Schmidt, D. Hirsemann, H. Kalo, B. Putz, J. Senker, J. Breu, *Langmuir* **2013**, *29*, 1280–1285.
- [13] S. Rosenfeldt, M. Stöter, M. Schlenk, T. Martin, R. Q. Albuquerque, S. Förster, J. Breu, *Langmuir* **2016**, *32*, 10582–10588.
- [14] Z. Wang, K. Rolle, T. Schilling, P. Hummel, A. Philipp, B. A. F. Kopera, A. M. Lechner, M. Retsch, J. Breu, G. Fytas, *Angew. Chem.* **2020**, *132*, 1302–1310.
- [15] a) H. Qu, D. Caruntu, H. Liu, C. J. O'Connor, *Langmuir* **2011**, *27*, 2271–2278; b) K. Araki, M. Uchiyama, S. Toma, S. Rodrigues, A. Shimada, R. Loiola, H. Rodriguez, P. Oliveira, M. Luz, S. Rabbani, H. Toma, S. H. P. Farsky, *Int. J. Nanomed.* **2015**, 4731–4731.
- [16] M. Thommes, K. Kaneko, A. V. Neimark, J. P. Olivier, F. Rodriguez-Reinoso, J. Rouquerol, K. S. W. Sing, *Pure Appl. Chem.* **2015**, *87*, 1051–1069.
- [17] Z. Orolínová, A. Mockovčiaková, V. Zeleňák, M. Myndyk, *J. Alloys Compd.* **2012**, *511*, 63–69.
- [18] J. Hühn, C. Carrillo-Carrión, M. G. Soliman, C. Pfeiffer, D. Valdeperez, A. Masood, I. Chakraborty, L. Zhu, M. Gallego, Z. Yue, M. Carril, N. Feliu, A. Escudero, A. M. Alkilany, B. Pelaz, P. del Pino, W. J. Parak, *Chem. Mater.* **2016**, *29*, 399–461.
- [19] A.-H. Lu, J.-J. Nitz, M. Comotti, C. Weidenthaler, K. Schlichte, L. C. W. O. Terasaki, F. Schüth, *J. Am. Chem. Soc.* **2010**, *132*, 14152–14162.

Received: February 17, 2020

Published Online: April 1, 2020

## Results

---

### 6.1.1 Supporting Information

*Z. Anorg. Allg. Chem.* **2020** · ISSN 0044–2313

#### **SUPPORTING INFORMATION**

**Title:** High Temperature Stable Maghemite Nanoparticles Sandwiched between Hectorite Nanosheets

**Author(s):** K. Ament, D. R. Wagner, F. E. Meij, F. E. Wagner, J. Breu\*

**Ref. No.:** z202000077

## Supporting information

### High temperature stable maghemite nanoparticles sandwiched between hectorite nanosheets

Kevin Ament, Daniel R. Wagner, Frederieke Meij, Friedrich E. Wagner and Josef Breu\*

**Abstract:** Maghemite ( $\gamma\text{-Fe}_2\text{O}_3$ ) is a metastable iron oxide phase and usually undergoes fast phase transformation to hematite at elevated temperatures ( $>350$  °C). Maghemite nanoparticles were synthesized by the polyol method and then intercalated into a highly swollen ( $>100$  nm separation) nematic phase of hectorite. A composite of maghemite nanoparticles sandwiched between nanosheets of synthetic hectorite was obtained. The confinement of the nanoparticles hampered Ostwald ripening up to 700 °C and consequently the phase transition to hematite is suppressed. Only above 700 °C  $\gamma\text{-Fe}_2\text{O}_3$  nanoparticles started to grow and then transformed to  $\alpha\text{-Fe}_2\text{O}_3$ . The structure and the phase transformation of the composite was evaluated using X-ray diffraction, TEM, SEM, physisorption, TGA/DSC and Mößbauer spectroscopy.

#### Table of Contents

- 1) Results of ICP-AAS
- 2) Ar-physisorption isotherms
- 3) Control study of unsupported  $\gamma\text{-Fe}_2\text{O}_3$  nanoparticles

## Results

---

### 1) Results of ICP-AAS

**Table S1.** Elemental composition according to ICP-AAS.

Element <sup>[a]</sup>	Weight fraction of the element [%]
Na	1
Mg	5.7
Fe	44.8

Interlayer Na<sup>+</sup> is completely replaced by "ion-exchange with the colloidal cations."

Assuming an ideal composition of Fe<sub>2</sub>O<sub>3</sub> the weight fraction can be calculated to be 64 wt%. Then the nominal formula was calculated to be (Fe<sub>2</sub>O<sub>3</sub>)<sub>4.2</sub>(Mg<sub>2.5</sub>Li<sub>0.5</sub>Si<sub>4</sub>O<sub>10</sub>F<sub>2</sub>). From this formula the weight fraction of Mg would be 5.9 wt% which is in decent agreement with the value found by ICP-AAS. Si was not detected directly via ICP-AAS. The amount of Si was rather calculated assuming the atomic ratio of Mg to Si of 2.5:4 as required by the Hec-composition.

2) Ar-physisorption isotherms

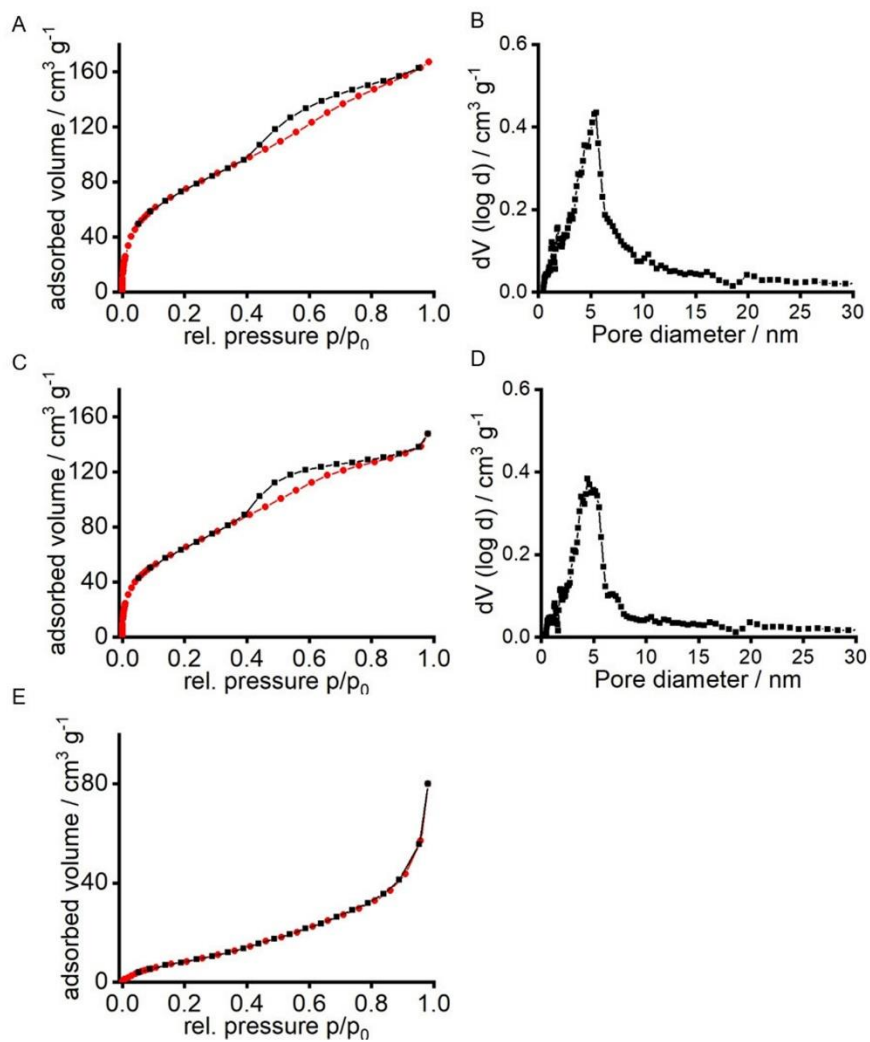


**Figure S2.** A) Ar-isotherm of  $\gamma\text{-Fe}_2\text{O}_3/\text{NaHec}$  and B) corresponding pore size distribution before heat treatment. C) Ar-isotherm and D) corresponding pore size distribution after treatment at  $700\text{ }^\circ\text{C}$ . E) Ar isotherme after treatment at  $800\text{ }^\circ\text{C}$ .

3) Control study of unsupported  $\gamma\text{-Fe}_2\text{O}_3$  nanoparticles

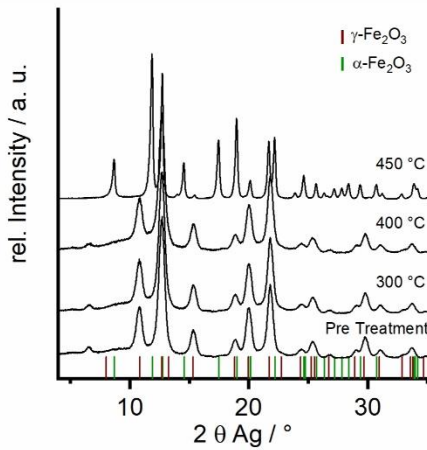


**Figure S3.** PXRD of unsupported  $\gamma\text{-Fe}_2\text{O}_3$  nanoparticles treated at 300, 400 and 450 °C in air for 20 h.

## 6.2 Nanoparticles Supported on Sub-Nanometer Oxide Films: Scaling Model Systems to Bulk Materials

### Nanoparticles Supported on Sub-Nanometer Oxide Films: Scaling Model Systems to Bulk Materials

Kevin Ament<sup>[a]</sup>, Nicolas Köwitsch<sup>[b]</sup>, Dianwei Hou<sup>[c]</sup>, Thomas Götsch<sup>[d]</sup>, Jutta Kröhnert<sup>[d]</sup>, Christopher J. Heard<sup>[c]</sup>, Annette Trunschke<sup>[d]</sup>, Thomas Lunkenbein<sup>[d]</sup>, Marc Armbrüster<sup>[b]</sup>, and Josef Breu<sup>[a]\*</sup>

*Angewandte Chemie International Edition* **2021**, *60*, 5890 - 5897

*Angewandte Chemie* **2021**, *133*, 5954 - 5961

Impact Factor (2019): 12.959

<https://doi.org/10.1002/anie.202015138> and <https://doi.org/10.1002/ange.202015138>

Reprinted under the terms of CC BY 4.0 license (<https://creativecommons.org/licenses/by/4.0/legalcode>)  
© 2020 The Authors. Angewandte Chemie International Edition published by Wiley-VCH GmbH.

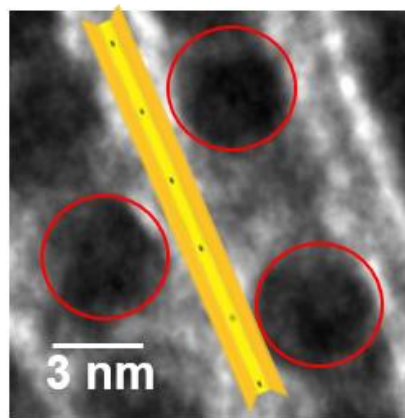
[a] Bavarian Polymer Institute and Department of Chemistry, University of Bayreuth, Universitätsstraße 30, 95447 Bayreuth (Germany)

[b] Faculty of Natural Sciences, Institute of Chemistry, Materials for Innovative Energy Concepts, Chemnitz University of Technology, Straße der Nationen 62, 09111 Chemnitz (Germany)

[c] Department of Physical and Macromolecular Chemistry, Charles University, Hlavova 8, 128 00 Prague 2 (Czech Republic)

[d] Department of Inorganic Chemistry, Fritz-Haber-Institut der Max-Planck-Gesellschaft, Faradayweg 4-6, 14195 Berlin (Germany)

\* E-mail: josef.breu@uni-bayreuth.de



#### Individual Contribution:

Prof J. Breu and I developed the concept of this publication. The manuscript was written by Prof J. Breu and me. Prof M. Armbrüster, C. J. Heard, A. Trunschke, and T. Lunkenbein commented on the manuscript. I designed the experiments, synthesized the catalysts and did

## Results

---

most of the characterisation. I performed the catalytic experiments with input on the evaluation by N. Köwitsch and Prof M. Armbrüster. D. Hou and C. J. Heard conducted the DFT calculations. J. Kröhnert performed CO-DRIFTS, and A. Trunschke commented on my interpretation of the data. T. Götsch measured EELS and T. Lunkenbein assisted with the interpretation of the data.

My contribution to the manuscript is approx. 80 %.

### 6.2.1 Nanoparticles Supported on Sub-Nanometer Oxide Films: Scaling Model Systems to Bulk Materials (International Edition)



## Nanoparticles Supported on Sub-Nanometer Oxide Films: Scaling Model Systems to Bulk Materials

Kevin Ament, Nicolas Köwitsch, Dianwei Hou, Thomas Götsch, Jutta Kröhnert, Christopher J. Heard, Annette Trunschke, Thomas Lunkenstein, Marc Armbrüster, and Josef Breu\*

**Abstract:** Ultrathin layers of oxides deposited on atomically flat metal surfaces have been shown to significantly influence the electronic structure of the underlying metal, which in turn alters the catalytic performance. Upscaling of the specifically designed architectures as required for technical utilization of the effect has yet not been achieved. Here, we apply liquid crystalline phases of fluorohectorite nanosheets to fabricate such architectures in bulk. Synthetic sodium fluorohectorite, a layered silicate, when immersed into water spontaneously and repulsively swells to produce nematic suspensions of individual negatively charged nanosheets separated to more than 60 nm, while retaining parallel orientation. Into these galleries oppositely charged palladium nanoparticles were intercalated whereupon the galleries collapse. Individual and separated Pd nanoparticles were thus captured and sandwiched between nanosheets. As suggested by the model systems, the resulting catalyst performed better in the oxidation of carbon monoxide than the same Pd nanoparticles supported on external surfaces of hectorite or on a conventional  $\text{Al}_2\text{O}_3$  support. XPS confirmed a shift of Pd 3d electrons to higher energies upon coverage of Pd nanoparticles with nanosheets to which we attribute the improved catalytic performance. DFT calculations showed increasing positive charge on Pd weakened CO adsorption and this way damped CO poisoning.

#### Introduction

Many nanoparticulate catalysts are prepared by wet impregnation on an oxidic support. The oxidic surface is often regarded as an “inert” support assuring stabilization and dispersion while hampering Ostwald ripening.<sup>[1]</sup> Recent results show, however, that the right choice of support can have significant influence on the selectivity and activity of catalysts.<sup>[2]</sup> In particular, the so called electronic-metal-support interaction

(EMSI) was shown to alter the catalytic performance of catalysts by electronic interaction between support and metal.<sup>[3]</sup> In the past years, model systems were applied, which are based on ultrathin oxidic films deposited on atomically flat metal surfaces, to study EMSI.<sup>[2a,4]</sup> A modification of the work function of the metal was observed when thin oxide films were deposited on flat metal surfaces.<sup>[5]</sup> This phenomenon can be attributed either to charge transfer between metal and support, electrostatic, or compression effects.<sup>[5a,6]</sup> For model catalysts composed of Pt<sup>[7]</sup> or Ir<sup>[8]</sup> clusters deposited on CeO<sub>2</sub> films, a charge transfer from the noble metal to the oxide was observed resulting in a positively charged metal cluster.

Such model catalysts helped to greatly deepen our understanding of the performance of real catalysts under working conditions. While model films can be fabricated with utmost control (Scheme 1),<sup>[9]</sup> synthesis protocols for sub-nanometer oxidic supports as required for bulk-scale materials are lacking.

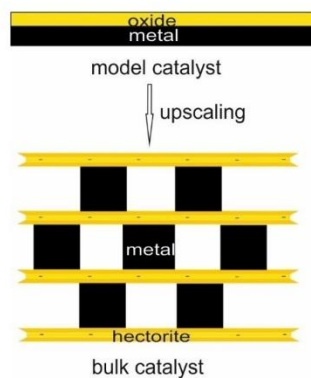
Negatively charged layered materials such as clays have been explored as supports for nanoparticles and their catalytic performance has been tested to some extent.<sup>[10]</sup> Taking advantage of the cation exchange capacity, desired cations have been introduced on and/or between the silicate layers followed by reduction (e.g. Pd, Cu, Ru)<sup>[11]</sup> or precipitation (e.g. CdS)<sup>[12]</sup> to obtain the final nanoparticulate catalysts. Typical cation exchange capacities for natural clays of < 100 mmol/100 g<sup>[10]</sup> limit the loading (e.g. ≈ 6 wt % Pd) that can be obtained via the cation exchange route corresponding to as little as one particle per 1500 nm<sup>2</sup> (assuming 3.5 nm sized particles). As natural clays typically come in lateral sizes smaller than 200 nm, the very few nanoparticles produced this way preferentially end up at external surfaces as suggested by Dékány et al.<sup>[13]</sup> and as indicated by insignificant shifts of the basal spacing.

\* M.Sc. K. Ament, Prof. Dr. J. Breu  
Bavarian Polymer Institute and Department of Chemistry, University of Bayreuth  
Universitätsstraße 30, 95447 Bayreuth (Germany)  
E-mail: josef.breu@uni-bayreuth.de  
M.Sc. N. Köwitsch, Prof. Dr. M. Armbrüster  
Faculty of Natural Sciences, Institute of Chemistry, Materials for Innovative Energy Concepts, Chemnitz University of Technology  
Straße der Nationen 62, 09111 Chemnitz (Germany)  
M.Sc. D. Hou, Dr. C. J. Heard  
Department of Physical and Macromolecular Chemistry, Charles University  
Hlavova 8, 128 00 Prague 2 (Czech Republic)

Dr. T. Götsch, Dipl. Ing. J. Kröhnert, Dr. A. Trunschke,  
Dr. T. Lunkenstein  
Department of Inorganic Chemistry, Fritz-Haber-Institut der Max-Planck-Gesellschaft  
Faradayweg 4–6, 14195 Berlin (Germany)

Supporting information and the ORCID identification number(s) for the author(s) of this article can be found under:  
<https://doi.org/10.1002/anie.202015138>.

© 2020 The Authors. Angewandte Chemie International Edition published by Wiley-VCH GmbH. This is an open access article under the terms of the Creative Commons Attribution License, which permits use, distribution and reproduction in any medium, provided the original work is properly cited.

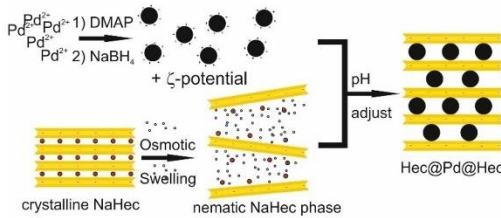


**Scheme 1.** Upscaling of a model architecture consisting of a single thin oxide layer ( $< 1$  nm) on bulk metal to a mesostructured catalyst with large accessible active area by exploiting the layered silicate hectorite as thin separator.

To achieve a higher loading of nanoparticulate catalysts, preformed particles comprising hundreds of atoms need to be intercalated. Given interlayer heights of less than 1 nm, this is, however, unlikely for kinetic reasons.

More recently, the synthetic clay sodium fluorohectorite, ( $\text{NaHec}$ ,  $[\text{Na}_{0.5}]_{\text{inter}}[\text{Mg}_{2.5}\text{Li}_{0.5}]^{10+}[\text{Si}_4]^{10-}\text{O}_{10}\text{F}_2$ ) which belongs to a handful of layered compounds that show the long-known<sup>[14]</sup> but rare phenomenon of osmotic swelling, became available.<sup>[15]</sup> Osmotic swelling is a thermodynamically allowed process<sup>[16]</sup> and therefore produces liquid crystalline phases with a uniform separation of adjacent silicate layers. For  $\text{NaHec}$  nanosheets with 0.96 nm thickness and a median diameter of 20  $\mu\text{m}$ ,<sup>[17]</sup> rotation of the nanosheets, even in very dilute suspensions ( $< 1$  vol %), is hindered and nematic liquid crystalline phases are formed instead of isotropic suspensions.<sup>[18]</sup> As has been reported for titanate nanosheets,<sup>[19]</sup> dilute aqueous dispersions of negatively charged  $\text{NaHec}$  nanosheets adopt a cofacial arrangement due to strong electrostatic repulsion. In this nematic state, adjacent  $\text{Hec}$  nanosheets are not only held in a coherent cofacial geometry, but are separated to long, well defined distances determined by the clay content, typically exceeding 50 nm. Loading these nematic phases with nanoparticles was previously proven by the intercalation of maghemite nanoparticles between the nanosheets.<sup>[20]</sup>

As we will show here, this nematic nanosheet phase offers a scalable route to produce nanoparticulate catalysts between sub-nanometer oxidic supports that resemble the model architectures (Scheme 1). Pdnanoarticles are first synthesized by established protocols<sup>[21]</sup> and capped with 4-dimethylaminopyridine (DMAP) yielding “nanoparticulate metal cations” that can easily diffuse into the open galleries between adjacent nanosheets similar to a cation exchange (Scheme 2). To probe the influence of the nanosheets on the properties of Pd nanoparticles, the mesostructured composite was tested in the oxidation of carbon monoxide (CO).



**Scheme 2.** Schematic outline of the synthesis of Pd intercalated Hec (Hec@Pd@Hec).

## Results and Discussion

### Synthesis and Characterization of Hec@Pd@Hec Catalysts

According to transmission electron microscope (TEM) images the as-synthesized spherical nanoparticles had a narrow size distribution of  $3.5 \pm 0.4$  nm (Figure S1a). They were readily dispersible in water with a hydrodynamic diameter of  $4.5 \pm 1.3$  nm as determined by dynamic light scattering (DLS). The  $\zeta$ -potential could be tuned from +34 to +14 mV by adjusting the pH in the range from 6 to 12, respectively (Figure S1b). At the given and fixed cation exchange capacity, the surface charge density of the  $\text{NaHec}$  determines the number of nanoparticles required for charge balance and thus the loading can be tuned via the pH (Table 1).

Typically, a 0.1 wt % dispersion of the Pd nanoparticles were added to a 1.5 wt % dispersion of a nematic phase of  $\text{NaHec}$  under vigorous stirring. At this  $\text{NaHec}$  content, the separation of adjacent parallel oriented nanosheets was found to be more than 60 nm by small angle X-ray scattering in aqueous dispersion (Figure S2). This large gallery height and the positive surface potential of Pd nanoparticles allowed for fast incorporation ( $< 30$  seconds) of the catalyst whereupon hetero-coagulation is triggered. Element mapping suggested a uniform loading of Pd (Figure S3). Moreover, as indicated by CHN analysis, the capping ligand could be completely removed by repeated centrifugation and washing (Table S1). To stress the sandwich confinement, we refer to the samples by  $\text{Hec}@\text{Pdx}@Hec$  where  $x$  corresponds to the weight fraction of Pd as determined by inductively coupled plasma optical emission spectroscopy (ICP-OES). The loading was cross-checked by scanning electron microscopy with energy dispersive X-ray spectroscopy (SEM-EDS) (Table 1). Moreover, interlayer  $\text{Na}^+$  had been completely replaced according to ICP-OES, SEM-EDS (no signal at 1.04 keV, Figure S3) or X-ray photoelectron spectroscopy (XPS, no signal for Na 1s at

**Table 1:** Weight fraction of Pd in the catalyst depending on the initial pH of hectorite and nanoparticle dispersion.

Sample	pH	$\zeta$ -potential [mV]	Pd-loading (ICP-OES) [wt %]	Pd-loading (SEM-EDS) [wt %]
Hec@Pd65@Hec	9.5	28	65.2	67.8
Hec@Pd72@Hec	10.8	22	72.5	76.0

around 1070 eV, Figure S4) indicating that  $\text{Na}^+$  was completely replaced and that the negative charge of Hec nanosheets was fully balanced by the intercalated Pd nanoparticles.

As expected for such a quasi-ion-exchange, the weight fraction of Pd increased to a maximum of 72.5 wt % with decreasing surface potential of the nanoparticles. Contrary to the simple ion-exchange route mentioned in the introduction, very high loadings were achieved by intercalation of positively charged nanoparticles. For instance, the sample containing 65.2 wt % Pd resulted in a stoichiometry of  $\text{Pd}_{0.7}\text{Mg}_{2.5}\text{Li}_{0.5}\text{Si}_4\text{O}_{10}\text{F}_2$ . For comparison, by simple ion exchange of  $\text{Na}^+$  for  $\text{Pd}^{2+}$  followed by reduction, the composition would be limited to  $\text{Pd}_{0.25}\text{Mg}_{2.5}\text{Li}_{0.5}\text{Si}_4\text{O}_{10}\text{F}_2$ .

Upon hetero-coagulation, the nematic structure collapses to lamellar composites and adjacent Hec nanosheets sandwich the Pd nanoparticles (Figure 1). The nanoparticles are not densely packed, but separated from each other (Figure 1b, inset). Each Pd nanoparticle is separated from the adjacent nanoparticle layer by exactly one silicate layer of 0.96 nm thickness. Since the Pd nanoparticle layers are randomly shifted relative to each other, thousands of architectures similar to what is sketched in Scheme 1 were obtained where a Pd nanoparticle is separated by a Hec nanosheet from an opposite mesopore (Figure 1b, inset). This architecture was further confirmed by a grayscale analysis (Figure S5) of TEM images along a line of adjacent Pd nanoparticles in a layer (red and blue line in Figure 1b). The nanoparticles retained their spherical shape after washing off the DMAP. In contrast, prolonged heating indeed caused some elongation of the nanoparticles (Figure S6).

Since monomodal Pd nanoparticles were applied, the restacking upon hetero-coagulation produces one-dimensional periodic composite structures along the stacking direction. The periodicity was determined to be  $4.6 \pm 0.7$  nm by TEM analysis. At higher loadings (Hec@Pd72@Hec), few multilayers of Pd nanoparticles were formed in the interlayer space (Figure S7) which represent defects in the periodicity. Apparently, the surface charge density at pH 10.8 (22 mV  $\zeta$ -potential) was too low to accomplish charge balance of the anionic hectorite nanosheets purely in monolayers of cationic Pd nanoparticles. Powder X-ray diffraction (PXRD) traces of textured samples confirm the one-dimensional crystalline

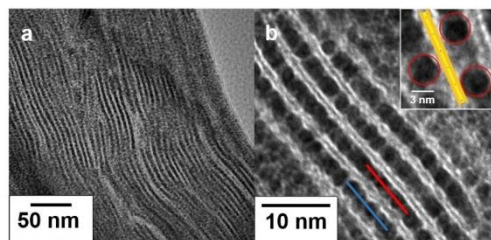


**Figure 1.** TEM images of cross sections of Hec@Pd65@Hec at different magnifications. The red and blue line were used for grey scale analysis (Figure S5). The inset shows adjacent Pd nanoparticles separated from each other.

order. In good agreement with the TEM results for Hec@Pd65@Hec, a rational  $00l$  series with a periodicity of 4.7 nm was observed (Figure 2). Summing the thickness of a Hec nanosheet of 0.96 nm and the diameter of the nanoparticles of 3.5 nm a value of 4.46 nm would be expected. At a loading of 72 wt % (Hec@Pd72@Hec), the few defects of interstratified Pd double layers caused the  $00l$  series to be apparently shifted to 5.5 nm. Concomitantly, these defects lead to a greatly increased full width at half maximum suggesting that the observed shift was actually an artefact due to random interstratification of mono- and double-layers. The X-ray beam then averages between the different d-spacings within its coherence length.

As already suggested by the TEM images, the Pd nanoparticles are not densely packed, but the Pd layers are porous as independently shown by Ar physisorption and CO chemisorption measurements (Table 2 and Figure S8). For instance, the  $d_{50}$  pore size for Hec@Pd65@Hec was 4.3 nm, which is in the same range as the size of the Pd nanoparticles, suggesting that some 50% of the volume of the Pd nanoparticle layers is actually empty space. With randomly stacked

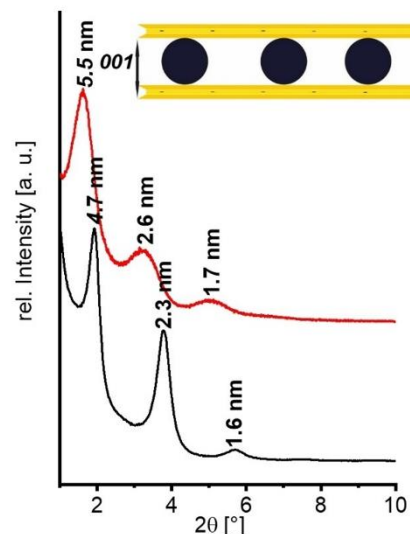


**Figure 2.** PXRD pattern of Hec@Pd65@Hec (black), and Hec@Pd72@Hec (red).

**Table 2:** Results of Ar adsorption<sup>[a]</sup> und chemisorption of CO.<sup>[b]</sup>

Sample	$S_{\text{BET}}$ [ $\text{m}^2 \text{g}^{-1}$ ]	Pore size [nm]	Pore volume [ $\text{cc g}^{-1}$ ]	Metal dispersion [%]
NaHec	4	/	/	/
Hec@Pd65@Hec	147	4.3	0.132	23.7
Hec@Pd72@Hec	87	3.8	0.088	19.9

[a] determined by Ar physisorption at 87 K. [b] determined by CO double isotherm method.

layers the chances of having such a pore arranged opposite of a Pd nanoparticle (Scheme 1) are high.

In contrast, the Ar-isotherm of pristine NaHec revealed a nonporous structure with a BET surface as low as  $4\text{ m}^2\text{ g}^{-1}$ . With this material, the galleries have collapsed and Ar has no access to the internal (interlayer) surfaces. The structure becomes porous only after intercalation of Pd nanoparticles acting as pillars.

The dispersion (ratio of surface to bulk atoms) for single, free-floating, spherical Pd nanoparticles of 3.5 nm diameter is expected to be 32%. Due to the good accessibility of the intercalated Pd nanoparticles, a surprisingly high experimental dispersion of 24% for Hec@Pd65@Hec was measured. Apparently, only a small share of the surface became shielded by supporting it from two sides by Hec nanosheets.

#### Evaluation of the Catalytic Activity

The oxidation of carbon monoxide (CO) to carbon dioxide ( $\text{CO}_2$ ) was chosen as a simple test reaction to study the catalytic performance and to probe for an electronic-metal-support interaction due to the special architecture. This reaction is one of the most studied heterogeneous catalytic reactions due to its simplicity yet enormous importance for exhaust gas purification as CO is highly toxic.<sup>[23]</sup> For each catalysis run the amount of catalyst was chosen to involve 1 mg of Pd in a feed gas stream of  $50\text{ mL min}^{-1}$  (1 vol% CO, 1 vol% O<sub>2</sub> in N<sub>2</sub> carrier gas) and light-off curves from 80°C to 220°C were recorded. Each catalyst was cycled three times. All three consecutive light-off curves of Hec@Pd65@Hec are shown in Figure S9. In Figure 3 the third light-off curve is presented (Figure 3 and Table 3).

For Hec@Pd65@Hec, which mimics the preferred architecture best (Scheme 1 and Figure 1), the temperature of 50% conversion ( $T_{50}$ ) was found to be as low as 145°C. The

**Table 3:** Catalytic light-off behavior in CO oxidation.

Sample	$T_{10}$ [°C]	$T_{50}$ [°C]	$T_{90}$ [°C]	$E_A$ [kJ mol <sup>-1</sup> ]
Hec@Pd65@Hec	124	145	156	42
Hec@Pd72@Hec	138	163	173	51
Pd <sub>ext</sub> @Hec	150	172	177	49
Pd <sub>ext</sub> @Al <sub>2</sub> O <sub>3</sub>	169	191	198	57

apparent activation energy  $E_A$  determined at conversions below 10% was 42 kJ mol<sup>-1</sup> (Figure S10), which is lower than reported values for Pd metal supported on conventional supports such as  $\gamma\text{-Al}_2\text{O}_3$  or MgO (55–80 kJ mol<sup>-1</sup>)<sup>[23]</sup> or silica (65–120 kJ mol<sup>-1</sup>).<sup>[24]</sup>

The good catalytic activity of Hec@Pd65@Hec might be related to several factors: First, influence of the structure inherent elements such fluoride. Second, stabilization of atomically dispersed Pd, third an influence of the mesoporous confinement, and fourth, an electronic interaction between support and metal as discussed in the introduction.

Although the structural fluoride is remote from the surface and not directly in contact with the Pd nanoparticles, we realize that such elements could have some influence on the catalytic behavior. This aspect can, however, only be addressed in future work when fluoride deficient layered supports will be investigated.

The Pd nanoparticles were dialyzed for several days before combining them with the nematic hectorite suspension. Dialysis is expected to remove smaller clusters. They still could have been freshly produced by dissolution during mixing with hectorite. Since the external basal planes of hectorite also carry a negative surface charge, they should be equally capable of stabilizing atomically dispersed Pd if indeed present. The same Pd nanoparticles (Pd<sub>ext</sub>@Hec, Figure S11a and Table S2) used to synthesize Hec@Pd65@Hec, but deposited on the outer surface of non-swollen Hec crystals instead of being sandwiched in the interlayer space, showed a much higher  $T_{50}$  of 172°C. This indicates that it is not, or at least not only, stabilization of smaller clusters or atomically dispersed Pd that improves the catalytic performance.

Hec@Pd65@Hec and Hec@Pd72@Hec loadings show similar pore size distributions while the metal dispersion of the latter is lowered by about 20%. The few double layers of Pd nanoparticles observed in Hec@Pd72@Hec, however, had a huge detrimental effect on catalytic activity.  $T_{50}$  increased from 145°C for Hec@Pd65@Hec to 163°C for Hec@Pd72@Hec, which is already close to the value of only external Pd (Pd<sub>ext</sub>@Hec). The activation energy also increased (42 kJ mol<sup>-1</sup>, 51 kJ mol<sup>-1</sup>, 49 kJ mol<sup>-1</sup> for Hec@Pd65@Hec, Hec@Pd72@Hec, and Pd<sub>ext</sub>@Hec, respectively). The reduction of the activity clearly is much larger than what is expected based on the smaller dispersion, which indicates that the mesoporosity may not be the determining effect for the good catalytic activity of Hec@Pd65@Hec.

It seems that the fourth factor, the special architecture might indeed be the determining factor for the activity. Applying a support with a less negative surface potential

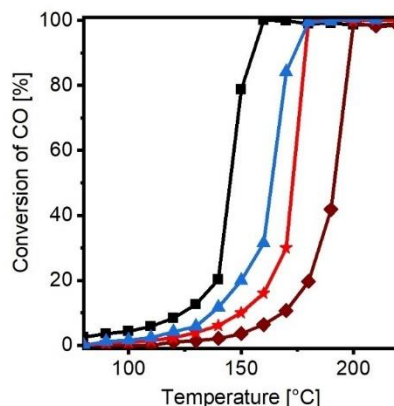


**Figure 3.** Light-off curves for CO oxidation: Hec@Pd65@Hec (black), Hec@Pd72@Hec (blue), Pd<sub>ext</sub>@Hec (red), and Pd<sub>ext</sub>@Al<sub>2</sub>O<sub>3</sub> (brown). Conditions:  $50\text{ mL min}^{-1}$  (1 vol% CO, 1 vol% O<sub>2</sub> balanced by N<sub>2</sub>).

( $-20$  mV at a pH of 10) like  $\gamma\text{-Al}_2\text{O}_3$  loaded with 1 wt % Pd nanoparticles ( $\text{Pd}_{\text{ext}}@\text{Al}_2\text{O}_3$ , Figure S11b and Table S2) yielded a catalyst with  $T_{50}$  of  $191^\circ\text{C}$  and  $E_A$  of  $57 \text{ kJ mol}^{-1}$  (Figure S10), values which are in good agreement with literature.<sup>[23a]</sup> Although the chemistry of  $\text{Al}_2\text{O}_3$  is different from Hec, this comparison suggests that the special support architecture potentially in collaboration with the fact that Pd has to counterbalance the large negative charge density (1 negative charge per  $48 \text{ \AA}^2$  of support) of Hec might indeed have some influence.

As mentioned earlier, Pd nanoparticles in Hec@Pd65@Hec have to balance the permanent negative charge of the Hec nanosheets. XPS of Pd 3d region of Hec@Pd65@Hec showed asymmetric signals of Pd 3d<sub>5/2</sub> and Pd 3d<sub>3/2</sub> at binding energies (BE) of  $335.8 \text{ eV}$  and  $341.0 \text{ eV}$ , respectively (Figure 4a).

These values are shifted to higher energies as compared to bulk Pd metal at  $335.0 \text{ eV}$ <sup>[25]</sup> or nanoparticles supported on  $\text{Al}_2\text{O}_3$  ( $335.0$ – $335.5 \text{ eV}$ )<sup>[26]</sup> or  $\text{SiO}_2$  ( $334.8$ – $335.4 \text{ eV}$ ).<sup>[27]</sup> This

shift might be attributed to an electron deficient species  $\text{Pd}^{4+}$ .<sup>[26a]</sup> Furthermore, as expected from the lower  $\zeta$ -potential of the Pd nanoparticles applied for Hec@Pd72@Hec the shift of the Pd 3d region was smaller ( $335.5 \text{ eV}$ , Figure S12). Pd 3d<sub>5/2</sub> of the same Pd nanoparticles applied in the synthesis of Hec@Pd@Hec, but supported on the external surface of NaHec ( $\text{Pd}_{\text{ext}}@\text{Hec}$ ) or  $\gamma\text{-Al}_2\text{O}_3$  ( $\text{Pd}_{\text{ext}}@\text{Al}_2\text{O}_3$ ) showed considerably lower BE of  $335.3 \text{ eV}$  and  $335.2 \text{ eV}$ , respectively (Figure 4a and S12). These trends clearly show that both the negative charge of the nanosheets and the special architecture obtained by intercalation of Pd into the nematic Hec phase, indeed seem to have an influence on the electronic structure of Pd nanoparticles. This trend is also in line with the increasing performance for the oxidation of CO.

It has also been discussed that “cationic” Au species are important for higher catalytic activity in the case of Au catalysts.<sup>[28]</sup> Furthermore, DFT calculations of Pd@zeolite FAU have indicated that positively charged Pd atoms lead to lower energy barriers assuming a Langmuir-Hinshelwood mechanism.<sup>[29]</sup> Based on DFT calculations, the higher activity of  $\text{Pd}^{4+}$  species was attributed to weaker CO binding to positively charged Pd.<sup>[23c]</sup>

As the CO adsorption is very sensitive to the Pd surface constitution, the stretching vibration region of CO chemisorbed to the Pd surface of Hec@Pd65@Hec and  $\text{Pd}_{\text{ext}}@\text{Al}_2\text{O}_3$  was recorded by diffuse reflectance infrared Fourier transform spectroscopy (CO-DRIFTS, Figure 4b). Massive shifts of the stretching frequency were observed with increasing CO partial pressure up to  $60 \text{ mbar}$  CO due to dipolar coupling with increasing surface coverage (Figure S13). After outgassing of CO to an equilibrium pressure of  $2 \text{ mbar}$  CO,  $\text{Pd}_{\text{ext}}@\text{Al}_2\text{O}_3$  showed four bands centered at  $2080$ ,  $1976$ ,  $1928$ , and  $1864 \text{ cm}^{-1}$ . These can be attributed to different binding modes of CO to the surface of Pd, that are CO linearly bound to corners ( $2080 \text{ cm}^{-1}$ )<sup>[30]</sup> and bridge bound CO on steps ( $1978 \text{ cm}^{-1}$ ).<sup>[31]</sup> The two broad bands at lower wavenumber ( $1928$  and  $1864 \text{ cm}^{-1}$ ) are ascribed to bridge or three-fold bonds on different planes.<sup>[31]</sup> At the same equilibrium pressure of CO, the DRIFT spectrum of Hec@Pd65@Hec showed also four bands at  $2094$ ,  $1991$ ,  $1945$ , and  $1877 \text{ cm}^{-1}$ , all shifted to higher wavenumbers as compared to  $\text{Pd}_{\text{ext}}@\text{Al}_2\text{O}_3$  (Figure 4b). A Pd surface with a partial positive charge as suggested for Hec@Pd65@Hec can back-donate less electrons to the antibonding  $\text{CO} 2\pi^*$  orbital that results in a stronger C–O bond and a wavenumber shift to higher wavenumbers.<sup>[31a]</sup> A weaker back-donation would also lead to weaker adsorption of the CO molecules to the Pd surface.

In order to further corroborate the hypothesis of the influence of a positive charge of Pd nanoparticles on the adsorption strength on CO, DFT calculations were performed to examine the adsorption of CO/O upon a representative nanoparticle model: icosahedral  $\text{Pd}_{147}$ . This nanoparticle has a diameter of  $1.5 \text{ nm}$  and contains  $(111)$  microfacets which closely approximate the extended  $(111)$  surface. CO and atomic oxygen were adsorbed onto the hcp hollow sites of the metallic particle at a local microfacet coverage of  $\theta=0.1$  (details of the model (Figure S14–S17) and methods are provided in the supporting information). Adsorption energies

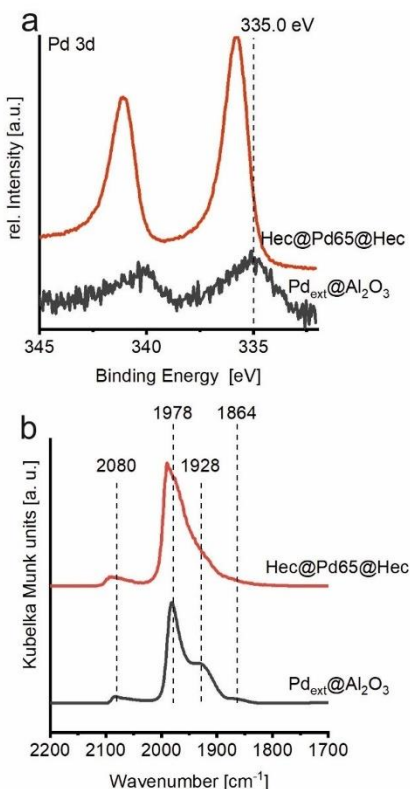


**Figure 4.** Characterisation of Pd nanoparticles of Hec@Pd65@Hec (red) and  $\text{Pd}_{\text{ext}}@\text{Al}_2\text{O}_3$  (black). a) XPS spectra of Pd 3d region and b) DRIFTS spectra of CO chemisorbed at  $300 \text{ K}$  to the surface of Pd at an equilibrium pressure of  $2 \text{ mbar}$  CO.

for CO were observed to decrease linearly with increasing positive charge on the particle over the considered range (of  $Pd_{147}$  to  $Pd_{147}^{71}$ ), while the O adsorption energies were unchanged (Figure 5). Concomitant with the reduction in CO adsorption energy, was a lengthening of the average Pd–C bond from 2.057 Å to 2.066 Å, and a shortening of the C–O bond, from 1.197 Å to 1.187 Å. Therefore, the present DFT calculations are consistent with the experimental DRIFTS results. This finding is understood in terms of molecule–metal bonding models that suggest the depletion of electrons in the metal d states near the Fermi energy reduce the occupation of the net-bonding  $\pi$  channel between CO and Pd. This in turn weakens adsorption and strengthens the internal C–O bond.<sup>[32]</sup> The nanoparticle charge may thus enhance CO oxidation by reducing CO poisoning. Furthermore, computational data<sup>[29]</sup> revealed lower energy barriers in the catalytic cycle for positively charged Pd sites due to the altered binding strength of CO that is in line with the observed lower activation energy of Hec@Pd@Hec.

For Hec@Pd@Hec, the high permanent negative charge density inherent to this support might not be the only source of hole formation in intercalated Pd. It has long been shown that for the special architecture (Scheme 1, Figure 1), charge transfer between metal and ultrathin yet neutral oxide layers may occur and thus have an influence on the work function of the metal.<sup>[5,6]</sup> It was found that an ultrathin layer of  $SiO_2$  deposited on Mo(112) increased the metal work function by 0.5–1 eV due to dipole effects arising from charge transfer from the metal to the oxide.<sup>[6b]</sup> To probe such a possible electronic interaction between the hectorite nanosheets and the Pd nanoparticles leading to an additional charge transfer from Pd to silicate support, electron energy loss spectra (EELS) at the Si  $L_{2,3}$  edge were measured (Figure 6).

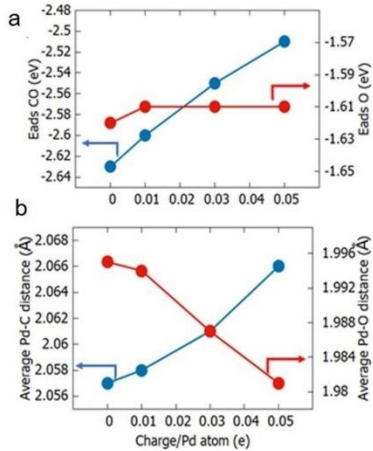


**Figure 5.** a) Calculated adsorption energies of low coverage CO (blue) and O (red) as a function of nanoparticle charge. b) Average Pd–C (blue) and Pd–O (red) bond lengths as a function of nanoparticle charge.

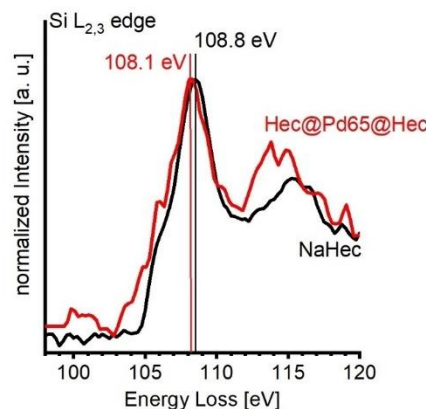


**Figure 6.** ELL spectra at the Si  $L_{2,3}$  edge of NaHec (black) and Hec@Pd65@Hec (red).

It revealed a chemical shift of both the white line at about 109 eV and the resonance at around 116 eV to lower energy losses for Hec@Pd65@Hec as compared to pristine NaHec. A chemical shift to lower energy losses of about 0.8 eV was also detected at the Si K edge (Figure S18). EELS thus suggests a slight but significant reduction to a  $Si^x$  ( $x < +4$ ) species upon intercalation of Pd nanoparticles corroborating an electronic interaction between Pd and the support.<sup>[33]</sup> As has been observed for model systems<sup>[5,6]</sup> and although the Pd already carries a positive charge for reasons of charge neutrality, “coating” the Pd nanoparticles triggers an additional transfer of electron density to Si in the hectorite structure. This also resembles observations by Li et al.<sup>[34]</sup> who synthesized Pd nanocubes covered with the Cu-containing MOF HKUST-1. They also reported similar shifts of Pd 3d BE as determined by XPS to higher energies, while concomitantly the Cu 2p BE is lowered. This was attributed to Cu–O groups acting as electron acceptors.<sup>[32a]</sup>

## Conclusion

For model architectures of ultrathin layers of oxides deposited on noble metals modulations of the metal electronic structures have long been established and are advantageous for catalytic activity. These architectures can be mimicked at bulk scale by sandwiching positively charged metal nanoparticles between negatively charged clay nanosheets. Like for the model system, a charge transfer from the Pd nanoparticles to the nanosheets was observed by XPS, EELS, and CO-DRIFTS and a higher catalytic activity in CO oxidation was observed as compared to Pd on conventional supports such as  $\gamma-Al_2O_3$ . The synthesis route via intercalation into nematic phases of anionic nanosheets is certainly not restricted to Pd metals nor to hectorite nanosheets, but is applicable for a broad spectrum of metal nanoparticles of various sizes and shapes<sup>[35]</sup> on one side, and other liquid

crystalline supports like lepidocrocite-type titanates,<sup>[15b]</sup> or layered antimony phosphates<sup>[15c,e]</sup> on the other side. Needless to say, the concept can also be extended to catalytically more attractive alloy nanoparticles.<sup>[36]</sup>

### Acknowledgements

This work was supported by the Deutsche Forschungsgemeinschaft (SFB 840, TP A2). K.A. thanks the Elite Network of Bavaria for a PhD fellowship and the elite study program "Macromolecular Science" for a fellowship. We thank Lena Geiling for SEM measurements and Marco Schwarzmair for preparation of samples for cross sectional TEM. We thank Renee Timmins for language polishing. We appreciate the support of the Keylab for Optical and Electron Microscopy of the Bavarian Polymer Institute (BPI). We thank Rhett Kempe for the access to his micro reactor and BayCEER for ICP-OES measurement. The XPS/UPS facility (PHI 5000 VersaProbe III system) at the Device Engineering Keylab of BPI is acknowledged and Michael Ertl for performing the measurements. C.J.H acknowledges the support of the Czech Science Foundation (20-26767Y). The authors also acknowledge financial support from the Bavarian-Czech Academic Agency (Bayerisch-Tschechische Hochschulagentur) in the framework of the project "Entwicklung und Designprinzipien für strukturierte Materialien" financed by funds of the Free State of Bavaria. This work was supported by The Ministry of Education, Youth and Sports from the Large Infrastructures for Research, Experimental Development and Innovations project "e-Infrastructure CZ—LM2018140. T.G. acknowledges funding by the Fonds zur Förderung der wissenschaftlichen Forschung (FWF, Austrian Science Fund) via project number J4278. Open access funding enabled and organized by Projekt DEAL.

### Conflict of interest

The authors declare no conflict of interest.

**Keywords:** Clay · CO oxidation · Metal support interaction · Palladium · Ultrathin oxide layer

- [1] G. Pacchioni, H.-J. Freund, *Chem. Soc. Rev.* **2018**, *47*, 8474–8502.
- [2] a) T. W. van Deelen, C. Hernández Mejía, K. P. de Jong, *Nat. Catal.* **2019**, *2*, 955–970; b) C. T. Campbell, *Nat. Chem.* **2012**, *4*, 597–598.
- [3] a) M. Xu, S. He, H. Chen, G. Cui, L. Zheng, B. Wang, M. Wei, *ACS Catal.* **2017**, *7*, 7600–7609; b) F. Wang, W. Ueda, J. Xu, *Angew. Chem. Int. Ed.* **2012**, *51*, 3883–3887; *Angew. Chem.* **2012**, *124*, 3949–3953.
- [4] H. J. Freund, *J. Am. Chem. Soc.* **2016**, *138*, 8985–8996.
- [5] a) G. Pacchioni, H. Freund, *Chem. Rev.* **2013**, *113*, 4035–4072; b) L. Giordano, G. Pacchioni, *Acc. Chem. Res.* **2011**, *44*, 1244–1252.
- [6] a) S. Prada, U. Martinez, G. Pacchioni, *Phys. Rev. B* **2008**, *78*, 235423; b) L. Giordano, F. Cinquini, G. Pacchioni, *Phys. Rev. B* **2006**, *73*, 045414.
- [7] a) Y. Lykhach, S. M. Kozlov, T. Skala, A. Tovt, V. Stetsovich, N. Tsud, F. Dvorak, V. Johanek, A. Neitzel, J. Myslivecek, S. Fabris, V. Matolin, K. M. Neyman, J. Libuda, *Nat. Mater.* **2016**, *15*, 284–288; b) G. N. Vayssilov, Y. Lykhach, A. Migani, T. Staudt, G. P. Petrova, N. Tsud, T. Skala, A. Bruix, F. Illas, K. C. Prince, V. Matolin, K. M. Neyman, J. Libuda, *Nat. Mater.* **2011**, *10*, 310–315.
- [8] Y. Lykhach, J. Kubat, A. Neitzel, N. Tsud, M. Vorokhta, T. Skala, F. Dvorak, Y. Kost, K. C. Prince, V. Matolin, V. Johanek, J. Myslivecek, J. Libuda, *J. Chem. Phys.* **2019**, *151*, 204703.
- [9] a) W. D. Schneider, M. Heyde, H. J. Freund, *Chem. Eur. J.* **2018**, *24*, 2317–2327; b) S. Shaikhutdinov, H. J. Freund, *J. Phys. Condens. Matter* **2015**, *27*, 443001; c) H. J. Freund, *Acc. Chem. Res.* **2017**, *50*, 446–449.
- [10] G. B. B. Varadwaj, K. M. Parida, *RSC Adv.* **2013**, *3*, 13583–13593.
- [11] a) G. M. Scheuermann, R. Thomann, R. Mühlaupt, *Catal. Lett.* **2009**, *132*, 355–362; b) M. Miyagawa, A. Shibusawa, K. Maeda, A. Tashiro, T. Sugai, H. Tanaka, *RSC Adv.* **2017**, *7*, 41896–41902; c) P. Upadhyay, V. Srivastava, *RSC Adv.* **2015**, *5*, 740–745.
- [12] I. Dékány, L. Turi, Z. Király, *Appl. Clay Sci.* **1999**, *15*, 221–239.
- [13] a) S. Papp, A. Szűcs, I. Dékány, *Appl. Clay Sci.* **2001**, *19*, 155–172; b) Z. Király, I. Dékány, A. Mastalir, M. Bartok, *J. Catal.* **1996**, *161*, 401–408.
- [14] A. Lerf, *Dalton Trans.* **2014**, *43*, 10276–10291.
- [15] a) L. J. Michot, I. Bihamnic, S. Maddi, S. S. Funari, C. Baravian, P. Levitz, P. Davidson, *Proc. Natl. Acad. Sci. USA* **2006**, *103*, 16101–16104; b) L. Wang, T. Sasaki, *Chem. Rev.* **2014**, *114*, 9455–9486; c) J. P. Gabriel, F. Camerel, B. J. Lemaire, H. Desvaux, P. Davidson, P. Batail, *Nature* **2001**, *413*, 504–508; d) Y. Liu, Z. Xu, W. Gao, Z. Cheng, C. Gao, *Adv. Mater.* **2017**, *29*, 1606794; e) P. Davidson, C. Penisson, D. Constantin, J. P. Gabriel, *Proc. Natl. Acad. Sci. USA* **2018**, *115*, 6662–6667.
- [16] a) M. Daab, N. J. Eichstaedt, C. Habel, S. Rosenfeldt, H. Kalo, H. Schiessling, S. Förster, J. Breu, *Langmuir* **2018**, *34*, 8215–8222; b) M. Daab, N. J. Eichstaedt, A. Edenharter, S. Rosenfeldt, J. Breu, *RSC Adv.* **2018**, *8*, 28797–28803.
- [17] M. Stöter, D. A. Kunz, M. Schmidt, D. Hirsemann, H. Kalo, B. Putz, J. Senker, J. Breu, *Langmuir* **2013**, *29*, 1280–1285.
- [18] S. Rosenfeldt, M. Stöter, M. Schlenk, T. Martin, R. Q. Albuquerque, S. Förster, J. Breu, *Langmuir* **2016**, *32*, 10582–10588.
- [19] K. Sano, Y. S. Kim, Y. Ishida, Y. Ebina, T. Sasaki, T. Hikima, T. Aida, *Nat. Commun.* **2016**, *7*, 12559.
- [20] K. Ament, D. R. Wagner, F. E. Meij, F. E. Wagner, J. Breu, *Z. Anorg. Allg. Chem.* **2020**, *646*, 1110–1115.
- [21] E. Coronado, A. Ribera, J. García-Martínez, N. Linares, L. M. Liz-Marzáñ, *J. Mater. Chem.* **2008**, *18*, 5682.
- [22] H. J. Freund, G. Meijer, M. Scheffler, R. Schlögl, M. Wolf, *Angew. Chem. Int. Ed.* **2011**, *50*, 10064–10094; *Angew. Chem.* **2011**, *123*, 10242–10275.
- [23] a) Y. Zhou, Z. Wang, C. Liu, *Catal. Sci. Technol.* **2015**, *5*, 69–81; b) X. Liu, R. Wang, L. Song, H. He, G. Zhang, X. Zi, W. Qiu, *Catal. Commun.* **2014**, *46*, 213–218; c) E. J. Peterson, A. T. DeLaRiva, S. Lin, R. S. Johnson, H. Guo, J. T. Miller, J. Hun Kwak, C. H. Peden, B. Kiefer, L. F. Allard, F. H. Ribeiro, A. K. Datye, *Nat. Commun.* **2014**, *5*, 4885.
- [24] a) R. Wang, H. He, L.-C. Liu, H.-X. Dai, Z. Zhao, *Catal. Sci. Technol.* **2012**, *2*, 575–580; b) J.-N. Park, A. J. Forman, W. Tang, J. Cheng, Y.-S. Hu, H. Lin, E. W. McFarland, *Small* **2008**, *4*, 1694–1697; c) J. Xu, T. White, P. Li, C. He, J. Yu, W. Yuan, Y.-F. Han, *J. Am. Chem. Soc.* **2010**, *132*, 10398–10406.
- [25] R. Arrigo, M. E. Schuster, S. Abate, S. Wrabetz, K. Amakawa, D. Teschner, M. Freni, G. Centi, S. Perathoner, M. Havecker, R. Schlögl, *ChemSusChem* **2014**, *7*, 179–194.
- [26] a) N. S. Babu, N. L. Lingaiah, R. Gopinath, P. S. S. Reddy, P. S. S. Prasad, *J. Phys. Chem. C* **2007**, *111*, 6447–6453; b) B. Stasinska,

- A. Machocki, K. Antoniak, M. Rotko, J. L. Figueredo, F. Gonçalves, *Catal. Today* **2008**, *137*, 329–334.
- [27] a) H. Wang, C.-j. Liu, *Appl. Catal. B* **2011**, *106*, 672–680; b) T. Cheng, J. Chen, A. Cai, J. Wang, H. Liu, Y. Hu, X. Bao, P. Yuan, *ACS Omega* **2018**, *3*, 6651–6659; c) G. Bektov, B. Heinrichs, J. P. Pirard, S. Chenakin, N. Kruse, *Appl. Surf. Sci.* **2013**, *287*, 293–298; d) T. H. Fleisch, R. F. Hicks, A. T. Bell, *J. Catal.* **1984**, *87*, 398–413; e) Y. Xu, J. Ma, Y. Xu, L. Xu, L. Xu, H. Li, H. Li, *RSC Adv.* **2013**, *3*, 851–858.
- [28] X. Wang, B. Chen, G. Chen, X. Sun, *RSC Adv.* **2016**, *6*, 87978–87987.
- [29] P. Begum, R. C. Deka, *ChemistrySelect* **2017**, *2*, 8847–8855.
- [30] B. Zhu, B. W. L. Jang, *J. Mol. Catal. A* **2014**, *395*, 137–144.
- [31] a) S. Bertarione, D. Scarano, A. Zecchina, V. Johánek, J. Hoffmann, S. Schauermann, M. M. Frank, J. Libuda, G. Rupprechter, H.-J. Freund, *J. Phys. Chem. B* **2004**, *108*, 3603–3613; b) K. Murata, E. Eleeda, J. Ohyama, Y. Yamamoto, S. Arai, A. Satsuma, *Phys. Chem. Chem. Phys.* **2019**, *21*, 18128–18137.
- [32] a) Y. Chen, O. Sakata, Y. Nanba, L. S. R. Kumara, A. Yang, C. Song, M. Koyama, G. Li, H. Kobayashi, H. Kitagawa, *Commun. Chem.* **2018**, *1*, 61; b) A. Nilsson, L. Pettersson, J. Norskov, *Chemical Bonding at Surfaces and Interfaces*, Elsevier, Amsterdam, **2008**.
- [33] a) M. T. Otten, B. Miner, J. H. Rask, P. R. Buseck, *Ultramicroscopy* **1985**, *18*, 285–289; b) H. Tan, J. Verbeeck, A. Abakumov, G. Van Tendeloo, *Ultramicroscopy* **2012**, *116*, 24–33.
- [34] G. Li, H. Kobayashi, J. M. Taylor, R. Ikeda, Y. Kubota, K. Kato, M. Takata, T. Yamamoto, S. Toh, S. Matsumura, H. Kitagawa, *Nat. Mater.* **2014**, *13*, 802–806.
- [35] J. Hühn, C. Carrillo-Carrion, M. G. Soliman, C. Pfeiffer, D. Valdeperez, A. Masood, I. Chakraborty, L. Zhu, M. Gallego, Z. Yue, M. Carril, N. Feliu, A. Escudero, A. M. Alkilany, B. Pelaz, P. del Pino, W. J. Parak, *Chem. Mater.* **2017**, *29*, 399–461.
- [36] a) Y. H. Ahmad, A. T. Mohamed, K. A. Mahmoud, A. S. Aljaber, S. Y. Al-Qaradawi, *RSC Adv.* **2019**, *9*, 32928–32935; b) E. D. Goodman, S. Dai, A.-C. Yang, C. J. Wrasman, A. Gallo, S. R. Barc, A. S. Hoffman, T. F. Jaramillo, G. W. Graham, X. Pan, M. Cargnello, *ACS Catal.* **2017**, *7*, 4372–4380; c) B. Huang, H. Kobayashi, T. Yamamoto, S. Matsumura, Y. Nishida, K. Sato, K. Nagaoaka, S. Kawaguchi, Y. Kubota, H. Kitagawa, *J. Am. Chem. Soc.* **2017**, *139*, 4643–4646; d) M. Armbrüster, *Sci. Technol. Adv. Mater.* **2020**, *21*, 303–322.

Manuscript received: November 12, 2020

Accepted manuscript online: December 8, 2020

Version of record online: January 28, 2021

### 6.2.2 Nanopartikel auf subnanometer dünnen oxidischen Filmen: Skalierung von Modellsystemen (German Edition)



**CO-Oxidation**

## Nanopartikel auf subnanometer dünnen oxidischen Filmen: Skalierung von Modellsystemen

Kevin Ament, Nicolas Köwitsch, Dianwei Hou, Thomas Götsch, Jutta Kröhnert, Christopher J. Heard, Annette Trunschke, Thomas Lunkenstein, Marc Armbrüster und Josef Breu\*

**Abstract:** Durch die Abscheidung von ultradünnen Oxidschichten auf atomar-flachen Metalloberflächen konnte die elektronische Struktur des Metalls und hierdurch dessen katalytische Aktivität beeinflusst werden. Die Skalierung dieser Architekturen für eine technische Nutzbarkeit war bisher aber kaum möglich. Durch die Verwendung einer flüssigkristallinen Phase aus Fluorhectorit-Nanoschichten, können wir solche Architekturen in skaliertem Maßstab imitieren. Synthetischer Natriumfluorhectorit (NaHec) quillt spontan und repulsiv in Wasser zu einer nematischen flüssigkristallinen Phase aus individuellen Nanoschichten. Diese tragen eine permanente negative Schichtladung, sodass selbst bei einer Separation von über 60 nm eine parallele Anordnung der Schichten behalten wird. Zwischen diesen Nanoschichten können Palladium-Nanopartikel mit entgegengesetzter Ladung eingelagert werden, wodurch die nematische Phase kollabiert und separierte Nanopartikel zwischen den Schichten fixiert werden. Die Aktivität zur CO-Oxidation des so entstandenen Katalysators war höher als z. B. die der gleichen Nanopartikel auf konventionellem  $\text{Al}_2\text{O}_3$  oder der externen Oberfläche von NaHec. Durch Röntgenphotoelektronenspektroskopie konnte eine Verschiebung der Pd-3d-Elektronen zu höheren Bindungsenergien beobachtet werden, womit die erhöhte Aktivität erklärt werden kann. Berechnungen zeigten, dass mit erhöhter positiver Ladung des Pd die Adsorptionsstärke von CO erniedrigt und damit auch die Vergiftung durch CO vermindert wird.

### Einleitung

Eine häufig genutzte Methode zur Generierung von Nanopartikeln auf oxidischen Trägern ist die Imprägnierung mit Präkursoren, gefolgt von chemischer oder thermischer Behandlung. In vielen Fällen wird der oxidische Träger als

inert angesehen und dient zur Dispergierung und Stabilisierung der Nanopartikel gegen Ostwald Reifung.<sup>[1]</sup> Allerdings kann die geschickte Auswahl des richtigen Trägers die Selektivität und Aktivität des nanopartikulären Katalysators signifikant verändern.<sup>[2]</sup> Es konnte gezeigt werden, dass sogenannte Elektronische-Metall-Träger-Wechselwirkungen (EMSI) Einfluss auf die katalytische Aktivität von Metallen nehmen können.<sup>[3]</sup> Um diese EMSI-Effekte zu studieren, wurden in den letzten Jahren Modellsysteme etabliert, die auf ultradünnen oxidischen Schichten auf Metalloberflächen beruhen.<sup>[2a,4]</sup>

Nach Abscheidung des Oxiids wurde eine Modifizierung der Austrittsarbeit des Metalls beobachtet.<sup>[5]</sup> Dieses Phänomen kann verschiedene Ursachen, wie Ladungstransfer, elektrostatische oder Kompressions-Effekte, haben.<sup>[5b,6]</sup> Für Cluster aus Pt<sup>[7]</sup> oder Ir<sup>[8]</sup> auf CeO<sub>2</sub> Filmen wurde zum Beispiel ein Ladungsfluss vom Edelmetall zum Oxid beobachtet. Dadurch wurde die Metalloberfläche positiv aufgeladen.

Mit Hilfe dieser Modelle konnte ein tieferes Verständnis der Arbeitsweise von Realkatalysatoren geschaffen werden. Zwar können diese Modelle mit höchster Präzision hergestellt werden, jedoch ist die Skalierung von subnanometerdicken Oxiidschichten in großem Maßstab nicht praktikabel (Schema 1).<sup>[9]</sup>

Schichtmaterialien mit permanenter negativer Schichtladung, wie Schichtsilikate, sind bekannte Träger für katalytisch aktive Nanopartikel.<sup>[10]</sup> Durch die Kationenaustauschkapazität der Schichtsilikate können die Zwischenschichtkationen durch Präkursoren ausgetauscht werden, aus denen durch Reduktion (z. B. Pd, Cu, Ru)<sup>[11]</sup> oder Fällung (CdS)<sup>[12]</sup> Nanopartikel generiert werden können. Diese Kationenaustauschkapazität von natürlichen Schichtsilikaten liegt in der Größenordnung von < 100 mmol/100 g,<sup>[10]</sup> was die maximal mög-

[\*] M.Sc. K. Ament, Prof. Dr. J. Breu

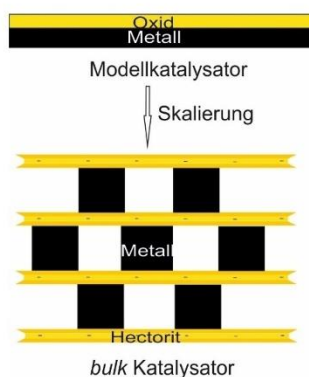
Bavarian Polymer Institute and Department of Chemistry, University of Bayreuth  
Universitätsstraße 30, 95447 Bayreuth (Deutschland)  
E-Mail: josef.breu@uni-bayreuth.de  
M.Sc. N. Köwitsch, Prof. Dr. M. Armbrüster  
Faculty of Natural Sciences, Institute of Chemistry, Materials for Innovative Energy Concepts, Chemnitz University of Technology  
Straße der Nationen 62, 09111 Chemnitz (Deutschland)  
M.Sc. D. Hou, Dr. C. J. Heard  
Department of Physical and Macromolecular Chemistry, Charles University  
Hlavova 8, 128 00 Prague 2 (Tschechische Republik)

Dr. T. Götsch, Dipl. Ing. J. Kröhnert, Dr. A. Trunschke,

Dr. T. Lunkenstein  
Department of Inorganic Chemistry, Fritz-Haber-Institut der Max-Planck-Gesellschaft  
Faradayweg 4–6, 14195 Berlin (Deutschland)

Hintergrundinformationen und die Identifikationsnummer (ORCID) eines Autors sind unter:  
<https://doi.org/10.1002/ange.202015138> zu finden.

© 2020 Die Autoren. Angewandte Chemie veröffentlicht von Wiley-VCH GmbH. Dieser Open Access Beitrag steht unter den Bedingungen der Creative Commons Attribution License, die jede Nutzung des Beitrages in allen Medien gestattet, sofern der ursprüngliche Beitrag ordnungsgemäß zitiert wird.



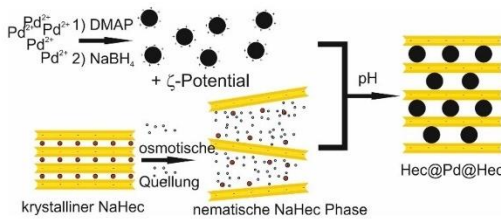
**Schema 1.** Skalierung der Modellarchitektur einer einzelnen oxidischen Lage ( $< 1 \text{ nm}$ ) auf einer Metalloberfläche zu einem mesostrukturierten Katalysator mit einer hohen zugänglichen und aktiven Oberfläche. Hierbei wird das Schichtsilikat Hectorit als dünne Oxidschicht verwendet.

liche Beladung limitiert. Im Falle von 3.5 nm großen Pd Nanopartikeln würde dies einer maximal möglichen Beladung von 6 Gewichtsprozent (Gew%) entsprechen, was einer Dichte von einem Nanopartikel pro  $1500 \text{ nm}^2$  Zwischenschichtraum entspricht.

Weiterhin ist die laterale Ausdehnung von natürlichen Schichtsilikaten typischerweise kleiner als 200 nm. Dékany et al.<sup>[13]</sup> beobachteten, dass Nanopartikel deswegen vor allem auf den äußeren Oberflächen oder Kavitäten erzeugt wurden. Dies spielte sich auch in insignifikanten Verschiebungen des Basalfächenaabstands wider. Durch die limitierende Kationenaustauschkapazität können höhere Beladungen nur realisiert werden, wenn bereits fertige Nanopartikel interkaliert werden. Bei Zwischenschichtabständen von weniger als einem Nanometer ist dies aus kinetischer Sicht jedoch unwahrscheinlich.

Das synthetische Schichtsilikat Natriumfluorhectorit (NaHec,  $[\text{Na}_{0.5}]_{\text{inter}}^{[\text{Mg}_{2.5}\text{Li}_{0.5}]^{[\text{loc}]}[\text{Si}_4]^{[\text{el}]}[\text{O}_{10}\text{F}_2]}$ ) besitzt die Eigenschaft osmotisch zu quellen.<sup>[14]</sup> Damit gehört es zu einem kleinen Kreis von Schichtmaterialien, bei denen dieses seltene Phänomen beobachtet werden kann.<sup>[15]</sup> Es handelt sich um einen thermodynamisch erlaubten Prozess<sup>[16]</sup> welcher eine flüssigkristalline Phase erzeugt. Einzelne Schichtsilikatlamellen sind dabei uniform voneinander entfernt. NaHec besitzt eine mittlere laterale Plättchenausdehnung von  $20 \mu\text{m}$ ,<sup>[17]</sup> was es den individuellen Schichten mit einer Dicke von 0.96 nm nicht ermöglicht selbst bei hohen Verdünnungen ( $< 1$  Volumenprozent) frei zu rotieren. Dadurch bildet sich eine natische flüssigkristalline Phase aus.<sup>[18]</sup> Wie auch für schichtförmige Titanate<sup>[19]</sup> gezeigt wurde, adaptieren verdünnte Dispersionen von NaHec durch die starke elektrostatische Abstoßung der gleichgeladenen Schichten eine co-faciale Orientierung. In der nematischen Phase wird diese Geometrie selbst bei großen Abständen zwischen den Schichten ( $> 50 \text{ nm}$ ) behalten.

Die Verwendung dieser nematischen Phase von NaHec zur Interkalation von Nanopartikeln wurde bereits anhand von Maghemit Nanopartikeln gezeigt.<sup>[20]</sup> Außerdem bietet die Nutzung einer nematischen Phase die Möglichkeit für eine skalierbare Syntheseroute hin zu nanopartikulären Katalysatoren zwischen subnanometer dicken oxidischen Schichten. Pd Nanopartikel werden zunächst über eine bekannte Synthese<sup>[21]</sup> hergestellt und mit 4-Dimethylaminopyridin (DMAP) als Ligand bedeckt. Auf diese Weise entstehen nanopartikuläre, metallische Kationen, die ohne kinetische Hinderung zwischen die separierten Nanoschichten diffundieren können. Dies entspricht im Prinzip einem Kationen-



**Schema 2.** Schema zur Synthese von Pd interkaliertem Hec (Hec@Pd@Hec).

austausch (Schema 2). Der Einfluss der Nanoschichten auf (elektronische) Eigenschaften der Pd Nanopartikel wurde anhand der Oxidation von Kohlenmonoxid (CO) untersucht.

## Ergebnisse und Diskussion

### Synthese und Charakterisierung der Hec@Pd@Hec Katalysatoren

Die synthetisierten Pd Nanopartikel besaßen laut Transmissionselektronenmikroskopie (TEM) eine enge Größenverteilung von  $3.5 \pm 0.4 \text{ nm}$  (Abbildung S1a). Diese waren laut Dynamischer Lichtstreuung (DLS) stabil in Wasser dispergierbar und wiesen einen hydrodynamischen Durchmesser von  $4.5 \pm 1.3 \text{ nm}$  auf. Durch Anpassung des pH-Wertes konnte das  $\zeta$ -Potential zwischen +34 und +14 mV eingestellt werden (Abbildung S1b). Da die Schichtladung und damit die Ladungsdichte von NaHec fix ist, bestimmt die Oberflächenladung der Nanopartikel die Beladung, die nötig für den Ladungsausgleich ist (Tabelle 1). Für die Interkalation wurden die Nanopartikel als 0.1 Gew% Dispersion verwendet und Hectorit wurde als 1.5 Gew% Dispersion

**Tabelle 1:** Gewichtsanteil an Pd abhängig von pH der NaHec- und Nanopartikel-Dispersion.

Bezeichnung	pH	$\zeta$ -Potential [mV]	Pd-Beladung (ICP-OES) [Gew%]	Pd-Beladung (REM-EDX) [Gew%]
Hec@Pd65@Hec	9.5	28	65.2	67.8
Hec@Pd72@Hec	10.8	22	72.5	76.0

unter Röhren zugegeben. Bei diesem Gehalt an NaHec betrug der Abstand zweier Nanoschichten mehr als 60 nm, was durch Kleinwinkelstreuung nachgewiesen wurde (Abbildung S2). Dieser hohe Abstand ermöglichte eine schnelle Diffusion der Nanopartikel zwischen den Schichten. Durch die gegensätzliche Ladung von Nanoschichten und Nanopartikeln wurde eine Heterokoagulation ausgelöst und die Nanopartikel zwischen den Lamellen fixiert. Laut energiedispersiver Röntgenpektroskopie (REM-EDX) ist das Pd uniform über das Schichtsilikat verteilt (Abbildung S3). Außerdem war laut Elementaranalyse (CHN) DMAP durch wiederholtes Zentrifugieren und Waschen komplett entfernt (Tabelle S1). Die so hergestellten Katalysatoren werden als Hec@Pdx@Hec bezeichnet, um die sandwichartige Architektur hervorzuheben. X bezeichnet dabei die Beladung in Gew% laut optischer Emissionspektrometrie mit induktiv gekoppeltem Plasma (ICP-OES). Die Beladung wurde zudem durch REM-EDX bestätigt (Tabelle 1). Das Zwischenschicht  $\text{Na}^+$  wurde laut ICP-OES, REM-EDX (kein Signal bei 1.04 keV, Abbildung S3) und Röntgenphotoelektronenspektroskopie (XPS, kein Signal für Na 1s bei 1070 eV, Abbildung S4) vollständig entfernt. Dies weist darauf hin, dass der Ladungsausgleich tatsächlich durch die interkalierten Pd Nanopartikel vollzogen wird.

Wie für einen Quasi-Ionenaustausch in der Einleitung vermutet wurde, konnte die Beladung an Pd bis zu einem Maximum von 72.5 Gew% (Hec@Pd72@Hec) gesteigert werden. Im Gegensatz zur üblichen Ionenaustausch-Route können durch Interkalation von positiv geladenen Nanopartikeln sehr hohe Beladungen erzielt werden. Eine Beladung mit 65.2 Gew% (Hec@Pd65@Hec) würde eine Stöchiometrie von  $\text{Pd}_{0.7}\text{Mg}_{2.5}\text{Li}_{0.5}\text{Si}_4\text{O}_{10}\text{F}_2$  bedeuten. Durch Ionenaustausch von  $\text{Na}^+$  durch  $\text{Pd}^{2+}$  und anschließender Reduktion wäre die Zusammensetzung auf  $\text{Pd}_{0.25}\text{Mg}_{2.5}\text{Li}_{0.5}\text{Si}_4\text{O}_{10}\text{F}_2$  limitiert.

Durch die Heterokoagulation kollabiert die nematische Phase zu einer lamellaren Struktur, wobei benachbarte Hec Nanoschichten die Nanopartikel fixieren (Abbildung 1). Dabei sind die Nanopartikel nicht dicht gepackt, sondern sind voneinander separiert (Abbildung 1b, inset). Jede Nanopartikelsschicht ist von der nächsten durch exakt eine 0.96 nm dicke Silikatschicht getrennt. Es entsteht eine Struktur wie in Schema 1 beschrieben, wobei die Nanopartikel gegeneinander verschoben sind und gegenüber einem Nanopartikel eine

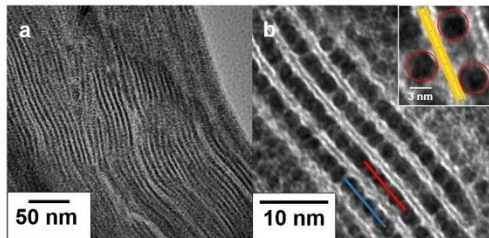


**Abbildung 1.** TEM Aufnahmen von Hec@Pd65@Hec bei verschiedenen Vergrößerungen. Die roten und blauen Linien wurden zur Graustufenanalyse (Abbildung S5) verwendet. Der Inset zeigt benachbarte Nanopartikel, die voneinander separiert sind.

Mesopore gefunden werden kann (Abbildung 1b, Inset). Dies wurde auch durch Graustufenanalyse entlang der blauen und roten Linie in Abbildung 1b weiter bestätigt (Abbildung S5). Es sollte erwähnt werden, dass die Nanopartikel ihre sphärische Form auch nach der Entfernung des Liganden behalten haben. Längeres Tempern führte jedoch zu einer Verformung (Abbildung S6).

Die monomodalen Pd Nanopartikel erzeugten entlang der Stapelung eine eindimensional periodische Struktur. Die Periodizität betrug laut TEM  $4.6 \pm 0.7$  nm. Bei noch höherer Beladung (Hec@Pd72@Hec) entstanden in einigen Zwischenschichten Multilagen an Pd Nanopartikeln (Abbildung S7), was als Störung der Periodizität angesehen werden kann. Dies geschieht vermutlich, da die Oberflächenladungsdichte bei pH 10.8 (22 mV ζ-Potential) zu niedrig war, um den Ladungsausgleich der anionischen Nanoschichten in einer Monolage zu erzielen. Pulverdiffraktometrie (PXRD) von texturierten Proben bestätigten die eindimensional kristalline Ordnung. Eine rationale  $001$  Serie mit einer Periodizität von 4.7 nm wurde gefunden, die in gutem Einklang mit der TEM-Bestimmung steht (Abbildung 2). Die Summe aus der Dicke einer Lamelle von 0.96 nm und dem Durchmesser eines Nanopartikels von 3.5 nm würde einen Wert von 4.46 nm ergeben. Bei einer Beladung von 72 Gew% (Hec@Pd72@Hec) führten die Störungen in der Periodizität durch die wenigen Multilagen zu einer statistischen Wechsellagerung und einer Verschiebung der  $001$  Serie zu 5.5 nm. Dies wurde von einer Erhöhung der Halbwertsbreite der Reflexe begleitet. Der höhere Schichtabstand lässt sich deswegen mit einer statistischen Wechsellagerung aus Mono- und Doppellagen aus Pd Nanopartikeln erklären, da der Röntgenstrahl über die unterschiedlichen Schichtabstände innerhalb seiner Kohärenzlänge mittelt.

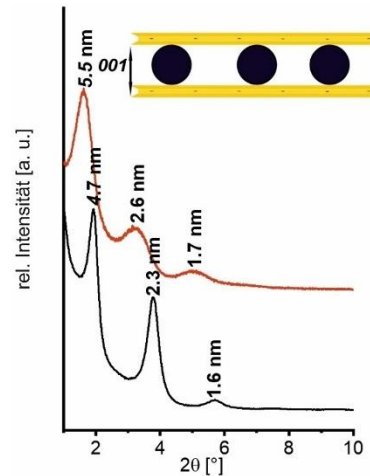


**Abbildung 2.** Diffraktogramme von Hec@Pd65@Hec (schwarz) und Hec@Pd72@Hec (rot).

**Tabelle 2:** Ergebnisse der Ar-Physisorption<sup>[a]</sup> und Chemisorption von CO.<sup>[b]</sup>

Bezeichnung	$S_{\text{BET}} [\text{m}^2 \text{g}^{-1}]$	Porengröße [nm]	Porenvolumen [ $\text{cc g}^{-1}$ ]	Metalldispersion [%]
NaHec	4	/	/	/
Hec@Pd65@Hec	147	4.3	0.132	23.7
Hec@Pd72@Hec	87	3.8	0.088	19.9

[a] bestimmt durch Ar-Physisorption bei 87 K. [b] bestimmt durch CO Doppelisothermen-Methode.

Die TEM Aufnahmen ließen bereits vermuten, dass die Nanopartikel in der Zwischenschicht nicht dicht gepackt sind, sondern Poren zwischen den Nanopartikeln existieren müssen. Dies konnte über Ar-Physisorption und CO-Chemisorption bestätigt werden (Tabelle 2 und Abbildung S8). Die  $d_{50}$  Porenverteilung von Hec@Pd65@Hec beträgt 4.3 nm, was in der Größenordnung eines Pd Nanopartikels liegt. Dies lässt annehmen, dass etwa die Hälfte des Zwischenschichtraums tatsächlich leerer Raum ist. Dies macht auch wahrscheinlich, dass sich gegenüber einem Nanopartikel auf der anderen Seite der Lamelle eine Mesopore befindet (Schema 1). Zum Vergleich deutete die Ar-Isotherme von reinem NaHec eine unporöse Struktur mit einer BET Oberfläche von lediglich  $4 \text{ m}^2 \text{ g}^{-1}$  an. Die Schichten sind kollabiert und Ar hat keinen Zugang zur internen Oberfläche von NaHec. Die Struktur wird nur durch Interkalation von Pd Nanopartikeln, die als Säulen fungieren, porös.

Die Metalldispersion (Verhältnis von Oberflächen- zu Volumenatomen) für einen freien, sphärischen Pd Nanopartikel mit einer Größe von 3.5 nm beträgt 32 %. Durch die gute Zugänglichkeit der Pd Nanopartikel betrug die experimentell bestimmte Dispersion von Hec@Pd65@Hec durch CO-Chemisorption 24 %. Der Oberflächenverlust kann mit der Bedeckung der Nanopartikel mit den Nanoschichten erklärt werden.

#### Untersuchung der katalytischen Aktivität

Die Oxidation von Kohlenmonoxid (CO) zu Kohlendioxid ( $\text{CO}_2$ ) wurde als einfache Testreaktion gewählt, um die Aktivität der Katalysatoren in Bezug auf elektronische Metall-Träger-Wechselwirkungen resultierend aus der besonderen Architektur zu untersuchen. Aufgrund der hohen Toxizität ist die CO-Oxidation von enormer Bedeutung für die Abgasnachbehandlung.<sup>[22]</sup> Für jeden katalytischen Test wurde die Menge an Katalysator so gewählt, dass 1 mg Pd verwendet wurde. Der Gasstrom betrug  $50 \text{ mL min}^{-1}$  (1 Vol % CO, 1 Vol %  $\text{O}_2$ , 98 %  $\text{N}_2$ ) und light-off Kurven im Temperaturfenster von  $80^\circ\text{C}$  bis  $220^\circ\text{C}$  wurden bestimmt. Jeder Katalysator wurde dreimal zyklisiert. Die dritte Kurve ist in Abbildung 3 und Tabelle 3 dargestellt. Alle drei konsekutiven Kurven werden exemplarisch für Hec@Pd65@Hec in Abbildung S9 gezeigt.

Die Temperatur bei 50 % Umsatz ( $T_{50}$ ) von Hec@Pd65@Hec, welches die Architektur aus Schema 1 am besten widerspiegelt, betrug  $145^\circ\text{C}$ . Die Aktivierungsenergie,  $E_A$ ,

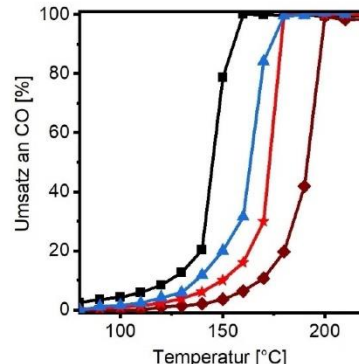


Abbildung 3: Light-off Kurven der CO Oxidation: Hec@Pd65@Hec (schwarz), Hec@Pd72@Hec (blau),  $\text{Pd}_{\text{ex}}@\text{Hec}$  (rot) und  $\text{Pd}_{\text{ex}}@\text{Al}_2\text{O}_3$  (braun). Bedingungen:  $50 \text{ mL min}^{-1}$  (1 Vol % CO, 1 Vol %  $\text{O}_2$  98 %  $\text{N}_2$ ).

**Tabelle 3:** Katalytische Charakterisierung der (Referenz)-Katalysatoren.

Probe	$T_{10} [\text{ }^\circ\text{C}]$	$T_{50} [\text{ }^\circ\text{C}]$	$T_{90} [\text{ }^\circ\text{C}]$	$E_A [\text{kJ mol}^{-1}]$
Hec@Pd65@Hec	124	145	156	42
Hec@Pd72@Hec	138	163	173	51
$\text{Pd}_{\text{ex}}@\text{Hec}$	150	172	177	49
$\text{Pd}_{\text{ex}}@\text{Al}_2\text{O}_3$	169	191	198	57

(unterhalb von 10 % Umsatz bestimmt) betrug  $42 \text{ kJ mol}^{-1}$  (Abbildung S10), was geringer als auf Trägern wie  $\gamma\text{-Al}_2\text{O}_3$  oder MgO ( $55\text{--}80 \text{ kJ mol}^{-1}$ )<sup>[23]</sup> oder Silica ( $65\text{--}120 \text{ kJ mol}^{-1}$ )<sup>[24]</sup> ist.

Die hohe katalytische Aktivität von Hec@Pd65@Hec könnte dabei auf verschiedene Faktoren zurückgeführt werden: Auf die extrem elektronegativen Fluoridanionen im Hectorit; auf die Stabilisierung von atomardispersierten Pd; das mesoporöse Konfinement oder auf elektronische Wechselwirkungen zwischen Träger und Metall, wie es bereits in der Einleitung vorgestellt wurde.

Das Fluorid ist nicht an der Oberfläche der Nanoschicht und damit nicht in direktem Kontakt zum Pd, dennoch könnte es Einfluss auf die Aktivität nehmen. Diese Fragestellung kann jedoch nur in Zukunft beantwortet werden, wenn schichtförmige Träger ohne Fluorid verwendet werden.

Zum zweiten Punkt: Die Nanopartikel wurden mehrfach dialysiert vor der Interkalation. Dadurch sollten kleine Cluster entfernt worden sein. Dennoch könnten diese auch durch Auflösung während der Interkalation entstanden sein. Die externen Flächen des Hectorits tragen auch eine negative Ladung und sollte demzufolge in der Lage sein diese Cluster ebenfalls zu stabilisieren. Aus diesem Grund wurden die gleichen Pd Nanopartikel, die auch für Hec@Pd65@Hec verwendet wurden, auf die äußere Oberfläche von nicht gequollenem NaHec abgelagert ( $\text{Pd}_{\text{ex}}@\text{Hec}$ , Abbildung S11a und Tabelle S2). Die bestimmte  $T_{50}$  war jedoch deutlich höher mit  $172^\circ\text{C}$ . Dies weist darauf hin, dass es nicht oder zumindest nicht nur kleine Cluster sein können, die für die hohe Aktivität verantwortlich sind.

Hec@Pd65@Hec und Hec@Pd72@Hec besitzen ähnliche Porengrößen, wobei die Metalldispersion von letzterem niedriger ist. Die katalytische Aktivität von Hec@Pd72@Hec ist dennoch deutlich geringer. Die  $T_{50}$  steigt von 145°C (Hec@Pd65@Hec) auf 163°C, was bereits nah am  $Pd_{ext}@Hec$  liegt. Weiterhin stiegen auch  $E_A$  auf 51 kJ mol<sup>-1</sup> für Hec@Pd72@Hec bzw. 49 kJ mol<sup>-1</sup> für  $Pd_{ext}@Hec$ . Die Verringerung der Aktivität ist deutlich ausgeprägter als es der Unterschied in der Dispersion erwarten lassen würde.

Es scheint, dass der letzte Aspekt, die besondere Architektur tatsächlich eine wichtige Rolle spielt. Aus diesem Grund wurde  $\gamma\text{-Al}_2\text{O}_3$  mit einer deutlich geringeren Oberflächenladungsdichte ( $-20\text{ mV}$  bei pH 10) mit 1 Gew% Pd Nanopartikel beladen ( $Pd_{ext}@Al_2\text{O}_3$ , Abbildung S11b und Tabelle S2). Die  $T_{50}$  lag hier bei 191°C und  $E_A$  bei 57 kJ mol<sup>-1</sup> (Abbildung S10), was in guter Übereinstimmung mit der Literatur ist.<sup>[23a]</sup> Natürlich ist die Oberflächenchemie von  $\text{Al}_2\text{O}_3$  anders als die des Hectorits, dennoch lässt dies vermuten, dass die besondere Architektur zusammen mit der hohen Ladungsdichte des Hectorits (1 negative Ladung pro 48 Å<sup>2</sup>) Einfluss auf die katalytische Aktivität nimmt.

Wie bereits zuvor erwähnt, müssen die Pd Nanopartikel die permanente negative Ladung der Hec Nanoschichten ausgleichen. XPS der Pd 3d Region von Hec@Pd65@Hec zeigte asymmetrische Signale mit Bindungsenergien (BE) von 335.8 eV für das Pd 3d<sub>5/2</sub> Signal und 341.0 eV für das Pd<sub>3/2</sub> Signal (Abbildung 4a).

Im Vergleich zu bulk Pd Metall (Pd 3d<sub>5/2</sub> Signal bei 335.0 eV) sind diese zu höheren Werten verschoben.<sup>[25]</sup> Pd Nanopartikel auf  $\text{Al}_2\text{O}_3$  zeigen Signale im Bereich von 335.0–335.5 eV<sup>[26]</sup> bzw. 334.8–335.4 eV auf  $\text{SiO}_2$ .<sup>[27]</sup> Die hier beobachtete Verschiebung könnte auf eine elektronendefizitäre Spezies  $\text{Pd}^{\delta+}$  zurück zu führen sein.<sup>[26a]</sup> Für Hec@Pd72@Hec wurde eine geringere Verschiebung beobachtet (335.5 eV, Abbildung S12), was auch durch das geringere Oberflächenpotential der Nanopartikel bei der Synthese zu erwarten war. Das Pd 3d<sub>5/2</sub> Signal der Pd Nanopartikel auf der äußeren Oberfläche von NaHec ( $Pd_{ext}@Hec$ ) oder auf  $\gamma\text{-Al}_2\text{O}_3$  ( $Pd_{ext}@Al_2\text{O}_3$ ) waren lediglich zu 335.3 eV bzw. 335.2 eV verschoben (Abbildung 4a und S12). Dieser Trend zeigt, dass sowohl die negative Schichtladung als auch die besondere Architektur von Hec@Pd@Hec Einfluss auf die elektronische Struktur der Pd Nanopartikel haben. Dieser Trend spiegelt sich auch in der katalytischen Aktivität wider. „Kationisches“ Gold wurde ebenfalls als Grund für eine erhöhte katalytische Aktivität in der CO Oxidation identifiziert.<sup>[28]</sup>

Berechnungen mit Hilfe der Dichtefunktionaltheorie (DFT) von Pd auf dem Zeolith FAU gaben Hinweise, dass positiv geladene Pd Atome zu geringeren Aktivierungsbarrieren im Langmuir-Hinshelwood Mechanismus führen.<sup>[29]</sup> Die erhöhte Aktivität von  $\text{Pd}^{\delta+}$  wurde mit einer geringeren Bindungssstärke von CO an positiv geladenes Pd erklärt.<sup>[23c]</sup>

Die Adsorption von CO ist sehr empfindlich in Bezug auf die Oberflächenbeschaffenheit von Pd. Eine Veränderung des Pd im Hinblick auf eine mögliche Oberflächenladung kann deshalb in der Veränderung der C-O Strettschwingung verfolgt werden. Aus diesem Grund wurde Diffuse Reflexions-Fourier-Transform-Infrarotspektroskopie (DRIFTS) an Hec@Pd65@Hec und  $Pd_{ext}@Al_2\text{O}_3$  durchgeführt (Abbildung 4b). Bei Erhöhung des CO Partialdrucks bis 60 mbar traten ausgeprägte Verschiebungen der Strettschwingung aufgrund von dipolaren Kopplungen durch die steigende Oberflächenbedeckung auf (Abbildung S13). Nach anschließender Einstellung eines Gleichgewichtsdrucks von CO auf 2 mbar konnten für  $Pd_{ext}@Al_2\text{O}_3$  vier Bänder bei 2080, 1976, 1928 und 1864 cm<sup>-1</sup> beobachtet werden (Abbildung 4b). Diese können verschiedenen Adsorptionsmoden von CO auf der Pd Oberfläche zugewiesen werden. Die Bande bei 2080 cm<sup>-1</sup> beschreibt die lineare Anbindung von CO an Ecken bzw. Kanten.<sup>[30]</sup> CO Moleküle, die verbrückend zwischen zwei Pd Atomen auf Stufen der Nanopartikel adsorbieren, können der Bande bei 1978 cm<sup>-1</sup> zugeordnet werden.<sup>[31]</sup> Die beiden breiten Bänder bei kleinerer Wellenzahl (1928 und 1864 cm<sup>-1</sup>) beschreiben verbrückte bzw. CO Moleküle zwischen drei Pd Atomen auf verschiedenen Kristallebenen.<sup>[31]</sup> Bei gleichem Gleichgewichtsdruck zeigt das DRIFT Spektrum von Hec@Pd65@Hec ebenfalls vier Bänder bei 2094, 1991, 1945 und 1877 cm<sup>-1</sup>. Im Vergleich zu  $Pd_{ext}@Al_2\text{O}_3$  waren diese alle zu höheren Wellenzahlen verschoben (Abbildung 4b). Bei einer leicht positiv geladenen

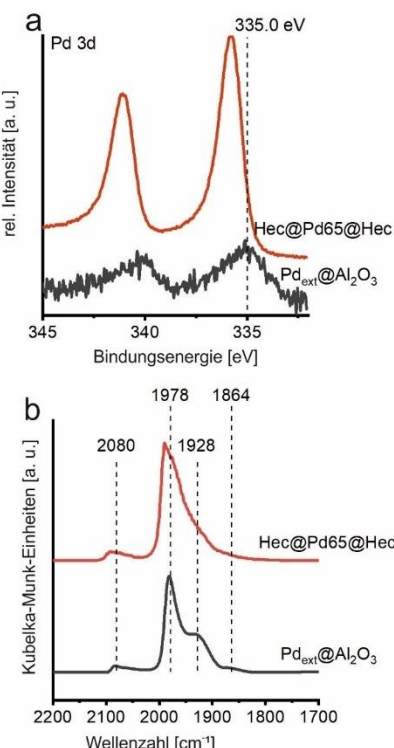


**Abbildung 4.** Charakterisierung der Pd Nanopartikel auf Hec@Pd65@Hec (rot) und  $Pd_{ext}@Al_2\text{O}_3$  (schwarz). a) XPS Spektren der Pd 3d Region und b) DRIFT Spektren von CO chemisorbiert bei 300 K an die Oberfläche des Pd bei einem Gleichgewichtsdruck von 2 mbar CO.

nen Oberfläche, wie es für Hec@Pd65@Hec hier vorgeschlagen wird, ist das Vermögen zur  $\pi$ -Rückbindung vermindert. Durch die verringerte Besetzung der anti-bindenden  $2\pi^*$  Orbitale des CO wird die interne C-O Bindung gestärkt, was zu einer Verschiebung der C-O-Streckschwingung zu höheren Wellenzahlen führt.<sup>[31a]</sup> Durch die geschwächte Rückbindung würde dies insgesamt zu einer verringerten Adsorptionsstärke des CO an die Pd Oberfläche führen.

Um diese Hypothese weiter zu untermauern, wurde der Einfluss einer positiven Oberflächenladung der Pd Nanopartikel auf die Adsorptionsstärke von CO mit Hilfe der DFT berechnet. Die CO/O Adsorption wurde an dem repräsentativen Modell eines ikosaedrischen Nanopartikels Pd<sub>147</sub> betrachtet. Dieser hat einen Durchmesser von 1.5 nm und besitzt (111) Mikrofacetten, die in sehr guter Näherung eine ausgedehnte (111) Oberfläche approximieren. CO und atomarer Sauerstoff wurden auf die *hcp* Besetzungsplätze einer metallischen Oberfläche adsorbiert, wobei ein Bedeckungsgrad 0 von 0.1 angenommen wurde (weitere Details des Modells und der Berechnungen sind in der SI zu finden, Abbildung S14–S17). Die Adsorptionsenergie von CO sank linear mit einer Erhöhung der positiven Ladung auf dem Nanopartikel im betrachteten Bereich von Pd<sub>147</sub> bis Pd<sub>147</sub><sup>7+</sup>. Dahingegen blieb die Adsorptionsenergie von O unverändert (Abbildung 5). Mit der Verringerung der CO Adsorptionsenergie verlängert sich auch die Pd-C Bindungslänge von 2.057 Å auf 2.066 Å und die C-O Bindungslänge verkürzt sich von 1.197 Å auf 1.187 Å. Dies bestätigt, dass eine Verschiebung der Banden der C-O-Streckschwingung von einer leicht positiv geladenen Pd Oberfläche herrühren kann. Die Verringerung von Elektronen in den Metall d-Zuständen nahe der Fermi-Kante führt zu einer verringerten Besetzung des nicht-bindenden  $\pi$ -Kanals zwischen CO und Pd. Dadurch wird die Adsorptionsenergie verringert, wobei gleichzeitig die interne C-O Bindung gestärkt wird.<sup>[32]</sup> Die positive Oberflächenladung könnte die CO Oxidation durch eine gemilderte

CO-Vergiftung der Pd Oberfläche begünstigen. Berechnungen<sup>[29]</sup> bestätigten zudem, dass die Energiebarrieren für ein positiv geladenes Pd durch die veränderte Bindungsstärke von CO gesenkt werden. Dies steht auch in Einklang mit den verringerten experimentell bestimmten Aktivierungsenergien für Hec@Pd@Hec.

Die permanente und hohe Schichtladungsdichte des Hec ist möglicherweise nicht der einzige Grund für die beobachtete positive Oberflächenladung der interkalierten Pd Nanopartikel. Wie bereits erwähnt, können elektronische Wechselwirkungen zwischen ultradünnen, jedoch neutralen Oxidschichten und Metall auftreten und die Austritsarbeit des Metalls beeinflussen.<sup>[5,6]</sup>

Eine ultradünnne Schicht aus SiO<sub>2</sub> auf Mo(112) erhöhte beispielsweise die Austritsarbeit um 0.5–1 eV durch Dipolwechselwirkungen aufgrund von Ladungsübertragung vom Metall auf das Oxid.<sup>[6b]</sup> Um einen möglichen Ladungstransfer zwischen Pd und Hec zu prüfen, wurde deswegen Elektronenenergieverlustspektroskopie (EELS) an der Si L<sub>2,3</sub> Kante durchgeführt (Abbildung 6). Im Vergleich zu reinem NaHec trat eine chemische Verschiebung beider Signale bei 109 eV und bei 116 eV zu kleineren Verlusten für Hec@Pd65@Hec auf. Eine Verschiebung von 0.8 eV zu kleineren Verlusten wurde auch an der Si K Kante beobachtet (Abbildung S18). Dies impliziert eine kleine, aber dennoch messbare Reduzierung der mittleren Oxidationsstufe von Si<sup>x</sup> ( $x < +4$ ) durch die Interaktion der Nanopartikel.<sup>[33]</sup> Wie bereits an den Modellsystemen<sup>[5,6]</sup> beschrieben und auch wenn das Pd bereits eine positive Ladung aufgrund des Ladungsausgleichs trägt, regt die Bedeckung des Pd mit Hec Nanoschichten einen zusätzlichen Transfer von Ladungsdichte an. Ein Ladungs-

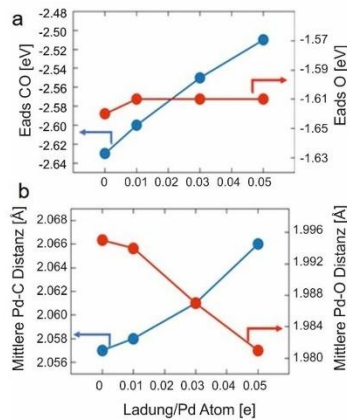


Abbildung 5. a) Berechnete Adsorptionsenergien bei geringer CO (blau) und O (rot) Bedeckung als Funktion der Nanopartikeloberflächenladung. b) Gemittelte Pd-C (blau) und Pd-O (rot) Bindungslängen als Funktion der Nanopartikeloberflächenladung.

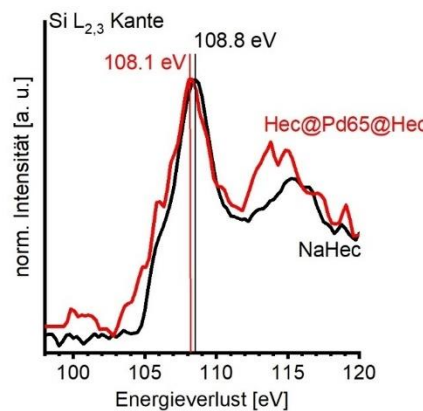


Abbildung 6. ELL Spektren an der Si L<sub>2,3</sub> Kante von NaHec (schwarz) und Hec@Pd65@Hec (rot).

transfer wurde unter anderem auch von Li et al.<sup>[34]</sup> gefunden, die Pd Nanowürfel mit dem Cu beinhaltenden MOF HKUST-1 überwuchsen. Auch hier wurde eine Verschiebung des Pd 3d Signals zu höheren BE durch Ladungstransfer festgestellt.

Cu-O Gruppen des MOF wurden dabei als die Ladungsempfänger festgestellt.<sup>[32a]</sup>

### Schlussfolgerung

Für Modellsysteme, bestehend aus ultradünnen Schichten eines Oxides auf einer Edelmetalloberfläche, konnte gezeigt werden, dass die elektronische Struktur des Metalls beeinflusst wird. Diese Architektur kann auf einer skalierbaren Ebene imitiert werden, indem positiv geladene Nanopartikel zwischen negativ geladene Schichtsilikatlamellen eingeklemmt werden. Wie auch für die Modellsysteme beobachtet, konnten elektronische Wechselwirkungen zwischen Pd und den Nanoschichten mit Hilfe von XPS, EELS und CODRIFTS nachgewiesen werden, die sich auch in einer erhöhten katalytischen Aktivität in der Oxidation von CO wider spiegelten. Die Verwendung einer nematischen Phase eines delaminierbaren Schichtmaterials zur Interkalation von Nanopartikeln ist keineswegs auf Pd oder NaHec beschränkt, sondern auf ein breites Spektrum von Metall-Nanopartikeln unterschiedlicher Größe und Form anwendbar.<sup>[35]</sup> Außerdem können andere schichtförmige Träger verwendet werden, die flüssigkristalline Phasen ausbilden, wie zum Beispiel Titanate<sup>[15b]</sup> und Antimonphosphate.<sup>[15c,e]</sup> Natürlich lässt sich dieses Konzept auch auf katalytisch attraktivere Legierungen aus Nanopartikeln ausweiten.<sup>[36]</sup>

### Danksagung

Diese Arbeit wurde von der Deutschen Forschungsgemeinschaft unterstützt (SFB 840, TP A2). K.A. dankt dem Elitenetzwerk Bayern für ein Promotionsstipendium und dem Elitestudiengang „Macromolecular Science“. Wir danken Lena Geiling für REM-Messungen und Marco Schwarzmann für die Präparation der Querschnitte für die TEM Messungen. Wir danken dem Keylab für Optische- und Elektronenmikroskopie des Bayerischen Polymerinstituts (BPI) für die Unterstützung. Wir danken Rhett Kempe für den Zugang zu seinem Mikroreaktor und dem BayCEER für die ICP-OES-Messung. Der XPS/UPS-Anlage (PHI 5000 VersaProbe III System) am Device Engineering Keylab des BPI wird gedankt und Michael Ertl für die Durchführung der Messungen. C.J.H. dankt für die Unterstützung durch die Czech Science Foundation (20-26767Y). Die Autoren danken auch für die finanzielle Unterstützung durch die Bayerisch-Tschechische Hochschulagentur im Rahmen des Projekts „Entwicklung und Designprinzipien für strukturierte Materialien“, das aus Mitteln des Freistaats Bayern finanziert wurde. Diese Arbeit wurde vom Ministerium für Bildung, Jugend und Sport aus dem Projekt „Große Infrastrukturen für Forschung, experimentelle Entwicklung und Innovationen“ e-Infrastructure CZ – LM2018140 gefördert. T.G. bedankt sich für die Förderung durch den Fonds zur Förderung der wissenschaftlichen Forschung (FWF) durch Projektnummer J4278. Open Access Veröffentlichung ermöglicht und organisiert durch Projekt DEAL.

### Interessenkonflikt

Die Autoren erklären, dass keine Interessenkonflikte vorliegen.

**Stichwörter:** CO-Oxidation · Metall-Träger-Wechselwirkung · Palladium · Schichtsilikat · Ultradünne Schichten

- [1] G. Pacchioni, H.-J. Freund, *Chem. Soc. Rev.* **2018**, *47*, 8474–8502.
- [2] a) T. W. van Deelen, C. Hernández Mejía, K. P. de Jong, *Nat. Catal.* **2019**, *2*, 955–970; b) C. T. Campbell, *Nat. Chem.* **2012**, *4*, 597–598.
- [3] a) M. Xu, S. He, H. Chen, G. Cui, L. Zheng, B. Wang, M. Wei, *ACS Catal.* **2017**, *7*, 7600–7609; b) F. Wang, W. Ueda, J. Xu, *Angew. Chem. Int. Ed.* **2012**, *51*, 3883–3887; *Angew. Chem.* **2012**, *124*, 3949–3953.
- [4] H. J. Freund, *J. Am. Chem. Soc.* **2016**, *138*, 8985–8996.
- [5] a) G. Pacchioni, H. Freund, *Chem. Rev.* **2013**, *113*, 4035–4072; b) L. Giordano, G. Pacchioni, *Acc. Chem. Res.* **2011**, *44*, 1244–1252.
- [6] a) S. Prada, U. Martinez, G. Pacchioni, *Phys. Rev. B* **2008**, *78*, 235423; b) L. Giordano, F. Cinquini, G. Pacchioni, *Phys. Rev. B* **2006**, *73*, 045414.
- [7] a) Y. Lykhach, S. M. Kozlov, T. Skala, A. Tovt, V. Stetsovych, N. Tsud, F. Dvorak, V. Johanek, A. Neitzel, J. Myslivecek, S. Fabris, V. Matolin, K. M. Neyman, J. Libuda, *Nat. Mater.* **2016**, *15*, 284–288; b) G. N. Vayssilov, Y. Lykhach, A. Migani, T. Staudt, G. P. Petrova, N. Tsud, T. Skala, A. Bruix, F. Illas, K. C. Prince, V. Matolin, K. M. Neyman, J. Libuda, *Nat. Mater.* **2011**, *10*, 310–315.
- [8] Y. Lykhach, J. Kubat, A. Neitzel, N. Tsud, M. Vorokhta, T. Skala, F. Dvorak, Y. Kosto, K. C. Prince, V. Matolin, V. Johanek, J. Myslivecek, J. Libuda, *J. Chem. Phys.* **2019**, *151*, 204703.
- [9] a) W. D. Schneider, M. Heyde, H. J. Freund, *Chem. Eur. J.* **2018**, *24*, 2317–2327; b) S. Shaikhutdinov, H. J. Freund, *J. Phys. Condens. Matter* **2015**, *27*, 443001; c) H. J. Freund, *Acc. Chem. Res.* **2017**, *50*, 446–449.
- [10] G. B. B. Varadawaj, K. M. Parida, *RSC Adv.* **2013**, *3*, 13583–13593.
- [11] a) G. M. Scheuermann, R. Thomann, R. Mülhaupt, *Catal. Lett.* **2009**, *132*, 355–362; b) M. Miyagawa, A. Shibusawa, K. Maeda, A. Tashiro, T. Sugai, H. Tanaka, *RSC Adv.* **2017**, *7*, 41896–41902; c) P. Upadhyay, V. Srivastava, *RSC Adv.* **2015**, *5*, 740–745.
- [12] I. Dékány, L. Turi, Z. Király, *Appl. Clay Sci.* **1999**, *15*, 221–239.
- [13] a) S. Papp, A. Szűcs, I. Dékány, *Appl. Clay Sci.* **2001**, *19*, 155–172; b) Z. Király, I. Dékány, A. Mastalir, M. Bartok, *J. Catal.* **1996**, *161*, 401–408.
- [14] A. Lerf, *Dalton Trans.* **2014**, *43*, 10276–10291.
- [15] a) L. J. Michot, I. Bihamnic, S. Maddi, S. S. Funari, C. Baravian, P. Levitz, P. Davidson, *Proc. Natl. Acad. Sci. USA* **2006**, *103*, 16101–16104; b) L. Wang, T. Sasaki, *Chem. Rev.* **2014**, *114*, 9455–9486; c) J. P. Gabriel, F. Camerel, B. J. Lemaire, H. Desvaux, P. Davidson, P. Batail, *Nature* **2001**, *413*, 504–508; d) Y. Liu, Z. Xu, W. Gao, Z. Cheng, C. Gao, *Adv. Mater.* **2017**, *29*, 1606794; e) P. Davidson, C. Penisson, D. Constantin, J. P. Gabriel, *Proc. Natl. Acad. Sci. USA* **2018**, *115*, 6662–6667.
- [16] a) M. Daab, N. J. Eichstaedt, C. Habel, S. Rosenfeldt, H. Kalo, H. Schiessling, S. Förster, J. Breu, *Langmuir* **2018**, *34*, 8215–8222; b) M. Daab, N. J. Eichstaedt, A. Edenhalter, S. Rosenfeldt, J. Breu, *RSC Adv.* **2018**, *8*, 28797–28803.
- [17] M. Stöter, D. A. Kunz, M. Schmidt, D. Hirsemann, H. Kalo, B. Putz, J. Senker, J. Breu, *Langmuir* **2013**, *29*, 1280–1285.
- [18] S. Rosenfeldt, M. Stöter, M. Schlenk, T. Martin, R. Q. Albuquerque, S. Förster, J. Breu, *Langmuir* **2016**, *32*, 10582–10588.

- [19] K. Sano, Y. S. Kim, Y. Ishida, Y. Ebina, T. Sasaki, T. Hikima, T. Aida, *Nat. Commun.* **2016**, *7*, 12559.
- [20] K. Ament, D. R. Wagner, F. E. Meij, F. E. Wagner, J. Breu, *Z. Anorg. Allg. Chem.* **2020**, *646*, 1110–1115.
- [21] E. Coronado, A. Ribera, J. García-Martínez, N. Linares, L. M. Liz-Marzán, *J. Mater. Chem.* **2008**, *18*, 5682.
- [22] H. J. Freund, G. Meijer, M. Scheffler, R. Schlögl, M. Wolf, *Angew. Chem. Int. Ed.* **2011**, *50*, 10064–10094; *Angew. Chem.* **2011**, *123*, 10242–10275.
- [23] a) Y. Zhou, Z. Wang, C. Liu, *Catal. Sci. Technol.* **2015**, *5*, 69–81; b) X. Liu, R. Wang, L. Song, H. He, G. Zhang, X. Zi, W. Qiu, *Catal. Commun.* **2014**, *46*, 213–218; c) E. J. Peterson, A. T. DeLaRiva, S. Lin, R. S. Johnson, H. Guo, J. T. Miller, J. Hun Kwak, C. H. Peden, B. Kiefer, L. F. Allard, F. H. Ribeiro, A. K. Datye, *Nat. Commun.* **2014**, *5*, 4885.
- [24] a) R. Wang, H. He, L.-C. Liu, H.-X. Dai, Z. Zhao, *Catal. Sci. Technol.* **2012**, *2*, 575–580; b) J.-N. Park, A. J. Forman, W. Tang, J. Cheng, Y.-S. Hu, H. Lin, E. W. McFarland, *Small* **2008**, *4*, 1694–1697; c) J. Xu, T. White, P. Li, C. He, J. Yu, W. Yuan, Y.-F. Han, *J. Am. Chem. Soc.* **2010**, *132*, 10398–10406.
- [25] R. Arrigo, M. E. Schuster, S. Abate, S. Wrabetz, K. Amakawa, D. Teschner, M. Freni, G. Centi, S. Perathoner, M. Havecker, R. Schlögl, *ChemSusChem* **2014**, *7*, 179–194.
- [26] a) N. S. Babu, N. L. Lingaiah, R. Gopinath, P. S. S. Reddy, P. S. S. Prasad, *J. Phys. Chem. C* **2007**, *111*, 6447–6453; b) B. Stasinska, A. Machocki, K. Antoniak, M. Rotko, J. L. Figueiredo, F. Gonçalves, *Catal. Today* **2008**, *137*, 329–334.
- [27] a) H. Wang, C.-j. Liu, *Appl. Catal. B* **2011**, *106*, 672–680; b) T. Cheng, J. Chen, A. Cai, J. Wang, H. Liu, Y. Hu, X. Bao, P. Yuan, *ACS Omega* **2018**, *3*, 6651–6659; c) G. Bektov, B. Heinrichs, J. P. Pirard, S. Chenakin, N. Kruse, *Appl. Surf. Sci.* **2013**, *287*, 293–298; d) T. H. Fleisch, R. F. Hicks, A. T. Bell, *J. Catal.* **1984**, *87*, 398–413; e) Y. Xu, J. Ma, Y. Xu, L. Xu, L. Xu, H. Li, H. Li, *RSC Adv.* **2013**, *3*, 851–858.
- [28] X. Wang, B. Chen, G. Chen, X. Sun, *RSC Adv.* **2016**, *6*, 87978–87987.
- [29] P. Begum, R. C. Deka, *ChemistrySelect* **2017**, *2*, 8847–8855.
- [30] B. Zhu, B. W. L. Jang, *J. Mol. Catal. A* **2014**, *395*, 137–144.
- [31] a) S. Bertarione, D. Scarano, A. Zecchina, V. Johánek, J. Hoffmann, S. Schauermann, M. M. Frank, J. Libuda, G. Rupprecht, H.-J. Freund, *J. Phys. Chem. B* **2004**, *108*, 3603–3613; b) K. Murata, E. Eleeda, J. Ohyama, Y. Yamamoto, S. Arai, A. Satsuma, *Phys. Chem. Chem. Phys.* **2019**, *21*, 18128–18137.
- [32] a) Y. Chen, O. Sakata, Y. Nanba, L. S. R. Kumara, A. Yang, C. Song, M. Koyama, G. Li, H. Kobayashi, H. Kitagawa, *Commun. Chem.* **2018**, *1*, 61; b) A. Nilsson, L. Pettersson, J. Norskov, *Chemical Bonding at Surfaces and Interfaces*, Elsevier, Amsterdam, **2008**.
- [33] a) M. T. Otten, B. Miner, J. H. Rask, P. R. Buseck, *Ultramicroscopy* **1985**, *18*, 285–289; b) H. Tan, J. Verbeek, A. Abakumov, G. Van Tendeloo, *Ultramicroscopy* **2012**, *116*, 24–33.
- [34] G. Li, H. Kobayashi, J. M. Taylor, R. Ikeda, Y. Kubota, K. Kato, M. Takaishi, T. Yamamoto, S. Toh, S. Matsumura, H. Kitagawa, *Nat. Mater.* **2014**, *13*, 802–806.
- [35] J. Hünn, C. Carrillo-Carrion, M. G. Soliman, C. Pfeiffer, D. Valdeperez, A. Masood, I. Chakraborty, L. Zhu, M. Gallego, Z. Yue, M. Carril, N. Feliu, A. Escudero, A. M. Alkilany, B. Pclaz, P. del Pino, W. J. Parak, *Chem. Mater.* **2017**, *29*, 399–461.
- [36] a) Y. H. Ahmad, A. T. Mohamed, K. A. Mahmoud, A. S. Aljaber, S. Y. Al-Qaradawi, *RSC Adv.* **2019**, *9*, 32928–32935; b) E. D. Goodman, S. Dai, A.-C. Yang, C. J. Wrasman, A. Gallo, S. R. Bare, A. S. Hoffman, T. F. Jaramillo, G. W. Graham, X. Pan, M. Cargnello, *ACS Catal.* **2017**, *7*, 4372–4380; c) B. Huang, H. Kobayashi, T. Yamamoto, S. Matsumura, Y. Nishida, K. Sato, K. Nagaoka, S. Kawaguchi, Y. Kubota, H. Kitagawa, *J. Am. Chem. Soc.* **2017**, *139*, 4643–4646; d) M. Armbrüster, *Sci. Technol. Adv. Mater.* **2020**, *21*, 303–322.

Manuscript erhalten: 12. November 2020

Akzeptierte Fassung online: 8. Dezember 2020

Endgültige Fassung online: 28. Januar 2021

### 6.2.3 Supporting Information



### Supporting Information

#### **Nanoparticles Supported on Sub-Nanometer Oxide Films: Scaling Model Systems to Bulk Materials**

*Kevin Ament, Nicolas Köwitsch, Dianwei Hou, Thomas Götsch, Jutta Kröhnert, Christopher J. Heard, Annette Trunschke, Thomas Lunkenbein, Marc Armbrüster, and Josef Breu\**

anie\_202015138\_sm\_miscellaneous\_information.pdf

### SUPPORTING INFORMATION

---

#### Table of Contents

- 1 Experimental Procedures
- 2 Results and Discussions
  - 2.1 Characterization of Pd nanoparticles
  - 2.2 PXRD of crystalline and nematic NaHec.
  - 2.3 Elemental analysis of Hec@Pd65@Hec
  - 2.4 XPS survey spectrum of Hec@Pd65@Hec
  - 2.5 Grayscale analysis of Pd layers in Hec@Pd65@Hec
  - 2.6 TE micrograph after prolonged heating
  - 2.7 Cross section of Hec@Pd72@Hec
  - 2.8 Physisorption isotherms
  - 2.9 Cycling test of Hec@Pd65@Hec
  - 2.10 Arrhenius plots
  - 2.11 Characterisation of reference catalysts
  - 2.12 XP spectra of Pd 3d region of reference materials
  - 2.13 Isotherms of CO chemisorbed to the Pd surface
  - 2.14 Additional computational information
  - 2.15 EEL spectroscopy at Si K edge
- 3 Author Contributions
- 4 References

#### 1 Experimental Procedures

##### Materials

PdCl<sub>2</sub> (99.999% Pd, Premion), NaCl, 4-Dimethylaminopyridine (DMAP), NaOH and NaBH<sub>4</sub> were purchased from Alfa Aesar. γ-Al<sub>2</sub>O<sub>3</sub> with high surface area was purchased from Alfa Aesar. The pellets were grounded to a powder before use. The used water was of MilliQ quality (18.2 MΩ).

##### Catalyst synthesis

###### Synthesis of Pd nanoparticles:

The synthesis of Pd nanoparticles was executed using a modified literature procedure.<sup>[1]</sup> Palladium(II) chloride (235 mg, 1.33 mmol) and Sodium chloride (155 mg, 2.66 mmol) were dissolved in 40 ml water and 4-Dimethylaminopyridine DMAP (833 mg, 6.82 mmol) in 80 mL water was added. After 20 min of stirring NaBH<sub>4</sub> (110 mg, 2.91 mmol) in 11 ml water was added dropwise under vigorous stirring resulting in a black dispersion. After 2 h the nanoparticle dispersion was dialyzed in 4 l water with water changes after 12 and 24 hours.

NaHec was synthesized via melt synthesis and is described elsewhere.<sup>[2]</sup>

###### Synthesis of Hec@Pd@Hec:

For the synthesis of the catalysts the Hectorite was delaminated to a 1.5 wt% dispersion to achieve a layer distance of about 60 nm. Both the aqueous particle and hectorite dispersions were adjusted with NaOH resulting in surface potentials of the nanoparticles of 28 mV or 22 mV, respectively. The nematic hectorite suspension was added rapidly to the nanoparticle dispersion under vigorous stirring. Visible flocculation appeared within 30 seconds. The black flocculate was separated from the supernatant by centrifugation. DMAP was removed by repeated washing cycles. Finally, the catalysts were freeze dried to obtain a fluffy powder.

### SUPPORTING INFORMATION

#### Synthesis of Pd<sub>ext</sub>Hec:

To a dispersion of Pd nanoparticles (1 mg/ml) crystalline NaHec was added under stirring. After 24 h the resulting black solid was separated by centrifugation and washed several times. The catalyst was freeze dried to obtain a fluffy powder.

#### Synthesis of Pd<sub>ext</sub>Al<sub>2</sub>O<sub>3</sub>:

To a dispersion of Pd nanoparticles (1 mg/ml) was added  $\gamma$ -Al<sub>2</sub>O<sub>3</sub> under stirring. The solvent was slowly removed under stirring at 80 °C. The catalyst was finally dried at 130 °C.

#### Measurement and Characterization Techniques

Dynamic light scattering (DLS) and determination of  $\zeta$ -potential were recorded on a Litesizer 500 (Anton-Paar). CHN analysis was acquired with an Elementar Vario EL III.

Powder X-ray diffraction (PXRD) measurements were done using a STOE Stadi P diffractometer. Cu<sub>Kα1</sub> radiation and a Mythen 1K silicon strip-detector were used. PXRD of traces of textured samples were recorded on a Bragg-Brentano type diffractometer (Empyrean, PANalytical) with nickel filter and Cu<sub>Kα</sub> radiation ( $\lambda = 1.54187 \text{ \AA}$ ).

SAXS data were measured using a "Double Ganesha AIR" system (SAXSLAB, Denmark). The X-ray source of this laboratory-based system is a rotating anode (copper, MicroMax 007HF, Rigaku Corporation, Japan) providing a microfocused beam. The data was recorded by a position sensitive detector (PILATUS 300 K, Dectris)

Transmission electron microscopy (TEM) images were acquired using a JEOL JEM-2200FS (200 kV). For cross sectional TEM the powder was embedded into a resin (EPO-TEK 301) and was cut with an Ar beam into thin slices using a Jeol Cryo Ion Slicer. Scanning electron microscopy (SEM) images and energy dispersive spectroscopy (EDS) were recorded on a FEI Quanta FEG 250.

Photoelectron spectroscopy (XPS) was conducted on a PHI 5000 Versa Probe III fitted with an Al K $\alpha$  excitation source and spectra were analyzed with Multipak software pack. Spectra were referenced to C 1s at 284.8 eV.

Electron energy loss spectroscopy (EELS) measurements were conducted using a double-corrected JEOL JEM-ARM200F microscope, operated at 200 kV and equipped with a Gatan GIF Quantum imaging filter with DualEELS capabilities. Plural scattering was removed from all spectra by Fourier ratio deconvolution.

Adsorption isotherms were recorded on a Quantachrome Autosorb-1 with Ar as adsorbate at 87 K. The isotherms were evaluated using Brunauer-Emmett-Teller (BET) method and pore size distribution was evaluated with NLDFT. Metal surface was acquired with a Quantachrome Autosorb-1 with CO at 35 °C using the double isotherm method.

To determine the elemental composition, to about 20 mg of the sample was added a mixture of 1.5 mL 30 wt% HCl (Merck), 0.5 mL of 85 wt% H<sub>3</sub>PO<sub>4</sub> (Merck), 0.5 mL 65 wt% HNO<sub>3</sub> (Merck) and 1 mL of 48 wt% HBF<sub>4</sub> (Merck). The sample was digested in a MLS 1200 Mega microwave digestion apparatus for 6.5 min and heated at 600W (MLS GmbH). The sample was allowed to cool to room temperature and the clear solution was diluted to 100 mL and analyzed with a Varian Vista-Pro radial ICP-OES.

Diffuse reflectance infrared Fourier transform (DRIFT) spectra were collected on a Cary 680 FTIR spectrometer from Agilent equipped with a MCT detector and a Praying Mantis™ low temperature reaction cell from Harrick. Spectra were recorded at a spectral resolution of 2 cm<sup>-1</sup> and accumulation of 1024 scans. Samples were dried at 130 °C under a flow of Ar (50 ml/min) over night and then reduced at 150 °C under a flow of H<sub>2</sub> (10 vol%) for 1 h. To remove H<sub>2</sub> the samples were evacuated at 150 °C for 30 min and then let allow to cool to room temperature. Spectra were taken at 300 K. CO isotherms were recorded by dosing CO at increasing equilibrium pressures ranging from 0.03 to 60 mbar. The spectra are presented in Kubelka-Munk units  $F(R_\infty) = (1 - R_\infty)^2/2R_\infty$

#### Catalysis

Catalytic tests were conducted in a fixed bed micro reactor with an internal diameter of 4 mm. The desired amount of catalyst was mixed with quartz to achieve an overall loading of 500 mg. The reactor was heated using a circular kiln. To record light-off curves the temperature was raised in 10 °C steps and the temperature was held for 12 min before analysis. A reactant mixture of 1 vol% CO, 1 vol% O<sub>2</sub> und 98 vol% nitrogen with a constant flow of 50 ml/min under atmospheric pressure was injected into the reactor. The composition of the gas mixture leaving the reactor was monitored using an Agilent 6890N gas chromatograph equipped with a 30 m GS CARBONPLOT column and a thermal conductivity detector. Prior to catalysis, the catalyst was conditioned for 2 h in the reactant mixture stream at 200 °C for 2 h.

#### Computational Models and Methods

##### Method

Geometry optimisation and calculation of activation energies for CO oxidation were performed using the periodic density functional method within the VASP 5.4 package,<sup>[3]</sup> employing the projector augmented-wave method,<sup>[4]</sup> and the Perdew-Burke-Ernzerhof exchange-correlation functional<sup>[5]</sup> with Grimme's D3 dispersion correction<sup>[6]</sup> and BJ damping.<sup>[7]</sup> The wavefunction expansion was truncated at 400 eV, and the Brillouin zone was approximated by the Gamma point only (except in slab calculations, for which a 4x4x1 Monkhorst-Pack<sup>[8]</sup> k point grid was employed). Electronic and force convergence criteria for local geometry optimization were set to 1x10<sup>-6</sup> eV and 2x10<sup>-2</sup> eV/ $\text{\AA}$ , respectively. Gaussian smearing was included, with a smearing width of 0.1 eV. All calculations were performed spin-unpolarized, except for the case of molecular oxygen, which exhibits a triplet ground state. Dipolar corrections to the energy were included in all three dimensions. The electrostatic potential was verified to converge to a stable vacuum level for each charged particle system, in order to ensure spurious electrostatic effects between images were avoided.

WILEY-VCH

### SUPPORTING INFORMATION

To model the palladium nanoparticles in experiment, unsupported icosahedral palladium nanoparticles comprising 147 atoms (approx. 1.5 nm diameter) were generated within a cubic box of 25x25x25 Å. The structure of the particle was locally optimised for each charge state, from initial structures for which the surface Pd-Pd distances were approximately 2.75 Å; in-line with the extended (111) surface nearest-neighbour distance. This nanoparticle model includes (111) microfacets, and contains all important CO adsorption sites (top, bridge, fcc hollow and hcp hollow) that are appropriate for a pristine (111) surface or larger nanoparticle. The model therefore approximates the effects of surface undercoordination and curvature appropriate for the experimental 3.5 nm particle. The charged nanoparticles were generated via explicit removal of electrons corresponding to a per-Pd charge of +0.01e-, +0.03e- and +0.05e- (one, four and seven electrons removed, respectively). Adsorption was modelled by the addition of a single adsorbate to the pristine nanoparticle, to the hcp hollow site closest to the centre of a (111) microfacet. Adsorption energies of adsorbates CO ( $E_{ads}(CO)$ ) and atomic O ( $E_{ads}(O)$ ) were calculated according to the following equations,

$$E_{ads}(CO) = E(CO@Pd147) - E(Pd147) - E(CO)(g)$$

$$E_{ads}(O) = E(O@Pd147) - E(Pd147) - 0.5 E(O2)(g)$$

where the isolated Pd147 particle and CO ( $r_{C-O} = 1.14 \text{ \AA}$ ) and O<sub>2</sub> ( $r_{O-O} = 1.23 \text{ \AA}$ ) molecules are calculated in the same cubic cell. The molecular oxygen reference was calculated with spin polarization, to account for the triplet oxygen ground state.

## SUPPORTING INFORMATION

## 2 Results and Discussion

## 2.1 Characterization of Pd nanoparticles

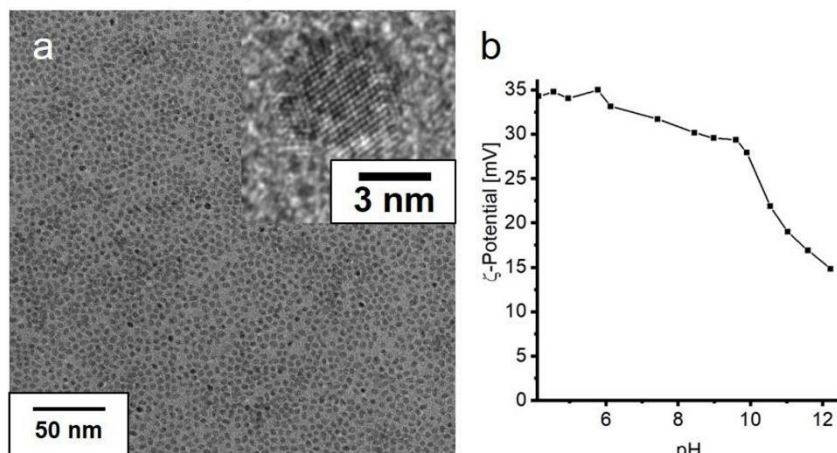


Figure S1. a) TEM image of monodisperse Pd nanoparticles. Inset: High magnification image. b)  $\zeta$ -Potential versus pH for DMAP stabilized Pd nanoparticles in 0.1M NaCl solution. Below a pH of 5 the nanoparticles aggregated quickly due to the protonation of the amino function of DMAP.

## 2.2 SAXS of nematic NaHec

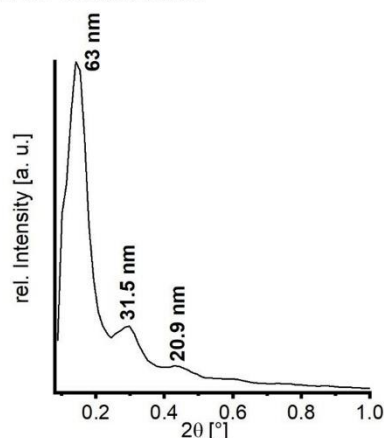


Figure S2. SAXS of a 1.5 wt% swollen nematic NaHec phase.

## SUPPORTING INFORMATION

## 2.3 Elemental analysis of Hec@Pd65@Hec

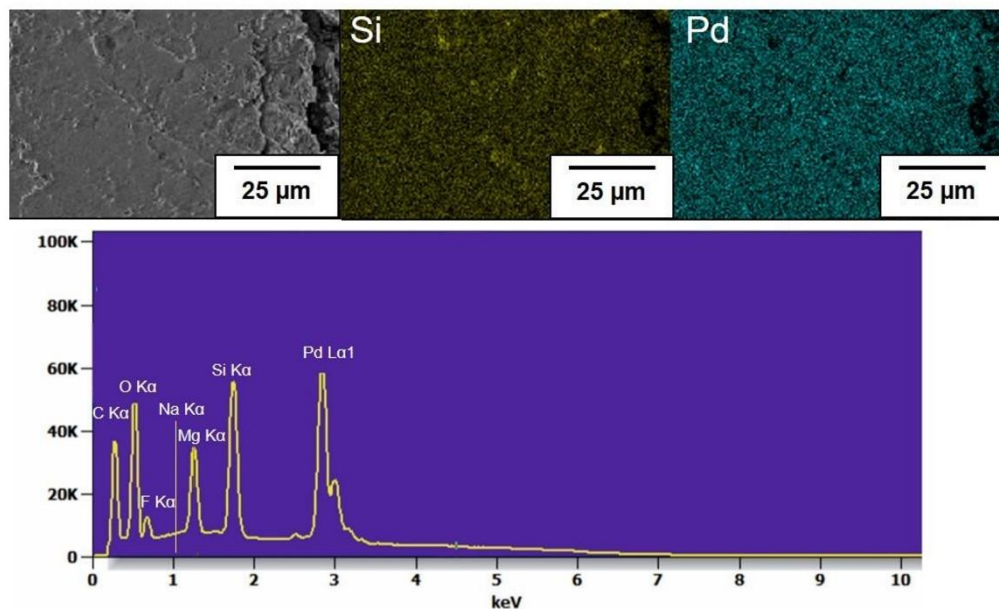


Figure S3. SEM-EDS elemental mapping of Hec@Pd65@Hec.

Table S1: Results of CHN analysis after washing.

Sample	Fraction of C [wt%]	Fraction of H [wt%]	Fraction of N [wt%]
Hec@Pd65@Hec	0.03	0.0	0.00
Pd@Hec72@Hec	0.04	0.0	0.02

SUPPORTING INFORMATION

2.4 XPS survey spectrum of Hec@Pd65@Hec.

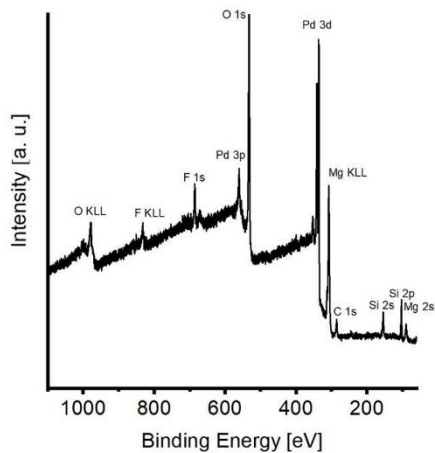


Figure S4. XPS survey spectrum of Hec@Pd65@Hec.

2.5 Grayscale analysis of Pd layers in Hec@Pd65@Hec

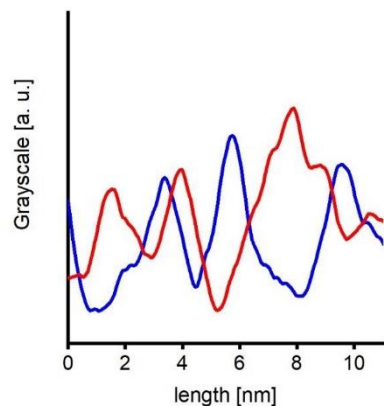


Figure S5. Grayscale analysis of two adjacent monolayers of Hec@Pd65@Hec separated by one nanosheet. It can be observed that nanoparticles of adjacent layers are shifted against each other.

SUPPORTING INFORMATION

---

2.6 TE micrograph after prolonged heating

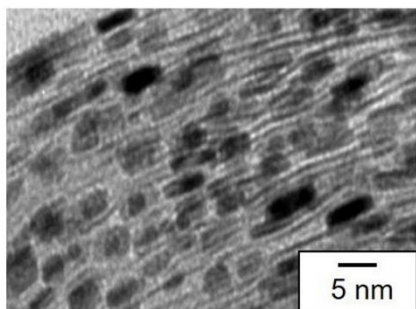


Figure S6. TE micrograph of Hec@Pd65@Hec after heating to 700 °C in Ar atmosphere for 10 h.

2.7 Cross section of Hec@Pd72@Hec

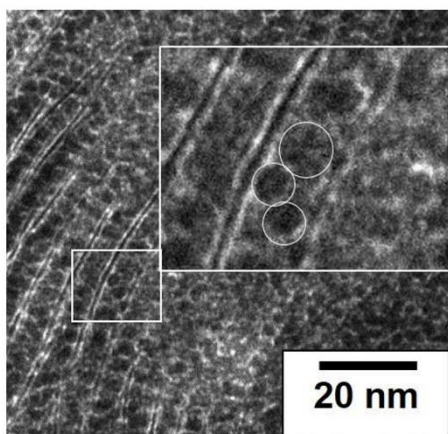
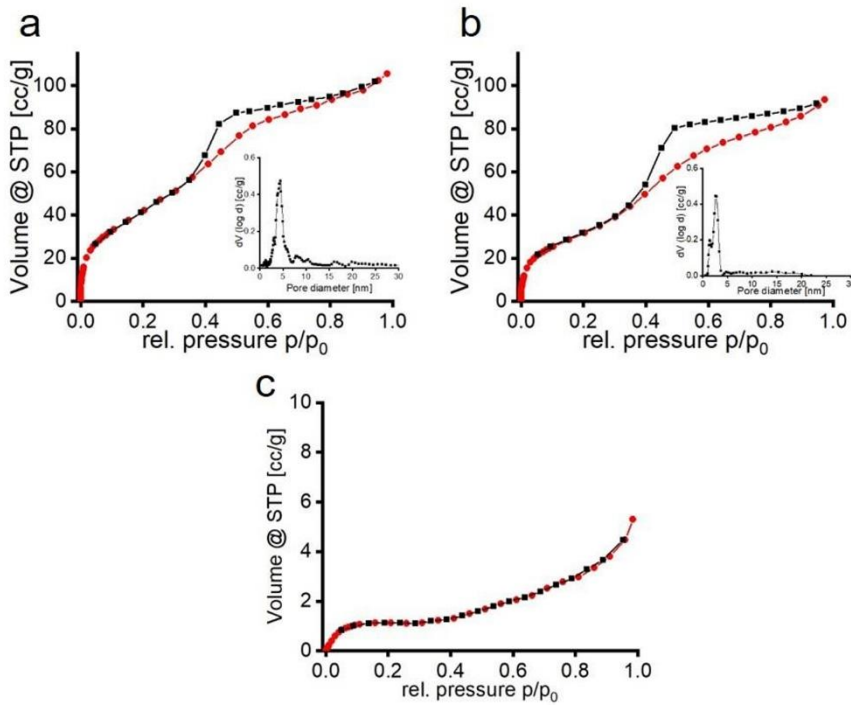


Figure S7. TE micrograph of cross section of Hec@Pd72@Hec showing domains with double layers of nanoparticles between the nanosheets.

## SUPPORTING INFORMATION

## 2.8 Physisorption isotherms



**Figure S8.** Ar-Isotherms and pore size distribution of a) Hec@Pd65@Hec, b) Hec@Pd72@Hec, and c) pristine NaHec. Hec@Pd@Hec samples show type IV(a) isotherms that correspond to a mesoporous network. The shape of the hysteresis can be attributed to the H2(b) type. This type of hysteresis in the desorption branch normally occurs due to pore necks of a larger size distribution. The distance of the particles can be seen as necks between the pores. As the particles have a size distribution, different sized necks are comprehensible.<sup>[9]</sup>

SUPPORTING INFORMATION

---

2.9 Cycling test of Hec@Pd65@Hec

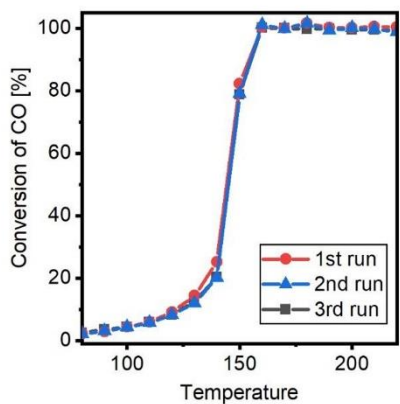


Figure S9. Cycling test of three runs of Hec@Pd65@Hec.

2.10 Arrhenius plots

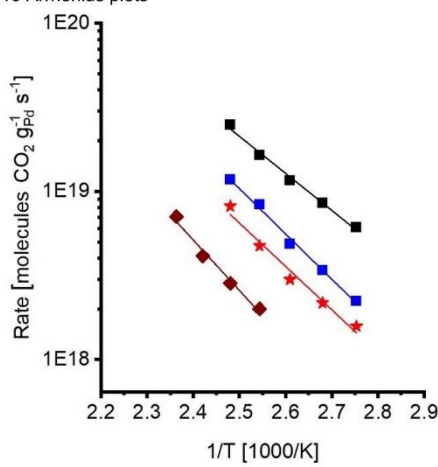


Figure S10. Arrhenius plot of Hec@Pd65@Hec (black), Hec@Pd72@Hec (blue), Pd<sub>ext</sub>@Hec (red), and Pd<sub>ext</sub>@Al<sub>2</sub>O<sub>3</sub> (brown).

## SUPPORTING INFORMATION

## 2.11 Characterization of reference catalysts

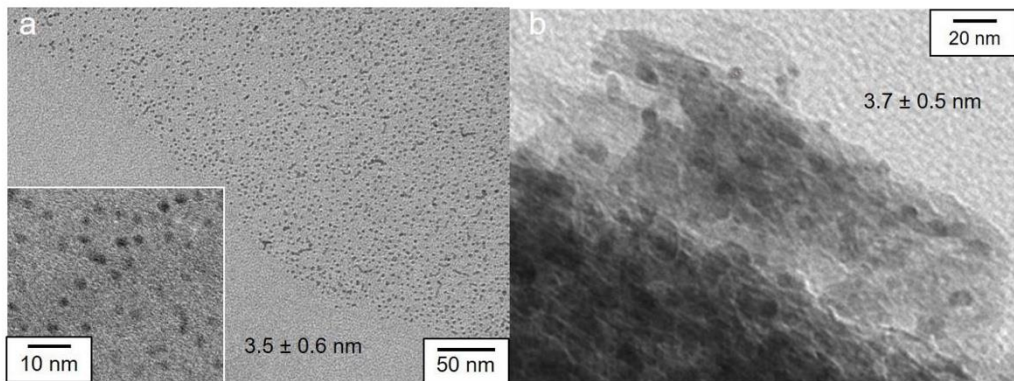


Figure S11. TE micrographs of a)  $\text{Pd}_{\text{ex}}@\text{Hec}$ , and b)  $\text{Pd}_{\text{ex}}@\text{Al}_2\text{O}_3$

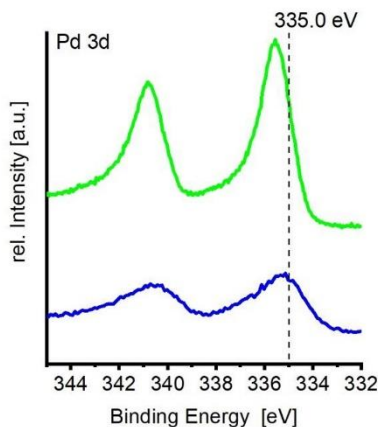
Table S2. Characterization of reference materials.

Sample	Loading [wt%] <sup>a</sup>	$S_{\text{BET}}$ [ $\text{m}^2/\text{g}$ ] <sup>b</sup>	Pore size [nm] <sup>b</sup>	Average Pd size [nm] <sup>c</sup>	Metal dispersion [%] <sup>d</sup>
$\text{Pd}_{\text{ex}}@\text{Al}_2\text{O}_3$	0.97	156	7.6	$3.7 \pm 0.5$	22.7
$\text{Pd}_{\text{ex}}@\text{Hec}$	0.98	4.7	/	$3.5 \pm 0.6$	19.6

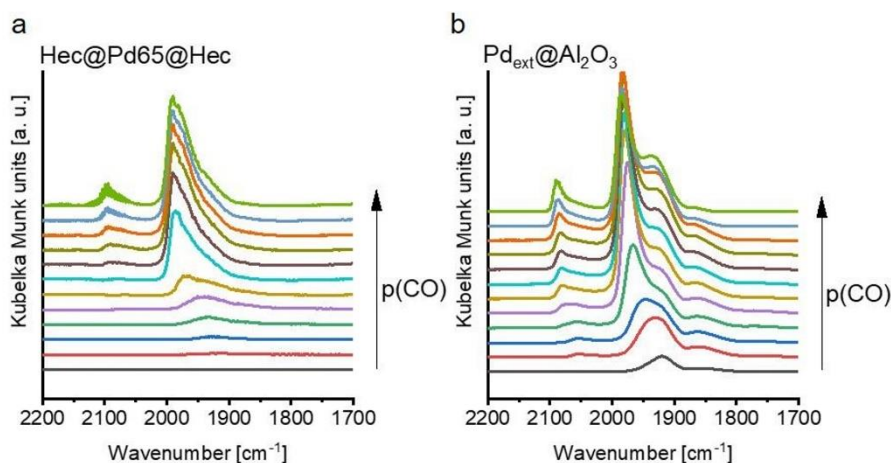
[a] determined by ICP-OES, [b] determined by Ar physisorption at 87 K, [c] core sized determined by TEM, [d] determined by CO double isotherm method.

## SUPPORTING INFORMATION

## 2.12 XP spectra of Pd 3d region of reference materials

Figure S12. XP spectra of Pd 3d region of  $\text{Pd}_{\text{ext}}@\text{Hec}$  (blue) and  $\text{Hec}@\text{Pd72}@\text{Hec}$  (green).

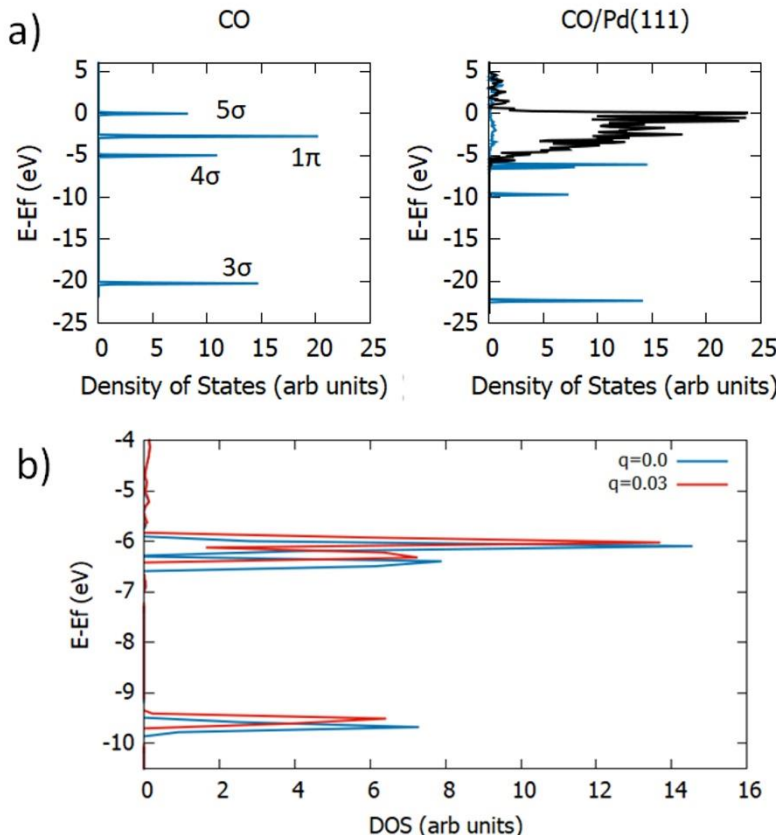
## 2.13 Isotherms of CO chemisorbed to the Pd surface

Figure S13. DRIFT spectra of CO-stretching vibration recorded at increasing CO equilibrium pressure of a)  $\text{Hec}@\text{Pd65}@\text{Hec}$  and b)  $\text{Pd}_{\text{ext}}@\text{Al}_2\text{O}_3$ .

## SUPPORTING INFORMATION

2.14 Additional computational information

## Electronic Density of States



**Figure S14.** a) Projected density of states for an isolated CO molecule and CO upon adsorption to neutral Pd hcp site at low coverage. CO s/p states have blue colour Pd d states have black colour. b) CO s/p states upon adsorption to neutral and charged Pd ( $q=0.03$ /atom).

The electronic structure of isolated and adsorbed CO is calculated within VASP, by projection of the electronic density of states onto atomic orbitals and separated into single atom contributions. The free CO molecule shows the hybridization of atomic orbitals into  $\sigma$  and  $\pi$  molecular orbital (MO) channels. Adsorption to the Pd surface induces an energetic downshift of adsorbate states and hybridization of the orbitals with the Pd s/d band. Figure S9a shows the full s/p states of CO and the d orbitals of Pd. Increasing Pd electron depletion leads to a relative upshift in CO adsorbate electronic states with respect to the Fermi energy. Figure S9b shows the upshift of states originating from CO  $4\sigma$  and  $1\pi$  orbitals.

## SUPPORTING INFORMATION

## Surface Calculations

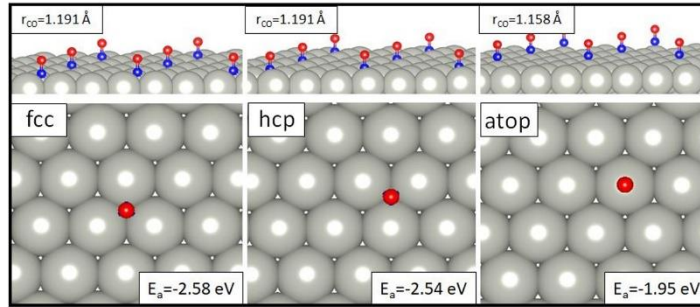


**Figure S15.** Adsorption energies of CO on the Pd(111) surface in fcc, hcp and top sites at a coverage of 1/9.

In order to identify the effect of undercoordination and cluster curvature on the adsorption properties on Pd, we calculated the adsorption of CO upon a pristine (111) surface. On the surface, the CO molecule was found to prefer hollow sites to top sites, while bridge sites were not found to be stable with respect to barrierless migration to a hollow site. Therefore, upon the nanoparticle only hollow sites were considered, with hcp hollows always found to be preferred over fcc sites. The adsorption is found to be moderately enhanced upon the nanoparticle, by less than 0.1 eV. Hence the 1.5 nm nanoparticle is a good approximation to the pristine extended surface, and therefore for the 3.5 nm nanoparticle in experiment.

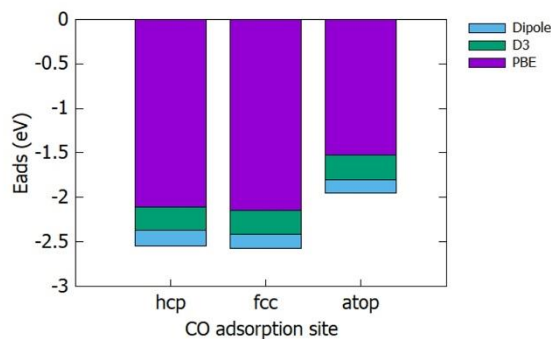


**Figure S16.** Energetic contributions to CO adsorption energy upon Pd(111). The dipole and D3 dispersion corrections provide a constant stabilisation for hcp, fcc and top adsorption modes.

The various contributions to adsorption energy are separated for a model of low-coverage CO adsorption on the pristine, neutral Pd(111) surface ( $\theta = 1/9$ ). Dispersion and dipolar corrections are found to provide a near-constant addition to adsorption energy of -0.27 eV and -0.16 eV, respectively, irrespective of adsorption mode. Neglect of these contributions gives GGA-only adsorption energies of -2.14 eV, -2.11 eV and -1.52 eV in fcc, hcp and top sites, respectively: in accord with literature values at the same level of theory.<sup>[10]</sup>

## SUPPORTING INFORMATION

## Coverage Effects

The role of particle charge in affecting the lateral repulsion between adsorbates was investigated. The coverage dependence of CO and O adsorption was modelled by occupation of a single (111) microfacet of Pd147 by adsorbates, in the range  $\theta = 0.1 - 0.6$  (between one and six adsorbates upon one microfacet). It is known that the preferred adsorption mode for CO varies with coverage. However, as the aim is to identify the effect of charge on energetic trends, rather than to locate the optimal adsorbate surface structure, hcp hollow sites were chosen as occupation sites for both species at all coverages. Increasing particle charge weakens the adsorption for all coverages of CO, with a constant upward shift in  $E_{ads}$ . For O adsorption, the destabilisation of O on the surface is a stronger function of coverage than CO. Additionally, the trend as a function of charge is different between CO and O. While CO is destabilised in a constant manner, oxygen is found to exhibit a charge effect, in which higher excess positive charge leads to a stronger destabilisation.

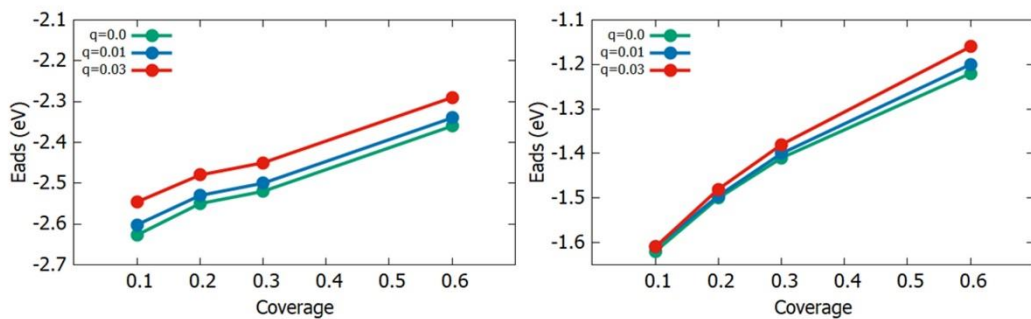


Figure S17. Coverage dependence of CO (left) and O (right) adsorption energies as a function of nanoparticle charge/Pd atom.

## 2.15 EEL spectroscopy at Si K edge

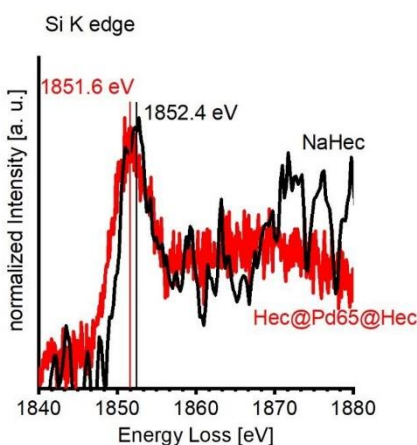


Figure S18. ELL spectra at the Si K edge of NaHec (black) and Hec@Pd65@Hec (red).

### SUPPORTING INFORMATION

---

#### 3 Author Contributions

Kevin Ament designed and performed the experiments, characterized the catalysts and evaluated the data. Kevin Ament and Josef Breu wrote the manuscript. Nicolas Kowitzch and Marc Armbrüster supported the evaluation of the conducted catalytic experiments and assisted with the writing of the manuscript. Dianwei Hou and Christopher J. Heard did the computational investigation and wrote this part of the manuscript. Thomas Götsch und Thomas Lunkenbein performed EELS. Jutta Kröhnert performed DRIFTS measurements and Annette Trunschke assisted with interpretation and commented on the manuscript.

#### 4 References

- [1] K. A. Flanagan, J. A. Sullivan, H. Müller-Bunz, *Langmuir* **2007**, *23*, 12508-12520.
- [2] M. Stöter, D. A. Kunz, M. Schmidt, D. Hirsemann, H. Kalo, B. Putz, J. Senker, J. Breu, *Langmuir* **2013**, *29*, 1280-1285.
- [3] a) G. Kresse, J. Hafner, *Phys. Rev. B* **1993**, *47*, 558; b) G. Kresse, J. Hafner, *Phys. Rev. B* **1994**, *49*, 14251; c) G. Kresse, J. Furthmüller, *Computational Materials Science* **1996**, *6*, 15; d) G. Kresse, J. Furthmüller, *Phys. Rev. B* **1996**, *54*, 11169.
- [4] P. E. Blöchl, *Phys. Rev. B* **1994**, *50*, 17953.
- [5] J. P. Perdew, K. Burke, M. Ernzerhof, *Phys. Rev. Lett.* **1997**, *78*, 1396.
- [6] S. Grimme, J. Antony, S. Ehrlich, H. Krieg, *The Journal of Chemical Physics* **2010**, *132*, 154104.
- [7] S. Grimme, S. Ehrlich, L. Goerigk, *J. Comput. Chem.* **2011**, *32*, 1456.
- [8] H. J. Monkhorst, J. D. Pack, *Phys. Rev. B* **1976**, *13*, 5188.
- [9] M. Thommes, K. Kaneko, A. V. Neimark, J. P. Olivier, F. Rodriguez-Reinoso, J. Rouquerol, K. S. W. Sing, *Pure Appl. Chem.* **2015**, *87*, 1051-1069.
- [10] a) C. J. Zhang, P. Hu, *Journal of the American Chemical Society* **2001**, *123*, 1166-1172; b) Z. Duan, G. Henkelman, *ACS Catalysis* **2014**, *4*, 3435-3443; c) N. M. Martin, M. Van den Bossche, H. Grönbeck, C. Hakanooglu, F. Zhang, T. Li, J. Gustafson, J. F. Weaver, E. Lundgren, *The Journal of Physical Chemistry C* **2014**, *118*, 1118-1128; d) Z. Hooshmand, D. Le, T. S. Rahman, *Surface Science* **2017**, *655*, 7-11.

### 6.3 Enhancing Hydrogen Storage Capacity of Pd Nanoparticles by Sandwiching between Inorganic Nanosheets

#### Enhancing Hydrogen Storage Capacity of Pd Nanoparticles by Sandwiching between Inorganic Nanosheets

Kevin Ament<sup>[a, b]</sup>, Hirokazu Kobayashi<sup>[c]</sup>, Kohei Kusada<sup>[c,d]</sup>, Josef Breu<sup>[a, b]\*</sup>, and Hiroshi Kitagawa<sup>[c]\*</sup>

*Zeitschrift für Anorganische und Allgemeine Chemie* **2022**, e202100370

Impact Factor (2017): 1.179

<https://doi.org/10.1002/zaac.202100370>

Reprinted under the terms of CC BY 4.0 license (<https://creativecommons.org/licenses/by/4.0/legalcode>)  
© 2022 The Authors. Zeitschrift für anorganische und allgemeine Chemie published by Wiley-VCH GmbH

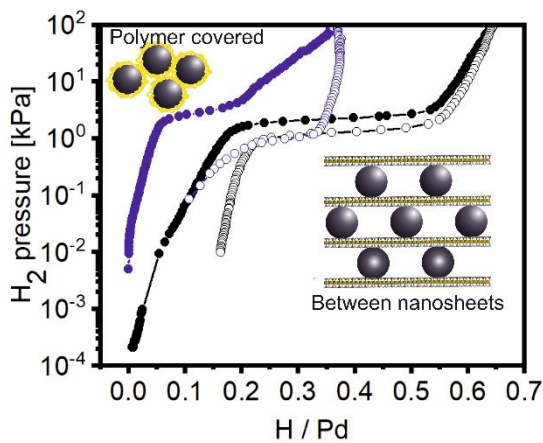
[a] Bavarian Polymer Institute, University of Bayreuth, Universitätsstraße 30, 95447 Bayreuth (Germany)

[b] Department of Chemistry, University of Bayreuth, Universitätsstraße 30, 95447 Bayreuth (Germany)

[c] Division of Chemistry, Graduate School of Science, Kyoto University, Kitashirakawa-Oiwakecho, Sakyo-Ku, Kyoto 606-8502 (Japan)

[d] The Hakubi Center for Advanced Research, Kyoto University, Kitashirakawa-Oiwakecho, Sakyo-Ku, Kyoto 606-8502 (Japan)

\* E-mail: josef.breu@uni-bayreuth.de, kitagawa@kuchem.kyoto-u.ac.jp



#### Individual Contribution:

The concept of the publication was developed by Prof J. Breu, Prof H. Kitagawa and me. The manuscript was written by Prof J. Breu and me. H. Kobayashi and H. Kitagawa commented on the manuscript. I synthesized and characterized the samples that were applied for H<sub>2</sub> sorption. I was invited to Kyoto University by Prof Kitagawa to perform the PC isotherm measurements together with H. Kobayashi and K. Kusada. H. Kobayashi conducted *in situ* XRD at SPRing-8.

My contribution to the manuscript is approx. 75 %.

DOI: 10.1002/zaac.202100370

## Enhancing Hydrogen Storage Capacity of Pd Nanoparticles by Sandwiching between Inorganic Nanosheets

Kevin Ament,<sup>[a, b]</sup> Hirokazu Kobayashi,<sup>[c]</sup> Kohei Kusada,<sup>[c, d]</sup> Josef Breu,<sup>\*[a, b]</sup> and Hiroshi Kitagawa<sup>\*[c]</sup>

Dedicated to Prof. Dr. Caroline Röhr on the Occasion of her 60<sup>th</sup> Birthday.

H<sub>2</sub> is regarded to play a crucial role in the transition from a fossil fuel-based energy economy towards an environmentally friendly one. However, storage of H<sub>2</sub> is still challenging, but palladium (Pd) based materials show exciting properties. Therefore, nanoparticulate Pd has been intensely studied for hydrogen storage in the past years. Here, we stabilize Pd nanoparticles by intercalation between inorganic nanosheets of hectorite (NaHec). Compared to nanoparticles stabilized by the polymer polyvinylpyrrolidone (PVP), the H<sub>2</sub> storage capacity was

found to be 86% higher for identical Pd nanoparticles being intercalated between nanosheets. We attribute this remarkably enhanced H<sub>2</sub> storage capacity to the partial oxidation of Pd, as evidenced by X-ray photoelectron spectroscopy (XPS). The higher amount of holes in the 4d band leads to a higher amount of H<sub>2</sub> that can be absorbed when Pd is stabilized between the nanosheets of hectorite compared to the PVP stabilized nanoparticles.

### Introduction

H<sub>2</sub> is of industrial importance, e.g. for hydrogenation reactions, synthesis of ammonia or oil refining.<sup>[1]</sup> Furthermore, interest has emerged in hydrogen as a clean energy source, e.g. for fuel cells.<sup>[2]</sup> These applications require reliable storage of H<sub>2</sub>. Materials with a high surface area that can bind H<sub>2</sub> physically, such as carbon materials (activated carbon, nanotubes, nanofibers)<sup>[3]</sup> or metal-organic frameworks<sup>[4]</sup> require typically low temperatures or high pressures.<sup>[5]</sup> Materials capable of binding hydrogen chemically are metal hydrides<sup>[6]</sup> (MgH<sub>2</sub>) or complex hydrides<sup>[7]</sup> (NaBH<sub>4</sub>), but these hydrides require high

temperatures to release H<sub>2</sub>. Transition metals represent another interesting class of hydrogen storage materials as they possess a high density of states (DOS) near the Fermi level. Among them, Pd is known to absorb high volumes of H<sub>2</sub> at ambient pressure and temperature.<sup>[8]</sup> The amount of hydrogen that can be absorbed is closely related to holes in the 4d band as the Pd–H bond is created by electron transfer of H 1s electrons to these holes.<sup>[9]</sup>

Nanoparticles show significantly altered physical and chemical properties<sup>[10]</sup> compared to their bulk counterparts, such as improved catalytic activity<sup>[11]</sup> or melting point depression.<sup>[12]</sup> Nano-sizing and confinement was recognized for complex metal hydrides to improve hydrogen uptake properties.<sup>[13]</sup> When complex metal hydride nanoparticles were incorporated into the pores of SBA-15<sup>[14]</sup> or nanoporous carbon<sup>[15]</sup> not only stability of the nanoparticles, but also the kinetics of H<sub>2</sub> uptake and release or thermodynamic phase stabilities at given H<sub>2</sub> pressure and temperatures were changed.

The nano-size effect on the H<sub>2</sub> storage behaviour of Pd nanoparticles was thoroughly investigated applying polyvinylpyrrolidone (PVP) covered nanoparticles. The polymeric capping ligand inhibited agglomeration while allowing H<sub>2</sub> to access the surface.<sup>[16]</sup> Nanoparticles of Pd demonstrated a clear size-dependent effect.<sup>[17]</sup> With decreasing size, the maximum H<sub>2</sub> absorption decreases accompanied by a narrowing of the two-phase region (coexistence phase of  $\alpha$  and  $\beta$ ) compared to bulk Pd. Alternatively, the storage capacity of Pd nanoparticles was improved by tuning their electronic structure. In this line, the H<sub>2</sub> storage capacity of nanoparticulate Pd cubes could be doubled by covering them with the metal-organic framework (MOF) HKUST-1 (copper(II) 1,3,5-benzenetricarboxylate).<sup>[18]</sup> The improvement of H<sub>2</sub> storage capacity was rationalized by a charge transfer from the Pd nanocubes to Cu–O groups of the MOF, which increases the number of holes in the 4d band.<sup>[9]</sup>

[a] K. Ament, Prof. Dr. J. Breu  
Bavarian Polymer Institute, University of Bayreuth,  
Universitätstraße 30, 95447 Bayreuth (Germany)  
E-mail: josef.breu@uni-bayreuth.de

[b] K. Ament, Prof. Dr. J. Breu  
Department of Chemistry, University of Bayreuth,  
Universitätstraße 30, 95447 Bayreuth (Germany)

[c] H. Kobayashi, K. Kusada, Prof. H. Kitagawa  
Division of Chemistry, Graduate School of Science,  
Kyoto University,  
Kitashirakawa-Oiwakecho, Sakyo-ku, Kyoto 606-8502 (Japan)  
E-mail: kitagawa@kuchem.kyoto-u.ac.jp

[d] K. Kusada  
The Hakubi Center for Advanced Research,  
Kyoto University,  
Kitashirakawa-Oiwakecho, Sakyo-ku, Kyoto, 606-8502 (Japan)

Supporting information for this article is available on the WWW under <https://doi.org/10.1002/zaac.202100370>

© 2022 The Authors. Zeitschrift für anorganische und allgemeine Chemie published by Wiley-VCH GmbH. This is an open access article under the terms of the Creative Commons Attribution License, which permits use, distribution and reproduction in any medium, provided the original work is properly cited.

Recently, Pd nanoparticles were intercalated between the nanosheets of synthetic hectorite ( $\text{NaHec}$ ,  $\text{Na}_{0.5}\text{Mg}_{2.5}\text{Li}_{0.5}\text{Si}_4\text{O}_{10}\text{F}_3$ ). NaHec is a 2 dimensional (2D) 2:1 layered silicate. The synthetic procedure involving melt synthesis and thermal annealing grants access to a phase pure material with a 3 dimensional crystalline order.<sup>[19]</sup> This makes the material more favourable for systematic studies over natural materials as it possess little defects and no impurities. Furthermore, the synthetic hectorite is a fluorohectorite. This renders this clay structure stable up to 750 °C.<sup>[20]</sup> As the silicate nanosheets carry a high permanent negative charge  $\text{Na}^+$  ions are located between these nanosheets to grant charge balance.<sup>[19b]</sup> When immersed in water, the nanosheets delaminate by repulsive osmotic swelling into individual nanosheets with a thickness of 9.6 Å.<sup>[21]</sup> The electrostatic repulsion and a large diameter of  $\approx 20000$  nm hold the nanosheets in a co-facial alignment even at high dilutions, forming a nematic liquid crystalline phase. This nematic phase was used to intercalate nanoparticles with a positive  $\zeta$  potential between the nanosheets to create a porous structure as sketched in Scheme S1.<sup>[22]</sup> The confinement between negatively charged nanosheets forces the Pd nanoparticles to be positively charged to balance the charge. Furthermore, the nanosheets even accept additional negative charge beyond what is expected for charge balancing of pristine NaHec as evidenced by electron energy loss spectroscopy (EELS) of Si.<sup>[22]</sup> Similar to what was reported for HKUST-1 embedded Pd nanoparticles, we find that the additional holes created by the described charge transfer for intercalated nanoparticulate Pd indeed also enhances the maximum  $\text{H}_2$  storage capacity compared to identical nanoparticles covered with PVP.

## Results and Discussion

Crystalline NaHec was delaminated in water to form a 1.5 wt% nematic sol. At this solid content, individual nanosheets were separated to about 60 nm according to small-angle X-ray scattering (SAXS, Figure S1). Pd nanoparticles with a positive  $\zeta$  potential were synthesized by reducing  $\text{Na}_2\text{PdCl}_4$  in the presence of 4-dimethylaminopyridine (DMAP).<sup>[23]</sup> The as-synthesized nanoparticles had a core size of  $3.5 \pm 0.4$  nm as determined by transmission electron microscopy (TEM, Figure S2a, b). The hydrodynamic diameter was found to be  $4.5 \pm 1.3$  nm applying dynamic light scattering (DLS, Figure S2c). As the layer charge of the NaHec nanosheets is fixed due to the isomorphous substitution of  $\text{Li}^+$  for  $\text{Mg}^{2+}$ , the number of nanoparticles that can be intercalated between the nanosheets can be controlled by the pH-dependent surface charge of the nanoparticles. The  $\zeta$  potential of the nanoparticles could be systematically varied by pH adjustment between 28 mV and 34 mV at a pH of 9.5 and 6.0, respectively (Figure S3). Typically, a 1.0 wt% dispersion of the Pd nanoparticles was added to a 1.5 wt% dispersion of the nematic sol of Hec under vigorous stirring. After flocculation of the oppositely charged species, the composite was repeatedly centrifuged and washed. The amount of Pd captured by NaHec was determined by energy-dispersive X-ray spectroscopy (EDS). At a pH of 6.0, the Pd

weight fraction was 39.3 % ( $\text{Hec@Pd39@Hec}$ ), whereas at pH 9.5, the amount of Pd was as high as 64.5 wt% ( $\text{Hec@Pd65@Hec}$ ). The amount of  $\text{Na}^+$  was below the detection limit of EDS. XPS of  $\text{Na } 1s$  region did not show a signal of remaining  $\text{Na}^+$ . In contrast, a clear signal was visible for pristine NaHec (Figure S4). According to CHN analysis, the DMAP capping ligand was completely removed during the washing steps suggesting that positively charged Pd nanoparticles solely guarantee the charge balance. This was cross checked by XPS analysis of the  $\text{N } 1s$  region showing no signal of residuals of the nitrogen-containing ligand (Figure S4b).

TEM images of both samples showed that the nanoparticles were captured between the nanosheets.  $\text{Hec@Pd39@Hec}$  had a disordered structure with collapsed areas. At this low pH, the Pd nanoparticles carry a high positive  $\zeta$  potential and consequently, very few nanoparticles were required to balance the negative surface charge. In turn, adjacent nanoparticles are too distant to keep the gallery between nanosheets open. The flexible nanosheets<sup>[24]</sup> completely encapsulated individual nanoparticles (Figure 1a). Since the nanosheets are impermeable for  $\text{H}_2$ ,<sup>[25]</sup> the Pd nanoparticles at this low loading turned out to be not accessible for CO chemisorption or Ar (Figure S5a). More nanoparticles that are closer to each other were required to prevent the nanosheets from collapsing. When the surface charge of the nanoparticles was lowered by increasing the pH to 9.5, and consequently, more nanoparticles were intercalated to achieve charge balance, an ordered lamellar structure was obtained (Figure 1b). The nanoparticles are sandwiched between two nanosheets while the gallery is kept open by sufficient nanoparticles serving as pillars (Figure 1c). Upon intercalation, the nanoparticles retained their size of  $3.5 \pm$

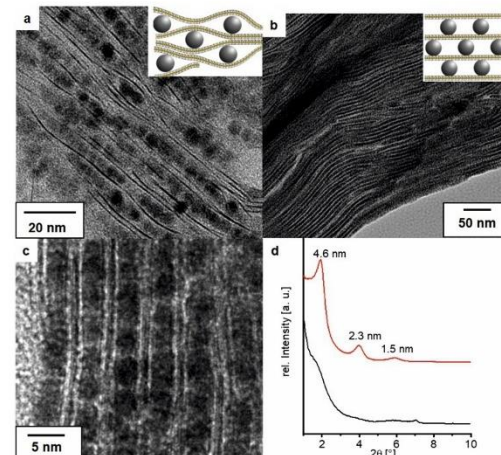


**Figure 1.** Structural characterization of  $\text{Hec@Pd39@Hec}$  and  $\text{Hec@Pd65@Hec}$ : a) TEM image of  $\text{Hec@Pd39@Hec}$ . b, c) TEM images of  $\text{Hec@Pd65@Hec}$ . d) PXRD at low angles of  $\text{Hec@Pd39@Hec}$  (black) and  $\text{Hec@Pd65@Hec}$  (red).

0.4 nm. This was confirmed at larger length scales as compared to TEM images by Powder X-ray diffraction (PXRD, Figure 1d). In line with the disorder apparent in TEM images, Hec@Pd39@Hec showed only a broad shoulder at low angles due to a random interstratification of occupied and unoccupied interlayer spaces. In contrast, for Hec@Pd65@Hec a series of reflections ( $00l$  series) was observed with a  $d$  spacing of 4.6 nm. This is in excellent agreement with the sum of a typical nanoparticle sized 3.4 nm and the 0.96 nm thick nanosheet. Furthermore, the coefficient of variation of 0.78% proved a rational series and a high degree of order along the stacking direction indicating a quite uniform  $d$  spacing.

Hec@Pd65@Hec was found to be mesoporous with a BET surface of 163 m<sup>2</sup>/g and a median pore size of 4.5 nm, suggesting that the Pd nanoparticles are not densely packed (Figure S5). The metal dispersion, determined by CO chemisorption, was 24%, demonstrating that the nanoparticles were accessible. In contrast, the BET surface of Hec@Pd39@Hec was as low as 18 m<sup>2</sup>/g, and chemisorption was below the detection limit.

Pressure-composition (PC) isotherms were acquired for Hec@Pd39@Hec and Hec@Pd65@Hec at 303 K (Figure 2). Furthermore, the DMAP covered Pd nanoparticles were stabilized with PVP as the polymer is regarded to take no influence on uptake behaviour.<sup>[17]</sup> The nanoparticles retained their size upon capping ligand exchange (Figure S6), and the metal content was 10.1 wt%, according to elemental analysis. The reference is denoted as PdPVP. Before the measurement, the samples were evacuated at 423 K for 6 h. Hec@Pd39@Hec did not absorb hydrogen, which proved that even the very small H<sub>2</sub> molecules could not diffuse between the collapsed nanosheets and access the encapsulated Pd nanoparticles. Only some external Pd could absorb small amounts of H. The H<sub>2</sub> uptake at 101 kPa H<sub>2</sub> pressure of the reference PdPVP nanoparticles was 0.35 H/Pd showing – as expected for such small nanoparticles– a clear nanosize effect compared to Pd black (~0.7 H/Pd) and the reduction observed here is in good accordance with the literature.<sup>[17]</sup> For Hec@Pd65@Hec, the amount of absorbed H

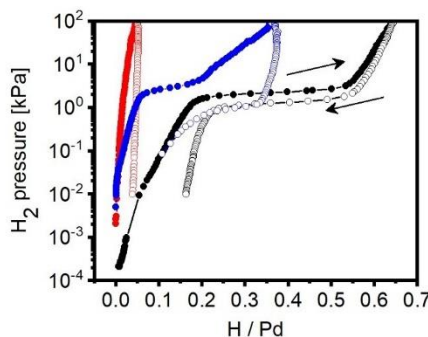


Figure 2. PC isotherms at 303 K of Hec@Pd39@Hec (red), Hec@Pd65@Hec (black), and PdPVP (blue).

increased with increasing H<sub>2</sub> pressure. At 101 kPa, Hec@Pd65@Hec absorbed 0.65 H/Pd. This was an increase of 86% compared to the 0.35 H/Pd of PdPVP. Additionally, the plateau-like region, where the solid solution of Pd and H ( $\alpha$ -phase) and the hydride formation ( $\beta$ -phase) coexist, is more pronounced compared to PdPVP. As the same nanoparticles were used for the synthesis of Hec@Pd65@Hec as well as PdPVP, the sandwich confinement by the Hec nanosheets seems to have impact on the H<sub>2</sub> uptake. Furthermore, while for sterically stabilized PdPVP the complete metal surface is accessible, for Hec@Pd65@Hec as little as 24% of the Pd atoms were measured to be accessible by CO chemisorption. When comparing the specific hydrogen densities of Hec@Pd65@Hec and PdPVP of 0.4 wt% and 0.03 wt%, respectively, the difference in the H<sub>2</sub> uptake is even higher due to higher density of Pd nanoparticles in Hec@Pd65@Hec. Nevertheless, the specific hydrogen density is lower compared to Pd black as it consists of 35 wt% Hec support.

To clarify whether the increased uptake of H<sub>2</sub> of Hec@Pd65@Hec was a spillover effect to the Hec support or absorbed into the lattice of Pd, *in situ* diffraction measurements at variable H<sub>2</sub> pressure were performed. The transition from  $\alpha$  to  $\beta$  phase is a first-order transition<sup>[26]</sup> and is accompanied by an expansion of the Pd lattice.<sup>[27]</sup> The change in the position of the fcc diffraction peaks of Pd was recorded *in situ* at various hydrogen pressures at Super Photon Ring SPring-8 (Figure 3a).<sup>[28]</sup> From vacuum to 1 kPa, the fcc peaks of Pd only gradually shifted to lower angles corresponding to the solid solution of the  $\alpha$ -phase. The transition appeared in a very narrow pressure range, and peaks completely shifted to lower angles already at 2 kPa and shifted back at 0.5 kPa during the desorption process. Le Bail fitting of the diffraction patterns proved that the lattice constant of Pd increased with hydrogen pressure and decreased when the hydrogen desorbed again (Figure 3b). The lattice constant returned to its original value after desorption, proving complete reversibility. It should be noted that the lattice was able to expand even though the

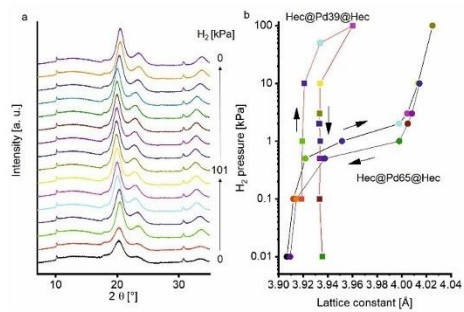


Figure 3. a) *In situ* powder XRD patterns of Hec@Pd65@Hec at various hydrogen pressures. b) Lattice constant estimated by Le Bail fitting for the diffraction patterns of Hec@Pd39@Hec and Hec@Pd65@Hec. The colour code of the diffraction patterns corresponds to the lattice constant in a). The diffraction patterns of Hec@Pd39@Hec can be found in Figure S7.

nanoparticles were sandwiched between the silicate nanosheets. The change in the lattice constant upon H<sub>2</sub> pressure is fully consistent with the course of the PC isotherm plotted in Figure 2 which is a good hint that H<sub>2</sub> uptake is due to the sorption into the lattice of Pd nanoparticles rather than a spillover process.

As expected, the lattice constant of Hec@Pd39@Hec hardly shifted upon the insignificant hydrogen uptake (Figure 3b and S7).

XP spectra of the Pd 3d region of Hec@Pd39@Hec and Hec@Pd65@Hec were recorded to investigate the influence of hectorite on the electronic structure of Pd nanoparticles (Figure 4). The signals of Hec@Pd65@Hec were fitted with a pair of asymmetric bands (3d<sub>5/2</sub> and 3d<sub>3/2</sub>) with a spin orbit coupling of 5.26 eV characteristic for Pd metal (Figure S8). The binding energies (BE) of Pd 3d<sub>5/2</sub> was 335.8 eV for Hec@Pd65@Hec, considerably shifted to higher values than the 335.0 eV of bulk Pd.<sup>[29]</sup> As the DMAP capped nanoparticles of Hec@Pd39@Hec had a higher ζ potential at synthesis, the Pd 3d<sub>5/2</sub> signal at this stage was at 336.0 eV. In contrast, Pd 3d<sub>5/2</sub> of PdPVP was found at a BE of 335.1 eV. The shift to higher BE values suggested that Hec covered nanoparticles were in a different electronic state from the PVP covered nanoparticles and were slightly electron-deficient. The negatively charged nanosheets forced the nanoparticles to be in a positively charged state. Furthermore, a charge transfer from Pd to the Si of the nanosheets was reported before.<sup>[22]</sup> The amount of hydrogen that can be absorbed strongly correlates with the amount of 4d band holes in the conduction band at the Fermi level.<sup>[30]</sup> Based on the band filling effect, the more holes in the 4d band, the more hydrogen can be absorbed as the transfer of H 1s electrons into these holes creates the Pd–H bonds.<sup>[31]</sup> Similar behaviour was also found for metal alloys of Pd–Ir<sup>[32]</sup> or Pd–Rh,<sup>[33]</sup> where a charge transfer from Pd to the other metal increased the number of

holes and total H<sub>2</sub> storage capacity. Furthermore, covering Pd nanocubes with HKUST-1 doubled the hydrogen uptake due to charge transfer from Pd to Cu–O centres.<sup>[9,18]</sup> In the same line, we propose that the electron-deficient Pd species created by intercalation between NaHec nanosheets can absorb more hydrogen due to an increased amount of holes in the 4d band.

## Conclusions

The results demonstrate that the amount of hydrogen absorbed by Pd nanoparticles can be significantly altered by intercalation between the permanently negatively charged 2D layered material hectorite. The nanosheets influence the electronic structure of the nanoparticles and thus modulate the amount of hydrogen that can be absorbed. Furthermore, it was shown that a proper adjustment of the ζ potential of the nanoparticles before intercalation was crucial to obtain mesoporous materials with Pd surfaces being accessible. The findings show that confinement between the Hec nanosheets can improve the H<sub>2</sub> storage capacity by alteration of the electronic structure. As the intercalation strategy can most likely be applied to other nanoparticulate materials, storage capacity of more abundant and cheaper nanoparticles might be tunable on the way to reliable and affordable H<sub>2</sub> storage materials.

## Experimental Section

### Materials

PdCl<sub>2</sub> (99.999% Pd, Preimion), NaCl, 4-Dimethylaminopyridine (DMAP), NaOH, NaCl and NaBH<sub>4</sub> were purchased from Alfa Aesar. Polyvinylpyrrolidone (PVP) with an average mol wt of 40000 was purchased from Sigma Aldrich. The used water was of MilliQ quality (18.2 MΩ).

### Synthesis of Pd nanoparticles

The synthesis of Pd nanoparticles was executed using a modified literature procedure.<sup>[23]</sup> Palladium (II) chloride (235 mg, 1.33 mmol) and Sodium chloride (155 mg, 2.66 mmol) were dissolved in 40 mL water and 4-Dimethylaminopyridine DMAP (833 mg, 6.82 mmol) in 80 mL water was added. After 20 min of stirring NaBH<sub>4</sub> (110 mg, 2.91 mmol) in 11 mL water was added dropwise under vigorous stirring resulting in a black dispersion. After 2 h the nanoparticle dispersion was dialyzed in 4 L water with water changes after 12 and 24 hours.

### Synthesis of NaHec

NaHec was synthesized via melt synthesis and is described elsewhere.<sup>[19b]</sup>

### Synthesis of Hec@Pd@Hec

For the synthesis of the composite materials the hectorite was delaminated to a 1.5 wt% dispersion to achieve a layer distance of about 60 nm. Both the aqueous nanoparticle and hectorite dispersions were adjusted resulting in surface potentials of the

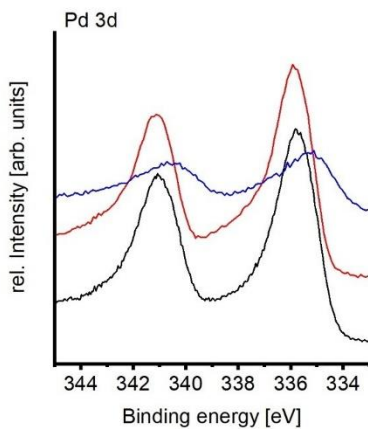


Figure 4. XP spectra of Pd 3d region of Hec@Pd65@Hec (black), Hec@Pd39@Hec (red), and PdPVP (blue).

nano particles of 28 mV or 34 mV, respectively. The nematic hectorite suspension was added rapidly to the nanoparticle dispersion under vigorous stirring. Visible flocculation appeared within 30 seconds. The black flocculate was separated from the supernatant by centrifugation. DMAP was removed by three washing cycles. Finally, the material was freeze-dried to obtain a fluffy powder.

#### Synthesis of PdPVP

Nano particles were covered with PVP by a ligand exchange process. To about 100 mg of DMAP capped Pd nano particles in aqueous dispersion (100 mL) was added 900 mg PVP. The dispersion was stirred for 2 days and the dispersion was then dialyzed in 4 L water with water changes after 12 and 24 hours. The material was dried at 130 °C.

#### Characterization

Dynamic light scattering (DLS) and determination of  $\zeta$ -potential were recorded on a Litesizer 500 (Anton-Paar).

CHN analysis was acquired with an Elementar Vario EL III.

PXRD of textured samples were recorded on a Bragg-Brentano type diffractometer (Empyrean, PANalytical) with nickel filter and  $\text{Cu}_{K\alpha}$  radiation ( $\lambda = 1.54187 \text{ \AA}$ ).

SAXS data were measured using a "Double Ganesh AIR" system (SAXSLAB, Denmark). The X-ray source of this laboratory-based system is a rotating anode (copper, MicroMax 007HF, Rigaku Corporation, Japan) providing a microfocused beam. The data is recorded by a position sensitive detector (PILATUS 300 K, Dectris).

Transmission electron microscopy (TEM) images were acquired using a JEOL JEM-2200FS (200 kV). For cross sectional TEM the powder was embedded into a resin (EPO-TEK 301) and was cut with an Ar beam into thin slices using a Jeol Cryo Ion Slicer.

Scanning electron microscopy (SEM) images and energy dispersive spectroscopy (EDS) were recorded on a FEI Quanta FEG 250.

Photoelectron spectroscopy (XPS) was conducted on a Versa Probe III fitted with an Al  $K_{\alpha}$  source. Spectra were referenced to C 1s at 284.8 eV.

Adsorption isotherms were recorded on a Quantachrome Autosorb-1 with Ar as adsorbate at 87 K. The isotherms were evaluated using Brunauer-Emmet-Teller (BET) method and pore size distribution was evaluated with NLDFT.

Metal surface was acquired via CO chemisorption with a Quantachrome Autosorb-1 using the double isotherm method at 35 °C.

PC isotherm measurements were acquired using a pressure-temperature apparatus (BEL JAPAN). Before measurement all samples were activated at 423 K under vacuum for 6 h. PC isotherms were measured from  $10^{-3}$  up to 101 kPa hydrogen pressure at 303 K. The adsorption/desorption process was repeated at least for three times to eliminate the possibility of surface oxide contamination.

In situ XRD measurements were acquired at Beamline BL02B2 at SPring-8. Samples were sealed in a glass capillary and were measured under controlled hydrogen pressure in the range from 0 to 101 kPa at 303 K. The radiation wave length was 0.8 Å and the step size was 0.006°.

#### Acknowledgements

This work was supported by the Deutsche Forschungsgemeinschaft (SFB 840, TP A2). K.A. thanks the Elite Network of Bavaria for a PhD fellowship. We thank Marco Schwarzmann for preparing samples for cross-sectional TEM and SEM-EDS measurements. We appreciate the support of the Keylab for Optical and Electron Microscopy of the Bavarian Polymer Institute (BPI). The XPS/UPS facility (PHI 5000 VersaProbe III system) at the Device Engineering Keylab of BPI is acknowledged. Open Access funding enabled and organized by Projekt DEAL.

#### Conflict of Interest

The authors declare no conflict of interest.

#### Data Availability Statement

Research data are not shared.

**Keywords:** hectorite • layered compounds • Palladium • hydrogen storage • nanoparticles

- [1] S. Dunn, *Int. J. Hydrogen Energy* **2002**, *27*, 235–264.
- [2] L. Schlappbach, A. Züttel, *Nature* **2001**, *414*, 353–358.
- [3] W. C. Xu, K. Takahashi, Y. Matsuo, Y. Hattori, M. Kumagai, S. Ishiyama, K. Kaneko, S. Iijima, *Int. J. Hydrogen Energy* **2007**, *32*, 2504–2512.
- [4] M. P. Suh, H. J. Park, T. K. Prasad, D.-W. Lim, *Chem. Rev.* **2012**, *112*, 782–835.
- [5] S. Dekura, H. Kobayashi, K. Kusada, H. Kitagawa, *ChemPhysChem* **2019**, *20*, 1158–1176.
- [6] N. A. A. Rusman, M. Dahari, *Int. J. Hydrogen Energy* **2016**, *41*, 12108–12126.
- [7] S.-I. Orimo, Y. Nakamori, J. R. Eliseo, A. Züttel, C. M. Jensen, *Chem. Rev.* **2007**, *107*, 4111–4132.
- [8] a) F. D. Manchester, A. San-Martin, J. M. Pitre, *J. Phase Equilib.* **1994**, *15*, 62–83; b) H. Kobayashi, M. Yamauchi, H. Kitagawa, Y. Kubota, K. Kato, M. Takata, *J. Am. Chem. Soc.* **2008**, *130*, 1828–1829.
- [9] Y. Chen, O. Sakata, Y. Nanba, L. S. R. Kumara, A. Yang, C. Song, M. Koyama, G. Li, H. Kobayashi, H. Kitagawa, *Commun. Chem.* **2018**, *1*, 61.
- [10] E. Roduner, *Chem. Soc. Rev.* **2006**, *35*, 583–592.
- [11] a) A. S. K. Hashmi, G. J. Hutchings, *Angew. Chem. Int. Ed.* **2006**, *45*, 7896–7936; *Angew. Chem.* **2006**, *118*, 8064–8105; b) D. Astruc, *Chem. Rev.* **2020**, *120*, 461–463.
- [12] a) P. Schlexer, A. B. Andersen, B. Sebok, I. Chorkendorff, J. Schiotz, T. W. Hansen, *Part. Part. Syst. Charact.* **2019**, *36*, 1800480; b) P. Buffat, J. P. Borel, *Phys. Rev. A* **1976**, *13*, 2287–2298.
- [13] P. E. de Jongh, P. Adelhelm, *ChemSusChem* **2010**, *3*, 1332–1348.
- [14] P. Ngene, P. Adelhelm, A. M. Beale, K. P. de Jong, P. E. de Jongh, *J. Phys. Chem. C* **2010**, *114*, 6163–6168.

## Results

Journal of Inorganic and General Chemistry

**ZAAC**

Zeitschrift für anorganische und allgemeine Chemie

**RESEARCH ARTICLE**

- [15] J. Gao, P. Adelhelm, M. H. W. Verkuijlen, C. Rongeat, M. Herrich, P. J. M. van Bentum, O. Gutfleisch, A. P. M. Kentgens, K. P. de Jong, P. E. de Jongh, *J. Phys. Chem. C* **2010**, *114*, 4675–4682.
- [16] a) H. Tsunoyama, H. Sakurai, Y. Negishi, T. Tsukuda, *J. Am. Chem. Soc.* **2005**, *127*, 9374–9375; b) N. J. J. Johnson, B. Lam, R. S. Sherbo, D. K. Fork, C. P. Berlinguette, *Chem. Mater.* **2019**, *31*, 8679–8684.
- [17] M. Yamauchi, R. Ikeda, H. Kitagawa, M. Takata, *J. Phys. Chem. C* **2008**, *112*, 3294–3299.
- [18] G. Li, H. Kobayashi, J. M. Taylor, R. Ikeda, Y. Kubota, K. Kato, M. Takata, T. Yamamoto, S. Toh, S. Matsumura, H. Kitagawa, *Nat. Mater.* **2014**, *13*, 802–806.
- [19] a) H. Kalo, W. Milius, J. Breu, *RSC Adv.* **2012**, *2*, 8452–8459; b) M. Stöter, D. A. Kunz, M. Schmidt, D. Hirsemann, H. Kalo, B. Putz, J. Senker, J. Breu, *Langmuir* **2013**, *29*, 1280–1285.
- [20] K. Ament, D. R. Wagner, F. E. Meij, F. E. Wagner, J. Breu, *Z. Anorg. Allg. Chem.* **2020**, *646*, 1110–1115.
- [21] S. Rosenfeldt, M. Stöter, M. Schlenk, T. Martin, R. Q. Albuquerque, S. Förster, J. Breu, *Langmuir* **2016**, *32*, 10582–10588.
- [22] K. Ament, N. Köwitsch, D. Hou, T. Götsch, J. Kröhner, C. J. Heard, A. Trunschke, T. Lunkenstein, M. Armbrüster, J. Breu, *Angew. Chem. Int. Ed.* **2021**, *60*, 5890–5897; *Angew. Chem.* **2021**, *133*, 5954–5961.
- [23] K. A. Flanagan, J. A. Sullivan, H. Müller-Bunz, *Langmuir* **2007**, *23*, 12508–12520.
- [24] D. A. Kunz, J. Erath, D. Kluge, H. Thurn, B. Putz, A. Fery, J. Breu, *ACS Appl. Mater. Interfaces* **2013**, *5*, 5851–5855.
- [25] C. Habel, E. S. Tsurko, R. L. Timmins, J. Hutschreuther, R. Kunz, D. D. Schuchardt, S. Rosenfeldt, V. Altstädt, J. Breu, *ACS Nano* **2020**, *14*, 7018–7024.
- [26] a) R. Bardhan, L. O. Hedges, C. L. Pint, A. Javey, S. Whitelam, J. J. Urban, *Nat. Mater.* **2013**, *12*, 905–912; b) A. Baldi, T. C. Narayan, A. L. Koh, J. A. Dionne, *Nat. Mater.* **2014**, *13*, 1143–1148; c) S. Syrenova, C. Wadell, F. A. A. Nugroho, T. A. Gschneidtner, Y. A. Diaz Fernandez, G. Nalin, D. Świtlik, F. Westerlund, T. J. Antosiewicz, V. P. Zhdanov, K. Moth-Poulsen, C. Langhammer, *Nat. Mater.* **2015**, *14*, 1236–1244.
- [27] M. Yamauchi, H. Kobayashi, H. Kitagawa, *ChemPhysChem* **2009**, *10*, 2566–2576.
- [28] E. Nishibori, M. Takata, K. Kato, M. Sakata, Y. Kubota, S. Aoyagi, Y. Kuroiwa, M. Yamakata, N. Ikeda, *Nuclear Instruments and Methods in Physics Research Section A: Accelerators, Spectrometers, Detectors and Associated Equipment* **2001**, *467*–468, 1045–1048.
- [29] a) R. Arrigo, M. E. Schuster, S. Abate, S. Wrabetz, K. Amakawa, D. Teschner, M. Freni, G. Centi, S. Perathoner, M. Havecker, R. Schlögl, *ChemSusChem* **2014**, *7*, 179–194; b) N. S. Babu, N. L. Lingaiah, R. Gopinath, P. S. S. Reddy, P. S. S. Prasad, *J. Phys. Chem. C* **2007**, *111*, 6447–6453.
- [30] a) D. A. Papaconstantopoulos, B. M. Klein, E. N. Economou, L. L. Boyer, *Phys. Rev. B* **1978**, *17*, 141–150; b) G. Alefeld, *Hydrogen in Metals II*, Springer: Berlin, Heidelberg, 1978.
- [31] E. Wicke, H. Brodowsky, H. Züchner, in *Hydrogen in metals II*, Springer: Berlin, Heidelberg, 1978, pp. 73–155.
- [32] H. Kobayashi, M. Yamauchi, R. Ikeda, T. Yamamoto, S. Matsumura, H. Kitagawa, *Chem. Sci.* **2018**, *9*, 5536–5540.
- [33] H. Kobayashi, H. Morita, M. Yamauchi, R. Ikeda, H. Kitagawa, Y. Kubota, K. Kato, M. Takata, S. Toh, S. Matsumura, *J. Am. Chem. Soc.* **2012**, *134*, 12390–12393.

Manuscript received: February 15, 2022

Revised manuscript received: February 7, 2022

Accepted manuscript online: February 10, 2022

6.3.1 Supporting Information

# **Zeitschrift für anorganische und allgemeine Chemie**

**Supporting Information**

## **Enhancing Hydrogen Storage Capacity of Pd Nanoparticles by Sandwiching between Inorganic Nanosheets**

Kevin Ament, Hirokazu Kobayashi, Kohei Kusada, Josef Breu,\* and Hiroshi Kitagawa\*

## Supporting information

### Enhancing Hydrogen Storage Capacity of Pd Nanoparticles by Sandwiching between Inorganic Nanosheets

Kevin Ament,<sup>[a,b]</sup> Hirokazu Kobayashi,<sup>[c]</sup> Kohei Kusada,<sup>[c,d]</sup> Josef Breu,<sup>\*[a,b]</sup> and Hiroshi Kitagawa<sup>\*[c]</sup>

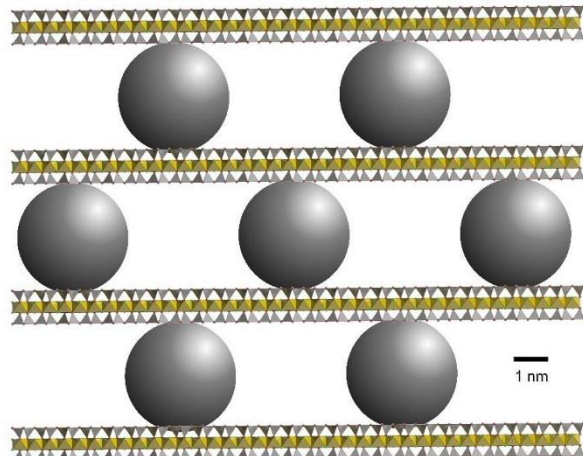
**Abstract:** H<sub>2</sub> is regarded to play a crucial role in the transition from a fossil fuel-based energy economy towards an environmentally friendly one. However, storage of H<sub>2</sub> is still challenging, but palladium (Pd) based materials show exciting properties. Therefore, nanoparticulate Pd has been intensely studied for hydrogen storage in the past years. Here, we stabilize Pd nanoparticles by intercalation between inorganic nanosheets of hectorite (NaHec). Compared to nanoparticles stabilized by the polymer polyvinylpyrrolidone (PVP), the H<sub>2</sub> storage capacity was found to be 86% higher for identical Pd nanoparticles being intercalated between nanosheets. We attribute this remarkably enhanced H<sub>2</sub> storage capacity to the partial oxidation of Pd, as evidenced by X-ray photoelectron spectroscopy (XPS). The higher amount of holes in the 4d band leads to a higher amount of H<sub>2</sub> that can be absorbed when Pd is stabilized between the nanosheets of hectorite compared to the PVP stabilized nanoparticles.

#### Table of Contents

1	Results and discussion .....	2
1.1	Sketch of the intended structure of sandwiched nanoparticles .....	2
1.2	SAXS of NaHec dispersion.....	2
1.3	Characterization of Pd nanoparticles. ....	3
1.4	Zeta Potential.....	4
1.5	XPS of Na 1s region .....	4
1.6	Ar-Isotherms .....	5
1.7	TEM of PVP covered Pd nanoparticles.....	5
1.8	<i>In situ</i> XRD of Hec@Pd39@Hec .....	6
1.9	Deconvolution of the Pd 3d region of Hec@Pd65@Hec.....	6
2	References .....	7

## 1 Results and discussion

### 1.1 Sketch of the intended structure of sandwiched nanoparticles



**Scheme S1.** Sketch of the porous structure of Pd intercalated between the inorganic nanosheets of Hec.

### 1.2 SAXS of NaHec dispersion

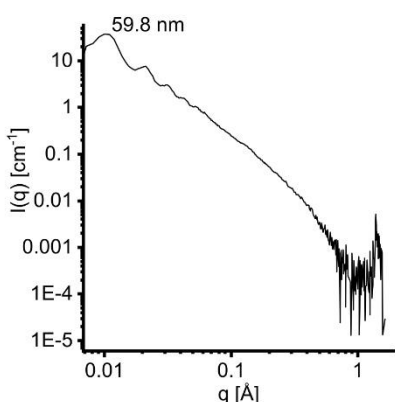


**Figure S1.** SAXS of a nematic sol of NaHec showing a  $00l$  series with a nanosheet separation of about 60 nm.

1.3 Characterization of Pd nanoparticles.

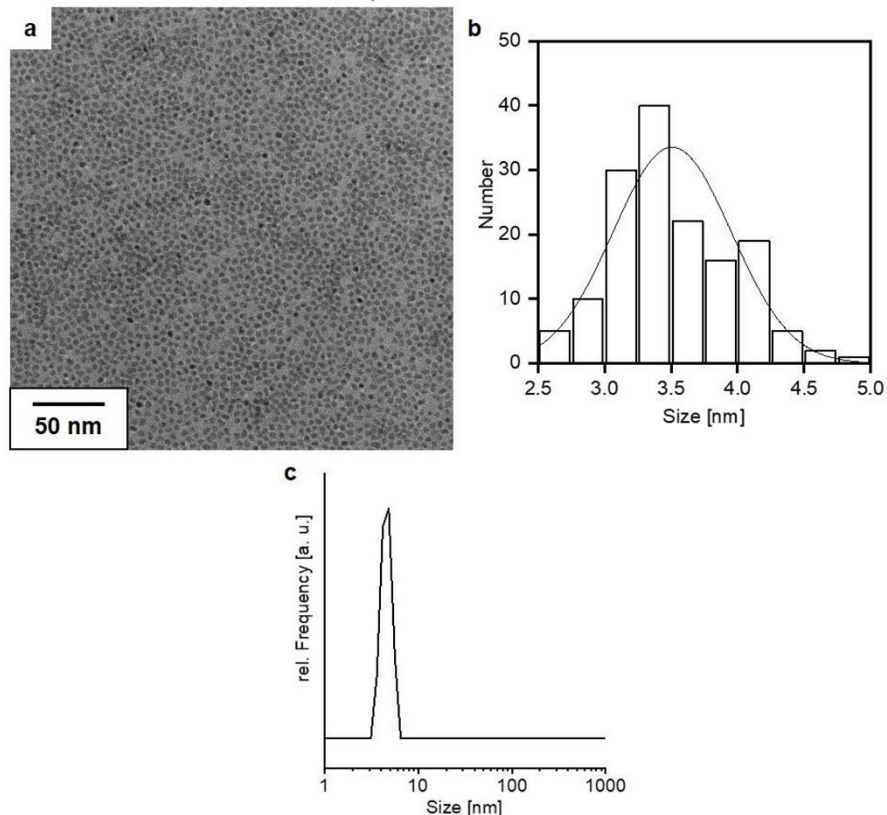


**Figure S2.** a) TEM image of DMAP capped Pd nanoparticles. b) Histogram of the core size of 200 nanoparticles, and c) hydrodynamic diameter in aqueous dispersion.

#### 1.4 Zeta Potential

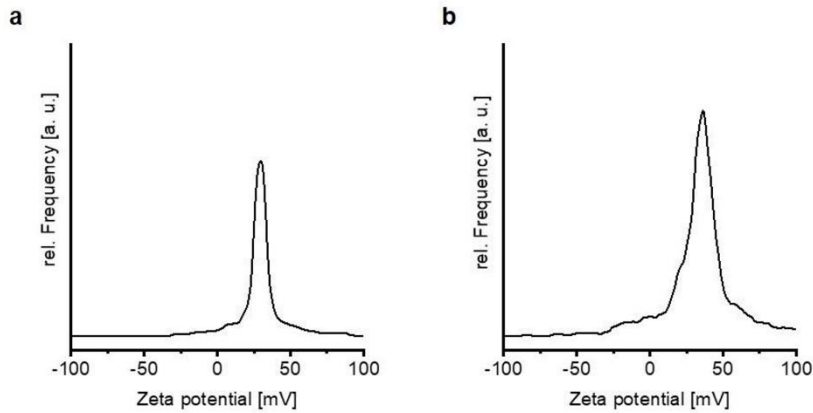


**Figure S3.**  $\zeta$  potential of Pd nanoparticles at a pH of a) 9.5 and b) pH 6.0.

#### 1.5 XPS of Na 1s region

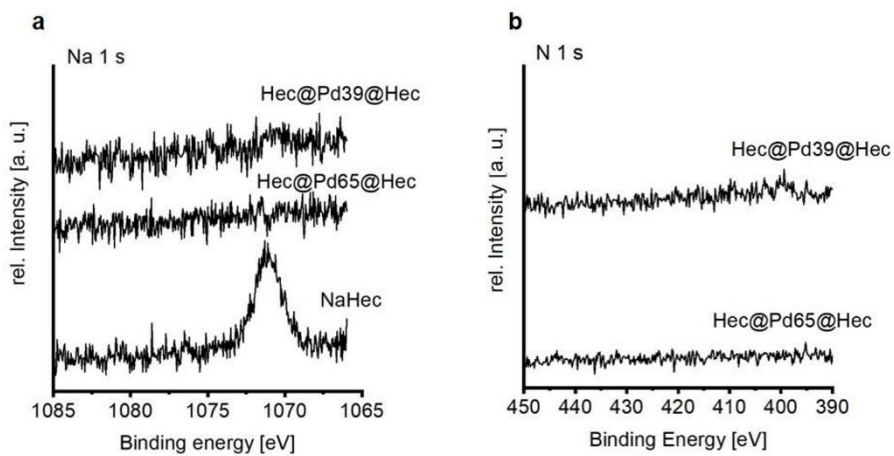


**Figure S4.** a) Na 1s region of NaHec, Hec@Pd39@Hec, and Hec@Pd65@Hec. After intercalation of Pd nanoparticles, there is no signal of residual Na left. b) N 1s region of Hec@Pd39@Hec and Hec@Pd65@Hec showing no signal of residual DMAP.

### 1.6 Ar-Isotherms

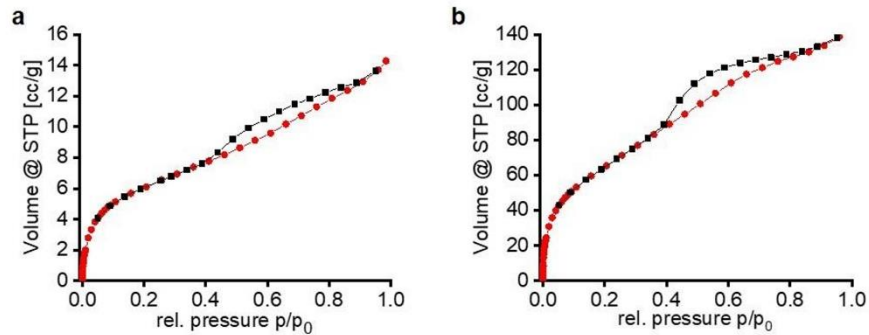


**Figure S5.** Ar-Isotherms of a) Hec@Pd39@Hec, and b) Hec@Pd65@Hec.

### 1.7 TEM of PVP covered Pd nanoparticles.

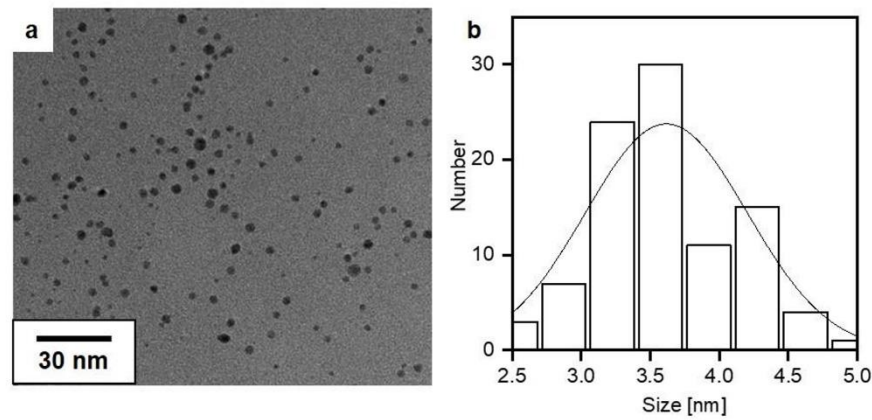


**Figure S6.** a) TEM image of PdPVP nanoparticles. b) Histogram of the core size of 100 nm.

### 1.8 *In situ* XRD of Hec@Pd39@Hec

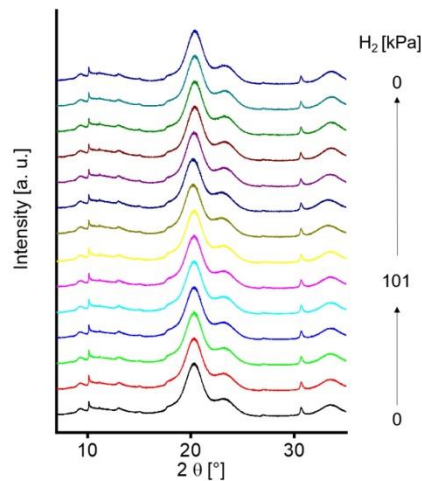


**Figure S7.** *In situ* XRD of Hec@Pd39@Hec at various H<sub>2</sub> pressure.

### 1.9 Deconvolution of the Pd 3d region of Hec@Pd65@Hec

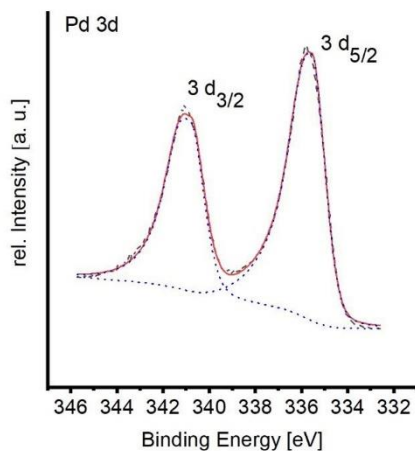


**Figure S8.** Deconvolution of the Pd 3d region of Hec@Pd65@Hec. Black is the measured spectrum, blue dots represent the deconvoluted asymmetric bands of metallic Pd and red is the overall fitted spectrum.

## 2 References

1. K. A. Flanagan, J. A. Sullivan and H. Müller-Bunz, *Langmuir*, 2007, **23**, 12508-12520.
2. M. Stöter, D. A. Kunz, M. Schmidt, D. Hirsemann, H. Kalo, B. Putz, J. Senker and J. Breu, *Langmuir*, 2013, **29**, 1280-1285.

## 6.4 Enhancing the Catalytic Activity of Palladium Nanoparticles via Sandwich-Like Confinement by Thin Titanate Nanosheets

### **Enhancing the Catalytic Activity of Palladium Nanoparticles via Sandwich-Like Confinement by Thin Titanate Nanosheets**

Kevin Ament<sup>[a]</sup>, Daniel R. Wagner<sup>[a]</sup>, Thomas Götsch<sup>[b]</sup>, Takayuki Kikuchi<sup>[c]</sup>, Jutta Kröhnert<sup>[b]</sup>, Annette Trunschke<sup>[b]</sup>, Thomas Lunkenbein<sup>[b]</sup>, Takayoshi Sasaki<sup>[c]\*</sup>, and Josef Breu<sup>[a]\*</sup>

ACS Catalysis 2021, 11, 2754-2762

Impact Factor (2019): 12.35

<https://pubs.acs.org/doi/10.1021/acscatal.1c00031>

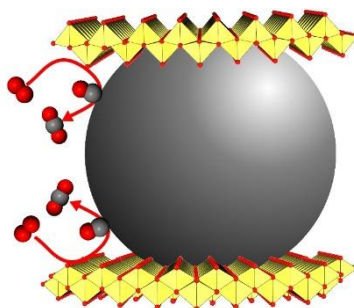
Reprinted under the terms of CC BY 4.0 license (<https://creativecommons.org/licenses/by/4.0/legalcode>)  
© 2021 The Authors. Published by American Chemical Society.

[a] Bavarian Polymer Institute and Department of Chemistry, University of Bayreuth, 95447 Bayreuth (Germany)

[b] Department of Inorganic Chemistry, Fritz-Haber-Institut der Max-Planck-Gesellschaft, 14195 Berlin (Germany)

[c] International Centre for Materials Nanoarchitectonics (WPI-Mana), National Institute for Materials Science (NIMS), Tsukuba, Ibaraki 305-0044 (Japan)

\* E-mail: josef.breu@uni-bayreuth.de, sasaki.takayoshi@nims.go.jp



#### **Individual Contribution:**

The concept of the publication was developed by Prof J. Breu, Prof T. Sasaki, and myself. The manuscript was written by Prof J. Breu and me. T. Götsch, A. Trunschke, Prof T. Sasaki, and T. Lunkenbein commented on the manuscript. I was invited to NIMS by Prof T. Sasaki to synthesize L-titanate with the assistance of T. Kikuchi. I designed the experiments, synthesized the catalysts and did most of the characterisation. D. Wagner assisted with the surface area determination and contributed to the scientific discussion. J. Kröhnert performed CO-DRIFTS and A. Trunschke commented on my interpretation of the data. T. Götsch measured EELS and T. Lunkenbein assisted with the interpretation of the data.

My contribution to the publication is approx. 85 %.



## Enhancing the Catalytic Activity of Palladium Nanoparticles via Sandwich-Like Confinement by Thin Titanate Nanosheets

Kevin Ament, Daniel R. Wagner, Thomas Götsch, Takayuki Kikuchi, Jutta Kröhnert, Annette Trunschke, Thomas Lunkenstein, Takayoshi Sasaki,\* and Josef Breu\*



Cite This: *ACS Catal.* 2021, 11, 2754–2762



Read Online

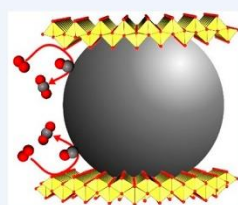
ACCESS |

Metrics & More

Article Recommendations

Supporting Information

**ABSTRACT:** As atomically thin oxide layers deposited on flat (noble) metal surfaces have been proven to have a significant influence on the electronic structure and thus the catalytic activity of the metal, we sought to mimic this architecture at the bulk scale. This could be achieved by intercalating small positively charged Pd nanoparticles of size 3.8 nm into a nematic liquid crystalline phase of lepidocrocite-type layered titanate. Upon intercalation the galleries collapsed and Pd nanoparticles were captured in a sandwichlike mesoporous architecture showing good accessibility to Pd nanoparticles. On the basis of X-ray photoelectron spectroscopy (XPS) and CO diffuse reflectance Fourier transform infrared spectroscopy (DRIFTS) Pd was found to be in a partially oxidized state, while a reduced Ti species indicated an electronic interaction between nanoparticles and nanosheets. The close contact of titanate sandwiching Pd nanoparticles, moreover, allows for the donation of a lattice oxygen to the noble metal (inverse spillover). Due to the metal–support interactions of this peculiar support, the catalyst exhibited the oxidation of CO with a turnover frequency as high as  $0.17 \text{ s}^{-1}$  at a temperature of 100 °C.



**KEYWORDS:** *layered titanate, palladium nanoparticles, CO oxidation, support–metal interaction, heterogeneous catalysis*

### 1. INTRODUCTION

Not only are supporting materials important to disperse and stabilize catalytically active nanoparticles but also extensive research gave convincing evidence for an active role of the support in the catalytic processes.<sup>1</sup> Charge transfer between a (noble) metal and the support modifies the electronic structure and thus modulates the interaction with adsorbate molecules, a phenomenon referred to as an electronic metal–support interaction (EMSI).<sup>2–6</sup> Furthermore, it was shown that catalytic reactions often occur at the perimeter between the support and metal, including spillover phenomena.<sup>7,8</sup> Especially, model catalysts fabricated by deposition of ultrathin layers of oxides on atomically flat metal surfaces by means of vapor deposition have attracted much interest.<sup>9–12</sup> These very defined model structures allowed systematic studies that led to fundamental insight into the catalytic performance. For instance, the metal work function can be significantly altered by the ultrathin oxide layer due to dipole effects arising from compression or charge transfer.<sup>13–15</sup> Along this line, the adsorption behavior of H<sub>2</sub> on a TiO<sub>2</sub> monolayer with a lepidocrocite structure deposited onto Pt(111) and Ag(100) was computationally investigated.<sup>16</sup> Charge transfer from Ag to the oxide was more pronounced than for Pt, and the accumulation of negative charge on the oxide disfavored the adsorption of H<sub>2</sub>. Furthermore, when the noble metal is only partially covered by the oxide layer, very reactive kinks between metal and oxide islands can be created.<sup>17</sup> Even though such model systems are most helpful to understand

fundamental mechanisms, transferring this knowledge to the bulk scale remains challenging.<sup>18</sup>

Recently, on application of a nematic phase of single nanometer thick and negatively charged hectorite nanosheets,<sup>19,20</sup> the transfer to bulk architectures was accomplished for Pd.<sup>21</sup> Sandwiching Pd nanoparticles between two highly negatively charged hectorite sheets resulted in a positive charge on the Pd. This in turn improved the catalytic performance for the oxidation of carbon monoxide (CO) in comparison to the same nanoparticles deposited on a conventional support such as γ-Al<sub>2</sub>O<sub>3</sub>.

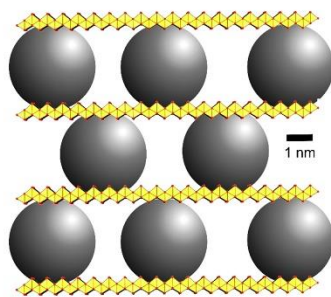
Nematic phases of coplanar nanosheets are also known for some transition-metal oxides. For instance, two-dimensional (2D) layered lepidocrocite-type titanates with a nominal formula of A<sub>x</sub>Ti<sub>2-x</sub>O<sub>4</sub>M<sub>y</sub> (A = K<sup>+</sup>, Cs<sup>+</sup>, Rb<sup>+</sup>, M = Li<sup>+</sup>; vacancy; x = 0.7–0.8; abbreviated as L-titanate)<sup>22,23</sup> appear promising in the context sketched above. These can be converted into a protonated form by acid treatment. Due to Ti<sup>4+</sup> vacancies in the lepidocrocite sheet, they possess a permanent negative layer charge and, similarly to hectorite, nematic phases of single nanosheets are obtained by repulsive osmotic swelling.<sup>24</sup>

Received: January 4, 2021

Revised: February 4, 2021

Due to the high layer charge, these nanosheets repel each other, which forces the nanosheets to adopt a cofacial orientation even at high dilutions, resulting in a liquid crystalline nematic phase showing structural colors.<sup>25</sup> At high dilutions (typically 2 g L<sup>-1</sup>), the nanosheet separation is sufficient (typically 60 nm) to grant access for nanoparticles to the gallery between the nanosheets, creating a structure as sketched in Scheme 1.

**Scheme 1. Sketch of the Porous Catalyst Structure Where Pd Nanoparticles Are Sandwiched between Adjacent L-Titanate Nanosheets**



For the oxidation of CO, redox-active supports that offer oxygen storage capacity, such as Co<sub>3</sub>O<sub>4</sub>, CeO<sub>2</sub>, and TiO<sub>2</sub>, are often used. A lattice oxygen of the support can then be donated to the oxide/metal perimeter, facilitating the oxidation reaction.<sup>4,26,27</sup> The redox-active metal of the oxide support is reduced, while a vacancy in the oxide sublattice is left behind. In a later step of the catalytic cycle this vacancy is refilled by O<sub>2</sub> from the gas phase. This mechanism is called the Mars–van Krevelen-mechanism. In the case of CO oxidation, this bypasses the CO poisoning at low temperatures that occurs on noble metals following the Langmuir–Hinshelwood mechanism, where CO and O<sub>2</sub> competitively adsorb on the metal surface.<sup>28–30</sup> Model catalysts proved that a direct relationship between the metal/support perimeter and activity existed and thus a maximized perimeter is desirable.<sup>31</sup> A sandwichlike fixation of the Pd metal as sketched in Scheme 1 would furthermore lead to an extended perimeter to the support and thus increase the catalytic activity in comparison to a nanoparticle only in contact with a support from one direction.

Here, we report the intercalation-like heteroassembly of positively charged Pd nanoparticles and negatively charged nanosheets of L-titanate. The architectures of Pd supported on/sandwiched between L-titanates, mimic the model catalysts of ultrathin layers deposited on metal surfaces. The resulting catalyst was highly active in the oxidation of CO.

## 2. RESULTS AND DISCUSSION

**2.1. Synthesis and Characterization of L-titanate@Pd@L-titanate.** H<sub>1.07</sub>Ti<sub>1.73</sub>O<sub>4</sub>·H<sub>2</sub>O (H<sup>+</sup>-L-titanate) was synthesized according to a published procedure via the solid-state synthesis of K<sub>0.8</sub>Ti<sub>1.73</sub>Li<sub>0.02</sub>O<sub>4</sub> followed by an HCl treatment.<sup>23</sup> To obtain a nematic phase, interlayer H<sup>+</sup> was then exchanged for TBA<sup>+</sup> (tetrabutylammonium) with a stoichiometric H<sup>+</sup>/TBA<sup>+</sup> ratio of 1. The solid content of (TBA)<sub>1.07</sub>Ti<sub>1.73</sub>O<sub>4</sub>·H<sub>2</sub>O

was 2 g L<sup>-1</sup>.<sup>24</sup> Upon mechanical shaking a nematic phase was obtained with individual nanosheets separated to 59 nm according to small-angle X-ray scattering (SAXS; Figure S1). As the nematic phase of the titanate nanosheets was only stable at pH ≥ 10, Pd nanoparticles were required to carry a positive surface ( $\zeta$ ) potential at this pH. Therefore, 4-dimethylaminopyridine (DMAP) was applied as the capping ligand for the Pd nanoparticles, which in turn were synthesized by reduction of Na<sub>2</sub>[PdCl<sub>4</sub>] with NaBH<sub>4</sub>.<sup>32</sup> The as-synthesized nanoparticles showed a narrow size distribution of 3.4 ± 0.4 nm, as determined by transmission electron microscopy (TEM; Figure S2a). According to dynamic light scattering (DLS), the nanoparticles were stable in aqueous dispersions at pH 10 with a hydrodynamic diameter of 4.5 ± 1.3 nm (Figure S2b), and a  $\zeta$  potential of +28 mV, as determined by an electrophoretic measurement. The  $\zeta$  potential of L-titanate was -39 mV at pH 10.

The Pd nanoparticles were added as a 0.1 wt % dispersion to the nematic phase of L-titanate under vigorous stirring, whereupon flocculation of the oppositely charged nano-objects occurred within 30 s. Elemental analysis (CHN) after repeated washing cycles showed that 5.77 wt % C and 0.44 wt % N remained in the catalyst (Table S1). This C/N ratio of 13.1 was much higher than for DMAP but was close to the expected value of 13.7 for TBA<sup>+</sup>, suggesting that ~20% of the cation exchange capacity of the TBA<sup>+</sup> remained in the structure after washing. Calcination in an air atmosphere for 5 h at 500 °C removed the residual organic content, as cross-checked by CHN analysis (Table S1). Furthermore, Fourier transform infrared spectroscopy (FTIR) was applied to detect possible OH groups left in the catalyst (Figure S3). No bands at around 3300 cm<sup>-1</sup> or at 1641 cm<sup>-1</sup> corresponding to the stretching and bending vibrations of H<sub>2</sub>O and H<sub>3</sub>O<sup>+</sup> between the nanosheets were observed.<sup>22,33</sup> Furthermore, no band between 950 and 1000 cm<sup>-1</sup> became apparent, which would indicate Ti-OH groups formed by calcination and concomitant removal of interlayer water.<sup>34</sup>

Upon calcination at 500 °C Pd was oxidized to PdO, which could easily be reduced back to metallic Pd under a flow of H<sub>2</sub> (10% in N<sub>2</sub>) at 200 °C (Figure S4). The loading of Pd in the catalyst after calcination was as high as 49 wt %, as determined by scanning electron microscopy combined with energy dispersive X-ray spectroscopy (SEM-EDS). Furthermore, elemental mapping showed a homogeneous distribution of Pd (Figure S5). Upon flocculation the nanoparticles were trapped between the nanosheets, reflecting a support from two sides and creating a lamellar structure that was preserved after the calcination and successive reduction step (Figure 1a). Adjacent layers of nanoparticles were separated by one nanosheet of approximately 0.75 nm thickness. Thus, an architecture as sketched in Scheme 1 was obtained where oxide layer covered nanoparticles were stacked upon each other. The nanoparticles were not densely packed, as indicated by a grayscale analysis (Figure S6). Moreover, in this architecture the nanoparticles were in contact with the layered oxide from the top and bottom, which increases the metal/support perimeter area in comparison to nanoparticles having contact only from one direction.

Due to the sandwichlike confinement, the nanoparticles were stabilized against Ostwald ripening and preserved a size of 3.8 ± 0.6 nm during calcination and reduction. The high one-dimensional order along the stacking direction as already indicated by the TEM image was confirmed on the bulk scale

## Results

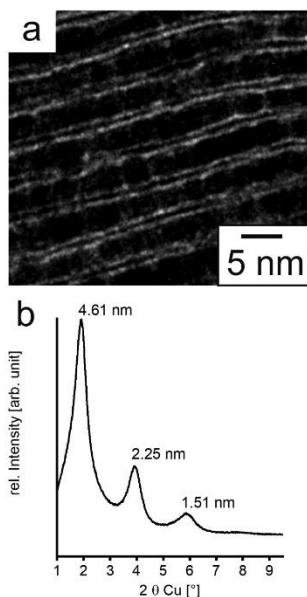


**Figure 1.** Evaluation of the lamellar structure of L-titanate@Pd@L-titanate: (a) TEM image of cross sections showing Pd nanoparticles confined between adjacent L-titanate nanosheets; (b) PXRD showing a series of basal reflections with a  $d$  value corresponding to the sum of the average diameter of the Pd nanoparticles and the thickness of single L-titanate nanosheets.

by powder X-ray diffraction (PXRD) showing a series of basal reflections with a periodicity of 4.61 nm (Figure 1b). The basal spacing reflects the distance between adjacent nanosheets and is well in agreement with the expected value based on the sum of the average size of a Pd nanoparticle (3.8 nm) and the thickness of a single L-titanate nanosheet (0.75 nm).

Furthermore, in transmission mode,  $hk\bar{h}$  bands were observed at 25.2, 47.9, and 62.1°  $2\theta$ , indicating that the two-dimensional structures of L-titanate nanosheets<sup>35</sup> were also preserved during preparation (Figure S4). This is in contrast to TBA<sup>+</sup> intercalated L-titanate that readily undergoes a phase transition to anatase when it is heated to 500 °C (Figure S7), indicating that the separation of the nanosheets by Pd nanoparticles stabilizes the layered structure.<sup>36</sup> When the nanosheets are kept at a 3.8 nm distance by intercalated Pd nanoparticles, this phase transition did not commence before 750 °C. This thermal stabilization is in line with observations that for single

nanosheets of  $Ti_{0.9}O_2^{0.36-}$  the onset of the phase transition was as high as 800 °C and rapidly decreased to 400 °C when six layers were stacked in close contact.<sup>37</sup>

Ar physisorption of L-titanate@Pd@L-titanate gave a type IV(a) isotherm with H2(b) hysteresis (Figure S8 and Table 1), which was attributed to a mesoporous structure.<sup>38</sup> The surface area on application of the BET equation was calculated to be 155  $m^2 g^{-1}$  and a median pore size of 6.5 nm was derived by applying the BJH method. The accessible metal dispersion was 19%, which expectedly was lower than for free-floating 3.8 nm Pd nanoparticles (29%), since sandwiching by the support covers a certain part of the surface (Table 1). Physisorption and chemisorption measurements both indicate that the nanoparticles were not densely packed, but mesopores between the nanoparticles make the Pd surface accessible.

As was already mentioned, deposition of ultrathin nanosheets is expected to have a significant effect on the electronic properties of a (noble) metal. XP spectra of the Pd 3d region were recorded to probe the potential influence of the special architecture as sketched in Scheme 1 on Pd. For comparison, the same Pd nanoparticles used for the fabrication of L-titanate@Pd@L-titanate were also deposited with 1 wt % loading on commercial supports having a slightly lower  $\zeta$  potential such as mesoporous  $\gamma-Al_2O_3$  ( $Pd_{ext}@Al_2O_3$ , -20 mV) and Degussa P25 (mixture of anatase and rutile,  $Pd_{ext}@P25$ , -27 mV) (Table 1).

Pd 3d spectra showed asymmetric signals of a spin orbit doublet with a splitting energy of 5.26 eV (Figure 2a). Asymmetric signals are derived from the high density of states of Pd at the Fermi level. The Pd 3d<sub>5/2</sub> signal of L-titanate@Pd@L-titanate was found at a binding energy (BE) of 335.6 eV, which was significantly shifted from the 335.0 eV reported for bulk Pd.<sup>39</sup> BEs of Pd nanoparticles deposited on  $TiO_2$  range from 334.6 to 335.5 eV.<sup>40-44</sup> These reported shifts in comparison to the value of bulk Pd might be ascribed to electronic metal–support interactions. Along this line, the shift to higher BE observed for L-titanate@Pd@L-titanate would indicate a slightly positively charged species of  $Pd^{0+}(\delta < 1)$ .<sup>45,46</sup> A shift to higher BE of small metal nanoparticles can, however, also originate from final state effects or an ill-defined reference level. The BE of the two reference catalysts  $Pd_{ext}@Al_2O_3$  and  $Pd_{ext}@P25$  were found at 335.1 and 335.3 eV, respectively. As these are comprised of identical nanoparticles, this indicates that the observed BE shift is indeed an initial state effect, rather than a final state effect. Moreover, the Ti 2p<sub>3/2</sub> signal of L-titanate@Pd@L-titanate is found at 458.5 eV, matching the literature value for pristine L-titanate (Figure 3a).<sup>47</sup> If the reference level would have been ill-defined, this peak should have been shifted to higher BE as well. The smaller shifts observed for the same Pd nanoparticles deposited on the reference supports therefore suggested a stronger

**Table 1.** Surface Areas, Nanoparticle Size, And Catalytic Properties of L-titanate@Pd@L-titanate and of Reference Catalysts after Calcination at 500 °C and Reduction at 200 °C

sample	$S_{BET}$ ( $m^2 g^{-1}$ ) <sup>a</sup>	pore $d_{50}$ (nm) <sup>b</sup>	$S_{Pd}$ ( $m^2 g^{-1}$ ) <sup>c</sup>	dispersion (%) <sup>c</sup>	core size of Pd (nm) <sup>d</sup>	$T_{50}$ (°C)	$E_A$ (kJ mol <sup>-1</sup> )
L-titanate@Pd@L-titanate	155	6.5	42	19	3.8 ± 0.6	86	38
$Pd_{ext}@P25$	32		0.8	18	3.8 ± 0.8	148	48
$Pd_{ext}@Al_2O_3$	156	7.6	1.0	23	3.6 ± 0.7	183	64

<sup>a</sup>Determined by Ar physisorption at 87 K and evaluated with the BET method. <sup>b</sup>Determined by the BJH method. <sup>c</sup>Determined by the CO chemisorption double isotherm method. <sup>d</sup>Determined by TEM.

## Results

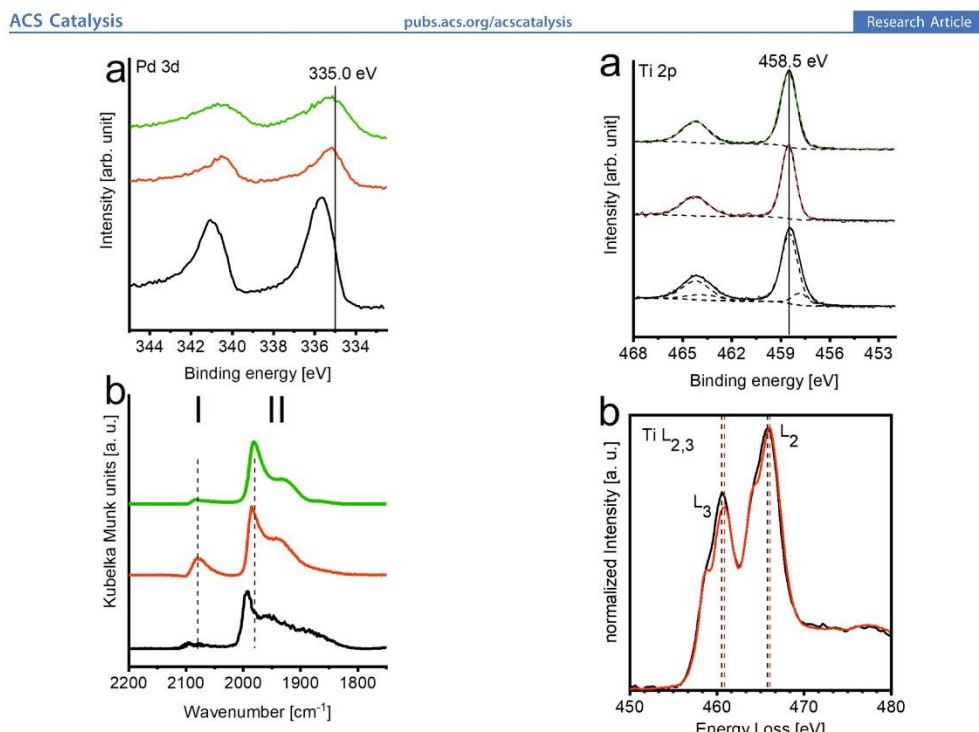


**Figure 2.** Evaluation of the surface oxidation state of Pd nanoparticles of L-titanate@Pd@L-titanate (black), Pd<sub>ext</sub>@P25 (red), and Pd<sub>ext</sub>@Al<sub>2</sub>O<sub>3</sub> (green): (a) XP spectra of the Pd 3d region; (b) CO DRIFT spectra recorded at room temperature after saturation of the surface at 60 mbar of CO partial pressure followed by outgassing to 2 mbar.

interaction between the Pd nanoparticles sandwiched in L-titanate.

Additionally, diffuse reflectance infrared Fourier transform spectroscopy (DRIFTS) of chemisorbed CO was applied to probe the oxidation state of surface Pd atoms. When the CO partial pressure was increased to 60 mbar, signals experienced a shift to higher wavenumbers due to dipolar coupling caused by increasing surface coverage (Figure S9). A closer look at the DRIFTS spectra recorded for samples that were outgassed to 2 mbar after having been saturated at a partial pressure of 60 mbar of CO yielded information on the electronic surface structure of Pd (Figure 2b) when they were compared with the reference samples. Two regions were observed for the C–O stretching vibration. In the case of Pd<sub>ext</sub>@Al<sub>2</sub>O<sub>3</sub>, the first region I with a peak centered around 2080 cm<sup>-1</sup> was ascribed to linearly bound CO to corners (Figure S9a).<sup>48,49</sup> The second and much broader region II is the superposition of several bands of CO bridge bound or 3-fold bound on different planes of Pd.<sup>50,51</sup> At the same equilibrium pressure of CO (2 mbar) the DRIFTS spectrum of L-titanate@Pd@L-titanate displayed the top band in region I with a peak centered at about 2090 cm<sup>-1</sup>. Furthermore, it appeared that the features of the second region also shifted by about 10–15 cm<sup>-1</sup> to higher wavenumbers. As the same nanoparticles were used to fabricate both materials, the shift to higher wavenumbers may be

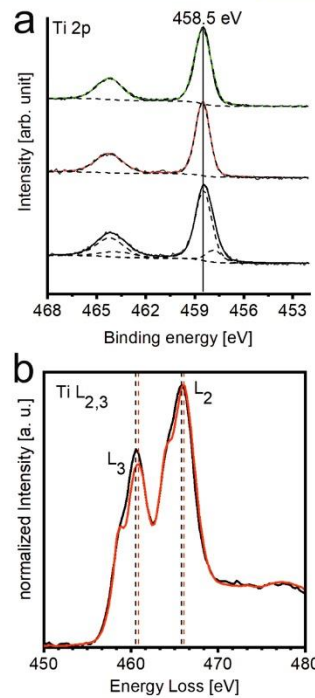


**Figure 3.** Evaluation of the charge state of Ti. (a) XP spectra of the Ti 2p region of L-titanate@Pd@L-titanate (black), H<sup>+</sup>-L-titanate (red), and Pd<sub>ext</sub>@P25 (green). The dashed lines are the peaks derived from deconvolution, and the colored lines are the overall fitted spectra. (b) EEL spectra at the Ti L<sub>2,3</sub> edge of L-titanate@Pd@L-titanate (black) and H<sup>+</sup>-L-titanate (red), normalized to L<sub>2</sub> maximum intensity.

attributed to weaker back-donation of electrons from the Pd surface to the antibonding CO  $2\pi^*$  orbital. This strengthens the C–O bond and consequently shifts the stretching vibration to higher wavenumbers. A partial positively charged Pd surface supported on L-titanate@Pd@L-titanate as suggested by XPS data might be the reason for reduced back-bonding.<sup>50</sup> The DRIFTS bands for the titania-supported reference (Pd<sub>ext</sub>@P25) are shifted in the direction of L-titanate@Pd@L-titanate in comparison to Pd<sub>ext</sub>@Al<sub>2</sub>O<sub>3</sub> but to a much lesser extent (e.g. 2083 cm<sup>-1</sup> for the top band). This is in line with the smaller positivation of Pd by the P25 support, as also corroborated by the XPS data.

The electron deficiency of Pd nanoparticles in L-titanate@Pd@L-titanate might actually arise from two factors. The first is the need to balance the permanent negative layer charge of L-titanate nanosheets. Furthermore, an additional contribution might originate from electronic interactions between the metal and the oxide that were reported between noble metals and noncharged TiO<sub>2</sub>.<sup>16,46</sup> To probe the latter, the Ti 2p regions in the XPS of L-titanate@Pd@L-titanate and of H<sup>+</sup>-L-titanate before intercalation of the nanoparticles were compared (Figure 3a). The Ti 2p<sub>3/2</sub> signal of H<sup>+</sup>-L-titanate was found at a BE of 458.5 eV, which can be ascribed to Ti<sup>4+</sup>.<sup>47</sup> For L-

titanate@Pd@L-titanate the Ti  $2p_{3/2}$  signal was significantly broadened and deconvolution of the signal gave an additional peak at 457.8 eV that might be attributed to  $Ti^{4+}(\delta < 4)$  sites. Additionally, electron energy loss spectroscopy (EELS) at the Ti  $L_{2,3}$  edge was conducted to further corroborate the existence of a slightly reduced Ti species (Figure 3b). The Ti  $L_{2,3}$  edge corresponds to the transition of Ti  $2p_{1/2}$  and Ti  $2p_{3/2}$  electrons into unoccupied states.<sup>52</sup> The signal position and shape for H<sup>+</sup>-L-titanate were in agreement with literature data.<sup>53</sup> The EEL spectrum of L-titanate@Pd@L-titanate was noticeably different from that of H<sup>+</sup>-L-titanate and supports the postulation of a reduced Ti species due to the presence of Pd. The white lines of Ti  $L_2$  and Ti  $L_3$  of L-titanate@Pd@L-titanate were shifted by about 0.35 eV to lower values in comparison to H<sup>+</sup>-L-titanate, as expected for reduced Ti species.<sup>52</sup> While this shift is small and is on the scale of the energy dispersion of these spectra (0.25 eV/channel), there are more spectral features that point toward reduced titanium: in the O K edge (Figure S10), the ionization edge is shifted to higher energies, which is in agreement with reduced Ti species.<sup>54</sup> Additionally, the induced crystal field splitting observed at the O K edge has been shown to decrease from Ti<sup>4+</sup> to more reduced species.<sup>54–56</sup> This effect is visible in the O K edge, as H<sup>+</sup>-L-titanate features a splitting of 2.2 eV, whereas this decreases to 1.8 eV upon introduction of Pd. This difference in crystal field can also be seen in the Ti L edge, where both the  $L_3$  and  $L_2$  edges of Ti<sup>4+</sup> are known to feature doublets due to this splitting.<sup>56</sup> The empty d band is split by a crystal field, and the resulting e<sub>g</sub> and t<sub>2g</sub> states then become part of the unoccupied conduction bands. The degree to which the d states are then filled up on partial charge transfer changes the intensities in the spectra and influences other effects that spectrally overlap with crystal-field splitting, such as exchange splitting, which results in different (apparent) e<sub>g</sub>/t<sub>2g</sub> ratios.<sup>55</sup> Finally, the  $L_2/L_3$  intensity ratios of Ti decrease with a decreasing average oxidation state of Ti.<sup>52,57</sup> Indeed, the ratio for L-titanate@Pd@L-titanate is 9% smaller than that for H<sup>+</sup>-L-titanate. All these EELS features are in line with the shifts in BE observed by XPS and indicated that the average oxidation number of Ti is slightly lowered after intercalation of Pd nanoparticles. In summary, XPS data for Pd and Ti, EELS for Ti, and CO-DRIFTS all gave significant evidence that electronic interactions between Pd nanoparticles and L-titanate nanosheets exist and might in turn influence the catalytic performance.

**2.2. Catalysis.** CO oxidation is one of the most frequently studied heterogeneous catalytic reactions due to its importance for exhaust gas purification or reduction of industrial emissions. Furthermore, as adsorbed CO is very sensitive to electronic influences of the support, the CO oxidation is ideally suited as a model reaction to probe for the potential influence of the special support architecture of L-titanate@Pd@L-titanate.<sup>58,59</sup> For the catalytic tests, the amount of catalyst was chosen to involve 1 mg of Pd in a fixed bed reactor with a feed gas stream of 50 mL/min (1 vol % CO, 1 vol % O<sub>2</sub>, balanced by N<sub>2</sub>). All catalysts were pretreated under the same conditions to ensure comparability (500 °C in an air atmosphere for 5 h, followed by H<sub>2</sub> treatment at 200 °C for 2 h). Three light-off curves were measured for each catalyst, and the third curve is presented in Figure 4.

L-titanate@Pd@L-titanate exhibited a high performance at low temperatures with temperatures for 50% conversion ( $T_{50}$ ) and for full conversion ( $T_{100}$ ) as low as 86 and 110 °C, respectively (Figure 4). The same Pd nanoparticles deposited

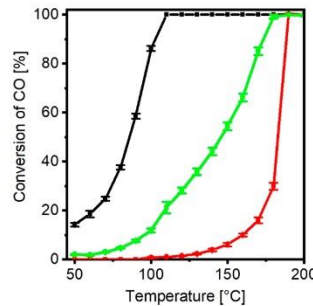


**Figure 4.** Light-off curves of L-titanate@Pd@L-titanate (black), Pd<sub>ext</sub>@P25 (green), and Pd<sub>ext</sub>@Al<sub>2</sub>O<sub>3</sub> (red). Conditions: 1 mg of Pd per catalysis; 50 mL/min (1 vol % CO, 1 vol % O<sub>2</sub>, balanced in N<sub>2</sub>).

on γ-Al<sub>2</sub>O<sub>3</sub> (Pd<sub>ext</sub>@Al<sub>2</sub>O<sub>3</sub>) were inferior by far with  $T_{50}$  and  $T_{100}$  values of 183 and 190 °C, respectively. The activation energy  $E_A$  of 64 kJ mol<sup>-1</sup> for Pd<sub>ext</sub>@Al<sub>2</sub>O<sub>3</sub> as derived from the Arrhenius plot (determined below conversions of 10%, Figure S11) matched reported values.<sup>58</sup> The low  $E_A$  of 38 kJ mol<sup>-1</sup> observed for L-titanate@Pd@L-titanate is in the range typically found for catalysts that follow a Mars–van Krevelen type reaction mechanism.<sup>60</sup>

The shape of the light-off curve of Pd<sub>ext</sub>@Al<sub>2</sub>O<sub>3</sub> showed a sharp increase in conversion at higher temperatures. CO oxidation for Pd@Al<sub>2</sub>O<sub>3</sub> catalysts follows the Langmuir–Hinshelwood mechanism.<sup>28</sup> CO and O<sub>2</sub> compete for adsorption at the Pd surface. CO binds strongly to the Pd surface at lower temperature and O<sub>2</sub> can only coadsorb at higher temperatures. As the reaction is highly exothermic, the conversion normally increases sharply after light-off.

As was recently reported,<sup>21</sup> sandwiching of Pd nanoparticles between the negatively charged nanosheets of the layered silicate hectorite (Hec@Pd65@Hec) decreased the  $T_{50}$  value from 191 to 145 °C for the oxidation of CO in comparison to the same nanoparticles deposited on γ-Al<sub>2</sub>O<sub>3</sub>. For Hec@Pd65@Hec a positive surface charge was observed by shifts in the XPS Pd 3d region and CO-DRIFTS. This positive surface charge was attributed not only to balancing of the negative layer charge but also to electronic interactions between the silicate nanosheets and Pd. As the CO reaction followed the Langmuir–Hinshelwood mechanism that requires adsorption of both CO and O<sub>2</sub> to the noble-metal surface, the positive surface charge of Pd decreased the adsorption energy of CO, which allowed O<sub>2</sub> to already coadsorb at lower temperatures. Here, negatively charged nanosheets of a different composition, but similar thickness and charge density, were applied. These nanosheets demonstrated a similar influence on the surface charge of Pd and the electronic interaction between the support and the metal (Figures 2 and 3). However, on application of the same catalytic conditions, the performance of L-titanate@Pd@L-titanate was much higher at low temperatures ( $T_{50}$  value of 86 °C). This implies that L-titanate must have some additional influence on the catalytic activity. A possible explanation is that L-titanate might be able to offer oxygen at the nanoparticle/oxide perimeter that omits the necessity of oxygen adsorption directly to the Pd surface. This would allow the reaction to already occur at lower temperatures. Kinetic measurements (Figure 5 and Tables S2 and S3)

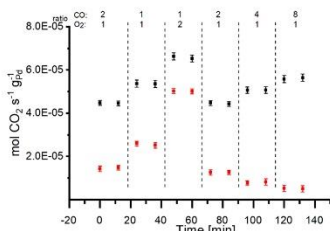


**Figure 5.** Kinetic rates of L-titanate@Pd@L-titanate at 70 °C (black) and Pd<sub>ext</sub>@Al<sub>2</sub>O<sub>3</sub> at 130 °C (red) at different partial pressures of CO and O<sub>2</sub>.

were applied to study the influence of the CO and O<sub>2</sub> partial pressures on the reaction rates. Therefore, the composition of the reactant flow was varied, while the temperature was kept constant at 70 and 130 °C for L-titanate@Pd@L-titanate and Pd<sub>ext</sub>@Al<sub>2</sub>O<sub>3</sub>, respectively. Additional information about the procedure is given in the Supporting Information.

The reaction order with respect to the O<sub>2</sub> partial pressure for Pd<sub>ext</sub>@Al<sub>2</sub>O<sub>3</sub> was +0.91, which is consistent with the expected order of 1 for a Langmuir–Hinshelwood mechanism.<sup>61,62</sup> In contrast, the reaction order with respect to the O<sub>2</sub> partial pressure of L-titanate@Pd@L-titanate is +0.29. The low order is a hint that oxygen is provided from the supporting oxide nanosheets rather than from the gas phase.<sup>28</sup> While oxygen donation is actually expected for oxides such as bulk anatase,<sup>26,29</sup> it is still somewhat surprising that even sub-nanometer thick corrugated single layers of condensed octahedra are capable of coping with the structural defects caused by donating oxygen. Furthermore, the reaction order with respect to CO was +0.13 for L-titanate@Pd@L-titanate, while it was −0.67 for Pd<sub>ext</sub>@Al<sub>2</sub>O<sub>3</sub>. The negative order for the latter is expected for metallic Pd, as strongly binding CO poisons the surface. In contrast to this, the positive order observed for L-titanate@Pd@L-titanate indicated that this catalyst system does not suffer from CO poisoning at lower temperatures.

The T<sub>50</sub> (148 °C) and E<sub>A</sub> values (48 kJ mol<sup>−1</sup>) for Pd<sub>ext</sub>@P25 were much higher than for L-titanate@Pd@L-titanate. As the P25 support can also provide oxygen from its lattice, the crucial factor for the higher activity of L-titanate@Pd@L-titanate appears to be the special sandwich architecture and the advantageous electronic interaction with the anionic support. Another activity-enhancing factor is the interface area between the support and the metal, through which oxygen can be donated from the support to the metal. The activity of model catalysts of Pd nanoparticles deposited on CeO<sub>2</sub> increased with the interface area between metal and support.<sup>31</sup> Due to the special architecture of L-titanate@Pd@L-titanate the nanoparticles are in contact with the oxide from the top and bottom, creating a large boundary in comparison with nanoparticles solely supported on external surfaces.

As single-atom and small Pd cluster catalytic systems have shown a higher catalytic activity,<sup>28</sup> the potential stabilization of such species might be an alternative explanation for the good performance of L-titanate@Pd@L-titanate. Since the preparation involved calcination at 500 °C followed by reduction, we regard it as highly unlikely that such small species could exist in L-titanate@Pd@L-titanate.

The sandwich architecture of L-titanate@Pd@L-titanate, moreover, inhibited catalyst deactivation. At 100 °C no significant reduction in the activity was observed after 72 h on stream (Figure S12a). Carbonate formation is reported to be one reason for catalyst deactivation,<sup>2</sup> but for L-titanate@Pd@L-titanate this seems to be insignificant (Figure S12b). The average nanoparticle diameter was determined to be 3.9 ± 0.7 nm, which within experimental error was unchanged, demonstrating a hampered sintering of the nanoparticles. Furthermore, L-titanate@Pd@L-titanate was calcined at 700 °C for 40 h to probe the efficiency of the sandwich confinement to hamper Ostwald ripening under harsh conditions. The light-off curve after this treatment revealed a T<sub>50</sub> value of 92 °C that was only slightly higher than the 86 °C observed for L-titanate@Pd@L-titanate after calcination at 500 °C (Figure S12c). This further demonstrated the good stability of L-titanate@Pd@L-titanate, making the catalyst promising for applications where the catalyst has to stand more demanding conditions.

## CONCLUSION

Ultrathin oxides have been demonstrated to alter the electronic structure of an underlying (noble) metal or create highly active perimeters on only partial coverage. This architecture can be mimicked by intercalation of positively charged metal nanoparticles between negatively charged nanosheets, as proven for L-titanate or previously for silicate nanosheets. Sandwiching Pd nanoparticles between negatively charged nanosheets triggers a partially oxidized state of the metal, as evidenced from an XPS shift of the Pd 3d region by +0.6 eV, and shifts of the C–O stretching bands of +10–20 cm<sup>−1</sup>, as derived from DRIFTS measurements. In contrast to the silicate nanosheets investigated previously, L-titanate nanosheets can additionally provide lattice oxygen, which further enhanced the performance (T<sub>50</sub> value of 86 °C) in comparison to the silicate nanosheets (T<sub>50</sub> value of 145 °C). Obviously, this special support architecture might also be attractive for other catalytic reactions such as methane combustion.<sup>63,64</sup> The synthesis route via intercalation into nematic phases of anionic nanosheets is not restricted to Pd or to titanate nanosheets. Other liquid crystalline supports such as layered antimony phosphates<sup>65,66</sup> will be explored in the future. Needless to say, the concept can also be extended to catalytically more attractive alloy nanoparticles.<sup>67–70</sup>

## ASSOCIATED CONTENT

### Supporting Information

The Supporting Information is available free of charge at <https://pubs.acs.org/doi/10.1021/acscatal.1c00031>.

Experimental section including catalyst preparation and measurement techniques, SAXS of the nematic L-titanate phase, TEM image of Pd nanoparticles, elemental analysis of L-titanate@Pd@L-titanate, FTIR spectrum of L-titanate@Pd@L-titanate, XRD patterns for phase evaluation, elemental mapping, grayscale analysis of L-titanate@Pd@L-titanate, Ar isotherms, DRIFT spectra at various CO partial pressures, EEL spectra at O K edge, Arrhenius plots, and details about the kinetic investigation and stability test (PDF)

## ■ AUTHOR INFORMATION

### Corresponding Authors

Takayoshi Sasaki — International Centre for Materials Nanoarchitectonics (WPI-MANA), National Institute for Materials Science (NIMS), Tsukuba, Ibaraki 305-0044, Japan;  orcid.org/0000-0002-2872-0427;  
Email: sasaki.takayoshi@nims.go.jp

Josef Breu — Bavarian Polymer Institute and Department of Chemistry, University of Bayreuth, 95447 Bayreuth, Germany;  orcid.org/0000-0002-2547-3950;  
Email: josef.breu@uni-bayreuth.de

### Authors

Kevin Ament — Bavarian Polymer Institute and Department of Chemistry, University of Bayreuth, 95447 Bayreuth, Germany

Daniel R. Wagner — Bavarian Polymer Institute and Department of Chemistry, University of Bayreuth, 95447 Bayreuth, Germany

Thomas Götsch — Department of Inorganic Chemistry, Fritz-Haber-Institut der Max-Planck-Gesellschaft, 14195 Berlin, Germany;  orcid.org/0000-0003-3673-317X

Takayuki Kikuchi — International Centre for Materials Nanoarchitectonics (WPI-MANA), National Institute for Materials Science (NIMS), Tsukuba, Ibaraki 305-0044, Japan

Jutta Kröhnert — Department of Inorganic Chemistry, Fritz-Haber-Institut der Max-Planck-Gesellschaft, 14195 Berlin, Germany

Annette Trunschke — Department of Inorganic Chemistry, Fritz-Haber-Institut der Max-Planck-Gesellschaft, 14195 Berlin, Germany;  orcid.org/0000-0003-2869-0181

Thomas Lunkenstein — Department of Inorganic Chemistry, Fritz-Haber-Institut der Max-Planck-Gesellschaft, 14195 Berlin, Germany;  orcid.org/0000-0002-8957-4216

Complete contact information is available at:  
<https://pubs.acs.org/10.1021/acscatal.1c00031>

### Author Contributions

The manuscript was written through contributions of all authors. All authors have given approval to the final version of the manuscript.

### Notes

The authors declare no competing financial interest.

## ■ ACKNOWLEDGMENTS

This work was supported by the Deutsche Forschungsgemeinschaft (SFB 840, A2). K.A. thanks the NIMS for internship and the Elite Network of Bavaria for a Ph.D. fellowship. We thank Marco Schwarzmann for the preparation of samples for cross-sectional TEM and SEM. We appreciate the support of the Keylab for Optical and Electron Microscopy of the Bavarian Polymer Institute (BPI). We thank Rhett Kempe for the access to his micro reactor. The XPS/UPS facility (PHI 5000 VersaProbe III system) at the Device Engineering Keylab in Bavarian Polymer Institute, University of Bayreuth, is acknowledged. T.G. acknowledges funding by the Fonds zur Förderung der wissenschaftlichen Forschung (FWF, Austrian Science Fund) via project number J4278.

## ■ REFERENCES

- (1) van Deelen, T. W.; Hernández Mejía, C.; de Jong, K. P. Control of Metal-Support Interactions in Heterogeneous Catalysts to Enhance Activity and Selectivity. *Nat. Catal.* **2019**, *2*, 955–970.
- (2) Wang, Y.; Widmann, D.; Behm, R. J. Influence of TiO<sub>2</sub> Bulk Defects on CO Adsorption and CO Oxidation on Au/TiO<sub>2</sub>: Electronic Metal-Support Interactions (EMSI) in Supported Au Catalysts. *ACS Catal.* **2017**, *7*, 2339–2345.
- (3) Bai, Y.; Huang, H.; Wang, C.; Long, R.; Xiong, Y. Engineering the Surface Charge States of Nanostructures for Enhanced Catalytic Performance. *Mater. Chem. Front.* **2017**, *1*, 1951–1964.
- (4) Chen, Y.; Chen, J.; Qu, W.; George, C.; Aouine, M.; Vermoux, P.; Tang, X. Well-Defined Palladium-Ceria Interfacial Electronic Effects Trigger CO Oxidation. *Chem. Commun.* **2018**, *54*, 10140–10143.
- (5) Lykhach, Y.; Kozlov, S. M.; Skala, T.; Tovar, A.; Stetsovych, V.; Tsud, N.; Dvorak, F.; Johaneck, V.; Neitzel, A.; Myslivecek, J.; Fabris, S.; Matolin, V.; Neyman, K. M.; Libuda, J. Counting Electrons on Supported Nanoparticles. *Nat. Mater.* **2016**, *15*, 284–288.
- (6) Lykhach, Y.; Kubat, J.; Neitzel, A.; Tsud, N.; Vorokhta, M.; Skala, T.; Dvorak, F.; Kosto, Y.; Prince, K. C.; Matolin, V.; Johaneck, V.; Myslivecek, J.; Libuda, J. Charge Transfer and Spillover Phenomena in Ceria-Supported Iridium Catalysts: A Model Study. *J. Chem. Phys.* **2019**, *151*, 204703.
- (7) Conner, W. C.; Falconer, J. L. Spillover in Heterogeneous Catalysis. *Chem. Rev.* **1995**, *95*, 759–788.
- (8) Lunkenstein, T.; Schumann, J.; Behrens, M.; Schlögl, R.; Willinger, M. G. Formation of a ZnO Overlayer in Industrial Cu/ZnO/Al<sub>2</sub>O<sub>3</sub> Catalysts Induced by Strong Metal-Support Interactions. *Angew. Chem., Int. Ed.* **2015**, *54*, 4544–4548.
- (9) Pacchioni, G.; Freund, H. Electron Transfer at Oxide Surfaces. The MgO Paradigm: From Defects to Ultrathin Films. *Chem. Rev.* **2013**, *113*, 4035–4072.
- (10) Freund, H. J. The Surface Science of Catalysis and More, Using Ultrathin Oxide Films as Templates: A Perspective. *J. Am. Chem. Soc.* **2016**, *138*, 8985–8996.
- (11) Pacchioni, G.; Freund, H.-J. Controlling the Charge State of Supported Nanoparticles in Catalysis: Lessons from Model Systems. *Chem. Soc. Rev.* **2018**, *47*, 8474–8502.
- (12) Giordano, L.; Pacchioni, G. Oxide Films at the Nanoscale: New Structures, New Functions, and New Materials. *Acc. Chem. Res.* **2011**, *44*, 1244–1252.
- (13) Jaouen, T.; Jézéquel, G.; Delhayé, G.; Lépine, B.; Turban, P.; Schieffer, P. Work Function Shifts, Schottky Barrier Height, and Ionization Potential Determination of Thin MgO Films on Ag(001). *Appl. Phys. Lett.* **2010**, *97*, 232104–13.
- (14) Giordano, L.; Cinquini, F.; Pacchioni, G. Tuning the Surface Metal Work Function by Deposition of Ultrathin Oxide Films: Density Functional Calculations. *Phys. Rev. B: Condens. Matter Mater. Phys.* **2006**, *73*, 045414–16.
- (15) Prada, S.; Martínez, U.; Pacchioni, G. Work Function Changes Induced by Deposition of Ultrathin Dielectric Films on Metals: A Theoretical Analysis. *Phys. Rev. B: Condens. Matter Mater. Phys.* **2008**, *78*, 235423.
- (16) Tosoni, S.; Pacchioni, G. Hydrogen Adsorption on Free-Standing and Ag-Pt Supported TiO<sub>2</sub> Thin Films. *J. Phys. Chem. C* **2019**, *123*, 7952–7960.
- (17) Pan, Q.; Li, L.; Shaikhutdinov, S.; Fujimori, Y.; Hollerer, M.; Sterrer, M.; Freund, H. J. Model Systems in Heterogeneous Catalysis: Towards the Design and Understanding of Structure and Electronic Properties. *Faraday Discuss.* **2018**, *208*, 307–323.
- (18) Schneider, W. D.; Heyde, M.; Freund, H. J. Charge Control in Model Catalysis: The Decisive Role of the Oxide-Nanoparticle Interface. *Chem. - Eur. J.* **2018**, *24*, 2317–2327.
- (19) Stöter, M.; Kunz, D. A.; Schmidt, M.; Hirsemann, D.; Kalo, H.; Putz, B.; Senker, J.; Breu, J. Nanoplatelets of Sodium Hectorite Showing Aspect Ratios of ≈20,000 and Superior Purity. *Langmuir* **2013**, *29*, 1280–1285.
- (20) Rosenfeldt, S.; Stöter, M.; Schlenk, M.; Martin, T.; Albuquerque, R. Q.; Förster, S.; Breu, J. In-Depth Insights into the

## Results

- Key Steps of Delamination of Charged 2D Nanomaterials. *Langmuir* **2016**, *32*, 10582–10588.
- (21) Ament, K.; Köwitsch, N.; Hou, D.; Götsch, T.; Kröhnert, J.; Heard, C. J.; Trunschke, A.; Lunkenstein, T.; Armbrüster, M.; Breu, J. Nanoparticles Supported on Sub-Nanometer Oxide Films: Scaling Model Systems to Bulk Materials. *Angew. Chem., Int. Ed.* **2021**, DOI: 10.1002/anie.202015138.
- (22) Sasaki, T.; Kooli, F.; Iida, M.; Michue, Y.; Takenouchi, S.; Yajima, Y.; Izumi, F.; Chakoumakos, B. C.; Watanabe, M. A Mixed Alkali Metal Titanate with the Lepidocrocite-Like Layered Structure. Preparation, Crystal Structure, Protonic Form, and Acid-Base Intercalation Properties. *Chem. Mater.* **1998**, *10*, 4123–4128.
- (23) Tanaka, T.; Ebina, Y.; Takada, K.; Kurashima, K.; Sasaki, T. oversized Titanate Nanosheet Crystallites Derived from Flux-Grown Layered Titanate Single Crystals. *Chem. Mater.* **2003**, *15*, 3564–3568.
- (24) Maluangnont, T.; Matsuba, K.; Geng, F.; Ma, R.; Yamauchi, Y.; Sasaki, T. Osmotic Swelling of Layered Compounds as a Route to Producing High-Quality Two-Dimensional Materials. A Comparative Study of Tetramethylammonium versus Tetrabutylammonium Cation in a Lepidocrocite-Type Titanate. *Chem. Mater.* **2013**, *25*, 3137–3146.
- (25) Sano, K.; Kim, Y. S.; Ishida, Y.; Ebina, Y.; Sasaki, T.; Hikima, T.; Aida, T. Photonic Water Dynamically Responsive to External Stimuli. *Nat. Commun.* **2016**, *7*, 12559.
- (26) Jin, M.; Park, J.-N.; Shon, J. K.; Kim, J. H.; Li, Z.; Park, Y.-K.; Kim, J. M. Low-Temperature CO Oxidation over Pd Catalysts Supported on Highly Ordered Mesoporous Metal Oxides. *Catal. Today* **2012**, *185*, 183–190.
- (27) Yoon, K.; Yang, Y.; Lu, P.; Wan, D.; Peng, H. C.; Stamm, Masiás, K.; Fanson, P. T.; Campbell, C. T.; Xia, Y. A Highly Reactive and Sinter-Resistant Catalytic System Based on Platinum Nanoparticles Embedded in the Inner Surfaces of CeO<sub>2</sub> Hollow Fibers. *Angew. Chem., Int. Ed.* **2012**, *51*, 9543–9546.
- (28) Peterson, E. J.; DeLaRiva, A. T.; Lin, S.; Johnson, R. S.; Guo, H.; Miller, J. T.; Hun Kwak, J.; Peden, C. H.; Kiefer, B.; Allard, L. F.; Ribeiro, F. H.; Datye, A. K. Low-Temperature Carbon Monoxide Oxidation Catalyzed by Regenerable Atomically Dispersed Palladium on Alumina. *Nat. Commun.* **2014**, *5*, 4885.
- (29) Zhai, X.; Liu, C.; Chang, Q.; Zhao, C.; Tan, R.; Peng, H.; Liu, D.; Zhang, P.; Gui, J. TiO<sub>2</sub>-Nanosheet-Assembled Microspheres as Pd-Catalyst Support for Highly-Stable Low-Temperature CO Oxidation. *New J. Chem.* **2018**, *42*, 18066–18076.
- (30) Suchorski, Y.; Kozlov, S. M.; Bespalov, L.; Datler, M.; Vogel, D.; Budinska, Z.; Neyman, K. M.; Rupprechter, G. The Role of Metal/Oxide Interfaces for Long-Range Metal Particle Activation During CO Oxidation. *Nat. Mater.* **2018**, *17*, S19–S22.
- (31) Cargnello, M.; Doan-Nguyen, V. V. T.; Grodon, T. R.; Diaz, R. E.; Stach, E. A.; Gorte, R. J.; Fornasiero, P.; Murray, C. B. Control of Metal Nanocrystal Size Reveals Metal-Support Interface Role for Ceria Catalysts. *Science* **2013**, *341*, 771–773.
- (32) Flanagan, K. A.; Sullivan, J. A.; Müller-Bunz, H. Preparation and Characterization of 4-Dimethylaminopyridine-Stabilized Palladium Nanoparticles. *Langmuir* **2007**, *23*, 12508–12520.
- (33) Gao, T.; Fjellvåg, H.; Norby, P. Protonic Titanate Derived from Cs<sub>x</sub>Ti<sub>2-x/2</sub>Mg<sub>x/2</sub>O<sub>4</sub> ( $x = 0.7$ ) with Lepidocrocite-Type Layered Structure. *J. Mater. Chem.* **2009**, *19*, 787–794.
- (34) Yuan, H.; Besselinck, R.; Liao, Z.; Ten Elshof, J. E. The Swelling Transition of Lepidocrocite-Type Protonated Layered Titanates into Anatase Under Hydrothermal Treatment. *Sci. Rep.* **2015**, *4*, 4584.
- (35) Sasaki, T.; Nakano, S.; Yamauchi, S.; Watanabe, M. Fabrication of Titanium Dioxide Thin Flakes and Their Porous Aggregate. *Chem. Mater.* **1997**, *9*, 602–608.
- (36) Wang, L.; Sasaki, T. Titanium Oxide Nanosheets: Graphene Analogues with Versatile Functionalities. *Chem. Rev.* **2014**, *114*, 9455–9486.
- (37) Fukuda, K.; Ebina, Y.; Shibata, T.; Aizawa, T.; Nakai, I.; Sasaki, T. Unusual Crystallization Behaviors of Anatase Nanocrystallites from a Molecularly Thin Titania Nanosheet and Its Stacked Forms: Increase in Nucleation Temperature and Oriented Growth. *J. Am. Chem. Soc.* **2007**, *129*, 202–209.
- (38) Thommes, M.; Kaneko, K.; Neimark, A. V.; Olivier, J. P.; Rodriguez-Reinoso, F.; Rouquerol, J.; Sing, K. S. W. Physisorption of Gases, with Special Reference to the Evaluation of Surface Area and Pore Size Distribution (IUPAC Technical Report). *Pure Appl. Chem.* **2015**, *87*, 1051–1069.
- (39) Arrigo, R.; Schuster, M. E.; Abate, S.; Wrabetz, S.; Amakawa, K.; Teschner, D.; Freni, M.; Centi, G.; Perathoner, S.; Havecker, M.; Schlögl, R. Dynamics of Palladium on Nanocarbon in the Direct Synthesis of H<sub>2</sub>O<sub>2</sub>. *ChemSusChem* **2014**, *7*, 179–194.
- (40) Yuan, X.; Wang, X.; Liu, X.; Ge, H.; Yin, G.; Dong, C.; Huang, F. Ti<sup>3+</sup>-Promoted High Oxygen-Reduction Activity of Pd Nanodots Supported by Black Titania Nanobelts. *ACS Appl. Mater. Interfaces* **2016**, *8*, 27654–27660.
- (41) Yamada, T.; Masuda, H.; Park, K.; Tachikawa, T.; Ito, N.; Ichikawa, T.; Yoshimura, M.; Takagi, Y.; Sawama, Y.; Ohya, Y.; Sajiki, H. Development of Titanium Dioxide-Supported Pd Catalysts for Ligand-Free Suzuki-Miyaura Coupling of Aryl Chlorides. *Catalysts* **2019**, *9*, 461.
- (42) Wu, J.; Lu, S.; Ge, D.; Zhang, L.; Chen, W.; Gu, H. Photocatalytic Properties of Pd/TiO<sub>2</sub> Nanosheets for Hydrogen Evolution from Water Splitting. *RSC Adv.* **2016**, *6*, 67502–67508.
- (43) Tapin, B.; Epron, F.; Espeel, C.; Ly, B. K.; Pine, C.; Besson, M. Study of Monometallic Pd/TiO<sub>2</sub> Catalysts for the Hydrogenation of Succinic Acid in Aqueous Phase. *ACS Catal.* **2013**, *3*, 2327–2335.
- (44) Selishchev, D. S.; Kolobov, N. S.; Bukhtiyarov, A. V.; Gerasimov, E. Y.; Gubanov, A. I.; Kozlov, D. V. Deposition of Pd Nanoparticles on TiO<sub>2</sub> Using a Pd(acac)<sub>2</sub> Precursor For Photocatalytic Oxidation of CO Under UV-LED Irradiation. *Appl. Catal., B* **2018**, *235*, 214–224.
- (45) Babu, N. S.; Lingaiah, N. L.; Gopinath, R.; Reddy, P. S. S.; Prasad, P. S. S. Characterization and Reactivity of Alumina-Supported Pd Catalysts for the Room-Temperature Hydrodechlorination of Chlorobenzene. *J. Phys. Chem. C* **2007**, *111*, 6447–6453.
- (46) Camposeco, R.; Castillo, S.; Hinojosa-Reyes, M.; Zanella, R.; López-Curiel, J. C.; Fuentes, G. A.; Mejía-Centeno, I. Active TiO<sub>2</sub>-Nanostructured Surfaces for CO Oxidation on Rh Model Catalysts at Low-Temperature. *Catal. Lett.* **2019**, *149*, 1565–1578.
- (47) Sasaki, T.; Ebina, Y.; Fukuda, K.; Tanaka, T.; Harada, M.; Watanabe, M. Titania Nanostructured Films Derived from a Titania Nanosheet Polyacrylate Multilayer Assembly via Heat Treatment and UV Irradiation. *Chem. Mater.* **2002**, *14*, 3524–3530.
- (48) Zhu, B.; Jang, B. W. L. Insights into Surface Properties of Non-Thermal RF Plasmas Treated Pd/TiO<sub>2</sub> in Acetylene Hydrogenation. *J. Mol. Catal. A: Chem.* **2014**, *395*, 137–144.
- (49) Oh, J.; Bathula, H. B.; Park, J. H.; Suh, Y.-W. A Sustainable Mesoporous Palladium-Alumina Catalyst for Efficient Hydrogen Release from N-Neterocyclic Liquid Organic Hydrogen Carriers. *Commun. Chem.* **2019**, *2*, 68.
- (50) Bertarione, S.; Scarano, D.; Zecchina, A.; Johánek, V.; Hoffmann, J.; Schauermann, S.; Frank, M. M.; Libuda, J.; Rupprechter, G.; Freund, H.-J. Surface Reactivity of Pd Nanoparticles Supported on Polycrystalline Substrates as Compared to Thin Film Model Catalysts: Infrared Study of CO Adsorption. *J. Phys. Chem. B* **2004**, *108*, 3603–3613.
- (51) Murata, K.; Eleeda, E.; Ohyama, J.; Yamamoto, Y.; Arai, S.; Satsuma, A. Identification of Active Sites in CO Oxidation over a Pd/Al<sub>2</sub>O<sub>3</sub> Catalyst. *Phys. Chem. Chem. Phys.* **2019**, *21*, 18128–18137.
- (52) Otten, M. T.; Miner, B.; Rask, J. H.; Buseck, P. R. The Determination of Ti, Mn and Fe Oxidation States in Minerals by Electron Energy-Loss Spectroscopy. *Ultramicroscopy* **1985**, *18*, 285–289.
- (53) Ohwada, M.; Kimoto, K.; Ebina, Y.; Sasaki, T. EELS Study of Fe- or Co-Doped Titania Nanosheets. *Microscopy* **2015**, *64*, 77–85.
- (54) Lee, D. K.; Choi, J. I.; Lee, G. H.; Kim, Y.-H.; Kang, J. K. Energy States of a Core-Shell Metal Oxide Photocatalyst Enabling Visible Light Absorption and Utilization in Solar-to-Fuel Conversion of Carbon Dioxide. *Adv. Energy Mater.* **2016**, *6*, 1600583.

## Results

- (55) Frati, F.; Hunault, M. O. J. Y.; de Groot, F. M. F. Oxygen K-Edge X-Ray Absorption Spectra. *Chem. Rev.* **2020**, *120*, 4056–4110.
- (56) Li, Y.; Yang, Y.; Shu, X.; Wan, D.; Wei, N.; Yu, X.; Breese, M. B. H.; Venkatesan, T.; Xue, J. M.; Liu, Y.; Li, S.; Wu, T.; Chen, J. From Titanium Sesquioxide to Titanium Dioxide: Oxidation-Induced Structural, Phase, and Property Evolution. *Chem. Mater.* **2018**, *30*, 4383–4392.
- (57) Tan, H.; Verbeeck, J.; Abakumov, A.; Van Tendeloo, G. Oxidation State and Chemical Shift Investigation in Transition Metal Oxides by EELS. *Ultramicroscopy* **2012**, *116*, 24–33.
- (58) Zhou, Y.; Wang, Z.; Liu, C. Perspective on CO Oxidation over Pd-Based Catalysts. *Catal. Sci. Technol.* **2015**, *5*, 69–81.
- (59) Freund, H. J.; Meijer, G.; Scheffler, M.; Schlögl, R.; Wolf, M. CO Oxidation as a Prototypical Reaction for Heterogeneous Processes. *Angew. Chem., Int. Ed.* **2011**, *50*, 10064–10094.
- (60) Liu, L.; Zhou, F.; Wang, L.; Qi, X.; Shi, F.; Deng, Y. Low-Temperature CO Oxidation over Supported Pt, Pd Catalysts: Particular Role of Fe<sub>3</sub>O<sub>4</sub> Support for Oxygen Supply During Reactions. *J. Catal.* **2010**, *274*, 1–10.
- (61) Johnson, R. S.; DeLaRiva, A.; Ashbacher, V.; Halevi, B.; Villanueva, C. J.; Smith, G. K.; Lin, S.; Datye, A. K.; Guo, H. The CO Oxidation Mechanism and Reactivity on PdZn Alloys. *Phys. Chem. Chem. Phys.* **2013**, *15*, 7768–76.
- (62) Han, B.; Li, T.; Zhang, J.; Zeng, C.; Matsumoto, H.; Su, Y.; Qiao, B.; Zhang, T. A Highly Active Rh<sub>1</sub>/CeO<sub>2</sub> Single-Atom Catalyst for Low-Temperature CO Oxidation. *Chem. Commun.* **2020**, *56*, 4870–4873.
- (63) Goodman, E. D.; Schwabe, J. A.; Cargnello, M. Mechanistic Understanding and the Rational Design of Sinter-Resistant Heterogeneous Catalysts. *ACS Catal.* **2017**, *7*, 7156–7173.
- (64) Cargnello, M.; Jaen, J. J. D.; Garrido, J. C. H.; Bakhtutsky, K.; Montini, T.; Gamez, J. J. C.; Gorte, R. J.; Fornasiero, P. Exceptional Activity for Methane Combustion over Modular Pd@CeO<sub>2</sub> Subunits on Functionalized Al<sub>2</sub>O<sub>3</sub>. *Science* **2012**, *337*, 713–717.
- (65) Davidson, P.; Penisson, C.; Constantin, D.; Gabriel, J. P. Isotropic, Nematic, and Lamellar Phases in Colloidal Suspensions of Nanosheets. *Proc. Natl. Acad. Sci. U. S. A.* **2018**, *115*, 6662–6667.
- (66) Gabriel, J. P.; Camerel, F.; Lemaire, B. J.; Desvaux, H.; Davidson, P.; Batail, P. Swollen Liquid-Crystalline Lamellar Phase Based on Extended Solid-Like Sheets. *Nature* **2001**, *413*, 504–508.
- (67) Ahmad, Y. H.; Mohamed, A. T.; Mahmoud, K. A.; Aljaber, A. S.; Al-Qaradawi, S. Y. Natural Clay-Supported Palladium Catalysts for Methane Oxidation Reaction: Effect of Alloying. *RSC Adv.* **2019**, *9*, 32928–32935.
- (68) Goodman, E. D.; Dai, S.; Yang, A.-C.; Wrasman, C. J.; Gallo, A.; Bare, S. R.; Hoffman, A. S.; Jaramillo, T. F.; Graham, G. W.; Pan, X.; Cargnello, M. Uniform Pt/Pd Bimetallic Nanocrystals Demonstrate Platinum Effect on Palladium Methane Combustion: Activity and Stability. *ACS Catal.* **2017**, *7*, 4372–4380.
- (69) Huang, B.; Kobayashi, H.; Yamamoto, T.; Matsumura, S.; Nishida, Y.; Sato, K.; Nagaoka, K.; Kawaguchi, S.; Kubota, Y.; Kitagawa, H. Solid-Solution Alloying of Immiscible Ru and Cu with Enhanced CO Oxidation Activity. *J. Am. Chem. Soc.* **2017**, *139*, 4643–4646.
- (70) Armbrüster, M. Intermetallic Compounds in Catalysis - A Versatile Class of Materials Meets Interesting Challenges. *Sci. Technol. Adv. Mater.* **2020**, *21*, 303–322.

#### 6.4.1 Supporting Information

## Supporting information

### Enhancing the Catalytic Activity of Palladium Nanoparticles via Sandwich-Like Confinement by Thin Titanate Nanosheets

Kevin Ament<sup>1</sup>, Daniel R. Wagner<sup>1</sup>, Thomas Götsch<sup>2</sup>, Takayuki Kikuchi<sup>3</sup>, Jutta Kröhnert<sup>2</sup>, Annette Trunschke<sup>2</sup>, Thomas Lunkenbein<sup>2</sup>, Takayoshi Sasaki<sup>3\*</sup>, and Josef Breu<sup>1\*</sup>

1 Bavarian Polymer Institute and Department of Chemistry, University of Bayreuth,  
95447 Bayreuth (Germany)

E-mail: josef.breu@uni-bayreuth.de

2 Department of Inorganic Chemistry, Fritz-Haber-Institut der Max-Planck-Gesellschaft, Faradayweg 4-6, 14195 Berlin (Germany)

3 International Centre for Materials Nanoarchitectonics (WPI-MANA), National Institute for Materials Science (NIMS), 1-1 Namiki, Tsukuba, Ibaraki 305-0044 (Japan)

E-mail: sasaki.takayoshi@nims.go.jp

## Results

S 2

**Table of contents**

1 Experimental Procedures

2 Results and Discussions

    2.1 Small angle X-ray scattering of a nematic titanate phase

    2.2 Characterization of DMAP capped Pd nanoparticles

    2.3 Elemental analysis of L-titanate@Pd@L-titanate

    2.4 Phase evaluation of Pd in L-titanate@Pd@L-titanate catalyst

    2.5 Elemental mapping over L-titanate@Pd@L-titanate

    2.6 Grayscale analysis of L-titanate@Pd@L-titanate

    2.7 Phase evaluation of L-titanate@Pd@L-titanate

    2.8 Ar-Isotherms

    2.9 DRIFT spectra at increasing CO pressure

    2.10 EEL spectra at the O K edge

    2.11 Arrhenius plots

    2.12 Evaluation of the kinetic experiments

    2.13 Long term stability of L-titanate@Pd@L-titanate

3 References

S 4

### 1 Experimental Procedures

#### Materials

PdCl<sub>2</sub> (99.999% Pd, Premion), NaCl, 4-Dimethylaminopyridine (DMAP), NaOH and NaBH<sub>4</sub> were purchased from Alfa Aesar. γ-Al<sub>2</sub>O<sub>3</sub> with high surface area was purchased from Alfa Aesar. The pellets were grounded to a powder before use. Degussa P25 was purchased from Sigma Aldrich. The used water was of MilliQ quality (18.2 MΩ).

#### Catalyst synthesis

##### Synthesis of Pd nanoparticles:

The synthesis of Pd nanoparticles was executed using a modified literature procedure.<sup>1</sup> Palladium(II) chloride (235 mg, 1.33 mmol) and Sodium chloride (155 mg, 2.66 mmol) were dissolved in 40 ml water and 4-Dimethylaminopyridine DMAP (833 mg, 6.82 mmol) in 80 mL water was added. After 20 min of stirring NaBH<sub>4</sub> (110 mg, 2.91 mmol) in 11 ml water was added dropwise under vigorous stirring resulting in a black dispersion. After 2 h the nanoparticle dispersion was dialyzed in 4 l water with water changes after 12 and 24 hours.

K<sub>0.6</sub>[Ti<sub>1.73</sub>Li<sub>0.27</sub>]O<sub>4</sub> was synthesized via solid state synthesis and is described elsewhere.<sup>2</sup> The protonic form was obtained by stirring the solid powder in 1 M HCl solution at room temperature. The solution was replaced each day for 3 days. After this treatment the solid was filtered and washed with excess water to obtain H<sub>1.07</sub>Ti<sub>1.73</sub>O<sub>4</sub> ·H<sub>2</sub>O. For delamination to 0.4 g protonic titanate an aqueous solution of TBAOH (10 %) was added to achieve a molar ratio TBA<sup>+</sup>/H<sup>+</sup> of 1. The mixture was mechanically shaken for 7 days to achieve a nematic phase. The final solid content was 2 g/L.

##### Synthesis of L-titanate@Pd@L-titanate:

Both the aqueous particle and titanate dispersions were adjusted with NaOH resulting in a surface potential of the nanoparticles of 28 mV. The nematic titanate suspension was added rapidly to the nanoparticle dispersion under vigorous stirring. Visible flocculation appeared within 30 seconds. The black flocculate was separated from the supernatant by centrifugation, repeatedly washed and dried at 120 °C. Residual organics were removed by calcination at 500 °C for 5 h. Pd nanoparticles were regenerated under a flow of 30 mL/min (10 % H<sub>2</sub> in N<sub>2</sub>) at 200 °C for 2 h.

##### Synthesis of Pd<sub>exi</sub>@P25:

To a dispersion of Pd nanoparticles (1 mg/ml) Degussa P25 was added under stirring. The amount was chosen to obtain 1 wt% of Pd. After 24 h the resulting black solid was separated by centrifugation and washed several times. The catalyst was dried at 130 °C.

### Synthesis of Pd<sub>ex</sub>@Al<sub>2</sub>O<sub>3</sub>:

To a dispersion of Pd nanoparticles (1 mg/ml) was added γ-Al<sub>2</sub>O<sub>3</sub> under stirring. The amount was chosen to obtain 1 wt% of Pd. The solvent was slowly removed under stirring at 80 °C. The catalyst was finally dried at 130 °C.

To obtain comparable conditions, all catalysts were calcined at 500 °C in flowing air for 5 h, followed by activation at 200 °C in a flow of H<sub>2</sub>(10 vol% in N<sub>2</sub>) for 2 h.

### Measurement and Characterization Techniques

Dynamic light scattering (DLS) and determination of ζ-potential were recorded on a Litesizer 500 (Anton-Paar).

CHN analysis was acquired with an Elementar Vario EL III.

Powder X-ray diffraction (PXRD) measurements were done using a STOE Stadi P diffractometer. Cu<sub>Kα1</sub> radiation and a Mythen 1K silicon strip-detector were used. PXRD of traces of textured samples were recorded on a Bragg-Brentano type diffractometer (Empyrean, PANalytical) with nickel filter and Cu<sub>Kα</sub> radiation ( $\lambda = 1.54187 \text{ \AA}$ ).

SAXS data were measured using a "Double Ganesha AIR" system (SAXSLAB, Denmark). The X-ray source of this laboratory-based system is a rotating anode (copper, MicroMax 007HF, Rigaku Corporation, Japan) providing a microfocused beam. The data is recorded by a position sensitive detector (PILATUS 300 K, Dectris)

Transmission electron microscopy (TEM) images were acquired using a JEOL JEM-2200FS (200 kV). For cross sectional TEM the powder embedded into a resin (EPO-TEK 301) and was cut with an Ar beam into thin slices using a Jeol Cryo Ion Slicer.

Scanning electron microscopy (SEM) images and energy dispersive spectroscopy (EDS) were recorded on a FEI Quanta FEG 250.

Photoelectron spectroscopy (XPS) was conducted on a PHI 5000 Versa Probe III fitted with an Al Ka excitation source and spectra were analyzed with Multipak software pack. Spectra were referenced to C 1s at 284.8 eV.

Electron energy loss spectroscopy (EELS) measurements were conducted using a double-corrected JEOL JEM-ARM200F microscope, operated at 200 kV and equipped with a Gatan GIF Quantum imaging filter with DualEELS capabilities. Plural scattering was removed from all spectra by Fourier ratio deconvolution.

## Results

---

Adsorption isothermes were recorded on a Quantachrome Autosorb-1 with Ar as adsorbate at 87 K. The isotherms were evaluated using Brunauer-Emmet-Teller (BET) method and pore size distribution was evaluated with BJH method. Metal surface was acquired with a Quantachrome Autosorb-1 with CO at 35 °C using the double isotherm method.

Diffuse reflectance infrared Fourier transform (DRIFT) spectra were collected on a Cary 680 FTIR spectrometer from Agilent equipped with a MCT detector and a Praying Mantis™ low temperature reaction cell from Harrick. Spectra were recorded at a spectral resolution of 2 cm<sup>-1</sup> and accumulation of 1024 scans. Samples were dried at 130 °C under a flow of Ar (50 ml/min) over night and then reduced at 150 °C under a flow of H<sub>2</sub> (10 vol%) for 1 h. To remove H<sub>2</sub> the samples were evacuated at 150 °C for 30 min and then let allow to cool to room temperature. Spectra were taken at 300 K. CO isotherms were recorded by dosing CO at increasing equilibrium pressures ranging from 0.03 to 60 mbar. The spectra are presented in Kubelka–Munk units  $F(R_\infty) = (1 - R_\infty)^2/2R_\infty$

### Catalysis

Catalytic tests were conducted in a fixed bed micro reactor with an internal diameter of 4 mm. The desired amount of catalyst was mixed with quartz to achieve an overall loading of 500 mg. The reactor was heated using a circular kiln. To record light-off curves the temperature was raised in 10 °C steps and the temperature was held for 12 min before analysis. A reactant mixture of 1 vol% CO, 1 vol% O<sub>2</sub> und 98 vol% nitrogen with a constant flow of 50 ml/min under atmospheric pressure was injected into the reactor. The composition of the gas mixture leaving the reactor was monitored using an Agilent 6890N gas chromatograph equipped with a 30 m GS CARBONPLOT column and a thermal conductivity detector. The catalysts were cycled three times from 50 to 200 °C and the third light-off curve was recorded. Kinetic experiments and reaction rates were determined well below a conversion of 10 %.

## 2 Results and Discussion

### 2.1 Small angle X-ray scattering of a nematic L-titanate phase.

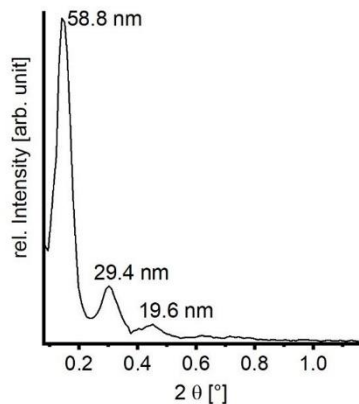


**Figure S1.** SAXS of a nematic L-titanate phase having a solid content of  $2 \text{ g} \cdot \text{L}^{-1}$ .

### 2.2 Characterization of DMAP capped Pd nanoparticles

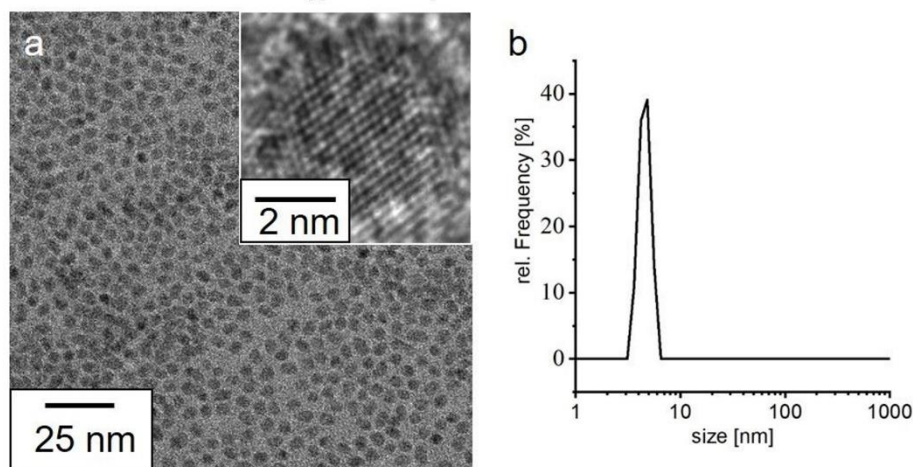


**Figure S2.** a) TEM image of as-synthesized Pd nanoparticles. Inset: High magnification image. b) Hydrodynamic diameter according to dynamic light scattering.

### 2.3 Elemental analysis of L-titanate@Pd@L-titanate

**Table S1.** Elemental composition of L-titanate@Pd@L-titanate

Sample	Fraction of C [wt%] <sup>a</sup>	Fraction of N [wt%] <sup>a</sup>	Fraction of H [wt%] <sup>a</sup>	Fraction of Pd [wt%] <sup>b</sup>
(TBA <sup>+</sup> /H <sup>+</sup> ) <sub>1.07</sub> Ti <sub>1.73</sub> O <sub>4</sub>	48.09	3.43	8.21	/
L-titanate@Pd@L-titanate	5.77	0.44	1.29	/ <sup>c</sup>
L-titanate@Pd@L-titanate after 500 °C for 5 h	0.2	0.01	0	49.3

<sup>a</sup> determined by CHN analysis

<sup>b</sup> determined by SEM-EDS

<sup>c</sup> not determined

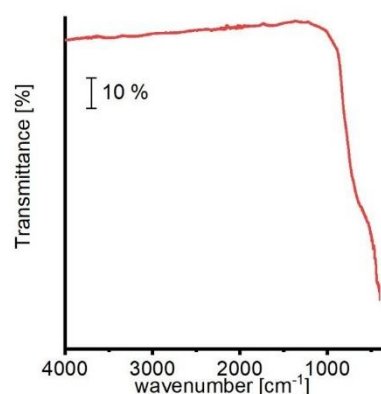


**Figure S3.** FTI spectrum of L-titanate@Pd@L-titanate.

2.4 Phase evaluation of Pd in L-titanate@Pd@L-titanate catalyst

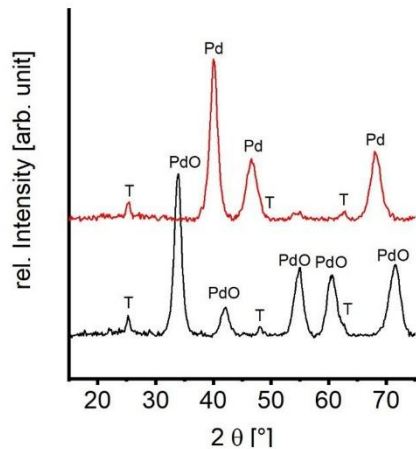


**Figure S4.** PXRD of L-titanate@Pd@L-titanate calcined for 5 h at 500 °C in air atmosphere (black) and after reduction at 200 °C for 2 h under a flow of H<sub>2</sub> (10 vol% in N<sub>2</sub>) (red). T stands for reflections derived from the L-titanate nanosheets.<sup>2</sup>

2.5 Elemental mapping over L-titanate@Pd@L-titanate

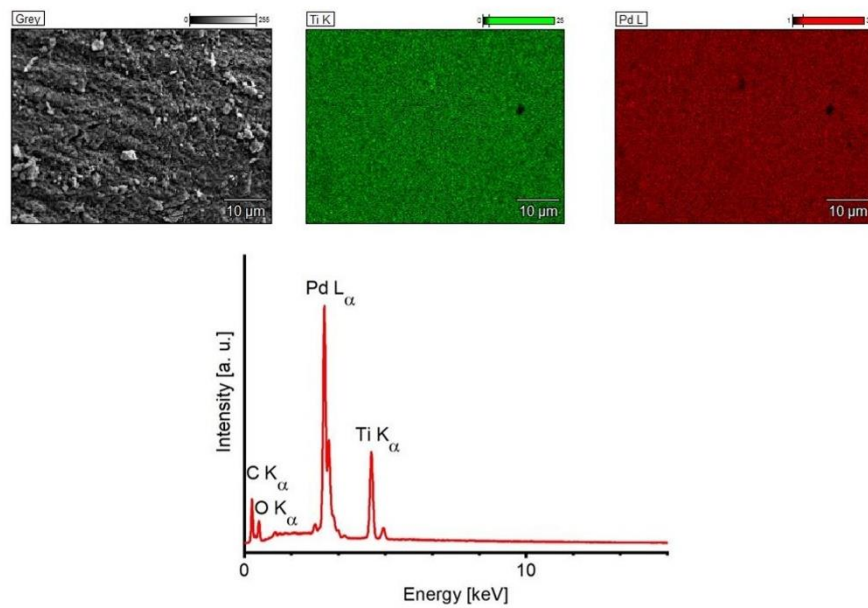


**Figure S5.** Elemental mapping of Ti and Pd showing a homogenous distribution of Pd and Ti over the tactoids and the corresponding spectrum.

2.6 Grayscale analysis of L-titanate@Pd@L-titanate

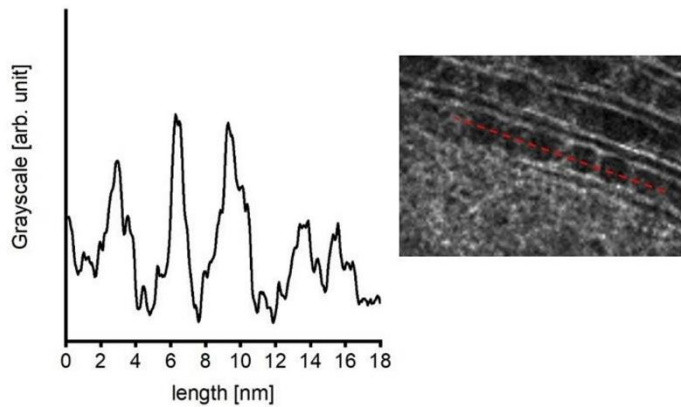


**Figure S6.** Grayscale analysis over a nanoparticle layer (red dotted line) between L-titanate nanosheets. The grayscale shows gaps between the nanoparticles proving a not densely packed assembly.

2.7 Phase evaluation of L-titanate@Pd@L-titanate

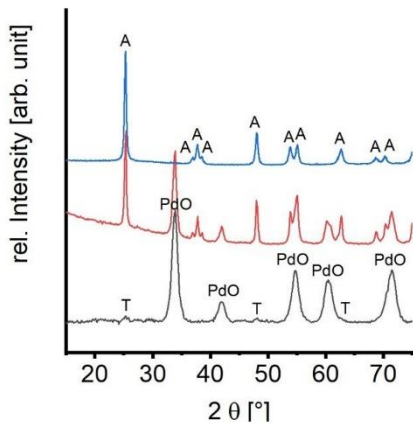


**Figure S7.** PXRD of L-titanate@Pd@L-titanate after calcination at 700 °C (black), calcination at 750 °C (red), and  $(\text{TBA}/\text{H})_{1.07}\text{Ti}_{1.73}\text{O}_4$  after calcination at 500 °C. T stands for reflections derived from the L-titanate nanosheets.<sup>2</sup> A stands for reflections from anatase phase. The PdO reflections remain very broad even after treatment at 700 °C. Only above 700 °C the network breaks down which allows the nanoparticles to grow (narrower reflections) and the L-titanate transforms to the anatase phase.

2.8 Ar-Isotherms

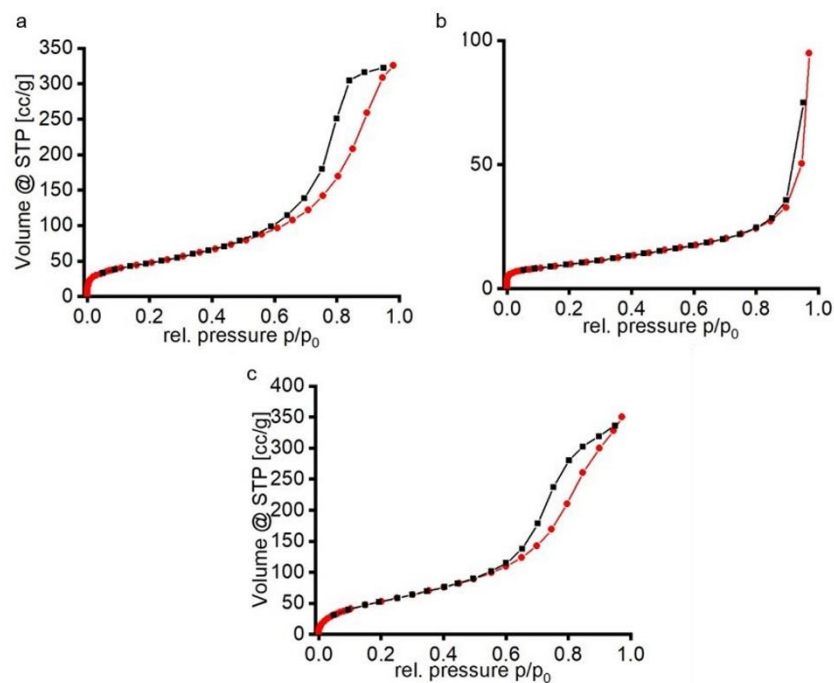


**Figure S8.** Ar Isotherms after calcination at 500 °C of a) L-titanate@Pd@L-titanate, b) Pd<sub>ext</sub>@P25, and c) Pd<sub>ext</sub>@Al<sub>2</sub>O<sub>3</sub>.

2.9 DRIFT spectra

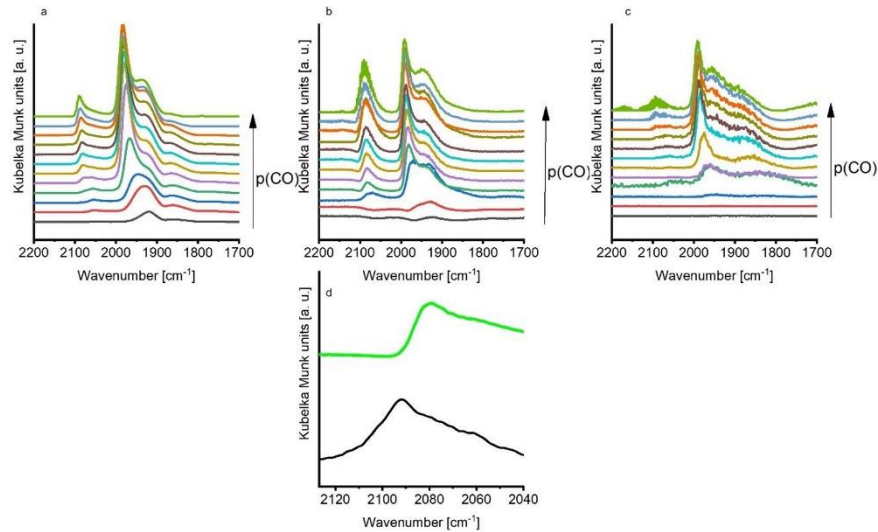


**Figure S9.** Drift spectra of a) Pd<sub>ext</sub>@Al<sub>2</sub>O<sub>3</sub>, b) Pd<sub>ext</sub>@P25, and c) L-titanate@Pd@L-titanate at increasing partial pressures of CO up to 60 mbar. d) zoom of the top region of L-titanate@Pd@L-titanate (black) and Pd<sub>ext</sub>@Al<sub>2</sub>O<sub>3</sub>.

2.10 EEL spectra at the O K edge

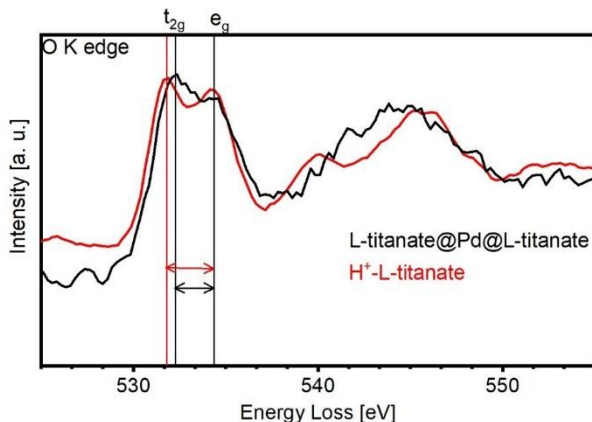


**Figure S10.** EEL spectra at the O K edge of L-titanate@Pd@L-titanate (black) and H<sup>+</sup>-L-titanate (red) showing different extends of crystal field splitting.

2.11 Arrhenius plots

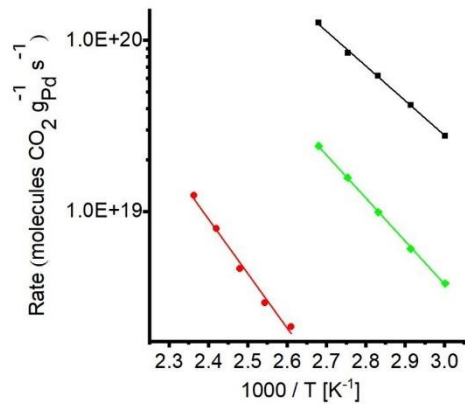


**Figure S11.** Arrhenius plots of L-titanate@Pd@L-titanate (black), Pd<sub>ext</sub>@P25 (green), and Pd<sub>ext</sub>@Al<sub>2</sub>O<sub>3</sub> (red).

## Results

---

### 2.12 Evaluation of the kinetic experiments

The rate of mol of CO<sub>2</sub> produced per second was calculated as follows:

$$rate = \frac{Flow\ rate\ of\ CO \left[ \frac{L}{min} \right] \cdot \frac{1\ mol}{22.4\ L} \cdot Conversion}{60 \left[ \frac{s}{min} \right] \cdot g_{Pd}}$$

The change in rate was measured in terms of various partial pressures of CO and O<sub>2</sub>. The kinetic equation is:

$$rate = k \cdot [CO]^a \cdot [O_2]^b$$

The partial pressure of one species was fixed while the other was changed in steps. The corresponding partial pressures of each step are listed in Table S2:

**Table S 2.** Gas partial pressures and reaction rates of L-titanate@Pd@L-titanate.

Point	ml/min (CO)	p(CO) [mbar]	ml/min (O <sub>2</sub> )	p(O <sub>2</sub> ) [mbar]	Rate [mol CO <sub>2</sub> s <sup>-1</sup> g <sup>-1</sup> Pd]
1	0.5	10.13	0.25	5.06	4.47607E-5
2	0.5	10.13	0.25	5.06	4.45398E-5
3	0.5	10.13	0.5	10.13	5.36554E-5
4	0.5	10.13	0.5	10.13	5.35515E-5
5	0.5	10.13	1.0	20.26	6.63204E-5
6	0.5	10.13	1.0	20.26	6.52704E-5
7	0.5	10.13	0.25	5.06	4.46675E-5
8	0.5	10.13	0.25	5.06	4.42985E-5
9	1.0	20.26	0.25	5.06	5.06409E-5
10	1.0	20.26	0.25	5.06	5.07298E-5
11	2.0	40.52	0.25	5.06	5.57622E-5
12	2.0	40.52	0.25	5.06	5.63976E-5

The calculation of *a* and *b* is demonstrated for the transition from point 2 to 3, when the partial pressure of O<sub>2</sub> is doubled.

$$\frac{4.45 \cdot 10^{-5} s^{-1} g^{-1}}{5.37 \cdot 10^{-5} s^{-1} g^{-1}} = \frac{k \cdot [10.13]^a \cdot [5.06]^b}{k \cdot [10.13]^a \cdot [10.13]^b} =$$

## Results

---

$$0.83 = 0.5^b$$

$$\ln(0.83) = \ln(0.5^b) = b \cdot \ln(0.5)$$

$$b = 0.27$$

The same calculations were done for the transition from point 4 to 5 which obtained  $b$  of 0.31. The average is 0.29.

The same calculations were done for variations of CO obtaining  $a$  of 0.13.

So the rate equation can be expressed as:

$$rate = k \cdot [CO]^{0.13} \cdot [O_2]^{0.29}$$

The calculations were done for Pd<sub>ext</sub>@Al<sub>2</sub>O<sub>3</sub> as well using the values from Table S 3:

**Table S 3.** Gas partial pressures and reaction rates of L-titanate@Pd@L-titanate

Point	ml/min (CO)	p(CO) [mbar]	ml/min (O <sub>2</sub> )	p(O <sub>2</sub> ) [mbar]	Rate [mol CO <sub>2</sub> s <sup>-1</sup> g <sup>-1</sup> Pd]
1	0.5	10.13	0.25	5.06	1.42724E-5
2	0.5	10.13	0.25	5.06	1.46914E-5
3	0.5	10.13	0.5	10.13	2.58875E-5
4	0.5	10.13	0.5	10.13	2.5091E-5
5	0.5	10.13	1.0	20.26	5.02798E-5
6	0.5	10.13	1.0	20.26	5.01251E-5
7	0.5	10.13	0.25	5.06	1.25558E-5
8	0.5	10.13	0.25	5.06	1.25683E-5
9	1.0	20.26	0.25	5.06	7.70412E-6
10	1.0	20.26	0.25	5.06	8.17334E-6
11	2.0	40.52	0.25	5.06	5.22527E-6
12	2.0	40.52	0.25	5.06	5.0282E-6

In this case the rate equation was determined to be:

$$rate = k \cdot [CO]^{-0.67} \cdot [O_2]^{0.91}$$

2.13. Long term stability of L-titanate@Pd@L-titanate

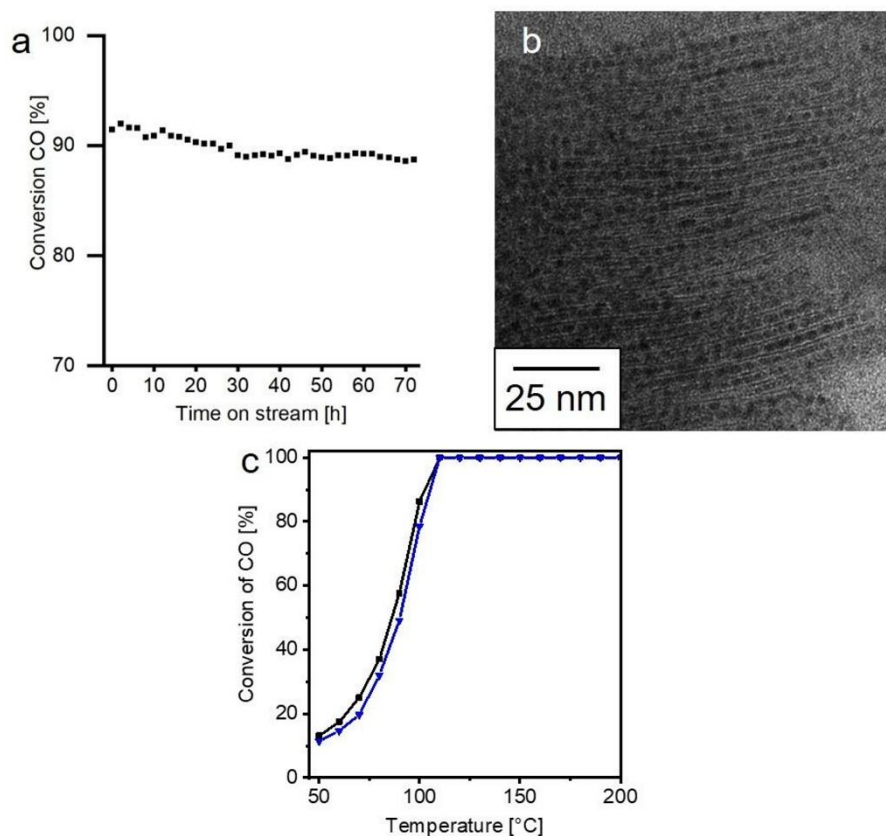


**Figure S12.** a) Stability test of L-titanate@Pd@L-titanate. Conditions: 100 °C, feed gas: 50 mL/min (1 vol% CO, 1 vol% O<sub>2</sub>, balanced by N<sub>2</sub>). b) TEM image of the used catalyst. C) Light-off curve of L-titanate@Pd@L-titanate after calcination at 500 °C for 5 h (black) and after calcination at 700 °C (blue).

### 3 References

- (1) Flanagan, K. A.; Sullivan, J. A.; Müller-Bunz, H. Preparation and Characterization of 4-Dimethylaminopyridine-Stabilized Palladium Nanoparticles. *Langmuir* **2007**, *23*, 12508-12520.
- (2) Tanaka, T.; Ebina, Y.; Takada, K.; Kurashima, K.; Sasaki, T. Oversized Titania Nanosheet Crystallites Derived from Flux-Grown Layered Titanate Single Crystals. *Chem. Mater.* **2003**, *15*, 3564-3568.

## 7 List of publications

### 7.1 First author publications

[1] **K. Ament**, D. R. Wagner, F. E. Meij, F. E. Wagner, J. Breu: High Temperature Stable Maghemite Nanoparticles Sandwiched between Hectorite Nanosheets, *Z. Anorg. Allg. Chem.* **2020**, 646, 1110-1115 DOI: 10.1002/zaac.202000077

[2] **K. Ament**, N. Köwitsch, D. Hou, T. Götsch, J. Kröhnert, C. J. Heard, A. Trunschke, T. Lunkenbein, M. Armbrüster, J. Breu: Nanoparticles Supported on Sub-Nanometer Oxide Films: Scaling Model Systems to Bulk Materials, *Angew. Chem. Int. Ed.* **2021**, 60, 5890-5897 DOI: 10.1002/anie.202015138

[3] **K. Ament**, N. Köwitsch, D. Hou, T. Götsch, J. Kröhnert, C. J. Heard, A. Trunschke, T. Lunkenbein, M. Armbrüster, J. Breu: Nanopartikel auf subnanometer dünnen oxidischen Filmen: Skalierung von Modellsystemen, *Angew. Chem.* **2021**, 133, 5954-5961 DOI: 10.1002/ange.202015138

[4] **K. Ament**, D. R. Wagner, T. Götsch, T. Kikuchi, J. Kröhnert, A. Trunschke, T. Lunkenbein, T. Sasaki, J. Breu: Enhancing the Catalytic Activity of Palladium Nanoparticles via Sandwich-Like Confinement by Thin Titanate Nanosheets, *ACS Catal.* **2021**, 11, 2754-2762 DOI: 10.1021/acscatal.1c00031

[5] **K. Ament**, H. Kobayashi, K. Kusada, J. Breu, H. Kitagawa: Enhancing Hydrogen Storage Capacity of Pd Nanoparticles by Sandwiching between Inorganic Nanosheets, *Z. Anorg. Allg. Chem.* **2022**, accepted DOI: 10.1002/zaac.202100370

### 7.2 Additional publications

[6] N. Deibl, **K. Ament**, R. Kempe: A Sustainable Multicomponent Pyrimidine Synthesis, *J. Am. Chem. Soc.* **2015**, 137, 12804-12807 DOI: 10.1021/jacs.5b09510

[7] E. S. Tsurko, P. Feicht, F. Nehm, **K. Ament**, S. Rosenfeldt, I. Pietsch, K. Roschmann, H. Kalo, J. Breu: Large Scale Self-Assembly of Smectic Nanocomposite Films by Doctor Blading versus Spray Coating: Impact of Crystal Quality on Barrier Properties, *Macromolecules* **2017**, 11, 4344-4350 DOI: 10.1021/acs.macromol.7b00701

[8] C. Bojer, **K. Ament**, H. Schmalz, J. Breu, T. Lunkenbein: Electrostatic attraction of nanoobjects - a versatile strategy towards mesostructured transition metal compounds, *CrystEngComm* **2019**, 21, 4840-4850 DOI: 10.1039/c9ce00228f

[9] D. R. Wagner, **K. Ament**, L. Mayr, T. Martin, A. Bloesser, H. Schmalz, R. Marschall, F. E. Wagner, J. Breu: Terrestrial solar radiation driven photodecomposition of ciprofloxacin in

clinical wastewater applying mesostructured iron(III) oxide, *Environ. Sci. Pollut. Res.* **2021**, *28*, 6222-6231 DOI: 10.1007/s11356-020-10899-6

### 7.3 Conference contributions

[1] **Presentation:** Ordered Heterostructures of Nanoparticles in Synthetic Hectorite as potential (High Temperature) Catalysts, BTHA workshop, 22. – 23.11.2017, Erlangen

[2] **Poster:** Synthesis and Applications of Sandwich-like Nanoparticle@Hectorite Catalysts, 19th International Symposium on the Reactivity of Solids, 15. – 18.07.2018, Bayreuth

[3] **Presentation:** Ordered Intercalation of Nanoparticles into Synthetic Hectorite for Catalytic Applications, Advances in Low-dimensional Materials, 18. - 21.09.2018, Liblice (Czech Republic)

[4] **Presentation:** Nanoparticle@Hectorite catalysts for high temperature and photocatalysis, BTHA workshop, 27. – 28.03.2019, Bayreuth

## 8 Acknowledgements

Eine Promotion ist niemals eine Einzelleistung, sondern bedarf der Unterstützung vieler.

Mein erster Dank soll natürlich meinem Doktorvater Josef Breu gebühren. Ich bin dankbar für die sehr spannende und anspruchsvolle Themenstellung. Ich bin sehr froh, dass ich immer „an der langen Leine laufen“ durfte und stets die Dinge verwirklichen durfte, die ich am spannendsten und vielversprechendsten hielt. Dies hat mich als Wissenschaftler reifen lassen. Trotzdem war er immer für intensive Diskussionen und einen guten Ratschlag da. Nicht zuletzt bin ich auch für die Unterstützung dankbar, die mir den Aufenthalt in Japan ermöglicht hat.

Lieber Josef, vielen Dank für die Zeit an deinem Lehrstuhl!

Ich danke Takayoshi Sasaki und Hiroshi Kitagawa für die freundlichen Einladungen, um in ihren Gruppen in Japan zu forschen. Ich bin dankbar für die überwältigende Gastfreundschaft und die grenzenlose Hilfsbereitschaft, die mir dort entgegengebracht wurden. Die Erfahrung im Ausland hat mich sehr geprägt und mich in meiner persönlichen Entwicklung weitergebracht.

Ich bedanke mich beim Elitenetzwerk Bayern, das mich sowohl mit einem Forschungsstipendium finanziell unterstützt hat, aber auch ideell durch die Aufnahme in das Elitestudienprogramm „Macromolecular Science.“

Während meiner Promotion durfte ich mit vielen Kooperationspartnern zusammenarbeiten. Deren Expertise und Hilfsbereitschaft wirkte sich sehr positiv auf meine Arbeit aus. Mein herzlicher Dank geht an „Fritz“ Wagner, Nicolas Köwitsch, Marc Armbrüster, Dianwei Hou, Christopher J. Heard, Thomas Götsch, Jutta Kröhnert, Annette Trunschke, Hirokazu Kobayashi, Kohei Kusada und Takayuki Kikuchi. Ich danke Rhett Kempe, dass er mir freie Hand an seinem Microreaktor gewährt hat. Ohne den Zugang zu diesem Gerät hätte ich die Katalysen nicht durchführen können. Ein besonderer Dank geht dabei an Thomas Lunkenbein, der meine Verbindung zum Fritz-Haber-Institut in Berlin war und mir Kontakt zu vielen Experten ermöglicht hat.

Arbeit kann nur Spaß machen und erfolgreich sein, wenn in der Arbeitsgruppe eine gute Atmosphäre herrscht. Ich hatte eine tolle Zeit im Labor mit Daniel, Matthias, Patrick und Lina. Ich bedanke mich bei allen weiteren Angehörigen der Lehrstühle AC1 und AC3 für Diskussionen, Hilfe und natürlich schöne gemeinsame Erlebnisse. Die Diskussionen mit Wolfgang Milius haben mir stets gut getan. Ich danke unseren Technikern Marco Schwarzmüller, Florian Puchtler und Lena Geiling für ihre unermüdliche Unterstützung.

Insbesondere möchte ich mich bei Daniel, Patrick und Simon für ihre Freundschaft, die weit über die Arbeit hinausgeht, bedanken. Ich habe jedes unserer kleinen Kaffeekränzchen

## Acknowledgements

---

genossen! Auch Tobi und Marion möchte ich für unsere Freundschaft danken. Ich hoffe wir bleiben auch über die Uni hinaus noch lange in Kontakt!

Während meiner Zeit in Bayreuth durfte ich viele interessante Leute kennen lernen. Viele Dank für all die Erlebnisse, die ich mit euch teilen durfte. Unsere Stammtische im Oskar werde ich sicherlich vermissen: Chris, Fredes, Martin und Fabi!

Während meiner Promotion durfte ich zahlreiche Praktikanten betreuen, die mich in meiner Arbeit unterstützt haben. Vielen Dank euch! Natürlich möchte ich meine beiden Bacheloranden Patrick und Freddy hier besonders hervorheben. Ihr habt gute Arbeit geleistet!

Ich möchte mich beim Alumni-Verein der Chemie „CSG e.V.“ für all die tollen Veranstaltungen bedanken und vor allem meinen Vorstandsmitgliedern während meiner Zeit als Vorstand für die tolle Unterstützung danken.

Natürlich möchte ich auch meine Freunde in der Heimat nicht vergessen. Ich bin dankbar, dass der Kontakt auch so lange nach der Schule immer noch so intensiv ist und wir uns immer noch regelmäßig auf ein Bierchen treffen.

Ich bedanke mich bei all denen, die diese Arbeit Korrektur gelesen haben und mir erklärt haben, ob meine Gedanken auch für andere verständlich sind.

Meinen vorletzten Dank möchte ich den stillen Anteilhabern an dieser Arbeit zukommen lassen: **Meiner Familie und meiner Freundin Bella.** Ihr habt mich immer und ohne Kompromisse unterstützt und wir haben in den letzten Jahren gemeinsam das ein oder andere Unwetter überstanden. Ohne euch wäre das alles nicht möglich gewesen!

Der letzte Dank gilt meiner **Oma Helga**, die mein ganzes Leben für mich da war und ihr letztes Hemd für mich gegeben hätte. Ich vermisste dich jeden Tag!

## 9 Erklärung des Verfassers

(Eidesstattliche) Versicherungen und Erklärungen

(§ 9 Satz 2 Nr. 3 PromO BayNAT)

Hiermit versichere ich eidesstattlich, dass ich die Arbeit selbstständig verfasst und keine anderen als die von mir angegebenen Quellen und Hilfsmittel benutzt habe (vgl. Art. 64 Abs. 1 Satz 6 BayHSchG).

(§ 9 Satz 2 Nr. 3 PromO BayNAT)

Hiermit erkläre ich, dass ich die Dissertation nicht bereits zur Erlangung eines akademischen Grades eingereicht habe und dass ich nicht bereits diese oder eine gleichartige Doktorprüfung endgültig nicht bestanden habe.

(§ 9 Satz 2 Nr. 4 PromO BayNAT)

Hiermit erkläre ich, dass ich Hilfe von gewerblichen Promotionsberatern bzw. -vermittlern oder ähnlichen Dienstleistern weder bisher in Anspruch genommen habe noch künftig in Anspruch nehmen werde.

(§ 9 Satz 2 Nr. 7 PromO BayNAT)

Hiermit erkläre ich mein Einverständnis, dass die elektronische Fassung meiner Dissertation unter Wahrung meiner Urheberrechte und des Datenschutzes einer gesonderten Überprüfung unterzogen werden kann.

(§ 9) Satz 2 Nr. 8 PromO BayNAT)

Hiermit erkläre ich mein Einverständnis, dass bei Verdacht wissenschaftlichen Fehlverhaltens Ermittlungen durch universitätsinterne Organe der wissenschaftlichen Selbstkontrolle stattfinden können.

---

Ort, Datum, Unterschrift